TESIS DE LA UNIVERSIDAD DE ZARAGOZA

2013

43

Irene Calvo Almazán

Molecular diffusion on surfaces: the diffusive behavior of aromatic compounds absorbed on graphitic surfaces studied with Quasi-Elastic-Neutron Scattering (QENS)

Departamento

Física de la Materia Condensada

Director/es

García Vinuesa, Luis Miguel
Fouquet, Peter
Miret Artés, Salvador

ISSN 2254-7606

Prensas de la Universidad Universidad Zaragoza

Universidad Zaragoza
1542

Tesis Doctoral

MOLECULAR DIFFUSION ON SURFACES: THE DIFFUSIVE BEHAVIOR OF AROMATIC COMPOUNDS ABSORBED ON GRAPHITIC SURFACES STUDIED WITH QUASI-ELASTIC-NEUTRON SCATTERING (QENS)

Autor

Irene Calvo Almazán

Director/es

García Vinuesa, Luis Miguel
Fouquet, Peter
Miret Artés, Salvador

UNIVERSIDAD DE ZARAGOZA

Física de la Materia Condensada

2013

Molecular diffusion on surfaces

–

The diffusive behavior of aromatic compounds adsorbed on graphitic surfaces studied with quasi-elastic neutron scattering (QENS)

Molecular diffusion on surfaces

–

The diffusive behavior of aromatic compounds adsorbed on graphitic surfaces studied with quasi-elastic neutron scattering (QENS)

Irene Calvo Almazán

A mis padres

Contents

Introduction

Diffusion on surfaces is an extremely wide subject of paramount importance for fundamental research in condensed matter physics and technological development in industry [1, 2]. We can cite some representative examples, among a large number of technological applications benefitting from our knowledge of the dynamics of atoms and molecules on surfaces. Material science is nowadays concerned by processes like aggregation, epitaxial growth and self-assembly of nano-structures on the surface [3]. All this process are governed by the diffusive behavior of adsorbates on the surface and the rate of growth of the nucleation phenomenon can be directly related to the adsorbates diffusivity [1, 4–7]. Heterogenous catalysis, is a central issue in industrial production of chemicals, and diffusion on the surface plays a key role since it usually involves mass transports of reactants and products [5, 8] Besides, the morphology of the reactants is influenced by diffusive processes on the surface which should be taken into account in view of an optimization of the catalytic reaction [7]. The diffusive behavior of adsorbates on a surface is a powerful tool to probe the microscopic origin of friction, and contributes to the discovery and improvement of lubricant materials [9–12]. Nano-technologies also benefits from a deep understanding of the nature of friction and the interaction between adsorbates and phonons or electrons on the surface of the substrate [13–15]. Recent investigations have succeed in designing and fabricating nano-devices driven by a thermally induced flow of phonons [13] and important efforts concentrate in atomic-scale mechanisms ruled by electric current [14, 15].

From the fundamental research standpoint, molecules adsorbed on a surface are an excellent probe to explore the surface energy landscape of the substrate [16, 17]. Besides, diffusion on surfaces is ubiquitous [6]: it takes place in all kind of substrates and involves all kind of adsorbates, from single atoms to large hydrocarbon chains. Thereby, the mechanisms underlying diffusion are manifold: from surface phonons creation/annihilation processes caused by the vibrations of the adsorbate in the adsorption energy minima, to electron-hole pair excitations, or a large variety of adsorbate-adsorbate interactions (colli-

sions, van der Waals forces or electrostatic interactions) [6]. It is clear that diffusion on surfaces is a very rich and complex field [6] where thermodynamical, structural and dynamical properties of the adsorbed layer are strongly interrelated. As a result, dressing a complete description of diffusive phenomena requires a multifaceted approach. Theoretical models to describe diffusive phenomena aim to connect the macroscopic properties of diffusion with the microscopic character of the atomic motion [18]. In the macroscopic scale, the diffusion of adsorbates on a substrate is governed by the Fick's laws [6]. The first Fick law relates the diffusion flux of adsorbates $\mathbf{J}(\mathbf{r},t)$ to the adsorbate density gradient $\nabla\rho(\mathbf{r},t)$ [6]:

$$\mathbf{J}(\mathbf{r},t) = -D_c\nabla\rho(\mathbf{r},t),$$

through the *diffusion coefficient* D_c, which is a scalar if the diffusion is isotropic, but becomes a tensor if the diffusion is anisotropic [5]. The second Fick law establishes the time evolution of the density of adsorbates [4]:

$$\frac{\partial\rho(\mathbf{r},t)}{\partial t} = -D_c\nabla^2\rho(\mathbf{r},t).$$

The first and successful attempt to connect the macroscopic quantity of the diffusion coefficient, D_t, to the atomic dynamics was achieved by Einstein [4,19] and yields:

$$D_t = \lim_{t\to\infty}\frac{1}{2dNt}\sum_{i}^{N}\left\langle\Delta\mathbf{r}_i^2\right\rangle$$

where $\left\langle\Delta\mathbf{r}_i^2\right\rangle$ is the mean square displacement of the i-th atom performing a random walk in a space of d dimensions, over time t. However, the resulting diffusion coefficient is the so-called *tracer diffusion coefficient*, D_t, because it is associated with the motion of single particles [5,6]. It should be distinguished from the diffusion coefficient appearing in the Fick's law, D_c, also known as the *the collective diffusion coefficient* which measures the decay of density fluctuations over very long times [4]. If there are no interaction between adsorbates, as if the system was behaving as an ideal gas, the tracer and the collective diffusion coefficient are equivalent [6] otherwise they are distinct and the connection between them is not trivial [4]. Starting from the Einstein discovery, and applying mechanical statics theories such as the fluctuation-dissipation theorem [20], it is possible to link the macroscopic description of diffusion (the diffusion coefficient) to specific functions portraying directly the dynamics in the atomic scale such as the velocity correlation function [4,21]. In the microscopic scale, atoms perform discrete jumps over the different adsorption sites on the substrate. Thus, the mean square displacement is a function of the distribution of jump lengths, $\left\langle l^2\right\rangle$, and of jump rates, Γ [4,6] and the tracer

diffusion coefficient can be written as a function of these microscopic parameters [6]:

$$D_t = \frac{1}{2d}\Gamma \left\langle l^2 \right\rangle .$$

If diffusion is an activated process because the adsorbates need to overcome energy barriers to pass from one equilibrium position to the next one, and tunneling is excluded, the jump rate follows an Arrhenius law [4]:

$$\Gamma = \Gamma_0 \exp\left[-\frac{E_a}{k_B T}\right]$$

where the activation energy E_a stems from the height of the barriers, and the pre-factor Γ_0 is the real dynamic quantity since it evaluates the attempt of the adsorbed particle to jump over the barrier [4,6]. It is a function of temperature and can be calculated through different methods such as the transition state theory [4]:

$$\Gamma_0 = \frac{k_B T}{h} \exp\left[-\frac{\Delta S}{k_B T}\right],$$

where k_B is the Boltzmann constant, T is the temperature, h is the Planck constant and ΔS is the activation entropy corresponding to the change in entropy in the system adsorbate/system when the adsorbate moves from the potential energy minimum to the saddle point (the top of the energy barrier). As a result, the diffusion of the atoms on the surface is strongly dependent on temperature. If the temperature of the system is such that $k_B T \ll E_a$, then adsorbates spend most of their time trapped in the equilibrium well and performing oscillations around the minimum position [5]. Occasionally they jump to neighboring sites. Since jumps are considered to be instantaneous and are separate by long lapse of times (of the order of $\sim 1/\nu_0$, where ν_0 is the frequency of the vibration of the adatom in the well), we assume that successive jumps are uncorrelated [5]. Thus, in the case of activated diffusion the tracer diffusion coefficient follows the Arrhenius law of temperature, exactly as the jump rate does [6]:

$$D_t = D_0 \exp\left[-\frac{E_a}{k_B T}\right]. \tag{1}$$

Conversely, when the temperature is high enough to provide the adsorbates with a thermal energy comparable with the activation energy, $k_B T \sim E_a$, the lateral barriers for motion become negligible and the adparticles diffuses. This regime can be described by a two dimensional Brownian motion, and the diffusion coefficient adopts the well known Einstein expression [5, 20]:

$$D_t = \frac{k_B T}{m\eta},$$

The second important macroscopic quantity characterizing diffusion is the friction parameter, η, which quantifies the exchange rate of energy between the

diffusing particle and its environment (the substrate or the neighboring particles) in the macroscopic scale . It is related to the velocity autocorrelation function via the Green-Kubo formula (or equivalently the fluctuation-dissipation theorem) [18, 20, 21]:

$$\eta = \frac{1}{k_B T} \int_0^\infty \langle \mathbf{v}(0)\mathbf{v}(t) \rangle \, dt.$$

The advent of computer science has also boosted significantly the progress in the theoretical aspect of diffusion. The simulation of the adsorbate trajectories allows the numerical calculation of essential microscopic functions like the mean square displacement or the velocity correlation functions [22]. The upgrade of computers power and the combination of molecular dynamics simulations with experimental techniques brings the interpretation of the experimental data beyond the traditional models for diffusion [23]. From the standpoint of experimental surface science, the progresses and achievements in the field are also impressive [1, 24]. The multiplication and improvement of surface specific techniques allows currently to investigate the atomic motion in scales of time and space covering the typical times of adsorbate-adsorbate interaction (the pico and nanosecond time scale) and distances were the discrete nature of matter becomes apparent (the sub-nanometer range) [1]. In this case, neutron scattering techniques appear as a singular method to probe the dynamics of atoms and molecules on the surface [25]. Despite of their well known capacity to penetrate matter, neutrons bring to light very interesting information about the nature of diffusive processes on the surface [26, 27] and are very sensitive to the diffusion of very light atoms like hydrogen which are difficult to spot with other techniques such as X-rays.

Motivations and outline

In this work we investigate in length the diffusion of aromatic rings, benzene molecules, adsorbed on the basal plane [0001] of graphite. This system is a prototype for modeling the forces binning together the layers of graphene which form graphite crystals [28]. Many studies exist addressing the question of benzene adsorption on graphite from different perspectives: thermodynamics (phase transitions and heat capacity) [29–36], structure of the adsorbed layer (debate about the direction of adsorption of the benzene molecules) [37–44]. We are interested in the dynamical aspect. There are many open questions concerning the physics underlying the diffusive behavior of benzene molecules on the graphite. Very recent studies show [45] that in the sub-monolayer regime, benzene molecules undergo a perfect Brownian motion. The origin of the friction was attributed to phononic annihilation/creation processes and no dependence on the coverage was observed. We intend to nail down in the influence

of coverage and temperature in the diffusive behavior of benzene molecules on the basal plane of graphite. For this purpose we have perform several measurements of neutron quasi-elastic spectrum of benzene adsorbed on graphite, at different coverages (from the very low coverage regime 0.1 ML to the complete monolayer 1.0 ML) and in a wide range of temperatures, from 60K to 140K. We use the neutron spectroscopy technique of time-of-flight and we combine measurements on hydrogenated C_6H_6 and deuterated benzene C_6D_6. Since neutrons can be coherent or incoherently scattered, the resulting quasi-elastic spectra arising from C_6H_6 or C_6D_6 displays differences which can be attributed to correlated dynamics in time and space. We obtain a complementary view on the diffusion process which helps us to improve the understanding of the physical mechanisms governing the diffusion, and in particular, to identify the main source of friction in this system.

The dissertation is organized as follows: Chapter 1 introduces the main experimental technique, neutron time-of-flight spectroscopy, which is compared to surface specific techniques. We aim to highlight the unique place of neutrons in surface studies, and the important role played by substrates like exfoliated graphite which display a large surface/volume rate. In Chapter 2 we review the theoretical framework within which surface diffusion models can be developed. We also provide a succinct description of molecular dynamics calculations, since it is a useful tool for the interpretation of neutron quasi-elastic data, even though in this work we do not present any MD simulation result. Chapter 3 contains the description of the samples and the experimental conditions in which we operate with the time of flight spectroscope IN6 (ILL, Grenoble, France). We also summarize the measured results (the scattering functions) making emphasis in their change with coverage and temperature. Chapter 4 deals with the analysis of the scattering functions. We test several diffusion models to fit the quasi-elastic energy profile. Chapter 5 discusses the results of the fits, and values for the diffusion coefficient and friction parameter are extracted. We drive our attention to the dependence of these parameters on temperature and coverage, since this carries the fingerprint of the physical mechanisms governing the diffusion of the molecules (phononic coupling between molecules and the substrate or collisions between molecules). We also compare the results obtained for deuterated and hydrogenated benzene with the measurements published in Ref. [45]. Finally, Chapter 6 is a summary of the main conclusions that we can draw from the neutron study of the diffusion of benzene adsorbed on the basal plane of graphite. We also give an outlook of possible perspectives for a future development of the present study.

Chapter 1

Quasi-elastic neutron scattering, applied to diffusion of adsorbed species on the surface

This chapter overviews the experimental aspects of neutron studies on surface diffusion. It is divided into two sections. The first section aims to underline the place of *quasi-elastic neutron scattering, QENS,* in surface diffusion studies. The comparison of QENS to other surface specific techniques highlights the kind of information about diffusion processes revealed by neutrons, its limits and the type of systems on which neutrons are especially powerfull. The second section focuses on the neutron time-of-flight technique, which is the main technique in use in this work. A detailed description of their modus operandi, the physical magnitudes which are measured and their dynamical window is provided.

1.1 QENS spectroscopy applied to surface diffusion

Surface diffusion is a complex and ubiquitous phenomenon: it can take place in a myriad of different substrates and involves manifold physical mechanisms. Accordingly there exists a large portfolio of surface specific techniques among which, one finds quasi-elastic neutron scattering. We start this section reviewing the main surface diffusion techniques in use. Then, we focus on the best suited systems to test the power of neutrons for probing surface diffusion. The combination of hydrogenated compounds adsorbed on substrates characterized by a large effective surface area for adsorption constitute excellent samples for the application of neutrons to surface studies.

1.1.1 QENS techniques vs surface specific techniques

A complete description of the diffusion process demands to relate the thermodynamical properties (like the melting and other phase transitions temperature, the coexistence of different phases, the vapor pressure) with the structure of the layer, its chemical composition and the dynamics of the adsorbed particles within the layer. Hence, a detailed study of diffusion process requires a multifaceted experimental approach. Comprehensive reviews discuss the characteristics, advantages and disadvantages of the available methods [5,6,46–49]. This section focuses on the techniques revealing similar aspects of diffusion than QENS techniques. The comparison of the time and distance scales, together with the type of substrates, the kind of diffusion (tracer or chemical diffusion) and the physical information (diffusion coefficients, friction parameters and structural information) affordable for each technique underlines the specific place that QENS occupies in surface diffusion studies. Nevertheless, the lack of overlap in the time and spatial scale between the different techniques [48] renders the comparison of experimental results arising from different measurement methods difficult. Therefore, there is no technique which can give a complete description of diffusion and the interplay between different experimental approach is mandatory.

There are many criterions to classify surface specific techniques: the physical mechanism underlying the measurement method or the way in which information released. For instance, Ref. [48] proposes to distinguish between techniques inducing inhomogeneities in the density of the adlayer which evolve in time according to the Fick's law or techniques measuring the thermal fluctuations of the system in its true thermal equilibrium state. The fluctuation-dissipation theorem allows, in the latter case, to extract the information about diffusion [20]. In general, the surface specific techniques surveying the dynamics and structure of adsorbed layers belong to the second group of techniques and require the sample to be in thermal equilibrium. They can be further classified into two broad groups. First of all, there is the group of microscopic techniques which image the diffusion of individual particles or clusters in real space and time [5,6,47]. On the other side, lie the diffraction and spectroscopy techniques where the dynamical and structural information is released in the Fourier transformed space of momentum and energy transfer. Amongst the latter we will discuss with detail the helium and neutron scattering techniques. The main properties of the experimental methods (resolution, time and length scales, remarks about the kind of samples) are summarized in Tab. 1.1.1 and displayed in Fig. 1.1.

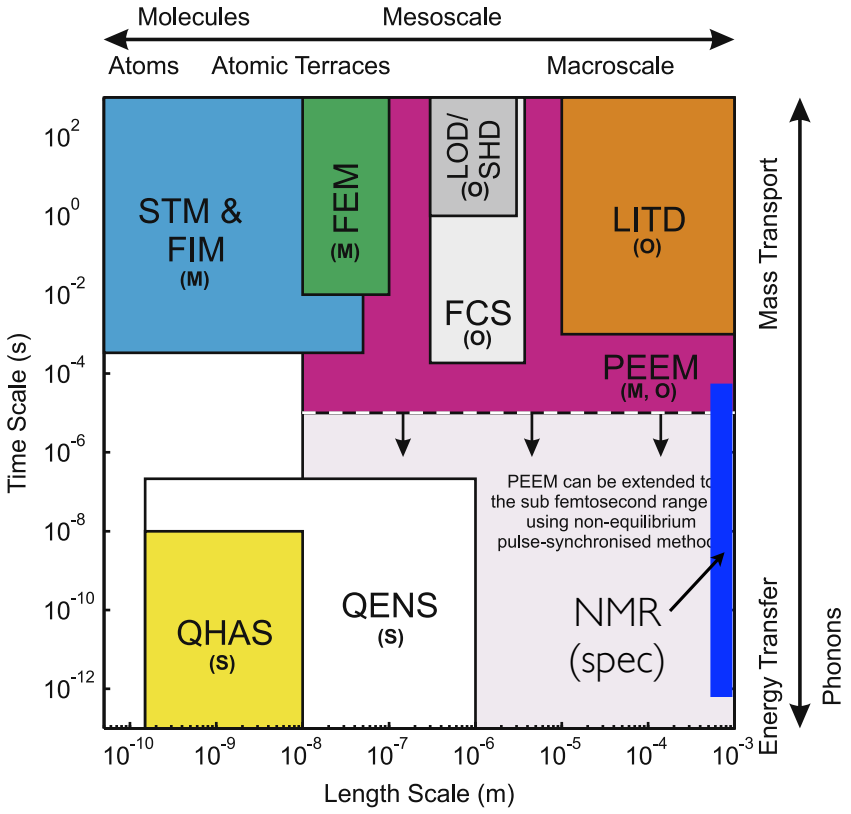

Figure 1.1: Comparison between the length and time scale covered by the most relevant surface specific technique. (M) means microscopic techniques, (O) refers to optical or laser based techniques and (S) refers to scattering techniques. The physical process and the structures observable at the different distances and times scales are also included. The graph has been taken from Ref. [1]. We incorporate the band in time covered by NMR spectroscopy, which does not have spatial resolution.

Thermodynamical techniques Well established *thermodynamical techniques* such as isotherm measurement can determine the area occupied by adsorbed particles and the adsorption dynamics. Calorimetry is an effective method for finding the temperatures of phase transitions and for determining the order of the transition. This techniques often surveys the macroscopic properties of surfaces like the melting temperature or the surface effective area for adsorption of materials.

Optical and laser techniques The idea underlying the application of laser techniques for studying diffusion is that desorption is sensitive to the lateral interaction between adsorbed species [50]. In other words, desorption techniques give also information about the lateral diffusion energetic barrier of the adsorbates and can measure chemical diffusion coefficients D_c (ensuing from the second Fick's law [1]). In the case of laser induced thermal desorption, LITD, a powerful laser pulse irradiates a small spot on the surface, rising the local temperature and desorbing the adparticles lying within the illuminated area. A second pulse is emitted after a lapse of time allowing for the refilling of the depleted region and provoking a new desorption process. In this way the rate of refilling is measured and can be related to the chemical diffusion coefficient (diffusion due to the chemical potential arising from inhomogeneities in the density of adatoms on the surface). Another related technique is the linear (also laser) optical diffraction (LOD) which monitors the smearing out with diffusion of an optical grating pattern [1,51]. LOD covers a very large range of diffusivities, although always over macroscopic distances and time scales. Finally, we include in this section the photoemission electron microscopy, PEEM, which measured the spreading of an adsorbed layer when a coverage gradient is created (by the means of LITD or deposition mask) [5]. On the side of equilibrium methods, we should mention the fluorescence correlation spectroscopy (FCS) which measures the spontaneous fluctuations of molecule concentration in a well defined area of the surface [1]. The diffusion coefficient can be extracted from the decay with time of the fluctuation autocorrelation function [52]. We can approach FCS to the spin-echo technique, as we shall see later.

Microscopic techniques One of the most widely used microscopic procedure for surface studies is the scanning tunneling microscopy, STM, based on the concept of quantum tunneling. STM instruments are made of a sharp and conducting tip whose position is controlled by a piezoelectric motor. When the distance between the tip and a conducting surface is within $\sim$ 1 nm, a tunneling current starts flowing. This current is kept constant by varying the position of the tip with respect to the surface: i.e applying a certain volt-

age to the piezoelectric motor which regulates the movement of the tip. If the voltage is recorded while the tip sweeps the surface, the topography of the surface is imaged. STM is an extremely powerful method for analyzing tracer diffusion on conducting surfaces [5]. It is able to follow an adsorbed atom in its migration on the surface with a resolution of around 10 Å [5]. It is possible to extract hopping rates from a statistical analysis of series of images taken with the microscope [5, 47] and diffusion coefficients of the order $10^{-19} \sim 10^{-16}$ cm^2.s^{-1} are measured [5]. It is worthwhile to mention as weel the atomic force microscopy, AFM: it is a modified STM microscope which pushes the adsorbed species with its tip and measures the force required to move the particle from one adsorption site to the neighboring site across the energy barrier [47]. Forces of the order of pico and nano-Newtons are accessible [53]. Magnitudes like the activation energy for diffusion or the binding energy between the adsorbate and the substrate are deduced from the integration of the forces over the diffusing path [47]. The friction parameter and a sketch of the potential energy surface can also been survey thanks to this method [46]. Other microscopic techniques like the field emission microscopy, FEM, measure the work function of a well localized small area of the surface: the density of electrons (in the form of an electric current) promoted from the conducting band of the substrate to the free state of the microscope metal tip under the influence of a high electric field [5]. Fluctuations in the density of adatoms related to diffusive processes affect the work function of the substrate and, hence, can be observed with the FEM method [47]. A similar idea is applied in field ion microscopy (FIM) which achieves images of surface with a resolution in the range of $3 \sim 50$ Å [5, 47, 48] and measures diffusion coefficients of single metal adatoms of the order of $10^{-17} \sim 10^{-15}$ cm^2.s^{-1} [48]. To summarize, microscopic techniques provide a wealth of information about adsorption processes on the surface with an atomic resolution. They can follow a tracer in their migration on the surface, describe their diffusive behavior and measure their diffusion coefficient and their mean square displacement. They also are sensitive to the binding energy of the adsorbate to the surface and to the activation barrier for lateral motion (translations). Nevertheless their applicability is still reduced to small adsorbates concentrations and slow diffusivities [5]: the typical atomic motion occurs at the picosecond scale which is orders of magnitude faster than the time windows affordable for microscopy techniques [16]. Furthermore, most of them require conducting surfaces to work properly. Finally, an important disadvantage is that the measurement process influences strongly the diffusion in the system: the equilibrium state of the adsorbed layer is seriously disturbed [5, 16].

Diffraction techniques The structure of the adsorbed layers, is studied by the means of diffraction techniques. Among them we can find the low energy electron diffraction (LEED). However, care must be taken with the study of physisorbed layers with LEED since the not very high current electron beam (~ 1 μA) can desorb weakly adsorbed particles [46]. Other techniques such as X-ray diffraction and neutron diffraction image the structure of the adsorbed layer in the Fourier reciprocal space of momentum transfer: the diffraction pattern. Information about the chemical composition of the surface can also be obtained. All this techniques reach perfectly the atomistic resolution (very high momentum transfer range). As a complement we can mention X-ray and neutron reflectometry supplying interesting details such as the surface roughness, morphology and growth processes [46].

Spectroscopy techniques Spectroscopy techniques yields information about the dynamics of adsorbates on the substrates. For instance, nuclear magnetic resonance (NMR) monitor the diffusion of ad-particles by measuring the spin-lattice relaxation spectra [5]. The position of the peaks and their broadening give valuable information about the translational and rotational dynamics of adsorbed species [37, 54, 55]. On the other side, infrared spectroscopy (IR) allows to study in detail the internal degrees of freedom of molecules. In particular it encourages and supplies experimental data for the development of models on the coupling between the vibration-orientation-translation modes of adsorbed molecules [46].

Helium and neutron scattering Quasi-elastic helium scattering and neutron scattering are closely related techniques whose main exprimental function is the scattering function, as it will be explained later, in section 1.2.1. In both cases, the dynamics and the structural information about adsorbates on a surface is probed in the Fourier transformed space of energy/momentum transfer (except for helium and neutron spin-echo which can access the time/momentum transfer domain [16, 46, 56, 57]). In particular, the quasi-elastic broadening arising from the energy exchange between the probes and the diffusing particles, depends on the diffusive regime of the latter. These techniques are unique to survey the diffusive motion reaching the atomic resolution and covering the picosecond-nanosecond time window . Diffusion coefficients above 10^{-6} cm^2.s^{-1} and over atomic distances can be measured [5]. In addition, we underline the non-destructive approach of these techniques: the equilibrium state of the adsorbed layer is only weakly perturbed by the scattering. It is precisely the fluctuations restoring the thermal equilibrium in the sample, which give rise to the energy distribution of helium or neutron scattered probes. The main distinction between helium and neutron probes stands in

their very different interaction with matter. While neutrons are scattered by the nuclei [56, 58–60], helium atoms are sensitive to the electronic cloud of atoms. This is reflected in the interaction potential which takes the simple form of the Fermi pseudo-potential [58] (see section 1.2.1 and in Eq. 1.3) for neutrons and differs from the helium interaction potential with the atoms on the surface or in a molecule. Therefore, neutrons can distinguish between different atoms in a molecule, while helium atoms feel the electronic cloud of the whole molecule. Conversely, helium atoms are a highly surface sensitive probe while neutrons are well-known bulk probes. Nevertheless, this disadvantage of neutron probes is overcome with the use of large effective surface area substrates as exfoliated graphite (see the next section 1.1.2). A further disparity between neutron and helium scattering arising from the nucleus-neutron interaction lies in the nucleus scattering length b for neutrons which is an operator acting on the neutron and nucleus spin [58, 61]. Thereby the scattering of neutrons by a collection of atoms has a twofold nature: the coherent scattering only changes the energy and the wave vector of the neutron whereas the incoherent scattering flips the neutron spin as well. The consequences of this peculiar feature of neutron-matter scattering endow neutrons with the capability of distinguishing between collective and individual diffusion. Conversely, helium scattering corresponds only to the coherent scattering of neutrons [1]. The theoretical models for diffusion are, in general, developed for the incoherent scattering (because of its easier interpretation in terms of individual atoms diffusive behavior) but can be extend to the coherent case [1, 2].

Table 1.1: Comparison between the principal surface techniques and the neutron scattering techniques.

Technique	Time window	Length resolution	Observable processes	Range of D [$cm^2.s^{-1}$]	Remarks
LITD	ms<	100-1000 μm	Collective or chemical diffusion	10^{-8}-10^{-5}	Well suited for studying physisorption, adsorption of gases or large molecules on single crystals [5] Provoke surface damage [1]. Requires UHV conditions.
LOD	s - 100 s	1 μm	Collective or chemical diffusion	10^{-15}-10^{-7}	Applicable to a large number of adsorbate-substrate systems. Measures down to the monolayer coverage.
STM	ms<	10 Å	Motion of individual atoms and molecules	10^{-19}-10^{-16}	Requires conducting surfaces. The tip-surface interaction affects the equilibrium state of the adsorbed elements. Ultra High Vacuum, UHV, conditions [48]. Direct space imaging.

FIM	ms<	3-50 Å	Tracking of trajectories of isolated diffusing species and small clusters [6]	10^{-17}-10^{-15}	Metal atoms and refractory metals [48]. Adsorbate/substrate with high binding energies [47]. Materials resisting very high electrical fields $\sim 10^{8}$V.cm^{-1} [6].
FEM (fluctuation mode)	ps	< 100Å	Adatom density fluctuations. Diffusion and jumping of individual atoms	10^{-14}-10^{-9}	Application of high electric field $\sim 10^{7}$V.cm^{-1} [6].
NMR	ps - 0.1 ms		Local density of electronic states. Identification of specific adsorption sites on a substrate Diffusion coefficients.		Weak signal from surfaces [55]. Requires metallic surfaces or nuclei with magnetic moment.
QHAS	ps - 10 ns	10 - 100 Å	Structure of adsorbed layer and dynamics of adsorbed species External (frustrated rotations and translations) of the adsorbed species	$>10^{-6}$	Information in the Fourier domain of $(\mathbf{Q}, \hbar\omega)$ Only measures coherent scattering. Requires ultra-high vacuum conditions. High surface sensitivity.
QENS	ps - 0.1 ms	10Å	Structure of adsorbed layer and dynamics of adsorbed species. Tunneling, internal (vibrations) and external (frustrated rotations and translations) modes of the adsorbed species	$>10^{-6}$	Information in the Fourier domain of $(\mathbf{Q}, \hbar\omega)$ Low surface sensitivity: substrates with high effective surface for adsorption. Flexible sample environment: do not require UHV. Extremely sensitive to hydrogen atoms.

1.1.2 Systems for a neutron surface study: carbon based molecules physisorbed on exfoliated graphite

One of the strongest limitation for the application of neutrons to surface study is the lack of signal arising from the atoms in the surface or in the edges of the system [1]. Neutrons are well known bulk probes: their weak interaction with matter enhances their penetration depth (of the order of cm) [62]. As a result, surfaces are invisible to neutrons. This has some advantages and provides neutrons with the capability of accessing buried phases when coexistence between an adsorbed and a liquid phase exists [63]. But, it is certainly not the best suited set-up for surface diffusion studies. The advent of materials with a large specific area for adsorption, such as exfoliated graphite or

MgO, has significantly boosted the study of surface structure and dynamics with neutrons [64,65]. This kind of materials maximizes the surface to volume ratio allowing to adsorb a sufficient amount of molecules while the quantity of molecules remaining in the liquid or gaseous phase is reduced to its minimum [64]. As a result, the contribution to the scattering coming from the adlayer is intense enough to generate a quasi-elastic signal which clearly differs from the statistical noise.

Exfoliated graphite Exfoliated graphite offers a 20 $m^2.g^{-1}$ effective area for adsorption [66–68]. This material results from the intercalation of chemical complexes: $SbCl_5$, $FeCl_3$ or sulfuric acid, which diffuse and form layered crystals in the plane edges of natural graphite [68]. If the temperature of the system suddenly rises, the layered crystals explode apart provoking the expansion of the graphite lattice parameter along the c axis hundreds of times [69]. The exfoliation process produces a very low density material consisting of empty galleries (60 % of the volume) of an averaged thickness of 300 Å which connect the graphite cyrstals of 600 Å size, according to WAXS measurements in Ref. [68]. Furthermore, exfoliated graphite can be rolled into binderless flexible sheets becoming *compressed exfoliated graphite*. Then, it benefits from the large surface effective area of exfoliated graphite and, in addition, presents a preferential orientation of the graphite microcrystals: their basal plane is parallel to the macroscopic surface. As a result, compressed exfoliated graphite supplies a high quality and well ordered substrate with a very large surface area where the fraction of non-oriented graphite crystallites is estimated to be 26 % [67]. It is the closest substrate to an ideal homogeneous surface for adsorption [66].

Physisorption of carbon based molecules on exfoliated graphite The physisorption of carbon based molecules on exfoliated graphite constitute an excellent sample to probe with neutrons. First of all, the weak binding of physisorbed layers (by the means of Van der Waals forces) gives rise to low frequency modes of the molecules: the so-called *external modes*, arising from frustrated translations or rotations, in contrast to the *internal modes* which are related to the internal degrees of freedom of the molecule in the gaseous or non-adsorbed phase [70]. The vibrational frequencies of the external modes display typical values below 15 meV [70]. They match the natural energy range surveyed by thermal neutrons, while they fall out of the range of other techniques such as infrared spectroscopy [27]. The second important point is that carbon based molecules such as methane, benzene, naphthalene or pyrene contain hydrogen. Neutrons are the best probe to identify and follow the dynamics of protons, because of the very large scattering cross-section of the

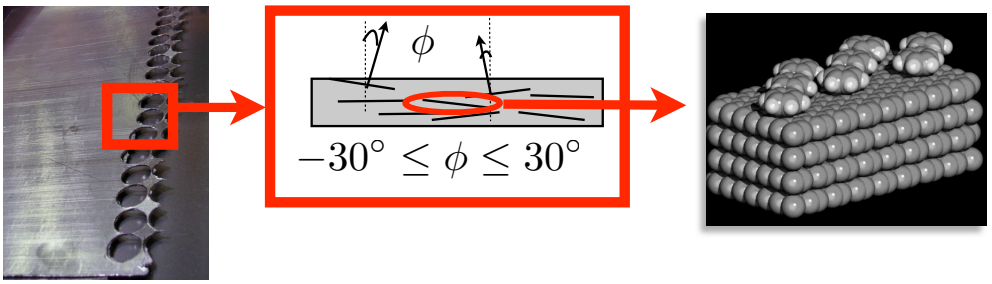

Figure 1.2: Left panel: the macroscopic compressed exfoliated graphite substrates, *Papyex*, which we use as substrates. Middle panel: schematic representation of a vertical cut in the compressed exfoliated graphite. The basal plane of graphite microcrystals is, in average, parallel to the macroscopic substrate within an error of ± 30 deg. Right panel: representation of benzene molecules lying on the basal plane of a graphite crystal. This pattern will be repeated in the whole volume of the sample and provides the large effective surface for diffusion. The figure is taken from Ref. [23]

hydrogen nucleus: 81.66 barns [56, 58, 60, 71] . As a result, if the beam of neutron is directed parallel to the macroscopic surface of an exfoliated graphite substrate containing alkanes or polyaromatic rings molecule adsorbed on its basal plane (see Fig. 1.3), most of the quasi-elastic neutron scattering signal comes from the adsorbed layer, and more precisely from the protons. Thereby, the momentum transfer $\mathbf{Q}$ which we measure, is parallel to the surface:

$$\mathbf{Q} = \mathbf{k}_f \sin\theta - \mathbf{k}_i \sin\theta. \tag{1.1}$$

Hence, neutrons yield highly detailed information about the the dynamics of adsorbed layers of alkanes, or aromatic ring based molecules on exfoliated graphite because there exists a pronounced contrast between the scattering cross-section of hydrogen and carbon (the scattering cross section of carbon is 5.55 barns [56]). This difference of scattering length allows to distinguish between the signal arising from the adlayer and from the substrate.

1.2 QENS spectroscopy and spectrometers

Now that we have dressed up a general picture of surface diffusion techniques, we survey the quasi-elastic neutron scattering techniques. First of all we provide a general description of the double differential scattering cross-section which is the main physical quantity delivered by a scattering experiment. Afterwards, we focus on the particularities of the quasi-elastic regime: the typical energies and distances and the shape of the scattering function in the energy/time domain. Then, we review the different instrumental techniques

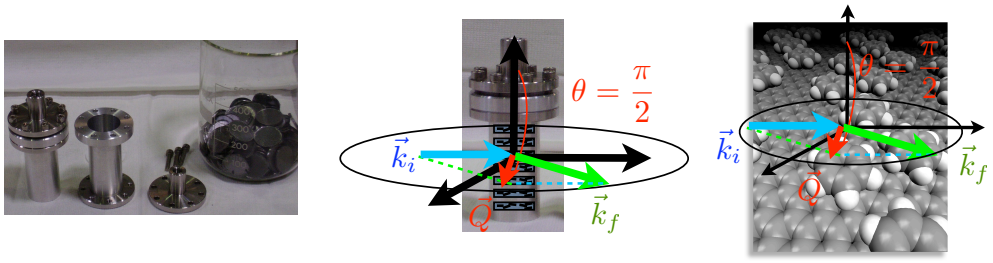

Figure 1.3: Left panel: aluminium sample holders and disk of exfoliate graphite. Central panel: diagram showing the stacking of the graphite disks within the sample holder and the directions of the incoming (blue arrow) and outgoing (green arrow) neutron beam. The red arrow is the momentum transfer vector. The azimuthal angle θ is kept constant at $\pi/2$ meaning that only the neutrons scattered in the plane are detected. Right panel: representation of the scattering geometry on a graphite crystallite where benzene molecules are adsorbed.

belonging to the QENS group and explain how the measurement is achieved. In a first glance, we can classify the instruments into two classes: on one side time-of-flight (ToF) and backscattering (BS) correspond to standard spectrometers where the experimental functions are probed in the momentum transfer/energy transfer domain. On the other side, neutron spin echo (NSE) is based on a different principle which makes use of the spin of the neutron. In this way, the physical information is given in terms of the momentum transfer/ real time. We shall discuss the similarities and differences of the various instruments. The essential point is to show that the combination of all the experimental techniques leads to a complete picture of the diffusive process.

1.2.1 The neutron scattering double differential cross section

In general terms, a scattering experiment measures *the differential scattering cross-section* $d^2\sigma/d\Omega d\omega$: the probability of counting a scattered probe in one space direction, described by the differential solid angle $d\Omega$, and within a differential energy transfer element $d\hbar\omega$ [58, 60]. The *Fermi's golden rule* expresses this probability in terms of state transitions [60, 72]:

$$\frac{d^2\sigma}{d\Omega d\omega} \propto \sum_{\mathbf{k}} W_{|\mathbf{k_0}\mu n\rangle \to |\mathbf{k}\mu' n'\rangle} = |\langle \mathbf{k}\mu' n'|\mathcal{V}|\mathbf{k}_0\mu n\rangle|^2 \delta\left\{\omega + \frac{E_n - E_{n\prime}}{\hbar}\right\}, \quad (1.2)$$

$W_{|\mathbf{k_0}\mu n\rangle \to |\mathbf{k}\mu' n'\rangle}$ being the probability that the system formed by the probe and the target passes from an initial state $|\mathbf{k_0}\mu n\rangle$ to a final state $|\mathbf{k}\mu' n'\rangle$, via an interaction potential $\mathcal{V}$. Here, $|\mathbf{k_0}\mu\rangle$ and $|\mathbf{k}\mu'\rangle$ denote the incoming and the scattered probe particle states. In particular, $\mathbf{k}_0$ and $\mathbf{k}$ are the incoming and

scattered probe particle wave vectors, respectively, while μ and μ' label its initial and final spin eigenstates (or polarization for the spinless probes) [59]. In contrast, $|n\rangle$ and $|n'\rangle$ are related to the initial and final states of the target system. If the Hamiltonian of the target system is independent of nuclear spins, its eigenstates $|n\rangle$ are a product of the form $|n\rangle = |s\rangle|\lambda\rangle$ [73]. The states $|\lambda\rangle$ form a complete set of stationary states of the rotation-translational Hamiltonian of the target system [73]. Conversely, $|s\rangle$ refers to its nuclear spin states.

In addition, the whole process must satisfy the energy conservation law. Therefore, the difference in energies between the incoming and the outgoing probe particle, $\hbar\omega$, needs to be equal to the difference in energies of the target[1], $E_n - E_{n'}$, when passing from state $|n\rangle$ to state $|n'\rangle$ [60].

Neutron probes: The Fermi pseudopotential In the case of neutrons, their interaction with matter is reduced to their scattering by nuclei and by magnetic moments [56, 58, 60]. In particular, the forces ruling the nuclear scattering act on a very reduced spatial range: 10^{-14} - 10^{-15} m if compared with the typical wavelength of a thermal neutron, which is of the order of 10^{-10} m [56, 58, 60]. Under this circumstances, nuclei can be considered as point scatterers and we can assume that the interaction is impulsive [56, 58, 60, 74]. Hence, in a first approximation known as the *Born approximation* [75], the potential describing the nuclear scattering is well approximated by the *Fermi pseudopotential* [56,58,59,61,74,75]. The Fermi pseudopotential for a collection of N atoms is:

$$\mathcal{V}(\mathbf{r}) = \left(\frac{m}{2\pi\hbar^2}\right)^{-1} \sum_j^N b_j \delta(\mathbf{r}_j - \mathbf{r}) \tag{1.3}$$

where m is the neutron mass and b_j is the scattering length of the j-th nucleus situated at $\mathbf{r}_j$.

The scattering length The scattering length of a nucleus quantifies its power as a neutron scatterer: how likely is it that the nucleus scatters the neutron? It can also be understood as an effective size of the nucleus from the neutron's perspective [76]. The scattering length depends on the composition of the nucleus (number of nuclides) and on the orientation of the nuclear spin

[1]The energies of the target, $\{E_n\}$ are defined as the eigenvalues of the Hamiltonian opertor of the target $\mathcal{H}$ corresponding to the set of eigenstates $\{|n\rangle\}$. Hence, they fulfill the Schroedinger equation, which is of the form:

$$\mathcal{H}|n\rangle = E_n|n\rangle.$$

with respect to the neutron spin[2] [58,59,61,77]. Consequently, neutrons detect the presence of different chemical species but also of different isotopes of the same chemical species, because the nucleus scattering length acts as a kind of identity label [58]. The complex nature of b_j is related to the probability of scattering (real part) and absorbing (imaginary part) neutrons [56, 58, 60, 61]. Fortunately, in most of the species of the periodical table of elements, the imaginary part is negligible and the real part is independent of the neutron energy (in the case of cold and thermal neutrons) [58, 60]. Whenever the incident neutron beam is fully depolarized and the nuclear spins of the sample are randomly oriented, the averages over the neutron spin and the nuclear spin can be calculated independently [58, 61]. The resulting averaged scattering length of the j-th nucleus, $\langle b_j \rangle$, becomes a real constant.

The neutron wave function and the main physical magnitudes Due to the instantaneous and impulsive interaction between neutrons and matter, the description of neutron scattering addopts an observation point far away from the target, the *asymptotic limit*, reduces to an incoming and an outgoing

[2] In general terms, the scattering length is defined as the sum of a complex coefficient A_j and the scalar product of operators acting on the neutrons spin state, $\hat{\sigma}$, and the scatterer nuclear spin state, $\hat{\mathbf{I}}$, weighted by another complex coefficient B_j [58, 59, 61, 77]:

$$\hat{b}_j = A_j + \frac{1}{2} B_j \hat{\sigma} \cdot \hat{\mathbf{I}}.$$

The complex parameters A_j and B_j account for the composition of the nucleus, while the scalar product between operators describes the effect on the scattering of the relative orientation of the neutron and the nuclear spins.

plane wave[3] [79]:

$$\begin{cases} |\mathbf{k_0}\rangle & = \dfrac{1}{\sqrt{V}} \exp(i\mathbf{k}_0 \cdot \mathbf{r}) \\ |\mathbf{k}\rangle & = \dfrac{1}{\sqrt{V}} \exp(i\mathbf{k} \cdot \mathbf{r}) \end{cases}, \tag{1.4}$$

where the modulus of the wave vector $\mathbf{k}$ is inversely proportional to the wavelength λ characterizing the spatial periodicity of the wave, $|\mathbf{k}| = 2\pi/\lambda$. Plane waves correspond to non-bound states [78]: neutrons behave as free particles. Accordingly, the neutron initial and final energy reduces to its kinetic energy and depends on the square of its wave vector [78]:

$$\begin{cases} E_i = \dfrac{\hbar^2}{2m} k_0^2 \\ E_f = \dfrac{\hbar^2}{2m} k^2 \end{cases}. \tag{1.5}$$

The energy transfer $\hbar\omega$ occurring during the scattering of the neutron is given by the difference in the neutron energy before and after the scattering [56]:

$$\hbar\omega = E_f - E_i = \frac{\hbar^2}{2m}(k^2 - k_0^2), \tag{1.6}$$

The momentum transfer, $\mathbf{Q}$, also called scattering vector [60], expresses the change in the scattered neutron direction with respect to its initial momentum, and reads [56]:

$$\mathbf{Q} = \mathbf{k} - \mathbf{k}_0. \tag{1.7}$$

The energy $\hbar\omega$ and the momentum transfer $\mathbf{Q}$ are the chief physical magnitudes that we aim to measure in a scattering experiment [56]. They contain all the dynamical and structural information that neutrons can extract from the sample, excluding the phase information (i.e. the spin state of the neutron).

[3] In the *Born approximation* [75], nuclear scattering will give rise to a completely isotropic scattered neutron wave:

$$\psi = -\frac{b}{r} \exp(ikr),$$

i.e. a spherical wave whose amplitude is characterized by the parameter b, known as the *scattering length* [56, 58, 60]. When the observation point is far away from the target, the distance being much longer than the typical lengths between scatterers in the sample, the total neutron wave after the scattering can be approximated by the summation of the incident plane wave and the spherical scattered wave [78]:

$$\psi_{fin} \simeq \frac{1}{\sqrt{V}} \exp(i\mathbf{k}_0 \cdot \mathbf{r}) - \frac{b}{r} \exp(ikr).$$

In the case of scattering by a collection of N atoms, the resulting neutron wave function, always considered in its asymptotic limit, will be the summation of waves of the form ψ_{fin}, but with a different scattered wave vector modulus k, depending on the energy exchanged with the scatterer. Because the detector (the observation point) fulfills the asymptotic condition, the neutron spherical scattered wave will appear as a plane wave [79].

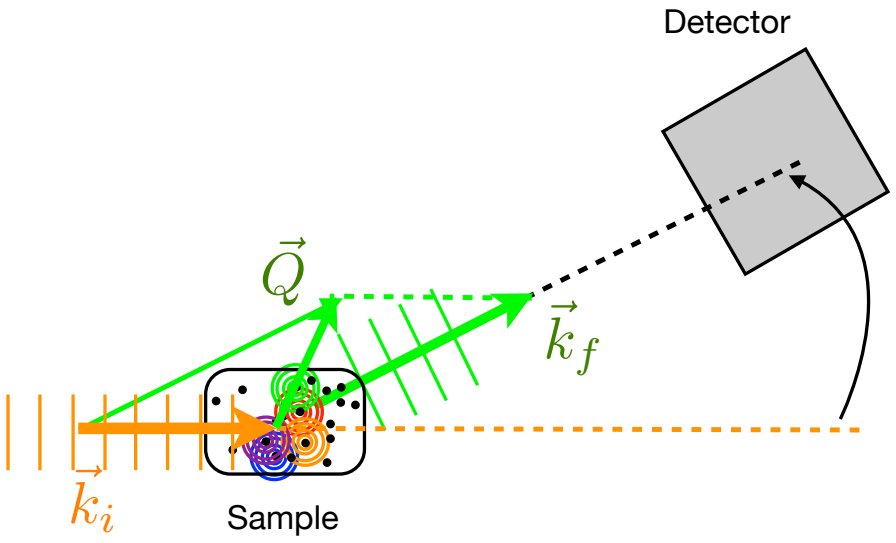

Figure 1.4: Representation of the scattering of a neutron by a collection of atoms. The incoming neutron is represented by a plane wave characterized by a well defined wave vector $\mathbf{k}_i$, or equivalently by a well defined wavelength λ_i. The interaction between the neutron and the nuclei in the sample gives rise to spherical waves: the scattered neutron density of states is isotropic, in a first approximation. However, in the asymptotic limit, the spherical scattered waves describing the outgoing neutron can be approximated by plane waves with well defined wave vectors $\mathbf{k}_f$, depending on the momentum and energy exchange with the target system. The momentum transfer vector, $\mathbf{Q}$, is the difference between the neutron wave vectors before and after the scattering (see Eq. 1.7).

Furthermore, it is worth to realize that the energy and the momentum transfer are related by the dispersion relation of the free neutron (Eq. 1.5) [80]:

$$\frac{\hbar^2}{2m}Q^2 = 2E_0 + \hbar\omega - 2\sqrt{(\hbar\omega + E_0)E_0}\cos\phi. \tag{1.8}$$

Eq. 1.8 implies that neutron scattering is restricted to a region of the energy-momentum transfer space $(\mathbf{Q}, \hbar\omega)$ (see Fig. 1.5), which depends on the the incident energy of the neutrons E_0 (or in its initial wavelength).

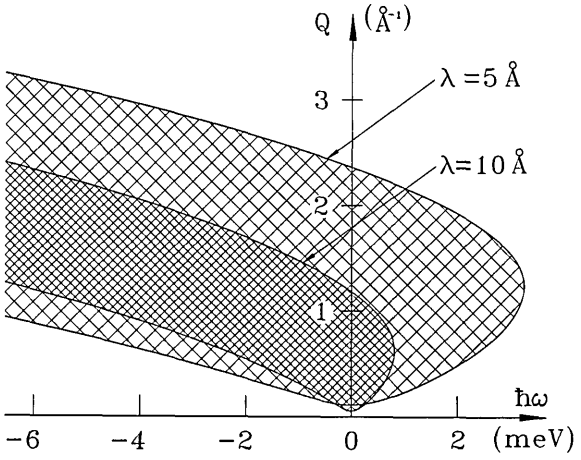

Figure 1.5: Attainable $(\mathbf{Q}, \hbar\omega)$ areas for incoming neutrons of 5 Å and 10 Å wavelength respectively. Graph taken from Ref. [80].

The scattering function and the intermediate scattering function Finally, inserting the Fermi pseudopotential (Eq. 1.3) into Fermi's golden rule (Eq. 1.2) leads to the differential scattering cross-section as function of the momentum and energy transfer, which are measured by the standard spectroscopic instruments [58, 60, 81]:

$$\frac{d^2\sigma}{d\Omega d\omega} = \frac{k}{k_0}\frac{1}{2\pi\hbar}\sum_{j,j'=1}^{N}\left\langle b_j^* b_{j'}\right\rangle \int_{-\infty}^{\infty} dt\exp(-i\omega t)\left\langle \exp(-i\mathbf{Q}\cdot\mathbf{r}_{j'}(t))\exp(i\mathbf{Q}\cdot\mathbf{r}_j(0))\right\rangle, \tag{1.9}$$

For a classical system whose equilibrium state follows the Boltzmann statistics [56, 59, 75], the averages over the thermally distributed spatial states and over the spin states can be performed independently [56, 58, 81]. It follows that the differential scattering cross section reads as the product of two terms. The first term is the product of the scattering lengths of nuclei j and j' averaged

over the neutron and the target system nuclear spin states. It contains all the information about the neutron-matter interaction:

$$\langle b_j^* b_{j'} \rangle = \sum_{\mu} \sum_{s} P_\mu P_s \langle s | \langle \mu | b_j^* b_{j'} | \mu \rangle | s \rangle. \tag{1.10}$$

The second term is the Fourier transform in time of a function averaged only over the thermal distribution of the translational-rotational states[4]of the target system, the so-called *correlation function* [58]:

$$\begin{aligned} Y_{j,j'}(\mathbf{Q}, t) &= \langle \exp(-i\mathbf{Q} \cdot \mathbf{r}_{j'}(t)) \exp(i\mathbf{Q} \cdot \mathbf{r}_j(0)) \rangle \\ &= \sum_{\lambda} P_\lambda \langle \lambda | \exp(-i\mathbf{Q} \cdot \mathbf{r}_{j'}(t)) \exp(i\mathbf{Q} \cdot \mathbf{r}_j(0)) | \lambda \rangle. \end{aligned} \tag{1.13}$$

The factorization of the differential cross-section stems from the weak interaction between neutrons and matter and, in particular, from the impulsive scattering due to the neutron-nuclear interaction [58, 75]. From this perspective, the scattering can be considered as a weak perturbation to the equilibrium state of the target, described by P_λ [56, 58]. Thus, the differential neutron scattering cross-section can be studied in the framework of the linear response theory: it measures the response of the target system, i.e. the thermal fluctuations restoring the equilibrium after the perturbation caused by the scattering of the neutron [56, 58, 75]. In the neutron scattering terminology, the response function is called the *scattering function* or *scattering law* [58]:

$$S(\mathbf{Q}, \omega) = \frac{1}{N} \sum_{j,j'} \int_{-\infty}^{\infty} dt \exp(-i\omega t) Y_{j,j'}(\mathbf{Q}, t). \tag{1.14}$$

It is the main function measured with backscattering or time of flight spectroscopy. It portrays the thermal fluctuations of the target system, its structure and dynamics, in the Fourier transformed space of the momentum transfer $\mathbf{Q}$ and the energy transfer $\hbar\omega$ [58]. From the point of view of diffusion, it contains valuable information about the diffusive behavior of the elements adsorbed on

[4]Note that $\mathbf{r}_{j'}(t)$ is the Heisemberg operator yielding the position of the j'-th nucleus obtained through the Hamiltonian $\mathcal{H}$ of the target system [58, 60]:

$$\exp\left(-i\frac{t}{\hbar}\mathcal{H}\right) \exp(-i\mathbf{Q} \cdot \mathbf{r}_{j'}) \exp\left(i\frac{t}{\hbar}\mathcal{H}\right) = \exp(-i\mathbf{Q} \cdot \mathbf{r}_{j'}(t)). \tag{1.11}$$

When $t = 0$, we have:

$$\exp\left(-i\frac{t}{\hbar}\mathcal{H}\right) \exp(-i\mathbf{Q} \cdot \mathbf{r}_j) \exp\left(i\frac{t}{\hbar}\mathcal{H}\right) |_{t=0} = \exp(-i\mathbf{Q} \cdot \mathbf{r}_j(0)) \tag{1.12}$$

the surface [1, 16, 57]. The scattering function reads as the time Fourier transform of the *intermediate scattering function (ISF)* [60]:

$$I(\mathbf{Q},t) = \frac{1}{N}\sum_{j,j'=1}^{N} Y_{j,j'}(\mathbf{Q},t), \tag{1.15}$$

which is the summation of the correlation functions for all the elements in the system, as defined in Eq. 1.13. It is also an experimental function but should be measured by means of special spectroscopy techniques such as neutron spin-echo spectroscopy [1, 16]. In contrast to the scattering function, it draws a picture of the dynamics of the system in time, even if the spatial information is still in the reciprocal space $\mathbf{Q}$.

1.2.2 QENS dynamical and spatial range

QENS techniques survey an energy-time window of meV-μeV/10^{-10}-10^{-12}s and a space windows reaching the atomic scale (from 0.1 to 10 Å). [56, 59, 82]. Hence, the dynamical region (dynamics and structure) revealed by QENS techniques matches the typical times and length scales for molecules diffusing on surfaces at technically interesting temperatures (between 100K and 300K) [13, 56]. Diffusing particles in the sample exchange small amounts of energy with neutron, lying in the *quasi-elastic* range of ±2meV [56]. As a result, the elastic peak broadens and the continuous distribution of energies arising from this "quasi-elastic" scattering is characterized by its the half width half maximum (HWHM): the so-called *quasi-elastic broadening* (see Fig. 1.6). Equivalently, the broadening of the elastic peak in the momentum/energy transfer domain $(\mathbf{Q}, \hbar\omega)$ translates into a decay with time of the intermediate scattering function lying in the momentum transfer/real time phase space $(\mathbf{Q}, t)$. The time constant characterizing this time decay is the Fourier transformed in time of the quasi-elastic broadening in energies. As a result, the dependency on the momentum transfer of the QENS broadening, or analogously of the time decay, is the experimental signature of the diffusive processes taking place in the system [1, 57, 83–85]. The major part of the models aim to predict a determinate shape for the quasi-elastic profile given a particular type of diffusion.

1.2.3 QENS spectrometers

As we have now briefly reviewed the basic theory for neutron scattering and we have defined the main physical quantities: energy and momentum transfer,

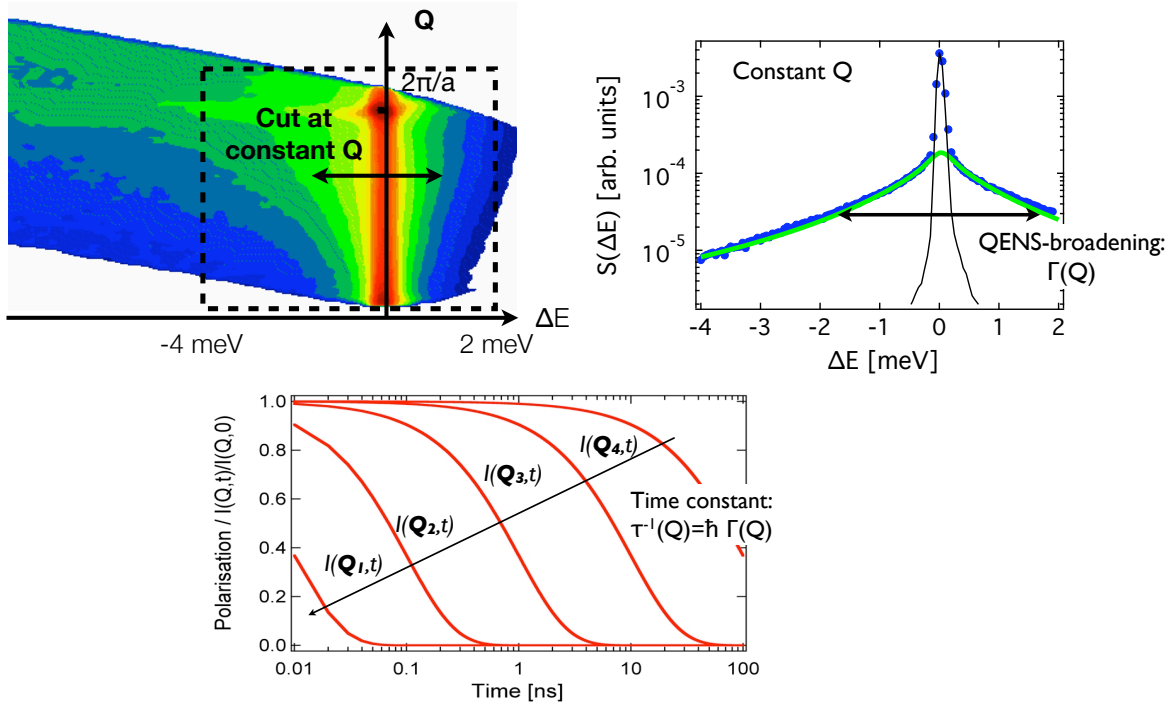

Figure 1.6: Left panel: typical QENS scattering law, $S(\mathbf{Q}, \Delta E)$, where we plot intensity versus momentum transfer $\mathbf{Q}$ and energy transfer $\Delta E = \hbar\omega$. Right panel: cut at constant Q of the scattering function. The quasi-elastic energy profile is highlighted by the green solid line Bottom panel: intermediate scattering function at different Q values. The so-called quasi-elastic window (left panel) is the green area around the elastic band, at $\Delta E = 0$, in red (the most intense signal). The shape of the quasi-elastic region is the characteristic fingerprint of a determined diffusive regime. This translates into a Q dependent time constant of the ISF (bottom panel). The form of the scattering function reproduces the energy/momentum transfer domain $(\mathbf{Q}, \hbar\omega)$ which is attainable with ToF spectroscopy for a given initial wave length (see Fig. 1.5 and Eq. 1.8).

together with the chief experimental functions, we can undertake the description of the QENS techniques. Above all we will explain the way in which the physical quantities are measured in every technique and the parameters determining the accessible dynamical window. There are two basic parameters shaping the accessible phase space $(\mathbf{Q}, \hbar\omega)$. First of all, the *instrumental resolution* sets the lower limit of the time/energy window: i.e. the slowest or less energetic processes visible by the technique in particular experimental conditions. Conversely, the *neutron incoming wavelength* gives the upper limit of the spectral range (see Eq. 1.8): i.e. the fastest or most energetic processes observable under given experimental conditions. We will start with the description of time of flight and backscattering spectroscopy, which correspond to standard spectroscopic techniques probing the energy/momentum transfer phase space. We will finish with the neutron spin-echo technique whose physical principle is completely different from the latter techniques, giving access to the time/momentum transfer domain.

Time-of-flight spectroscopy

Time-of-flight (ToF) spectroscopy is a powerful technique for investigating dynamical processes in condensed matter [80]. Its principal strength lies in the wide domain of $(\mathbf{Q}, \hbar\omega)$ that ToF instruments can access [80, 86]. There are two main reasons which open the access to a large spectral range. First of all, the resolution covers a wide spread of energies from 10 μeV up to 1000 μeV [87]. The second reason is that ToF instruments can work under any initial wavelength condition (from cold neutrons of wavelength 30 Å $\sim$ 3 Å to very hot neutrons of wavelength 1 Å $\sim$ 0.2 Å), provided that they are equipped with the appropriate mechanical devices for chopping the beam [86]. As a result, ToF spectroscopy is a very flexible technique. It can, in one side, reach the time domain of magnetic and phononic low energy excitations or tunneling processes (in the range of 2.5 meV up to 10 meV), which falls out of the energy range of high energy triple axis spectrometers [80]. But, on the other side, it also covers perfectly the so-called quasi-elastic energy range [80], where translational and rotational dynamics of atoms and molecules in condensed matter takes place (with characteristic diffusion coefficients for translations between $10^{-12}\mathrm{m}^2.\mathrm{s}^{-1}$ and $10^{-8}\mathrm{m}^2.\mathrm{s}^{-1}$ [87], or residence times shorter than 10^{-9}s for reorientations [27]) . Hence ToF spectroscopy is one of the best suited techniques for exploring surface diffusion with neutrons.

Time-of-flight principle Neutrons extracted from a moderator source, are lead in most cases to the instruments by neutron guides. If the slits that the neutron beam encounters along its path are large if compared with the

neutron wavelength, then, neutrons can be treated as classical particles and travel with a well defined velocity [86]. The ToF method relies in the behavior of neutrons as classical particles for defining the energy of the incident neutron beam (the monochromatization of the incident beam) and for measuring the energy transfer between the neutron and the sample. A neutron of mass m_n with a well defined velocity, needs a certain time Δt to cover a distance L: *the time of flight* [56,86]. The connection between the neutron wavelength and its velocity, the De Broglie relation $m_n v = h/\lambda$ [78], yields:

$$\Delta t = \frac{L}{v} = L\frac{m_n \lambda_i}{h}. \tag{1.16}$$

Eq. 1.16 states the key for extracting a monochromatic beam out of the neutron white beam traveling in the guide by means of a ToF energy selector made of a pulsing and a monochromator chopper system. The principle is illustrated in the top panel of Fig. 1.7 and 1.8: the distance between the chopper devices, L_{ch}, and their opening frequencies are synchronized in order to achieve a precise initial energy of the neutron pulses: if L_{ch} and Δt_{ch} are settled fix, then, only the neutrons traveling with the appropriated wavelength λ_i will pass through the pulsing and the monochromator chopper (see Fig 1.8). The outgoing pulse will only contain neutrons with the desired wavelength, i.e. traveling with the same velocity. However, some ToF instruments, like IN5 (ILL) [88] make use of a single crystal monochromator for selecting the incoming wave length, and chop the incoming beam afterwards with a Fermi chopper (see bottom panel of Fig. 1.7). On the other side, the link between the time-of-flight of a neutron and its kinetic energy is straightforward:

$$E = \frac{1}{2}m_n v^2 = \frac{\hbar^2 k^2}{2m_n} = \frac{h^2}{2m_n \lambda^2} = \frac{1}{2}m_n \left(\frac{L}{\Delta t}\right)^2. \tag{1.17}$$

The exchange of energy during the scattering is inferred from the scattered neutron time of flight: a change in the neutron wavelength due to inelastic scattering will be immediately translated into a change of time-of-flight and will be recorded [80]. The ToF instruments which apply the time of flight principle for selecting the initial wavelength and measuring the energy transfer are called *direct geometry ToF spectrometers* (see the top panel in Fig. 1.8). In contrast, there exist ToF instruments where single crystals analyze the final energy of the neutrons according to Bragg law (see the lower panel in Fig. 1.8). These are the *indirect geometry ToF spectrometers*. They can attain a very large dynamical window (very large energy transfer up to 500 meV [27]) and are particularly suited for performing molecular vibrational spectroscopy with very high resolution [86].

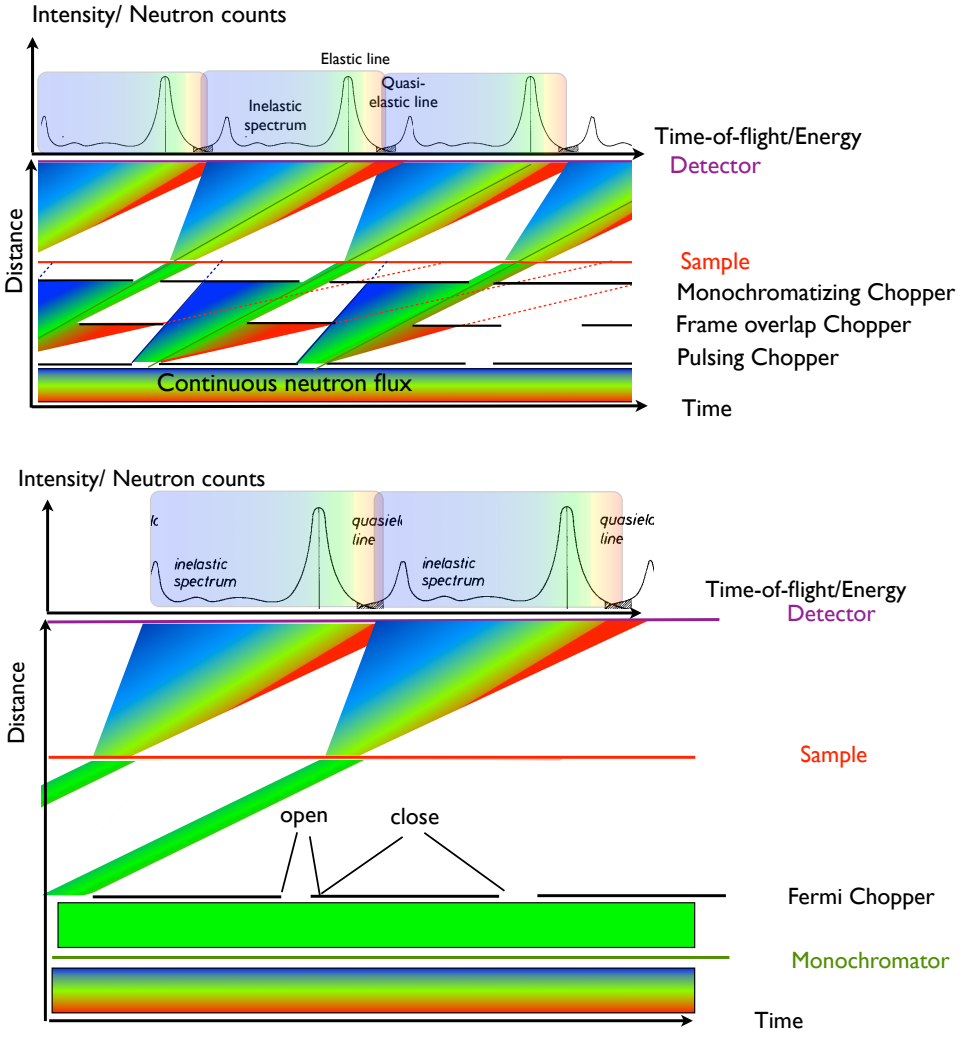

Figure 1.7: Time-distance diagram. The distance traversed by neutrons is plotted against the time. The slope is given by the velocity of the neutron. Top panel: The pulsing chopper cuts the continuous neutron flux into neutron pulses. Since the pulsing chopper has a finite opening time, there exists a certain wavelength dispersion in the neutron pulse since not all the neutrons travel with exactly the same velocity (different slopes in the distance-time diagram). This initial dispersion in energies gives rise to the instrumental resolution. Next, the overlap frame chopper prevents the slowest neutrons from one pulse to mix at the detector with the fastest neutrons of next pulse (dotted red lines). Later, the monochromator chopper, rotating in synchrony with the pulsing chopper, allows the passage only to the neutrons with the desired initial energy while it absorbs the rest of neutrons traveling faster or slower. Bottom panel: The initial wavelength is selected with a monochromator. Afterwards, beam is pulsed with a Fermi chopper. In any case, a monochromatic neutron pulse reaches and is scattered by the sample. Finally, the detector counts the number of neutrons arriving at a certain time: the time-of-flight spectrum. Elastically scattered neutrons constitute the so-called elastic line. Neutrons winning energy from the target will arrive before the elastic neutrons while neutrons loosing energy in the target will arrive later.

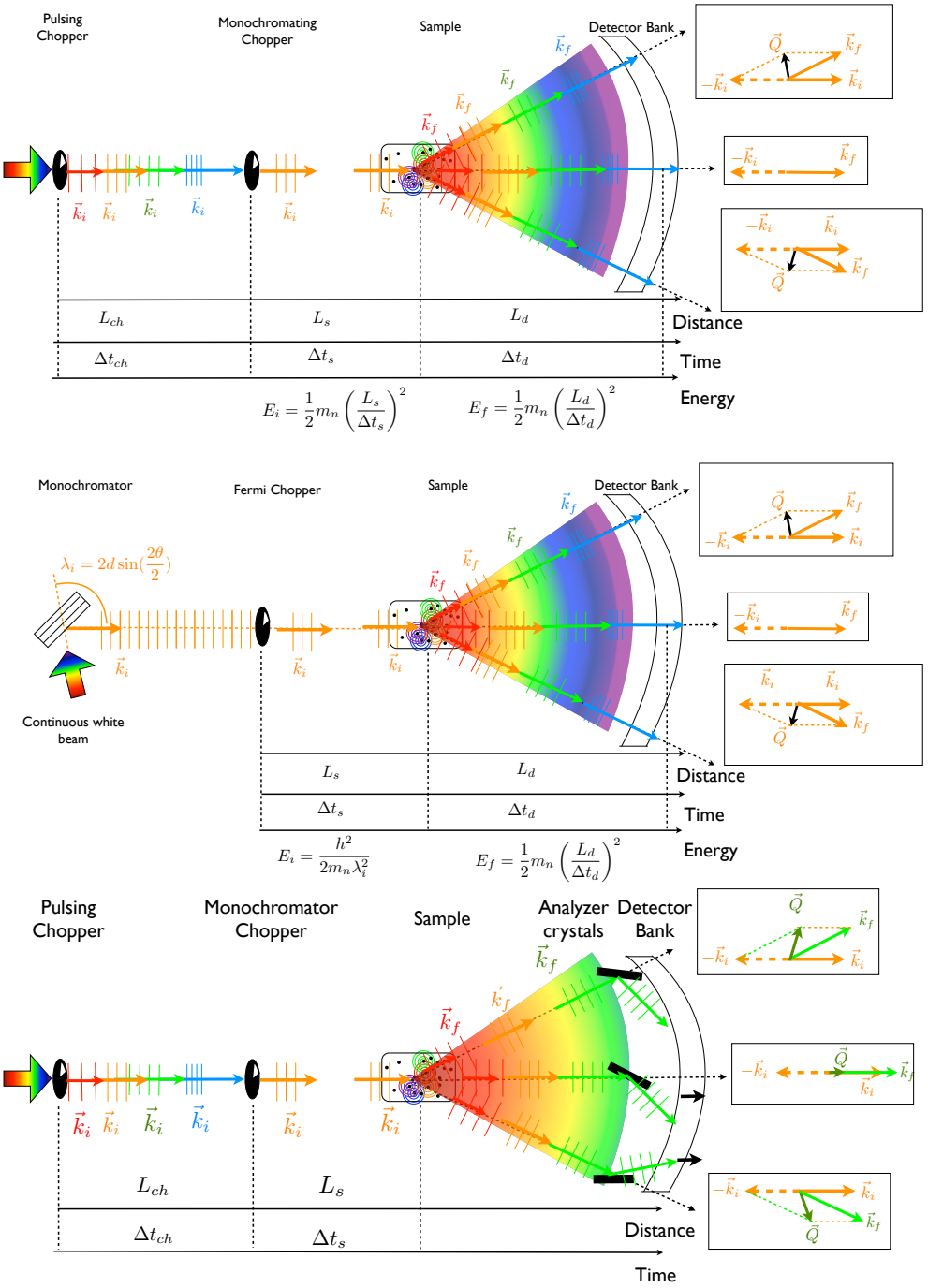

Figure 1.8: Top and medium panel: direct ToF spectrometer. In the first case the time of flight principle is at work for selecting the incoming wavelength. In the second case a single crystal is used to obtain a monochromatic beam. Bottom panel: indirect geometry ToF spectrometer. The first part devoted to the selection of the initial neutron wavelength is identical to the direct ToF spectrometer. Conversely, analyzer crystals are used for estimating the kinetic energy of the scattered neutrons.

In any case, for both types of spectrometers, it follows from the time-of-flight measurement principle that ToF spectroscopy requires pulsed beams to work properly. Neutrons in a continuous and monochromatic incoming beam are indistinguishable [86]. Pulsing the beam permits to label each neutron and assign it a characteristic initial time: by definition, all the neutrons traveling together in a monochromatic pulse have the same initial time. Conversely, they differ in their arrival time to the detector bank, which depends on wether they have gained, lost or conserved their energy when scattered by the sample. In pulsed neutron sources, the emission of neutrons is already performed into packets and the source itself acts as an initial clock reference for the neutrons time of flight [86]. Even though, choppers are still useful in spallation sources: the source acts as the first chopper, but monochromatization requires, at least, a system of two choppers. Conversely, when the neutron source is continuous, like in a nuclear reactor, the incoming neutron beam must be chopped. For this purpose, two different mechanical devices exist: in the first case the pulsing is done by the means of a collimator turning around an axis perpendicular to the direction of the beam, this is a *Fermi chopper* [80, 86]. The beam is already monochromatized before reaching the Fermi chopper with a single crystal in the appropriate orientation for diffracting the desired initial wavelength (see lower panel of Fig. 1.7). In a second case, the beam passes through absorbing disks with transparent slits turning in the plane perpendicular to the beam direction. These are the *disks choppers* [80, 86]. This second methods allows to monochromatize and pulse the beam simultaneously (see top panel of Fig. 1.7 and Fig. 1.8). It turns out that the dispersion in the incoming wavelengths $\delta\lambda/\lambda$ is tuned by the dimensions of the opening α and the rotatinal velocity ω of the chopper. These two parameters tailor the shape of the neutron pulse in time and space. For instance, in the Fermi chopper the time width of the pulse is [86]:

$$\tau = \frac{\alpha}{\omega}, \tag{1.18}$$

which gives rise to a wavelength dispersion at any time t of (see Eq. 1.16):

$$\frac{\delta\lambda}{\lambda} = \frac{\tau}{t} \Rightarrow \frac{\delta\lambda}{\lambda} = \frac{\alpha}{\omega t}. \tag{1.19}$$

The typical chopper rotating frequencies for achieving a 1% relative error in the wavelength accuracy are of the order of 6000 rpm [86]. The total resolution of a ToF instrument comprehends the wavelengths dispersion of the incoming neutron pulse and the uncertainty related to the flying path [86]. The latter includes, the beam divergence, the thickness of the sample and the detector size [86,87]. Many improvements on the resolution function have raised the experimental resolution to the order of 10 μeV [56,86]. For instance the addition of choppers avoids the frame overlap (see top panel in Fig. 1.7): i.e the simultaneous arrival to the detector bank of the fastest neutrons of one pulse with

the slowest neutrons from the previous pulse. However, the increasing of the resolution and the possibility to survey a large region of the $(\mathbf{Q}, \hbar\omega)$ domain are paid by a loss of the intensity of the measured signal. Hence, upgrades in thermal neutron sources provide more intense incoming fluxes which compensate the loss of intensity which inevitably follows an increase in the resolution. In the particular case of the IN6 time-of-flight spectrometer, the high flux at the sample position is achieved thanks to the *time focusing technique* [56].

The IN6 spectrometer at ILL Most of the measurements that we have performed, were carried out at the IN6 ToF spectrometer at the Institut Laue-Langevin (ILL). It is located on the H15 neutron guide (ILL7 guide hall). The range of initial wavelengths spans from 4 Å to 6 Å . The monochromatization of the beam is achieved using three pyrolitic graphite crystals, in order to perform time focusing and maximize the flux arriving on the sample. It makes use of the time-of-flight principle for measuring the final energy of neutrons. Hence it is a direct geometry ToF spectrometer. The energy window of IN6 goes from an energy gain of 3 meV down to an energy loss of 200 meV. The maximum momentum transfer is 2.6 Å^{-1} and the resolution for an incoming wavelength of 5.1 Å, used during our experiments, is 70 μeV.

Backscattering spectroscopy

The backscattering (BS) spectroscopy surveys with an ultra-high energy resolution of the order of 1 μeV - 0.1 μeV [87] the time window comprised between 10^{-7}s to 10^{-9}s [87] where the most interesting dynamics for diffusion, molecular rotation and tunneling spectroscopy take place [27]. BS instruments work as triple-axis spectrometers as represented in Fig. 1.10: first of all a white beam of neutrons is monochromatized by the means of a single crystal at the appropriate orientation according to Bragg's law. Then, the monochromatic beam reaches the sample and gets scattered: neutrons exchange energy and linear momentum with the sample or are elastically scattered. Finally, the energy of the scattered neutrons is analyzed for every direction of the space, making use, once again, of analyzer single crystals and the Bragg's law for diffraction. This procedure leads to the scattering function $S(\mathbf{Q}, \hbar\omega)$ in the momentum transfer $\mathbf{Q}$ and the energy transfer $\hbar\omega$ domain.

Backscattering geometry The BS spectroscopy, reaches a very high resolution thanks to a particular geometry which reduces to its minimum the wavelength dispersion during the monochromatization and the analysis of the neutron beam. Monochromatizors and analyzers are single crystals which re-

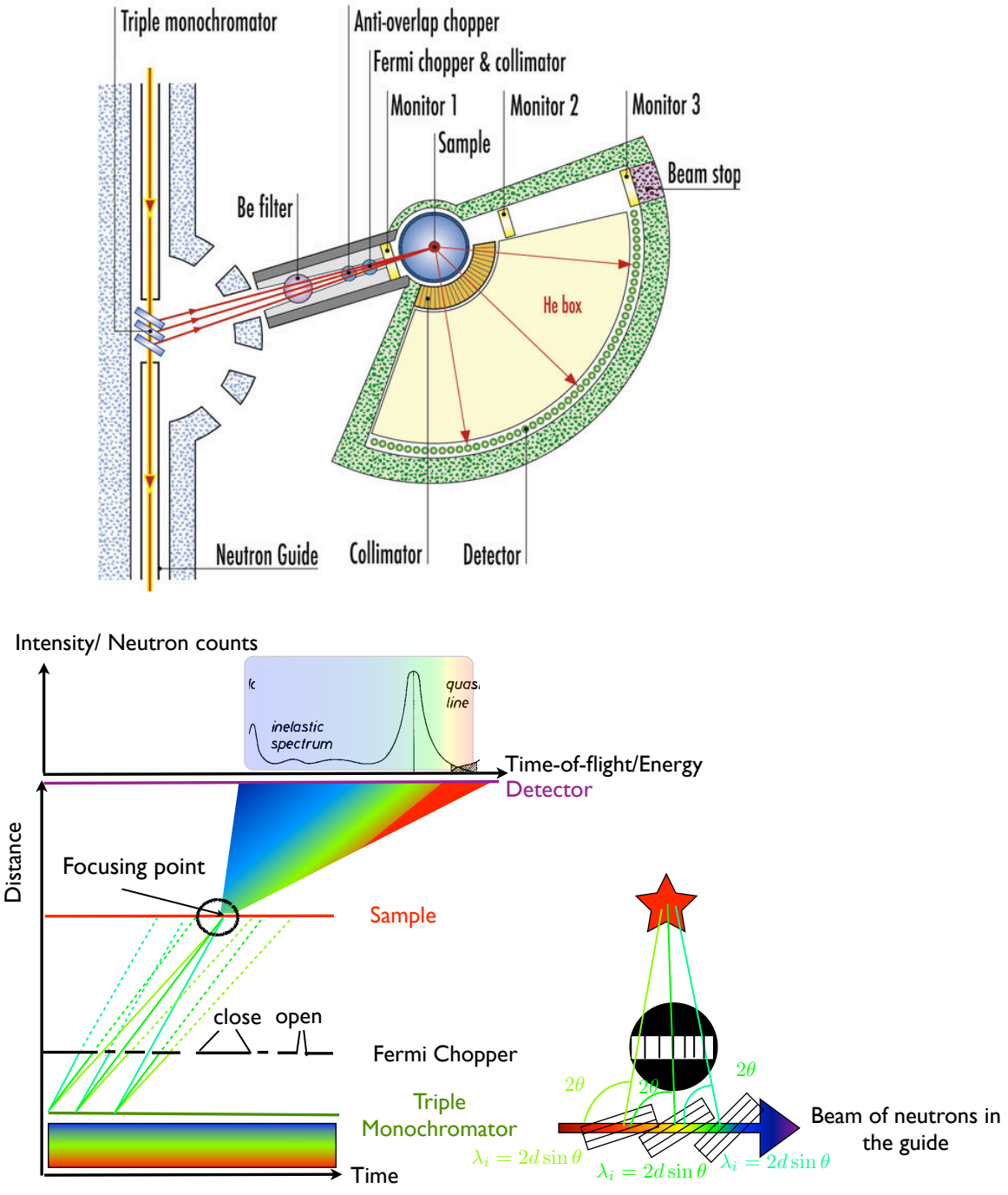

Figure 1.9: Top panel: Schematic representation of the experimental set-up of the IN6 ToF spectrometer at ILL, taken from `www.ill.eu`. Bottom panel: illustration of the time focusing technique.

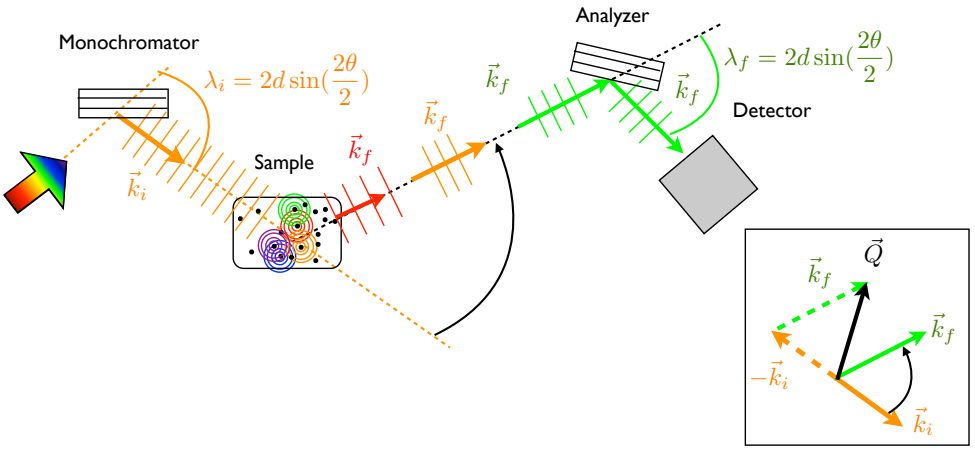

Figure 1.10: Schematic representation of the triple-axis spectroscopy principle. The monochromator selects the incoming neutron energy, by the means of Bragg law diffraction. The continuous and monochromatic neutron beam is scattered by the sample. Afterwards the scan in final energies is performed in every direction of the space. Once again, Bragg's law for diffraction is in use: only neutrons whose final wavelength matches the interplanar distance of the analyzer crystal at a given incident angle will be diffracted. As a result, the detector counts the number of neutrons with a precise final energy and momentum transfer. In the inset we represent the momentum transfer vector **Q** corresponding to the configuration of the measurement (the direction of the incident beam and the direction of analysis of the scattered neutrons).

flect only the incoming wavelengths matching their interplanar distance, d (i.e. Bragg's law):

$$\lambda = 2d \sin\left(\frac{2\theta}{2}\right). \tag{1.20}$$

In the so-called *backscattering geometry*, an incident angle $\theta \sim \pi/2$ (the plane of the crystal is perpendicular to the direction of the beam) minimizes the dispersion of the incoming or scattered wavelengths [56]. This can be seen in the resolution which is obtained from the differentiation of the Bragg's law with respect to the angle θ and the d-space d of the family of planes producing the diffraction:

$$\delta\lambda = 2d\cos\left(\frac{2\theta}{2}\right)\delta\theta + 2\sin\left(\frac{2\theta}{2}\right)\delta d \Rightarrow \frac{\delta\lambda}{\lambda} = \frac{\delta\theta}{\tan\theta} + \frac{\delta d}{d} \Rightarrow \lim_{\theta\to\pi/2}\frac{\delta\lambda}{\lambda} = \frac{\delta d}{d}. \tag{1.21}$$

However the resolution remains always finite and can not be lowered down to the uncertainty in d-spacing arising from the spread of interplanar distances in the monochromator and analyzer single crystal [46]. Besides, the orientation of the monochromator should be fixed in backscattering conditions in order to maintain the high resolution. In that case, only the elastically scattered neutrons will fulfill the Bragg condition at the monochromator and the analyzer and, thus, will be detected. This type of measurement are the so-called *fixed energy window scan* and records the intensity of scattered neutrons at a fixed energy transfer: $\hbar\omega = 0$ [87]. This is an efficient tool for testing the suitability of the instrument time window to the dynamics in the sample and the thermal range which can be surveyed. In general, the thermal activation of a diffusing mechanism (rotation or translation for example) translates into a fraction of neutrons, which are no longer elastically scattered due to the interaction with the moving elements of the target. This gives rise to a loss in the elastic intensity and a step in the elastic scan at the activation temperature. Hence, varying the temperature while performing an elastic window scan helps to evaluate the number of different activated processes occurring (the number of steps) and estimate their typical relaxation times (the slope of the step) [87]. Conversely, the scan in energies or wavelengths is performed by a Doppler drive moving the monochromator with a speed v_D [87]. Varying the position of the monochromator with a constant speed is equivalent for the neutron probes to change the effective d-spacing of the single crystal and hence the wavelength of the Bragg scattered neutrons [86]:

$$\Delta E = 2E\frac{v_D}{v} + O\left[\left(\frac{v_D}{v}\right)^2\right] \tag{1.22}$$

Unfortunately, this procedure allows to scan only a narrow range of energies going up to energy transfers of 30 μeV [86]. The energy range can be broadened as well if the monochromator is heated such that the d-spacing increases.

But this is a slow technique and requires long times of counting [86]. After the scattering, neutrons are analyzed by a range of single crystals, again, in backscattering geometry. IN16 is a classical BS spectrometer which attains an experimental resolutions of 0.9μeV [89].

The OSIRIS Backscattering-ToF spectrometer at ISIS, UK OSIRIS is the prototypical instrument for ToF inverse geometry spectrometry, which was previously described in section 1.2.3. It combines both: time-of-flight technique for selecting the initial wavelength and backscattering geometry in the analyzer crystals for measuring the scattered neutron energy with the highest resolution. In particular it is very well suited for molecular diffusion studies. Its energy resolution, 24.5 μeV FWHM [90], gives rise to a time window ranging between 10^{-9} - 10^{-10} s, so that the instrument is highly sensitive to molecular diffusive motion with typical times $\sim 10^{-11}$ s [91]. Furthermore, its intense flux (2.7×10^{7}n.cm^{-2}.s^{-1} at the sample position in white beam conditions at ISIS maximal intensity [90]) provides very high quality data (high statistics). Finally the wide momentum transfer range which is available: 0.18 to 1.8 Å^{-1} in the PG002 configuration and 0.37 to 3.6 Å^{-1} in the PG004 configuration [90], allows to probe separately the quasi-elastic scattering from different diffusive mechanism with different typical length scale such as translational and rotational modes.

Spin-echo spectroscopy

Finally, the last technique to be described is the neutron spin-echo (NSE) spectroscopy developed in the 1970's, which extends the dynamical window of the QENS techniques to the nano-micro second region with an ultra-high resolution (in the sub-μeV range [86]). NSE is a singular spectroscopy technique, which is able to measure directly the effect of the scattering on each neutron velocity (before and after), without the need to convert it into a difference of energy [56]. As a result, it measures the intermediate scattering function $I(\mathbf{Q},t)$ [56], this is the correlation function (see Eq. 1.13) in the momentum transfer/real time domain.

The spin-echo principle The spin-echo principle makes use of the magnetic moment (in a semi-classical picture) or the spin (in a quantum view) for labeling and following each neutron of the beam before and after the scattering. It is based on the Larmor precession of the magnetic moment of neutrons around a perpendicular magnetic field [92, 93], or on the Zeeman effect from a

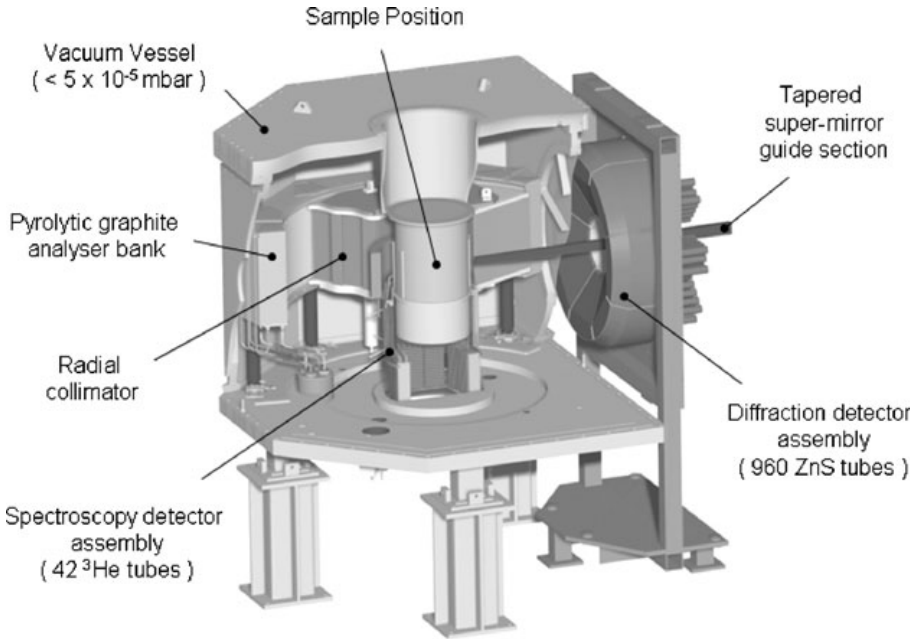

Figure 1.11: Scheme of the OSIRS spectrometer at ISIS, taken from Ref. [90].

quantum point of view. Nevertheless we will stick to the classical description of NSE. Spin-echo instruments are made of two coils surrounding the sample (see scheme in Fig. 1.12). The incoming beam of neutrons is initially polarized perpendicular to its direction before entering in the first coil of length L which generates a magnetic field, B_1 along the direction of the beam. The magnetic moments of each neutron precess while they go through the coil, and their rotation angle depends on the Larmor frequency $\omega_L = \gamma B_1$ and the time spent in the coil l/v_1 [94]:

$$\phi_1 = \int_0^{L/v_1} \omega_L dt = \frac{\gamma}{v_1} \int_0^L B dl \tag{1.23}$$

Since each neutron travels with a different speed, because no initial wavelength needs, a priori, to be selected [86, 93], then, by the end of the first coil the polarization of the beam is totally lost. Once the scattering process takes place, the outgoing neutrons are collected into a second coil on which a magnetic field of the same intensity but opposite direction is applied, $B_2 = -B$. Once again, the Larmor precession of the neutron magnetic momentums takes place but in the opposite direction (due to the inversion of the magnetic field), thus:

$$\phi_2 = \int_0^{L/v_2} \omega_L dt = -\frac{\gamma}{v_2} \int_0^L B_2 dl = \frac{\gamma}{v_2} \int_0^L B dl \tag{1.24}$$

If the scattering is elastic then neutrons travel through the coils with exactly the same velocity: $v_1 = v_2$ and the full polarization of the beam, $P = \langle \cos(\Delta\phi) \rangle$ should be recovered ($P = 1$) at the end of the second coil because

$$\Delta\phi = \phi_1 - \phi_2 = \gamma \int_0^L Bdl \left(\frac{1}{v_1} - \frac{1}{v_2} \right). \tag{1.25}$$

Conversely if the scattering is inelastic, then, the velocities of the neutrons in each coil are different: $v_1 \neq v_2$. Consequently, a loss of the polarization will be observed (see Fig. 1.12). As a result, NSE measures the polarization of the beam at the end of the second coil and yields the intermediate scattering function $I(\mathbf{Q}, t)$ [16, 93] thanks to the following relation:

$$P = \frac{\int d\hbar\omega S(\mathbf{Q}, \hbar\omega) \cos(\hbar\omega t)}{\int d\hbar\omega S(\mathbf{Q}, \hbar\omega)} = \mathrm{Re} \left[\frac{I(\mathbf{Q}, t)}{I(\mathbf{Q}, 0)} \right]. \tag{1.26}$$

The use in NSE of Larmor precession as an internal clock of each neutron, not only extends the probing power of neutrons to time scales of picosecond maintaining a sub-μeV resolution [16] but it also decouples the energy resolution from the momentum transfer resolution. The ability of encoding the velocity information of neutrons in the number of Larmor precessions undergone by their magnetic moment of the neutron in its way through the coils, free us to select the initial wavelength. As a result, NSE overcomes the conflict between resolution and intensity thanks to an intelligent use of neutrons properties.

The neutron spin-echo spectrometer IN11 at ILL IN11 is one of the spin-echo spectrometers at the ILL and it is located in the ILL7 guide hall at the end of the cold guide H141. It can access a very broad range of incoming wavelengths from 3.1 Å to 12 Å and can achieve a Fourier time range spanning over three orders of magnitude (from 0.2 ps to 3 ns) for an incoming wavelength of 4 Å and using the IN11C configuration (see Fig. fig:IN11). This corresponds to an energy window of 2×10^{-4} - 0.15 meV. The momentum transfer range for the same initial wavelength is of 0.02 - 2.7 Å^{-1}. Finally its resolution in terms of the relative error in the wavelength, $\Delta\lambda/\lambda$ is of 15% under this conditions.

Conclusion: why neutrons?

To conclude, we have seen that there exist several experimental techniques for surveying surface diffusion in all the distance and times scales. However, we can not designate one of them to be the perfect and the most complete method, since all of them present limitations, advantages and disadvantages.

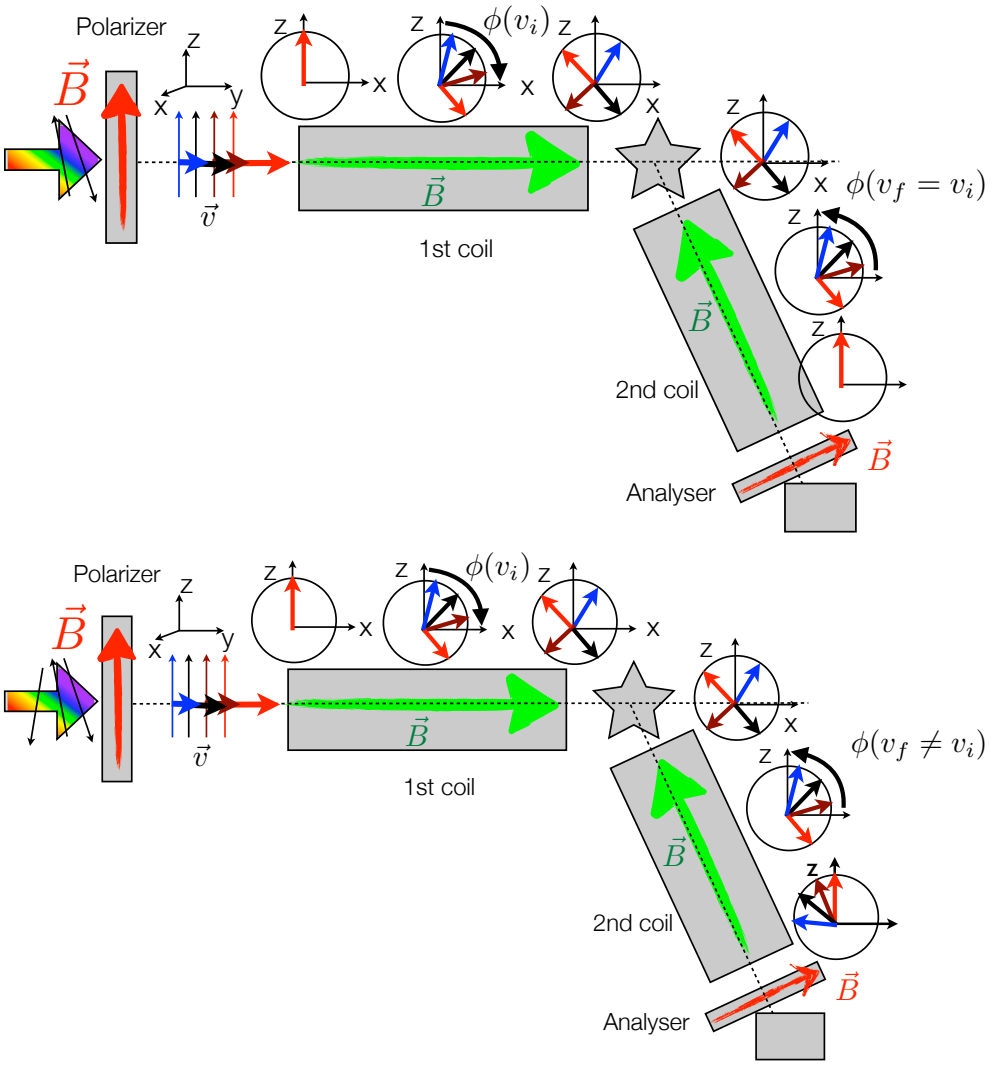

Figure 1.12: Illustration of the spin-echo principle. The target is represented by the star. Left panel: elastic process in which the full polarization of the beam is recovered at the end of the second coil. Right panel: inelastic scattering where a loss in polarization is recorded, due to the difference of the velocities of the neutrons in the first and second coil.

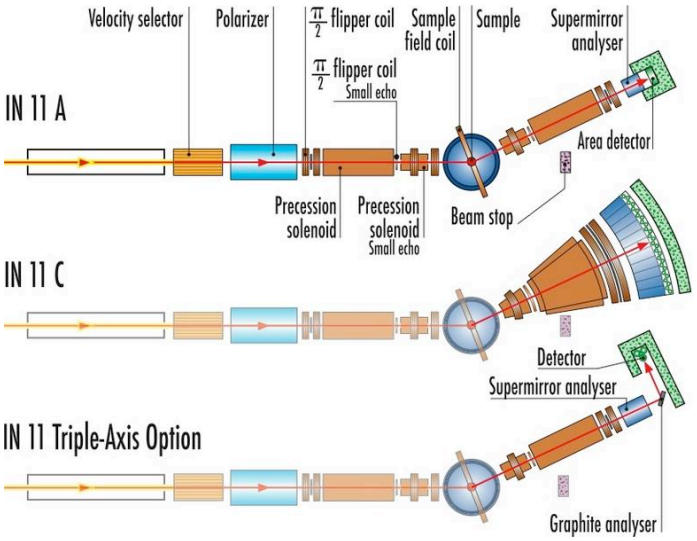

Figure 1.13: Scheme of the IN11 spectrometer at ILL, taken from `www.ill.eu`.

Table 1.2: Summary of the chief characteristics of QENS techniques: the energy resolution and the energy transfer, $\hbar\omega$, which give rises to a finite time window. We also include the reciprocal range covered and its corresponding distances in the direct space. Finally we enumerate the physical mechanisms which are visible under the experimental conditions. The numerical indications are taken from Refs. [27, 56, 72, 86, 87, 89, 95].

Technique Instruments	Energy resolution/ time window	$\hbar\omega$	Q[Å^{-1}]/ distance [Å]	Observable processes
Direct Time-of-flight IN4, IN6, IN5 at ILL	1000 - 10 μeV 10^{-13} - 10^{-9} s	$<$ 3 meV	$\leq$ 2.6 Å^{-1} 2 Å $<$	Tunneling rotation Diffusion coefficients: 10^{-8} - 10^{-4} cm^2.s^{-1} Molecular rotation
Indirect Time-of-flight OSIRIS (ISIS, UK)	16 - 1 μeV 10^{-13} - 10^{-9} s	$<$500 meV	$\leq$ 2.6 Å^{-1} 2 Å $<$	External modes of adsorbed layers Vibrational spectroscopy: 10^{-14}-10^{-12}s.
Backscattering IN16 (ILL)	1 - 0.1 μeV 100 ps - 0.01 μs	-30 μeV - 30 μeV	0.1 - 2.0 Å^{-1} 3 - 60 Å	Diffusion Molecular reorientation
Spin-echo IN11 (ILL)	$\sim$ 10 neV 10 ps - 100 ns	0.2 μeV - 0.15 meV	0.3 - 3 Å^{-1}	Translational diffusion Rotational diffusion

In our case, we seek for understanding the diffusion of physisorbed aromatic rings compounds (benzene, naphthalene or pyrene) adsorbed on the basal plane of graphite. Despite of their bulk character, neutrons turn to be an extremely well suited probe for this diffusion study. First of all, QENS techniques match perfectly the time and distance scale on which relevant aspects of diffusion occur. Secondly, neutrons can distinguish between atoms in the molecule and they are extremely sensitive to the presence of hydrogen. It is very difficult to spot such a light atom with other techniques such as photons or He atoms. Finally, the use of exfoliated compressed graphite, *Papyex*, allows to adsorb a sufficient amount of molecule in order to have a reliable quasi-elastic signal arising from the adsorbates. All this reasons encourages us to undergo a neutron study of the diffusion of aromatic compounds adsorbed on the basal plane of graphite. We shall see in the next chapter how theory and MD simulations enables to understand the experimental data with great detail.

Chapter 2

Theoretical background for diffusion studies with neutron scattering

This chapter deals with the theoretical formalism for understanding neutron scattering data arising from diffusive process of surface adsorbed species. The *Van Hove formalism*, enlarges the concept of the pair correlation function to space and time. It is a powerful theoretical tool for understanding the neutron differential scattering cross-section in terms of the diffusive regime of the atoms in the sample. Furthermore, it also gives a physical meaning to one of the most striking features of neutron scattering: the coherent and incoherent scattering. With this solid theoretical framework, it is possible to predict the shape of the differential neutron cross-section, and in particular of the quasi-elastic line, according to the behavior of the diffusing system. However, even if the development of a reliable theoretical support is crucial for the application of neutron scattering to diffusion studies, the recent improvement in computing power play an essential role. The capability of performing molecular dynamics (MD) simulations with large systems and realistic force fields fosters the interpretation of experimental data beyond the traditional analytical models. It contributes to building up new approaches and tackle the underlying complexity in diffusive processes.

The chapter is organized as follows. First of all, we introduce the *Van Hove formalism* and its chief function: the *Van Hove correlation function* which contains all the dynamical information about the system. Afterwards, we review the most classical models builded based on this formalism, highlighting the fingerprint of the different diffusive regimes in the experimental data. The final

section is devoted to the MD simulations: the description of the main methods and the role it plays for the interpretation of neutron scattering experimental data.

2.1 The Van Hove formalism

In the previous chapter we saw how neutron scattering dress an atomic description of the dynamical processes and the structural properties of the target. Besides, the weak interaction of neutrons with matter, reduced to the nuclear scattering in the case of non-magnetic systems, allows the factorization of the differential scattering cross-section. In a first approximation, the neutron experimental data are the product of a term containing all the information about the neutron interaction with the nuclei in the system (the scattering length b) and a function related to the dynamics and structure of the system: the scattering function. Neutron scattering perturbs slightly the thermal equilibrium state of the system. Following the linear response theory, and more precisely the fluctuation-dissipation theorem, the scattering function images in the reciprocal space of momentum and energy transfer $(\mathbf{Q}, \hbar\omega)$ the thermal fluctuations restoring the equilibrium of the system. The Van Hove formalism, supplies the theoretical tools to link the scattering function, and hence the response of the system to a weak perturbation, with the diffusion of atoms or molecules adsorbed on the substrate.

2.1.1 The Van Hove correlation function

The main function in the center of the formalism is the *Van-Hove generalized correlation function* [75], $G(\mathbf{r}, t)$, defined as the probability of finding a particle at a position, $\mathbf{r}$ at time, t, provided there was a particle (the same or a different one) at the origin, $\mathbf{r} = \vec{0}$, at $t = 0$ [58, 60, 72, 75]:

$$G(\mathbf{r}, t) = \frac{1}{N} \sum_{j,j'=1}^{N} \int \langle \delta(\mathbf{r}_j(0) - \mathbf{r}') \delta(\mathbf{r}_{j'}(t) + \mathbf{r} - \mathbf{r}') \rangle d\mathbf{r}', \tag{2.1}$$

We would like to stress that in this chapter we only treat classical systems: the Heisemberg operators for the position of the particles j and j', $\mathbf{r}_j(0)$ and $\mathbf{r}_{j'}(t)$, commute [57,60]. On the contrary, if the system presents a quantum behavior, the position operators at different times would not commute anymore[1]. As a

[1]The Baker-Hausdorff or *disentangling theorem* helps to deal with operations of non-commutative operators [57]. If A and B are two operators, then the BH theorem states:

$$\exp A \exp B = \exp([A, B]/2) \exp(A + B).$$

result, the Van Hove correlation function would have an imaginary part, arising from the nonzero commutator between $\mathbf{r}_j(0)$ and $\mathbf{r}_{j'}(t)$. A complex correlation function is the signature of a quantum system [57, 75].

The delta function properties[2] link the Van-Hove correlation function with the previously described neutron scattering function and the intermediate scattering function, ISF. Indeed, $G(\mathbf{r},t)$ reads as the space-momentum transfer Fourier transform of the intermediate scattering function, ISF (see Eq. 1.15) [60, 75, 96]:

$$G(\mathbf{r},t) = \frac{1}{(2\pi)^3}\int I(\mathbf{Q},t)\exp(-i\mathbf{Q}\cdot\mathbf{r})d\mathbf{Q}, \tag{2.2}$$

or, equivalently, it is related through the Fourier transform in time–energy and space to the scattering law [60]:

$$G(\mathbf{r},t) = \frac{\hbar}{(2\pi)^3}\int\int \exp(-i(\mathbf{Q}\cdot\mathbf{r}-\omega t))S(\mathbf{Q},\omega)d\mathbf{Q}d\omega. \tag{2.3}$$

If we split the summation running over all the atoms in the system in Eq. 2.1, function $G(\mathbf{r},t)$ can be separated into two contributions [75]: (i) The *self correlation function* G_s $(j = j')$ [75]:

$$G_s(\mathbf{r},t) = \frac{1}{N}\sum_j^N \int \langle\delta(\mathbf{r}_j(t)-\mathbf{r}')\delta(\mathbf{r}_j(0)+\mathbf{r}-\mathbf{r}')\rangle d\mathbf{r}', \tag{2.4}$$

which gives the probability of finding the j-th atom at position $\mathbf{r}$ at time t if this atom was at the origin at time $t = 0$. (ii) The *distinct correlation function* G_d, where $j \neq j'$ [75]:

$$G_d(\mathbf{r},t) = \frac{1}{N}\sum_{j\neq j'}^N \int \langle\delta(\mathbf{r}_j(t)-\mathbf{r}')\delta(\mathbf{r}_{j'}(0)+\mathbf{r}-\mathbf{r}')\rangle d\mathbf{r}', \tag{2.5}$$

probes the probability of finding the j-th atom at position $\mathbf{r}$ at time t provided a different atom, j', was at the origin at time $t = 0$. Adding together both functions, we recover the original correlation function:

$$G(\mathbf{r},t) = G_s(\mathbf{r},t) + G_d(\mathbf{r},t). \tag{2.6}$$

and $[A, B]$ is a complex number. In the case of the Van Hove correlation function, the non-commutative operators A and B are $\mathbf{r}_j(0)$ and $\mathbf{r}_j(0)$. Since $[\mathbf{r}_j(0), \mathbf{r}_j(0)]$ is a complex number, the Van Hove correlation function turns into a complex function.

[2] In particular, the relation between the delta function and the integral over all the space of the exponential function (in three dimensions):

$$\delta(\mathbf{r}-\mathbf{r}') = \frac{1}{(2\pi)^3}\int_{\text{all space}} \exp(i\mathbf{Q}\cdot(\mathbf{r}-\mathbf{r}'))d\mathbf{Q}$$

As a result, the Fourier transformations in time and space connect the Van Hove correlation function describing the dynamics of the system, with experimental neutron functions such as the ISF or the scattering law [56,58,60,75,96]. Thereby a neutron spectrum measures the correlations in time and space of atomic positions in the system. We will see in the next section, how the distinction between the self and the distinct correlation function endow with a physical meaning the coherent and incoherent scattering of neutrons by diffusing atoms.

2.1.2 The coherent and incoherent scattering according to the Van Hove formalism

The interaction between the neutron probes and the atom nuclei generates two mechanisms of scattering: the so-called *coherent* and *incoherent* scattering. The origin of the twofold nature of neutron scattering stems from the the specificity of each nucleus scattering length b and, also, from its dependence on the neutron and nuclear spin operators [58,97]. The power of the Van Hove formalism is asserted by its capacity to associate each kind of scattering to the individual (for the incoherent scattering) and to the collective (in the case of coherent scattering) dynamics of the diffusing elements in the sample.

Each isotope has a specific scattering length b for neutrons, since neutron scattering is a nuclear interaction [56, 58]. In a collection of N atoms, there is a statistical distribution of chemical species and of isotopes of each specie. As a consequence, when neutrons are scattered by a crystal, even if it is made of identical atoms, the interaction potential is not homogeneous but varies from atom to atom [58]. However, the effects on the neutron scattering of such statistical distribution in space of the system-neutron interaction potential can be addressed by calculating the average potential and its corresponding standard deviation.

The coherent neutron scattering We assume that all the atoms in the system have the same scattering length, taken to be the statistical average of the scattering lengths:

$$\langle b \rangle = \sum_{j}^{N} c_j b_j, \tag{2.7}$$

provided we know the relative density of the j-th species, c_j (where $\sum_j^N c_j = 1$) [58, 60, 61]. The total number of neutrons scattered by this completely homogeneous system is readily found by substituting by $\langle b \rangle$, the b_j for j over all the nuclei in the system and integrating the differential scattering cross

section (Eq. 1.9 in the section 1.2.1 Chap. 1) in all the space and for all the energies:

$$\sigma_{coh} = \int \frac{d^2\sigma}{d\Omega d\omega} d\Omega d\omega = 4\pi \langle b \rangle^2 . \tag{2.8}$$

This is the so-called *bound coherent scattering cross section* and it is proportional to the squared average of b [56]. However it should be noted that in such a system, it is impossible to tell which specific atom scatters a given incoming neutron, for all the nuclei have the same scattering label. It is preferably to say that the neutron is scattered by all the set of N atoms: i.e the neutron adopts a wave behavior [97] such that a proper trajectory can not be associated. Therefore the average of the system scattering potential gives rise to *interference* effects [58,60]: the intensity of neutrons presents a strong anisotropy and intensity peaks only appear for particular directions of the scattered beam in which the Bragg condition is satisfied. The resulting momentum transfer corresponds to the Bravais lattice vectors $\mathbf{G}$ describing the arrangement of the elements in the sample in the reciprocal space:

$$\mathbf{k} - \mathbf{k}' = \mathbf{G}. \tag{2.9}$$

Hence, the wave nature of neutron allows to do diffraction experiments and to measure diffraction patterns (the ensemble of intensity peaks at given directions of the space). But coherent scattering scope does not reduce to structural information: it enlightens the dynamics of collective processes and can be fruitfully exploited for the study of diffusion. Indeed, coherently scattered neutron exchange energy and momentum with the sample by exciting or annihilating collective modes: the interaction is always with a collection of atoms and never with single atoms [97].

The incoherent scattering Conversely, the deviations of the scattering potential with respect to its average are randomly distributed in space [58,60]: the isotopes of an atom have not allocated positions, but there exists a certain probability to find a given isotope in a certain position. Such deviations are quantified by the standard deviation of the averaged scattering length [58,60]:

$$\left\langle b^2 \right\rangle - \langle b \rangle^2 = \sum_j^N c_j (b_j)^2 - \left(\sum_j^N c_j b_j \right)^2 , \tag{2.10}$$

which describes the degree of heterogeneity in the system. Furthermore, the scattering of a neutron by a nucleus depends also on the relative orientation of the neutron and the nuclear spin. Therefore, there exists the possibility of flipping the neutron and the nucleus spin during the scattering process [97], apart from exchanging energy and momentum with the nucleus. Thereby, in

contrast with the coherent scattering, we can identify which atom of the system interacts with the neutron [97]. In other words, we can reconstruct the neutron probe trajectory [97] meaning that we deal with a particle rather than with a wave. This kind of contribution to the scattering can not be analyzed in terms of interferences between waves. It corresponds to single neutron - single nucleus interaction and is completely isotropic: this is the so-called *incoherent scattering* [58,60]. Consequently, the part of neutrons scattered by a statistical distribution of chemical species and isotopes in the system [60] needs to be proportional to the standard deviation of scattering lengths [56]:

$$\sigma_{inc} = 4\pi(\langle b^2 \rangle - \langle b \rangle^2). \tag{2.11}$$

This is the *bound incoherent scattering cross-section.*

To conclude, the coherent/incoherent scattering is nothing else than the manifestation of the wave-particle duality of neutrons [97]. Some systems will enhance the neutron wave behavior while other systems will stress the neutron particle nature. In the so-called coherent systems, the scattering length distribution present negligible deviations with respect to its average. The corresponding incoherent cross section is small if compare with the coherent cross section. Hence, neutron probes tend to interact with these kind of systems acting as waves and the scattered intensity presents strong variations with the momentum transfer, due to the constructive/destructive interferences. A clear example are the carbon based or the deuterated systems (see Tab. 2.1). On

σ [barns=10^{-24}cm]	H	D	C
σ_{inc}	80.27	2.05	0.0005
σ_{coh}	1.76	5.59	5.564

Table 2.1: Incoherent and coherent scattering cross-sections of hydrogen and carbon atoms [58].

the other side, systems containing hydrogen atoms are well-known for their high incoherent cross section [56] and neutrons interact with protons behaving as particles. The scattered intensity will be isotropic [58], the interaction is always between a single neutron and a single nucleus whose spins are coupled and change during the scattering, in such a way that every nucleus gets tagged and becomes recognizable [97]. Finally, the total cross-section σ of a system is the total number of neutrons scattered by the system, in all directions and energies. It comprehends both contributions arising from the coherent and incoherent scattering cross sections [56]. It reads as the summation of the

coherent and incoherent bound cross-sections:

$$\sigma = \sigma_{inc} + \sigma_{coh}, \tag{2.12}$$

if we assume once again the independence of the scattering from the neutron or the nuclear spin (i.e when the neutron beam is fully depolarized or the nuclear spins are randomly oriented [61]).

In order to distinguish between the coherent and incoherent contributions within the differential scattering cross-section (Eq. 1.9), whose mathematical expression we recall here:

$$\frac{d^2\sigma}{d\Omega d\omega} = \frac{k}{k_0}\frac{1}{2\pi\hbar}\sum_{j,j'=1}^{N}\left\langle b_j^* b_{j'}\right\rangle \int_{-\infty}^{\infty} dt \exp(-i\omega t)\left\langle \exp(-i\mathbf{Q}\cdot\mathbf{r}_{j'}(t))\exp(i\mathbf{Q}\cdot\mathbf{r}_j(0))\right\rangle,$$

it is important to calculate the cross products $\left\langle b_j^* b_{j'}\right\rangle$:

$$\begin{cases} \langle b_j^* b_j\rangle = \langle b^2\rangle \text{ for } j = j' \\ \langle b_j^* b_{j'}\rangle = \langle b_j\rangle\langle b_{j'}\rangle = \langle b\rangle^2 \text{ for } j \neq j', \end{cases} \tag{2.13}$$

provided that the scattering lengths of the j-th and the j'-th nuclei are uncorrelated, and can be considered as real constants (no absorption process, only scattering) [58,60]. Accordingly, the double summation in the differential scattering cross-section in Eq.1.9 splits into two summations. The first term sums together the *self-correlation functions*, $Y_{jj}(\mathbf{Q},t)$, which come from equating both indexes $j = j'$ in Eq. 1.13. The second term holds the so-called *distinct correlation function*, $Y_{jj'}(\mathbf{Q},t)$, where both indexes are different $j \neq j'$ in Eq. 1.13. The result of the summation separation reads:

$$\frac{d^2\sigma}{d\Omega d\omega} = \frac{k}{k_0}\frac{1}{2\pi\hbar} \left[\left\langle b^2\right\rangle \sum_{j=j'=1}^{N}\int_{-\infty}^{\infty} dt \exp(-i\omega t) Y_{jj}(\mathbf{Q},t)\rangle + \langle b\rangle^2 \sum_{j\neq j'=1}^{N}\int_{-\infty}^{\infty} dt \exp(-i\omega t) Y_{jj'}(\mathbf{Q},t)\right]. \tag{2.14}$$

Besides, the distinct part can be expressed as a difference between the double summation over all the elements in the system (without any constrain) and the self part [60]:

$$\sum_{j\neq j'=1}^{N} Y_{jj'} = \sum_{j,j'=1}^{N} Y_{jj'} - \sum_{j=j'=1}^{N} Y_{jj}. \tag{2.15}$$

Replacing the distinct part in Eq. 2.14 by Eq. 2.15, yields the final expression of the differential neutron scattering cross-section in terms of the coherent and incoherent contribution to the scattering [58, 60]:

$$\frac{d^2\sigma}{d\Omega d\omega} = \frac{k}{k_0}\frac{N}{4\pi}\left[\sigma_{coh}S_{coh}(\mathbf{Q},\omega) + \sigma_{inc}S_{inc}(\mathbf{Q},\omega)\right]. \tag{2.16}$$

The first term is the *coherent* scattering function:

$$S_{coh}(\mathbf{Q},\omega) = \frac{1}{2\pi\hbar}\int_{-\infty}^{\infty} dt \exp(-i\omega t)\frac{1}{N}\sum_{j,j'=1}^{N} Y_{jj'}(\mathbf{Q},t) \tag{2.17}$$

which can be Fourier transformed in time leading to the *coherent* ISF:

$$I_{coh}(\mathbf{Q},t) = \frac{1}{N}\sum_{j,j'=1}^{N} Y_{jj'}(\mathbf{Q},t). \tag{2.18}$$

The *coherent scattering* arises from the scattering of the neutron wave by two different nuclei j and j', giving rise to interferences [58, 60], or by the same nucleus j at different times [60] (there is no restriction on the value of the indexes j and j' in the summations of Eqs. 2.17 or 4.60). The second term is the *incoherent* scattering function:

$$S_{inc}(\mathbf{Q},\omega) = \frac{1}{2\pi\hbar}\int_{-\infty}^{\infty} dt \exp(-i\omega t)\frac{1}{N}\sum_{j=j'=1}^{N} Y_{jj}(\mathbf{Q},t), \tag{2.19}$$

and in analogy with the coherent case, there exist in the Fourier transformed space of real time the *incoherent* ISF:

$$I_{inc}(\mathbf{Q},t) = \frac{1}{N}\sum_{j}^{N} Y_{jj}(\mathbf{Q},t) \tag{2.20}$$

In contrast to the coherent scattering, the incoherent scattering depends only on the self-correlation functions $Y_{jj}(\mathbf{Q},t)$ and, hence, comes only from the scattering of the very same nucleus at different times [60].

The coherent, incoherent neutron scattering and the Van Hove correlation functions The splitting of the Van Hove correlation function into a self and a distinct function corresponds to the separation of the neutron scattering cross section into a coherent and an incoherent part [56, 58, 60, 75]. Indeed,

it is easy to demonstrate the following relations between the coherent and incoherent scattering law with the distinct and self correlation function [60]:

$$\begin{aligned} S_{coh}(\mathbf{Q},\omega) &= \frac{1}{2\pi\hbar}\int dt \exp(-i\omega t)\int G(\mathbf{r},t)\exp(i\mathbf{Q}\cdot\mathbf{r})d\mathbf{r}, \\ S_{inc}(\mathbf{Q},\omega) &= \frac{1}{2\pi\hbar}\int dt \exp(-i\omega t)\int G_s(\mathbf{r},t)\exp(i\mathbf{Q}\cdot\mathbf{r})d\mathbf{r}. \end{aligned} \tag{2.21}$$

By Fourier transforming the previous equations in time, we find the analogous relations for the coherent and incoherent ISF [60]:

$$\begin{aligned} I_{coh}(\mathbf{Q},t)) &= \int \exp(i\mathbf{Q}\cdot\mathbf{r})G(\mathbf{r},t)d\mathbf{r}, \\ I_{inc}(\mathbf{Q},t)) &= \int \exp(i\mathbf{Q}\cdot\mathbf{r})G_s(\mathbf{r},t)d\mathbf{r}. \end{aligned} \tag{2.22}$$

Thereby , the measured differential scattering cross section can be connected and understood in the basis of the Van Hove formalism:

$$\begin{aligned} \frac{d^2\sigma}{d\Omega d\omega} =& \frac{k}{k_0}\frac{N}{4\pi}\left[\sigma_{coh}\frac{1}{2\pi\hbar}\int_{-\infty}^{\infty} dt\exp(-i\omega t)\int_{-\infty}^{\infty} d\mathbf{r}\exp(i\mathbf{Q}\cdot\mathbf{r})G(\mathbf{r},t)\right. \\ &\left. +\sigma_{inc}\frac{1}{2\pi\hbar}\int_{-\infty}^{\infty} dt\exp(-i\omega t)\int_{-\infty}^{\infty} d\mathbf{r}\exp(i\mathbf{Q}\cdot\mathbf{r})G_s(\mathbf{r},t)\right]. \end{aligned} \tag{2.23}$$

This is particularly useful for diffusion studies because the self and the distinct Van Hove correlation functions enlighten the meaning of the coherent and incoherent scattering when neutrons interact with diffusing particles. Thus, neutron probes bring to light information about different but complementary features of diffusion. In particular, we observe that the incoherent scattering highlights single atom motion while the coherent scattering is also sensitive to correlations in the motion of different atoms and collective dynamics.

2.2 Traditional models for diffusion in QENS spectroscopy

As we have already stated, the continuous spread of energies around the elastic peak, the so-called *quasi-elastic profile*, or the analogous decay in time of the ISF, results from the interaction between diffusing targets and neutrons. Its profile, and in particular the dependence of its *quasi-elastic broadening* (its HWHM) on the momentum transfer $\mathbf{Q}$, bears the experimental signature of the diffusive mechanisms [56]. Theoretical models based on the Van Hove correlation functions formalism [56, 58, 72, 96, 98] predict the profile of the QENS scattering law, or the ISF, according to the kind of dynamics in the system.

They were first intended to describe the particle or molecule self-correlation functions through the incoherent scattering. Now, they can be extended to the coherent scattering thanks to the Vineyard approximation: the distinct correlation function, G_d (Eq. 2.5) is expressed as the convolution of the self-correlation function, G_s (Eq. 2.4) with the ordinary radial distribution function $g(\mathbf{r})$ [2, 99].

Roughly speaking, there are three "standard" cases for diffusion: continuous, jump, and ballistic diffusion. The dependences on $\mathbf{Q}$ of the QENS broadening predicted for each diffusive regime are compared in Fig. 2.1. In the following we describe the corresponding theoretical models: the type of quasi-elastic profile arising from each diffusive regime, the dependence with the momentum transfer $\mathbf{Q}$ of its quasi-elastic broadening and how microscopic information about the diffusive process emerges.

However, prior to start, it is interesting to understand the relation between the mean square displacement, dressing a direct portrait of the diffusion process at the atomic level, and the dependence in time or energy of the different quasi-elastic profiles. From this brief introduction, the different models for diffusion emerge naturally from the statistical mechanics theory and we can discuss clearly the underlying assumptions.

The cumulant expansion and the Gaussian approximation As we have seen in the previous section in Eq. 2.20, the incoherent intermediate scattering function (ISF) measures the sum of the self correlation functions for each element in the system.:

$$I_{inc}(\mathbf{Q},t) = \frac{1}{N}\sum_{j}^{N} Y_{j,j}(\mathbf{Q},t).$$

When we deal with classical particles, the position Heisenberg operators of each scatterer commute [57]. It follows that the original expression of the self-correaltion function (Eq. 1.13) can be rewritten into a more convenient form:

$$I_{inc}(\mathbf{Q},t) = \frac{1}{N}\sum_{j=1}^{N} \langle \exp\left[-i\mathbf{Q}\cdot(\mathbf{r}_j(t)-\mathbf{r}_j(0))\right]\rangle = \frac{1}{N}\sum_{j,j'=1}^{N} \langle \exp\left[-i\mathbf{Q}\cdot\Delta\mathbf{r}_j(t)\right]\rangle, \tag{2.24}$$

where we have replaced the displacement of the j-th particle, $\mathbf{r}_j(t)-\mathbf{r}_j(0)$, by the more compact expression $\Delta\mathbf{r}_j(t)$. However, the Eq. 2.24 does not provide a useful expression of the incoherent ISF for the average $\langle\ldots\rangle$ over the thermal distribution of the rotational-translational states remains non-computed.

Fortunately, the evaluation of this average is easily performed with the help of the *cumulant theorem*[3] [101, 102] which allows to expand an average in terms of the moments of its statistical distribution function [100]. In the case of the incoherent ISF, each self-correlation function $Y_{j,j}(\mathbf{Q},t)$ can be cumulant expanded, where the statistical distribution function coming into play is precisely the Van Hove self-correlation function (compare each of the terms in the sum of Eq. 2.24 with Eq. 2.25). The cumulant expansion of the incoherent ISF reads [101, 103]:

$$I_{inc}(\mathbf{Q},t) = \frac{1}{N}\sum_{j}^{N} \exp\left(\sum_{n=1}^{\infty} \frac{1}{n!} K_n^{(j)} \mathbf{Q}^n\right) \tag{2.29}$$

where $K_n^{(j)}$ are the so-called *cumulants*. They are given by the following expression:

$$K_n^{(j)} = \frac{d^n \ln\left[e^{-i\mathbf{Q}\cdot\Delta\mathbf{r}_j(t)}\right]}{d\mathbf{Q}^n}|_{\mathbf{Q}=\mathbf{0}} = \begin{cases} K_1^{(j)} = i\left\langle \Delta\mathbf{r}_j \right\rangle \\ K_2^{(j)} = -i^2(\left\langle \Delta\mathbf{r}_j^2 \right\rangle - \left\langle \Delta\mathbf{r}_j \right\rangle^2) = \left\langle \Delta\mathbf{r}_j^2 \right\rangle - \left\langle \Delta\mathbf{r}_j \right\rangle^2 \\ K_3^{(j)} = i^3(2\left\langle \Delta\mathbf{r}_j \right\rangle^3 - 3\left\langle \Delta\mathbf{r}_j^2 \right\rangle \left\langle \Delta\mathbf{r}_j \right\rangle + \left\langle \Delta\mathbf{r}_j^3 \right\rangle) \\ K_4^{(j)} = i^4(-6\left\langle \Delta\mathbf{r}_j \right\rangle^4 + 12\left\langle \Delta\mathbf{r}_j^2 \right\rangle \left\langle \Delta\mathbf{r}_j \right\rangle^2 - 4\left\langle \Delta\mathbf{r}_j^3 \right\rangle \left\langle \Delta\mathbf{r}_j \right\rangle \\ \qquad - 3\left\langle \Delta\mathbf{r}_j^2 \right\rangle^2 + \left\langle \Delta\mathbf{r}_j^4 \right\rangle) \\ \quad \dots \end{cases} \tag{2.30}$$

and $\left\langle \Delta\mathbf{r}_j^n \right\rangle$ is the n-th moment of $G_s(\mathbf{r}_j, \mathbf{r}_j(0), t)$:

$$\left\langle \Delta\mathbf{r}_j^n \right\rangle = \int G_s(\mathbf{r}_j, \mathbf{r}_j(0), t) \Delta\mathbf{r}_j^n d\mathbf{r}_j, \tag{2.31}$$

[3] The cumulant theorem is extremely helpful for computing the following kind of averages:

$$G(\mathbf{Q}) = \left\langle e^{i\mathbf{Q}\cdot\mathbf{R}} \right\rangle = \int d\mathbf{r} e^{i\mathbf{Q}\cdot\mathbf{r}} P(\mathbf{r}), \tag{2.25}$$

where $G(\mathbf{Q})$ is called the *characteristic function* [100] and $P(\mathbf{r})$ is the distribution function. If we take the logarithm of the characteristic function:

$$\ln\left[G(\mathbf{Q})\right] = \ln\left[\int d\mathbf{r} e^{i\mathbf{Q}\cdot\mathbf{r}} P(\mathbf{r})\right], \tag{2.26}$$

we can easily Taylor expand it around $\mathbf{Q} = 0$:

$$\ln\left[G(\mathbf{Q})\right] = \ln\left[G(\mathbf{0})\right] + \sum_{n=1}^{\infty} \frac{1}{n!} \frac{d^n \ln\left[G(\mathbf{Q})\right]}{d\mathbf{Q}^n} |_{\mathbf{Q}=\mathbf{0}} \mathbf{Q}^n \tag{2.27}$$

The cumulants are defined as the terms of the expansion:

$$K_n = \frac{d^n \ln\left[G(\mathbf{Q})\right]}{d\mathbf{Q}^n}|_{\mathbf{Q}=\mathbf{0}}. \tag{2.28}$$

where $\mathbf{r}_j(0) = \vec{0}$ and $\Delta\mathbf{r}_j(t) = \mathbf{r}_j(t)$ if we assume that the j-th scatterer is at the origin at $t = 0$ (see previous section 2.1.1).

A remarkable simplification in the calculation of the cumulant expansion results if the statistical distribution function displays a Gaussian profile. The parity of the Gaussian function annihilates all the odd moments of the distribution function, such that only the even moments contribute to the cumulant expansion. As a result, in a system where particles diffuse in a space of d dimensions[4], if the Van Hove correlation function is:

$$G_s^{(d)}(\mathbf{r}_j, \mathbf{r}_j(0), t) = \left(\frac{1}{2\pi\sigma^2(t)}\right)^{d/2} \exp\left(-\frac{\Delta\mathbf{r}_j^2}{2\sigma^2(t)}\right) \tag{2.32}$$

then, the variance needs to be [58, 60]:

$$\sigma^2(t) = \frac{1}{d}\left\langle \Delta\mathbf{r}_j^2 \right\rangle, \tag{2.33}$$

which corresponds to the mean square displacement (MSD) of the j-th atom in the system [58], divided by the dimensionality of the space of diffusion, d. In many cases (in a liquid or in a gas) the main mechanism governing the diffusive process are collisions between particles, or between particles and phonons on a surface or in a crystal. The time between two successive collisions sets the reference scale for defining long and short times. It can be proven that the Van Hove correlation function displays a Gaussian form, for very short or very long times [60,102,104]. Thus, we can approximate the self-correlation function and, hence, the incoherent ISF by the first term of the cumulant expansion [60,101]:

$$Y_{jj}(\mathbf{Q}, t) \simeq \exp\left[-\frac{Q^2}{2}\sigma^2(t)\right] = \exp\left[-\frac{Q^2}{2}\frac{1}{d}\left\langle \Delta\mathbf{r}_j^2 \right\rangle\right] \Rightarrow I_{inc}(\mathbf{Q}, t) \simeq \exp\left[-\frac{Q^2}{2}\sigma^2(t)\right] \tag{2.34}$$

This is the *Gaussian approximation* [102]. Besides, the connection between the MSD of a particle and its velocity correlation function, $\langle \mathbf{v}_j(0)\mathbf{v}_j(\tau)\rangle$ is readily deduced [60, 101, 102, 104]:

$$\Delta\mathbf{r}_j(t) = \int_0^t dt' \mathbf{v}_j(t') \Rightarrow \left\langle \Delta\mathbf{r_j}^2 \right\rangle = \left\langle \left(\int_0^t dt' \mathbf{v}_j(t')\right)^2 \right\rangle = 2\int_0^t d\tau (t-\tau) \left\langle \mathbf{v}_j(0)\mathbf{v}_j(\tau)\right\rangle, \tag{2.35}$$

and vice-versa, we can easily obtain the velocity correlation function from the MSD [60]:

$$\langle \mathbf{v}_j(0)\mathbf{v}_j(t)\rangle = \frac{1}{2}\frac{d^2}{dt^2}\left\langle \Delta\mathbf{r_j}^2 \right\rangle. \tag{2.36}$$

[4] d equals 1 if the diffusion is in a single direction, 2 on a surface and 3 in a volume.

As a consequence, the incoherent ISF, $I_{inc}(\mathbf{Q},t)$, brings to light the microscopic mechanisms of diffusion, since it measures the time dependence of the MSD or, equivalently, of the velocity correlation function of the particles diffusing in the system $\left\langle v^{\mathbf{Q}}(0)v^{\mathbf{Q}}(\tau)\right\rangle$ [60, 104] in the direction of the momentum transfer $\mathbf{Q}$:

$$I_{inc}(\mathbf{Q},t) \simeq \exp\left[-Q^2\frac{1}{d}\int_0^t d\tau(t-\tau)\left\langle v^{\mathbf{Q}}(0)v^{\mathbf{Q}}(\tau)\right\rangle\right], \tag{2.37}$$

where $v^{\mathbf{Q}} = \mathbf{Q}\cdot\mathbf{v}$ is the projection of a particle velocity on the direction of $\mathbf{Q}$. Even if the MSD and the velocity correlation function bear information about single particle motion, we drop the index j in the notation because these functions are averages over the statistical ensemble associated to the equilibrium state of the system. Hence, they characterize the averaged dynamics of single particles in the system, but, without making any distinction between individual elements.

To conclude, we have seen that every diffusive regime is characterized by a particular velocity correlation function, resulting on the way the microscopic mechanisms drive the diffusion (the frequency of collisions for instance). Thereby, the temporal evolution of the MSD changes according to the way particles diffuse [58, 60] and determines the temporal evolution of the incoherent ISF and the profile in energies of the corresponding scattering function [60]. Thus, neutrons can extract very detailed information from the atomic point of view about the dynamics of the system and can identify the main diffusive regimes. The models that are described in the following are build on the basis of the Van-Hove formalism and the Gaussian approximation.

The Brownian diffusion The *Brownian model* describes the continuous diffusion of an adparticle colliding randomly with the other adparticles in an energy dissipative environment (high frictional coupling between adsorbate and substrate) [56]. In the long time limit, when the time between two successive collisions becomes negligible, the mass transport is governed by Fick's second law and described by the Ficks's equation [60]:

$$\frac{\partial n(\mathbf{r},t)}{\partial t} = D\nabla_d^2 n(\mathbf{r},t) \tag{2.38}$$

where $n(\mathbf{r},t)$ is the density of atoms at the spatial point $\mathbf{r}$ at time t, D is the *diffusion coefficient* and ∇_d^2 is the Laplacian operator for a space of d dimensions[5]. Here, we consider isotropic diffusion, such that D is a constant. However, if the diffusion is anysotropic, then D becomes a tensor. Consequently, for

[5] ∇_d^2 is expressed in cartesian, cylindrical or polar coordinates, depending if the particles diffuse in one dimension, on a surface or in a volume respectively.

isotropic diffusion, the Van-Hove self-correlation function $G_s^{(d)}(\mathbf{r}, \mathbf{r}(0), t)$, giving the probability of finding a particle at a certain point provided the same particle was at $\mathbf{r}(0)$ when $t = 0$, must fulfill Fick's equation for diffusion [101]:

$$\frac{\partial G_s^{(d)}(\mathbf{r}, \mathbf{r}(0), t)}{\partial t} = D\nabla_d^2 G_s^{(d)}(\mathbf{r}, \mathbf{r}(0), t). \tag{2.39}$$

A suitable solution is $G_s^{(d)}(\mathbf{r}, \mathbf{r}(0), t)$ being a Gaussian function, provided that the variance, or mean square displacement, satisfies the following constrain [58, 60]:

$$\frac{d}{dt}\sigma^2(t) = \frac{1}{d}\frac{d}{dt}\left\langle \Delta\mathbf{r}^2 \right\rangle = 2D \Rightarrow \left\langle \Delta\mathbf{r}^2 \right\rangle (t) = 2dD|t| + c. \tag{2.40}$$

Consequently, in the long time limit, the diffusion coefficient reads as a function of the velocity correlation function, via Eq. 2.35 [101]:

$$D = \frac{1}{d}\lim_{t\to\infty}\int_0^t \left(1 - \frac{\tau}{t}\right)\langle \mathbf{v}(0)\cdot\mathbf{v}(\tau)\rangle\, d\tau = \frac{1}{d}\int_0^\infty \langle \mathbf{v}(0)\cdot\mathbf{v}(\tau)\rangle\, d\tau. \tag{2.41}$$

Eq. 2.41 is a *Green-Kubo formula* [21] and belongs to the class of relations stated by the fluctuation-dissipation theorem [20]. These are the bridge between macroscopic magnitudes such as D with microscopic functions like the velocity correlation function [20, 21]. On the other hand, Einstein's solution of the equation of motion of a Brownian particle, the well-known *Langevin equation*, which describes the motion of a particle subject to a random force representing the effect of collisions $\mathbf{F}(t)$ and a frictional force $-\eta m\dot{\mathbf{r}}(t)$ [101, 105]:

$$\begin{gathered} m\ddot{\mathbf{r}}(t) = -\gamma m\dot{\mathbf{r}}(t) + \mathbf{F}(t), \\ \text{where } \langle\dot{\mathbf{r}}(t)\rangle = 0 \text{ and } \langle\mathbf{F}(t)\rangle = 0 \Rightarrow \left\langle\dot{\mathbf{r}}(t)\cdot\mathbf{F}(t')\right\rangle = \langle\dot{\mathbf{r}}(t)\rangle\left\langle\mathbf{F}(t')\right\rangle = 0, \end{gathered} \tag{2.42}$$

yields an alternative formula for the diffusion coefficient D connected to the friction parameter η. This latter parameter, η quantifies the exchange of energy between adsorbate and substrate [101]. A solution of Eq. 2.42 for the velocity reads [101, 105]:

$$\dot{\mathbf{r}}(t) = \dot{\mathbf{r}}(0)\exp(-\gamma|t|) + \frac{1}{m}\int_0^t \mathbf{F}(t')\exp\left[-\frac{\eta}{m}(t-t')\right] dt', \tag{2.43}$$

and requires that the velocity correlation function follows an exponential decay of time [101, 105]:

$$\langle\mathbf{v}(0)\cdot\mathbf{v}(t)\rangle \equiv \langle\dot{\mathbf{r}}(0)\cdot\dot{\mathbf{r}}(t)\rangle = \left\langle v(0)^2\right\rangle\exp(-\eta|t|). \tag{2.44}$$

If we substitute Eq. 2.44 into the fluctuation-dissipation Eq. 2.41, we obtain[6]:

$$D = \frac{\langle v(0)^2 \rangle}{d} \int_0^\infty \exp(-\eta|\tau|) d\tau = \frac{1}{d} \frac{\langle v(0)^2 \rangle}{\gamma} = \frac{k_B T}{m\eta}. \tag{2.45}$$

Combining the Einstein formula with the fluctuation dissipation theorem leads to an expression for the inverse of the friction parameter in terms of the velocity correlation function:

$$\frac{1}{\eta} = \frac{m}{k_B T} \frac{1}{d} \int_0^\infty \langle \mathbf{v}(0)\mathbf{v}(\tau) \rangle \, d\tau. \tag{2.46}$$

In terms of neutron scattering, the linear time dependence of the MSD generates a single exponential decay in the momentum transfer/real time domain measured with the incoherent ISF (substitute $\sigma^2(t)$ in Eq. 2.34 by Eq. 2.40):

$$I_{inc}(\mathbf{Q}, t) = \exp\left[-Q^2 D|t|\right]. \tag{2.47}$$

Correspondingly, the quasi-elastic peak as a function of the energy transfer, $(\mathbf{Q}, t)$, has a Lorentzian shape:

$$S_{inc}(\mathbf{Q}, \hbar\omega) = \frac{1}{2\pi} \frac{\hbar D Q^2}{(\hbar\omega)^2 + (\hbar D Q^2)^2} \tag{2.48}$$

where the quasi-elastic broadening Γ (its HWHM) follows a square law of the momentum transfer Q:

$$\Gamma(\mathbf{Q}) = \hbar D Q^2. \tag{2.49}$$

Ballistic diffusion In contrast to the Brownian motion, a different diffusive landscape appears when the adsorbed particles do not feel any significant frictional coupling with the substrate and the collisions with other adsorbates become less frequent. In essence this behavior matches with the perfect gas behavior and is known as the *ballistic diffusion*. As a result, particles move freely on the surface or in the volume without any force exerting over them.

[6] In the last step, we substitute $\langle v^2(0) \rangle$ by its calculated value according to the equipartition theorem. For the general case of d dimensions, the equipartition theorem applied to $\langle v^2(0) \rangle$ leads to:

$$\langle v^2(0) \rangle = \int d\mathbf{v}^{(d)} v^2(0) \Phi^{(d)}(v) \propto \int d|\mathbf{v}| v^{d+1} \exp\left(-\frac{\beta}{2} m v^2\right) \Rightarrow \langle v^2(0) \rangle = \frac{d}{m\beta},$$

where $d\mathbf{v}^{(d)}$ is the differential volume in d dimensions, $\Phi^{(d)}(v)$ is the corresponding Botzmann distribution function of velocities and $\beta = 1/k_B T$.

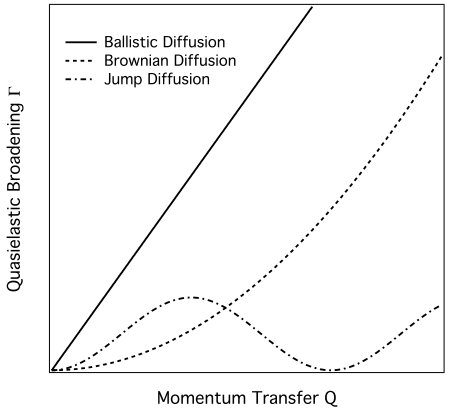

Figure 2.1: Signatures of the archetypal diffusion processes in plots of quasi-elastic line broadening or inverse relaxation times versus momentum transfer. Lines are shown for ballistic diffusion (solid line), Brownian diffusion (dashed line), and jump diffusion (dashed-dotted line).

This gives rise, in the case of classical particles whose dynamics is governed by the second law of Newton, to a rectilinear and uniform motion. Hence, the corresponding MSD is very simply related to the its averaged squared velocity and time [106]:

$$\langle \Delta \mathbf{r} \rangle = \left\langle v^2(0) \right\rangle t^2 \tag{2.50}$$

and the correlation function is deduced from Eq. 2.36:

$$\langle \mathbf{v}(0) \cdot \mathbf{v}(t) \rangle = \left\langle v^2(0) \right\rangle . \tag{2.51}$$

The constant value of the velocity correlation function is consistent with the absence of forces acting on the particle and producing any accelaration. This reflects the typical behavior of classical particles in a gas: the density is so diluted that they rarely interact with each other. Hence, the frequency of collisions between them decreases significantly, or in other words, the time between collisions becomes longer. Thus, particles spend most of the time in the free particle state, undergoing straight trajectories until they collide with another particle [106]. The incoherent ISF is readily deduced from the MSD of ballistic particles (see Eq. 2.37):

$$I_{inc}(\mathbf{Q}, t) = \exp\left[-\frac{Q^2}{2}\frac{1}{d}\left\langle v^2(0) \right\rangle t^2\right] = \exp\left[-\frac{Q^2}{2}\frac{k_B T}{M} t^2\right] \tag{2.52}$$

where we make use once again of the equipartition theorem for deducing the value of $\left\langle v^2(0) \right\rangle$ in d dimensions, dk_BT/M. The incoherent ISF displays a Gaussian profile with time. Accordingly, the incoherent scattering function is

the Fourier transformed in time–energy of the ISF and has a Gaussian dependence on the energy[7]:

$$S_{inc}(\mathbf{Q},\omega) = \frac{1}{\hbar}\sqrt{\frac{M}{\pi k_B T}}\frac{1}{Q}\exp\left(-\frac{M}{2k_B T Q^2}\omega^2\right) \tag{2.53}$$

The ballistic scattering function is characterized by a FWHM rising linearly with the momentum transfer, Q [98]:

$$\Gamma(\mathbf{Q}) = 2\hbar\sqrt{\frac{2\ln(2)k_B T}{M}}|\mathbf{Q}| \tag{2.54}$$

M being the mass of the particle. Finally, the Van-Hove self correlation function can be inferred from the Fourier transformation in momentum transfer/real space of the incoherent ISF and follows a Gaussian profile of $\Delta\mathbf{r}_j$.

It is interesting to note that in the short time range (between two successive collisions), Brownian particles move freely and ballistically [58,60]. As a result, Eq. 2.40 describes the long time limit behavior of Brownian particles while Eq. 2.50 gives the short time behavior, when Brownian particles behave as free particles and diffuse ballistically [60]. In this sense, a general form of the ISF holding for the short time and the long time behavior of Brownian particles can be found if we introduce directly the velocity autocorrelation function, Eq. 2.44 into Eq. 2.37 and integrate over the time [57]:

$$\begin{aligned} I_{inc}(\mathbf{Q},t) &\simeq \exp\left[-Q^2\frac{1}{d}\int_0^t d\tau(t-\tau)\left\langle v(0)^2\right\rangle\exp(-\eta|t|)\right] \\ &= \exp\left[-\chi^2(e^{-\eta t}+\eta t-1)\right] \end{aligned} \tag{2.55}$$

[7] A more exact derivation of the scattering law arising from ballistic motion and comprehending non classical particles, consists in replacing in the differential cross-section (Eq. 1.2) the translational-rotational state of the target system, $|\lambda\rangle$, and its corresponding energy eigenvalues E_λ by the states and energy eigenvalues of a free particle i.e. planes waves [60]:

$$|n_j\rangle = \frac{1}{\sqrt{V}}e^{i\boldsymbol{\xi}_j\cdot\mathbf{r}_j} \Rightarrow E_{n_j} = \frac{\hbar^2}{2M}|\boldsymbol{\xi}_j|^2$$

$\boldsymbol{\xi}_j$ being the wavevector of the j-th particle, analogously to $\mathbf{k}$ being the wavevector of the incoming neutron, represented as well by a plane wave. On the condition that the momentum transfer is conserved: $\boldsymbol{\xi}'_j = \mathbf{Q}+\boldsymbol{\xi}_j$ [60], the incoherent scattering function becomes a Gaussian function of the energy transfer [60]:

$$S_{inc}(\mathbf{Q},\hbar\omega) = \left(\frac{\beta}{4\pi E_r}\right)^{1/2}\exp\left\{-\frac{\beta}{4E_r}(\hbar\omega-E_r)^2\right\},$$

centered at $E_r = \hbar^2Q^2/2M$, the so-called *recoil energy* due to the linear momentum exchange between the free nucleus and the neutron probe when the scattering takes place [60]. The corresponding ISF and Van Hove correlation function are deduced thanks to the application of the Fourier transformation in time and space on the ballistic scattering function. Nevertheless, the resulting MSD and velocity correlation function match with their classical limit in Eqs. 2.50 and 2.51, respectively.

where χ^2 is the *shape parameter* [57] defined as:

$$\chi^2 = \frac{\langle v(0)^2 \rangle Q^2}{\eta^2}. \tag{2.56}$$

In the very short time scale (below the lapse of time between two collisions), Eq. 2.55 can be Taylor expanded around $t = 0$ yielding a Gaussian dependence of time [57]:

$$t << 1 \Rightarrow e^{-\eta t} \simeq 1 - \eta t + \frac{1}{2}(\eta t)^2 \Rightarrow I_{inc}(\mathbf{Q}, t) \simeq \exp\left[-\langle v(0)^2 \rangle Q^2 t^2\right] \tag{2.57}$$

where the friction parameter is cancelled out. This is the ISF arising from the ballistic behavior of Brownian particles between collisions. Conversely, in the very long time limit, the term $e^{-\eta t}$ vanishes and the ISF becomes a single exponential decay [57]:

$$t >> 1 \Rightarrow e^{-\eta t} \to 0 \Rightarrow I_{inc}(\mathbf{Q}, t) \simeq \exp\left[\chi^2\right] \exp\left[-\frac{\langle v(0)^2 \rangle Q^2}{\eta} t\right], \tag{2.58}$$

where we recover the diffusion coefficient, $D = \langle v(0)^2 \rangle / \eta$, as defined in Eq. 2.45. On the other hand, the value of the friction parameter η also affects the time dependence of the ISF in Eq. 2.55 [57]. In situations of very high coverage, molecules are constantly colliding against each other and the part of the friction related to interaction between adsorbates is significant. As a result, the term $e^{-\eta t}$ vanishes and Eq. 2.55 is a single decay [57]:

$$\eta \gg 1 \Rightarrow \chi^2 \ll 1, \chi^2 \eta \ll 1 \Rightarrow I_{inc}(\mathbf{Q}, t) \simeq \exp[-2\chi^2 \eta t], \tag{2.59}$$

On the contrary, for two dimensional gases where molecules rarely interact with each other, the collisional friction parameter will be close to zero. Then, we Taylor expand $e^{-\eta t}$ around $\eta = 0$ and obtain a Gaussian function of time [57]:

$$\eta \ll 1 \Rightarrow \chi^2 \gg 1, \chi^2 \eta \gg 1 \Rightarrow I_{inc}(\mathbf{Q}, t) \simeq \exp\left[-\frac{1}{2}\langle v_0^2 \rangle Q^2 t^2\right]. \tag{2.60}$$

As a result, Eq. 2.55 delivers a very general form of the ISF which reaches the short and long time behavior of Brownian particles [57], and, in addition which is sensitive to the friction and yields the correct time dependence for a system of colliding particles (Brownian system) or for a gas like system where the interaction between particles is nearly insignificant [57]. The so-called *shape parameter* monitors the change in the ISF profile with friction [57].

Jump diffusion Finally, the *Chudley-Elliott* jump diffusion model describes the dynamics of particles when they experience very high energy barriers for

diffusion and little friction. Their motion is no longer continuous but stepwise: the adparticles are trapped in equilibrium positions for a time τ where they undergo vibrations around the potential energy minimum [56, 106, 107]. Spontaneous thermodynamical fluctuations can push them to jump towards another equilibrium site [56, 72, 96, 107]. The probability $P(\mathbf{r}, t)$ of finding a particle at position $\mathbf{r}$ at the instant t follows a master equation of the form:

$$\frac{\partial}{\partial t}P(\mathbf{r},t) = \frac{1}{n}\sum_m \frac{1}{\tau_m}\left[P(\mathbf{r}+\mathbf{l}_m,t) - P(\mathbf{r},t)\right], \tag{2.61}$$

where the set of vectors $\{\mathbf{l}_m\}$ links together the set of accessible neighboring sites for a particle lying at $\mathbf{r}$. They form a Bravais lattice and τ_m is the residence time of the particle in the m-th, site and n is the total number of available sites from an initial position. Since the Bravais lattice implies the equivalence between adsorption sites [107–109], τ_m or equivalently the jump rate from one to another, $1/\tau_m$, is the same for all the sites. Hence the jump rate can be taken out of the summation. Furthermore, the Fourier transformation in space, allows to factorize the master equation as the product of a time depending function and a function accounting for the for the spatial distribution of the adsorption sites in the lattice:

$$\frac{\partial}{\partial t}\int d\mathbf{r}\exp(i\mathbf{Q}\cdot\mathbf{r})P(\mathbf{r},t) = \frac{1}{n}\frac{1}{\tau}\sum_m \left[\exp(-i\mathbf{Q}\cdot\mathbf{l}_m) - 1\right]\int d\mathbf{r}\exp(i\mathbf{Q}\cdot\mathbf{r})P(\mathbf{r},t). \tag{2.62}$$

The master equation turns into a simple differential equation in time:

$$\frac{\partial}{\partial t}I(\mathbf{Q},t) = \frac{1}{n}\frac{1}{\tau}\sum_m \left[\exp(-i\mathbf{Q}\cdot\mathbf{l}_m) - 1\right] I(\mathbf{Q},t) \tag{2.63}$$

where we recognize in the space Fourier transform of the probability $P(\mathbf{r}, t)$, the intermediate scattering function ISF, $I(\mathbf{Q}, t)$.The solution of Eq. 2.63 is straighforward and leads to a single exponential decay on time:

$$I(\mathbf{Q},t) = I(\mathbf{Q},0)\exp[-M(\mathbf{Q})t]. \tag{2.64}$$

As a result, the hopping of species on a Bravais lattice provokes a single exponential decay of the neutron intensity with time in the time-momentum transfer domain $(\mathbf{Q}, t)$ measured by spin-echo or, equivalently, a single Lorentzian shaped spread of energies in the energy-momentum transfer space $(\mathbf{Q}, \hbar\omega)$ probed with standard spectroscopy neutron techniques:

$$S(\mathbf{Q},\hbar\omega) = \frac{1}{2\pi\hbar}\frac{M(\mathbf{Q}}{\omega^2 + M(\mathbf{Q})^2} \tag{2.65}$$

The time constant $M(\mathbf{Q})$ characterizing the ISF time exponential decay or, analogously, the HWHM of the Lorentzian scattering function contains the

information about the geometry of the lattice:

$$M(\mathbf{Q}) = -\frac{1}{n}\frac{1}{\tau}\sum_{m}\left[\exp(-i\mathbf{Q}\cdot\mathbf{l}_m) - 1\right]. \tag{2.66}$$

In the limits of long times (after many jumps have been performed) the underlying Van-Hove self-correlation function is once again a Gaussian function [107, 110].

A detailed description of these models can be found in many general books on neutron scattering (see Refs. [56, 58, 72, 96]) or recent review articles (see for instance Ref. [83, 98]). Nevertheless, diffusion processes are often rather complex and cannot always be easily categorized into the previous simple cases. Further analytical developments, which combine different types of diffusion mechanism are required. Beyond the analytical models, it has become widely accepted that molecular dynamics (MD) simulations hold the key for the interpretation of the data. Nowadays, the available computational power and the various advances in software [83, 111], have encouraged the use of simulation tools to address complex diffusion problems.

2.3 Molecular dynamics simulations and QENS spectroscopy

In general terms, molecular dynamics MD simulations consist in solving numerically the equations of motion for a given system and a given (mostly classical) Hamiltonian. The resulting trajectories for each particle in the system enable to calculate many of the function bearing microscopic information about the dynamics such as the mean square displacement or the Van Hove correlation function [22]. Therefore they supply an extremely useful complement to neutron measurements, since the Fourier transformations in space and time of the simulated correlation function provide simulated ISF and scattering laws to be compared with the experimental data [23]. On the other side, the MD simulations results and all the underlying approximation which allow to run the calculations should be validated. Experimental data play an essential role: they are the benchmark for evaluating the pertinence of the theoretical hypothesis on which simulations are performed and the accuracy of the input parameters [22, 112]. Neutrons measurements are specially important because they extract very precise knowledge about the density of states of the target sample in the length and time scale which can be computed with MD simulations [22, 112]. As a result, MD simulations and by simulating the atomistic behavior while the MD simulations approximations receive a feedback from the

comparison with experimental data.

2.3.1 Driving Force Fields technique

The driving force fields, technique provides an analytical approach to the potential energy surface, $U(\mathbf{r}_1, \ldots, \mathbf{r}_N)$ depending on the coordinates of the N particles in the system and arising from all the possible interactions ruling the dynamics of the system [22]. The trajectories of the elements in the system are the solutions of the classical equations of motion (Newton's second law of mechanics) [22]:

$$m_i \frac{d^2}{dt^2}\mathbf{r}_i = \mathbf{f}_i = -\frac{d}{d\mathbf{r}_i}U(\mathbf{r}_1, \mathbf{r}_2, \ldots, \mathbf{r}_j, \ldots, \mathbf{r}_N). \tag{2.67}$$

A force field FF consists of a simplified and analytical function which substitutes the true interatomic energy potential in the equations of motion [112]. Molecules, for instance, are defined as groups of atoms connected by harmonic forces [22]. The crucial point is that the simplified model playing the role of interatomic potential is only valid in the region and for the system to be simulated. It follows that a universal definition for a FF can not exist [112]. On the contrary, it requires a set of parameters for adapting the exact form of the model function to each system and each problem [22]. The parametrization of the FF is done according to *ab-initio* calculations or taking experimental data from neutrons, X-rays or electron diffraction and NMR, infrared or X-ray and neutron spectroscopy. Although a standard FF can not be defined, a typical expression may contain the following terms [22]:

$$\begin{aligned} U(\mathbf{r}_1, \ldots, \mathbf{r}_N) = & \sum_{bonds} \frac{1}{2}k_0(r - r_0)^2 + \sum_{angles} \frac{1}{2}k_a(\theta - \theta_0)^2 + \sum_{torsions} \frac{V_n}{2}[1 + \cos(n\phi - \delta)] \\ & + \sum_{improper} V_{imp} + \sum_{LJ} 4\epsilon_{ij}\left(\frac{\sigma_{i,j}^{12}}{r_{i,j}^{12}} - \frac{\sigma_{i,j}^{6}}{r_{i,j}^{6}}\right) + \sum_{Coulomb} \frac{q_i q_j}{r_{ij}}. \end{aligned} \tag{2.68}$$

where the four first terms describe the intramolecular interactions while the two last summations refer to the repulsive coulombic interaction and the Van der Waal forces (the 12-6 Lennard-Jones potential). Finally, solving the equation of motion, Eq. 2.67, demands initial (the set of positions and velocities of the particles) and boundary conditions. The choice of suitable initial conditions is extremely important since most of the information extracted from MD simulations are averages. Thus, the initial conditions should reproduce a representative configuration of the statistical equilibrium ensemble [112]. A correct initial configuration may be achieved by *thermalizing the system*: running the simulation at a given temperature where the particles in the system

are provide with an initial Maxwellian velocity distribution. After a certain number of simulation steps, the system forgets the initial values of the velocities and adopts a velocity distribution corresponding to the equilibrium state at the simulation temperature. This configuration can be adopted as a valid initial condition on which we can run a longer simulation [22, 112]. On the other side, to find appropriate boundary conditions is essential for a successful simulation. The cyclic boundary conditions in which the box containing the simulated system is repeated with a certain periodicity (characterized by a wavelength λ) fit perfectly to the simulation of ordered systems. However, they introduce an artificial symmetry in disordered systems [22]. In this case, the periodicity should not be smaller than the size of the box, in order to avoid effects of self-interaction between particles [22]. Thereby, systems or situation presenting long-range interaction, like phase transitions are difficult to handle [112].

Finally, we note that the driving force field technique suits well the situations in which chemical bonds are maintained and the thermodynamical conditions (temperature and pressure) do not affect dramatically the electronic structure of the system [112]. Hence, chemical reactions can not be simulated with this technique, but require a different approach. On the other side, they present several advantages like the power of deal with very large systems [112], their versatility to adapt to very precise and different problems [22] or the simplicity with which they describe intra-molecular interactions, for instance.

2.3.2 The Langevin equation

The Langevin equation (see paragraph 2.2 in section 2.2) sets the equation of motion for the ith particle of mass m including the friction force, $\gamma \mathbf{v}_i$, an external force generated by the substrate free energy potential, $-\nabla V_{eff}(x, y)$ [113], and a summation of random forces reproducing the kicks of phonons on the surface, $\xi_i(t)$, and the collisions with other adsorbates, $\mathbf{F}_{ij}(t)$ [83]:

$$m\ddot{\mathbf{r}}_i(t) = -\nabla V_{eff}(x, y) - \gamma m\dot{\mathbf{r}}_i(t) + \xi_i(t) + \sum_{j \neq i} \mathbf{F}_{ij}(t). \tag{2.69}$$

The subsequent trajectories are found by integrating the Langevin equation. The underlying physical basis as potentials and parameters (in particular the friction parameter) can be freely adapted to generate simulation results that fit the experimental findings. We have already see how the Langevin equation yields detailed information on the microscopic nature of diffusion (in the paragraph 2.2 in section 2.2).

The *Langevin approach* is well suited for heterogeneous adsorption or weakly physisorbed molecules where the interactions between the adatoms and the atoms of the substrate interaction do not involve exchange processes (of electrons for instance, i.e, chemical reactions) or many-body interactions [83]. It is also appropriate when there are no large displacements of substrate atoms [83]. On the other side, the adsorbate-adsorbate interaction is included in the Langevin equation by the addition of further pair interaction potentials [83].

2.4 Conclusion

As a short conclusion for the chapter, we have summarized the theoretical framework which allows to understand and analyze neutron experimental data. The Van Hove formalism, whose chief function is the Van Hove correlation function, connects the scattering law or the intermediate scattering function measured with neutron quasi-elastic techniques, with the dynamics of the atoms diffusing in the system. Furthermore, it offers an explanation of the coherent and incoherent scattering in terms of collective and self-diffusion. On the basis of this powerful theoretical ground, basic models describing the main diffusive regimes have been developed. However, the upgrade and improvement of simulation techniques has also brought new insights and perspectives in the data treatment. The capability of simulating very large systems at the atomistic level and covering the typical time and spacial windows which is accessible to neutrons probes, allows to push the interpretation of the data further beyond the traditional models. Nevertheless the comparison between the experimental and the simulated data is paramount since the hypothesis and the selection of input parameters on the basis of a simulation should be validate. Therefore the interplay between simulations and experiments enhances the power in both directions: the application of neutrons to diffusion studies and the improvement of the simulation techniques towards more realistic results. Simulations can not substitute experiments, but can deepen and improve our understanding of the physical mechanisms driving the diffusion process, provided that the basic assumptions are realistic.

Chapter 3

ToF measurements on benzene adsorbed on the basal plane of exfoliated graphite substrates

This chapter summarizes the experimental data set which grounds our study of the diffusion of benzene adsorbed on the basal plane of graphite. We consider mainly the effect of temperature and coverage on the diffusive behavior of molecules. Diffusion can be a thermally activated process (if quantum tunneling diffusion is ignored) where temperature plays a central role, enhancing or hindering the motion of molecules on the surface. On the other side the coverage highlights the effect of the interaction between molecules on their mobility. Finally, the possibility of switching between hydrogenated and deuterated benzene provides a vivid picture of the differences between coherent and incoherent scattering. Altogether, benzene adsorbed on graphite is an excellent prototypical system to test the power of neutrons for surface diffusion studies.

The first section describes the sample preparation, the measurement protocol and the experimental set up. In the second section, we summarize the experimental scattering function measured for hydrogenated and deuterated benzene at different temperatures and the full set of coverages.

3.1 Sample preparation and measurement protocol

3.1.1 Sample morphology

The samples consist of several disks of exfoliated graphite *Papyex (Le Carbone Lorraine)* [114] of 2.5 cm diameter each stacked up in a cylindrical sample holder made of aluminum of 6 cm height. The total volume of the sample holder is 42.4 cm^3. The effective surface area of the *Papyex* exfoliated graphite substrate was measured through BET isotherms and presents a value of 25.5 $m^2.g^{-1}$, in concordance with the value given in Ref. [68]. The surface occupied by a molecule of benzene lying flat on the basal plane of exfoliated graphite is 36.7$Å^2$ as measured with low energy electron diffraction (LEED) [44] and X-ray diffraction [115]. The substrate effective surface area and the size of a benzene molecule flat on the surface determine the amount of benzene to cover a certain area of the total surface area of graphite in the sample holder. We define the coverage as the percentage of adsorption sites on the graphite substrate which are occupied by the benzene adsorbates. For instance 0.1 monolayers (ML) coverage corresponds to the occupancy of only 10 % of the available adsorption sites.

In total, we have prepared six samples: four of them contain 0.1 ML, 0.2 ML, 0.5 ML and 1.0 ML of h-benzene and two of them are made of 0.5 ML and 0.9 ML of d-benzene. The adsorption process is carried out from the liquid phase at room temperature. We use for this purpose a liquid sample of h-benzene (Merck 99.7%) and d-benzene (Merck 99.7%). We are only interested in the sub-monolayer regime: molecules should lie on a single layer, always in contact with the graphite basal plane. The lower coverages are limited by the intensity of the scattering arising from the adsorbed layer: the signal should be distinguishable from the background and the scattering coming from the substrate. Since d-benzene is a weaker scatterer (79.2 barns of scattering cross section) if compared to h-benzene (525.5 barns), coverages below 0.5 ML produce a signal of poor statistical quality. The main physical parameters of h-benzene and d-benzene are summarized in in Tab. 3.2. We have included the cross-sections, the mass, the moment of inertia and the De Broglie wavelength fixing the range of distances in which quantum effects are significant. We also summarize the relevant parameters of exfoliated graphite in Tab. 3.3, such as the density, the effective surface area for adsorption or the Debye temperature which is related to phononic processes on the surface.

Table 3.1: Set of samples considered for the experimental work. We specify the mass of exfoliated graphite and the volume of hydrogenated C_6H_6 and deuterated C_6D_6 benzene and the scattering cross section of each sample. The latter is the product of the density of scatterers of each specie (benzene molecules $\rho_{benzene}$ or carbon atoms ρ_C from the substrate) multiplied by its corresponding total scattering cross-section $\sigma_{benzene}$ and σ_C (which include the coherent, incoherent scattering and absorption scattering cross-sections $\sigma_{scatt} = \sigma_{inc} + \sigma_{coh} + \sigma_{abs}$): $\sigma_{scatt.} = \rho_C \times \sigma_C + \rho_{benzene} \times \sigma_{benzene}$. It has inverse distance dimensions. Its inverse is the mean free path l of a neutron in the sample [56]. Finally, we include the scattering cross-section and the mean free path associated exclusively to the adsorbed amount of benzene.

	C_6H_6				C_6D_6		Graphite
	0.1 ML	0.2 ML	0.5 ML	1.0 ML	0.5 ML	0.9 ML	
Mass of exfoliated graphite $\pm 1 \times 10^{-3}$[g]	18.363	19.960	13.330	13.330	21.249	13.676	18.36
Density of carbon atoms in substrate, ρ_C, $\times 10^{22}$ [cm^{-3}]	2.17	2.36	1.58	1.58	2.51	1.62	2.17
Vol. of adsorbate $\pm 1 \times 10^{-3}$ [cm^3]	0.019	0.041	0.080	0.160	0.103	0.126	0
Density of benzene molecules, $\rho_{C_6H_6}$, $\times 10^{19}$ [cm^{-3}]	0.30	0.65	1.08	2.17	1.73	2.00	0
Density of scattering cross section $\sigma_{scatt.}$ [cm$^-$1]	0.122	0.134	0.0931	0.0988	0.141	0.0931	0.12
Mean free path l [cm]	8.2	7.4	10.7	10	7.1	11	8.3
Density of scattering cross section due to the adsorbed layer $\sigma_{scatt.}$ $\times 10^{-2}$ [cm$^-$1]	0.16	0.34	0.57	0.11	0.14	0.16	
Mean free path associated to the adsorbed layer l $\times 10^2$ [cm]	6.38	2.93	1.76	0.88	7.32	6.31	

Table 3.2: Summary of the relevant physical parameters of h-benzene C_6H_6 d-benzene C_6D_6.

Benzene:	C_6H_6	C_6D_6
Radius [Å]	2.55	2.55
Mass $\times 10^{-25}$[kg]	1.29	1.39
Density [g.cm^{-3}]	0.88	0.95
Area occupied when adsorbed flat on the graphite basal plane [Å^2] [44]	36.7	
Scattering cross-sections [barns=10^{-24} cm^2] [56]		
Incoherent	4.79×10^2	1.22×10^1
Coherent	4.39×10^1	6.69×10^1
Absorption	2.02	2.7×10^{-2}
Total	5.25×10^2	7.92×10^1
Moments of inertial [kg.m^2]		
$I_{xx} = I_{yy}\times10^{-45}$ [kg.m^2]	1.37	1.69
I_{zz} $\times10^{-45}$[kg.m^2]	2.07	2.69
Flipping frequency: $\hbar/(4\pi I)$ [s^{-1}]		
$\hbar/(4\pi I_{xx})$ $\times10^9$[s^{-1}]	6.1	5.0
$\hbar/(4\pi I_{zz})$ $\times10^9$[s^{-1}]	4.05	3.1
De Broglie wavelength $\lambda_{Br} = \hbar/\sqrt{2Mk_BT}$ [Å]		
λ_{Br} at 2K	0.39	0.37
λ_{Br} at 40K	0.08	0.08
λ_{Br} at 60K	0.07	0.07
λ_{Br} at 140K	0.05	0.05

Table 3.3: Summary of the relevant physical parameters of exfoliated graphite, *Papyex*.

Graphite:		
Mass of a carbon atom $\times 10^{-26}$[kg]	1.99	
Density of *Papyex* [g.cm^{-3}] [68]	0.95	
Eff. surface for adsorption [m^2.g^{-1}]	25.5	
Scattering cross-sections [barns=10^{-24} cm^2]		
Incoherent	1×10^{-3}	
Coherent	5.54	
Absorption	3.50×10^{-3}	
Total	5.54	
Debye Temperature Θ_D [K]		
along [0001] direction	730 (on the surface) [116]	800 (in the volume) [116]
in the [0001] plane [116]	1400	
Graphite lattice parameters [Å] [117]		
a, b	2.462	
c	3.34	

3.1.2 Sample preparation

The first step in the sample preparation consists in cutting the disks out of the large sheets of commercial exfoliated graphite *Papyex (Le Carbone Lorraine)* [114]. Afterwards we clean the substrates in a pyrolytic oven: we put the graphite disks inside a quartz tube connected to a turbo system. The furnace temperature is settled at 350 ℃ and we leave the graphite during approximatively 20 hours for outgassing. Then, the disks are introduced in the sample holder where we also pipette the volume of benzene corresponding to a given coverage. Finally we close and seal hermetically the sample holder with steel knife seal. These two last operations are performed in a non controlled atmosphere (open air) and at room temperature. Thus, there will be air within the sample holder and it is possible that water adsorbs as well on the substrate. However the amount of benzene (see Tab. 3.1) will be much higher than the quantity of water diluted in the air within the volume of the sample holder (roughly estimated to be, at least, two orders of magnitude smaller than the amount of benzene for 0.1 ML)[1]. Furthermore the scattering cross section of the water molecule (167.6 barns) is five times smaller than the one of benzene (523.3 barns). As a result, most of the scattering will come from the benzene molecules adsorbed on the graphite, rather than from the water occasionally trapped in the sample holder. Once the sample holder is closed hermetically, preventing any contact of the inner volume with open air, we can store the samples until the experiment takes place.

3.1.3 Measurement protocol

We have a fixed measurement protocol in order to obtain a comparable set of experimental data. To cover a wide thermal range from 1.5K to 300K we work with an *orange standard cryostat* constructed and developed at the ILL [88]. The sample holder is screwed to the bottom of a sample stick which is introduced into the main chamber of the cryostat. The temperature and the rate of cooling (the cold valve opening) are controlled through the main computer of the instrument. Orange cryostats work with nitrogen for cooling the temperature down to 70K and continue with helium down to 1.5 K [88]. The

[1] In order to calculate the amount of water diluted in the air within the sample holder, we assume that there was a relative humidity of 30 % and that the temperature was of 20 ℃ in the room where we prepared the sample. This conditions give rise to an absolute humidity, AH, of 5.2 g.m^{-2}. If the sample holder (whose volume is of $V_{sh} = 42.4$ cm^3) is completely fill with air, the mass of water trapped inside is: $m_{H_2O} = AH \times V_{sh} = 220.5 \times 10^{-6}$ g. Since the density of water vapor is 0.804 g.cm^{-3}, we estimate that the volume of water inside the sample is of 0.274×10^{-3} cm^3. This volume needs to be compared with the volume of benzene needed to obtain a certain coverage, in Tab. 3.1.

resolution function is measured at 2K where there should not be any dynamics and molecules are frozen on the surface. Afterwards we measure the different temperatures starting at 40K, 60K, 75K (only for 1.0 ML of h-benzene and 0.9 ML of d-benzene), 100K, 140K and 200K. The desorption of the benzene molecule on exfoliated graphite starts at 150K [28, 45]. Thus, the coverage of the surface is no longer constant at 200K. However our hermetic sample holders allow to measure beyond the desorption temperature because the sample volume is kept constant and a thermodynamical equilibrium exists between the gaseous and the adsorbed phases of benzene. As a result, the coverage on the surface is still constant at 200K, but it will be different from the nominal coverage at 140K.

All the measurements have been performed with an incoming wavelength of 5.12 Å . In addition, we have also performed short scans using a slightly longer incoming wavelength of 5.9 Å, in order to explore multiple scattering issues. A longer wavelength shifts the momentum transfer range towards smaller values but provides a gain in the energy resolution. The main instrumental parameters such as the incoming wavelength, λ_i, the energy resolution, ΔE_{res}, the maximum energy loss of neutrons ΔE_{max} and the momentum transfer range have been summarized in Tab. 3.4. We complete the experimental data set with an empty cell made only of graphite and a vanadium sample. The former is useful to evaluate the substrate contribution to the total scattering. The latter is necessary for the normalization of the experimental sample. Vanadium is a perfect incoherent elastic scatterer in the energy/momentum transfer range surveyed by the spectrometer in the quasi-elastic configuration (i.e. when the incoming wavelength is 5 Å , see Tab. 3.4). The vanadium spectrum gives the distribution of neutron energies in the incoming flux (the monitor counts).

Table 3.4: Summary of the experimental conditions adopted for the measurements in the IN6 ToF spectrometer at the ILL [88].

IN6 Time of Flight spectrometer parameters:		
Incoming wavelength, λ_i, [Å]	5.12	5.9
Energy resolution, ΔE_{res}, [meV]	0.07	0.05
Neutron maximum energy loss $\Delta E_{max} = h^2/(2\lambda_i^2 m_n)$ [meV]	3.1	2.4
Momentum transfer range $Q = (4\pi/\lambda_i)\sin(2\theta/2)$ [Å^{-1}]	0.21, ..., 2.08	0.19, ..., 1.8

3.1.4 Multiple scattering issues

In scattering theory, neutrons are scattered only once by the sample. However this might not be the case when the sample has an important scattering cross-section or large dimensions. Multiple scattering changes the energy profile of the outgoing neutrons and can lead to a misunderstanding of the physical mechanisms at work in the sample system [56]. In time of flight spectroscopy, the energy exchange between the sample and the neutron probe is encoded into the neutron time of flight. If the distance between the chopper and the sample, L_s, and from the sample to the detector bank, L_d, are well known, then, the initial and the final energy of the neutron are perfectly established (see section 1 in Chap. 1):

$$E_i = \frac{1}{2} m_n \left(\frac{L_s}{\Delta t_s} \right)^2$$
$$E_f = \frac{1}{2} m_n \left(\frac{L_d}{\Delta t_d} \right)^2.$$

The multiple scattering modifies the neutron effective flight path and, hence, its time of flight. The energy uncertainty related to the flying path is the following:

$$\delta E = 2E \frac{\delta L}{L_d}. \tag{3.1}$$

Multiple scattering effects should be taken into account when the mean free path of the neutron within the sample is of the same order of magnitude than the size of the sample or when the sample presents a transmission of the direct beam lower than 90 % [56]. In our case, we specify the mean free path l of the neutrons in Tab. 3.1. We also include the scattering density cross section and the corresponding mean free path corresponding to the adsorbed layer for every coverage. Even though these values do not have a physical relevance, when we compare them to the scattering cross section of the substrate, they give an idea of which is the main scatterer in our sample and the most probable source of multiple scattering. Since the scattering cross section of the adsorbed layer is two orders of magnitude lower than the scattering cross section of the whole sample, most of the intensity comes from the substrate. Therefore, the mean free path for different samples do not depends on the coverage but on the mass of graphite contained in the sample. Thereby, we expect that multiple scattering is mostly due to the substrate.

All the samples are characterized by a total mean free path around 10 cm which is of the same order of magnitude than the radius, 1.25 cm, and the

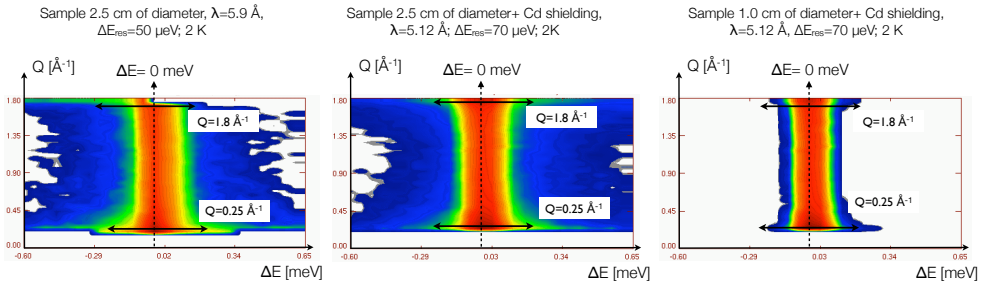

Figure 3.1: Left panel: scattering function for a sample containing 0.5 ML of hydrogenated benzene. The sample holder has a cylindrical shape. The diameter is of 2.5 cm and the height is of 6 cm. The incoming neutron wavelength is of 5.9 Å and the energy resolution is 50 μeV. Medium panel: scattering function for a sample of the same characteristics than the previous one, except for the presence of cadmium adsorbing disks in between the exfoliated graphite disks. The shielding disks are equidistantly placed and the distance between them is of 1 cm. Right panel: Scattering function measured for a sample of 0.5 ML of h-benzene in a cylindrical sample holder of diameter 1.0 cm, height 6 cm and containing six equidistant cadmium shielding disks. For the two last samples, the incoming wavelength of neutrons is of 5.12 Å and the resolution in energies is of 70 μeV.

height, 6 cm, of the sample holder. Thus, we need to take care in identifying the parts of the scattering function $S(Q, \Delta E)$ with a high probability of being contaminated. Experimentally, we carry out measurement on samples of different diameters and containing cadmium shielding disks between the exfoliated graphite disks. Varying the diameter of the sample affects the probability of neutrons which are scattered in the plane parallel to the sample to be scattered later. On the other side, the introduction of cadmium absorbing disks, prevent neutrons scattered once out of the plane to be scattered again and reach the detector bank [56]. Fig. 3.1 displays the scattering functions of three different samples containing 0.5 ML but with different diameters and with cadmium shielding. We observe that the introduction of cadmium disks and the reduction of the sample diameter affects the areas of low momentum transfer, around $Q = 0.2$ Å^{-1}, and around the Bragg peak of graphite at 1.80 Å^{-1}. These two regions of the spectrum are dominated by the coherent scattering of the carbon atoms of the substrate. Multiple scattering is often attributed to incoherent systems [56]. Conversely, in our case, the multiple scattering attenuation seems to affect the intensity arising from the coherent contribution of the substrate atoms, rather than the intensity measured in the spectral area containing most of the h-benzene incoherent contribution (between 0.3 Å^{-1} and 1.8 Å^{-1}). The reason can be that, in all of our samples, the quantity of carbon atoms in the substrate is, at least, two orders of mag-

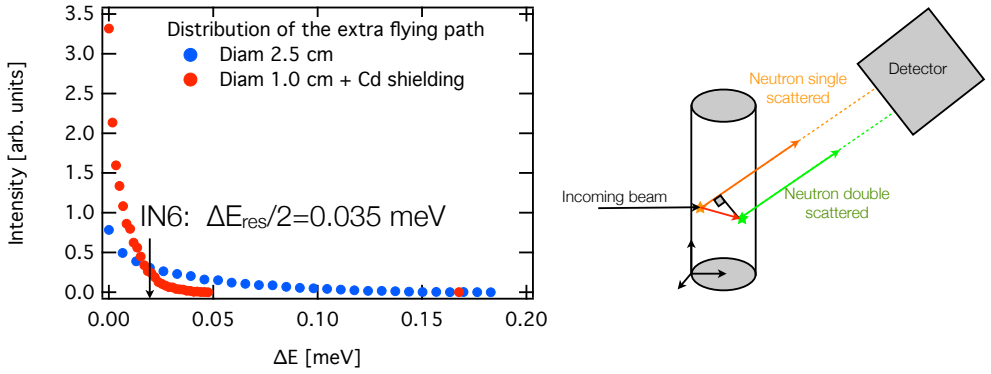

Figure 3.2: Left panel: Distribution of the additional neutron flying path introduced by the geometry of two cylindrical sample with different diameters and heights. The resolution of IN6 is of 0.07 meV when the incoming wavelength is of 5.12 Å. The broadening due toe the thinner sample with the cadmium shielding is still observable, since we only consider the HWHM of the energy resolution, 0.035 meV. Right panel: scheme of the Monte Carlo simulation. We take a cylindrical and homogeneous sample (the scattering cross section is the one calculated for the 0.5 ML sample). We evaluate the probability of the neutron to be scattered twice within the volume of the sample (the intensity). The distance of the two scatterers projected on the direction of the outgoing flux gives the additional length that the neutron needs to cover before arriving to the detector. Within this framework, the flying path can only get longer when multiple scattering ocurs. This translates into an asymmetry of the scattering function, which is already observable in the resolution function, since it arises from the geometry and the size of the sample and not from the dynamics of the system.

nitude greater than the amount of protons in the adsorbed benzene molecule (see Tab. 3.1). Eventually, the density of protons in the sample is extremely diluted and the multiple scattering events from collisions between protons and neutrons are very low, in comparison with the frequency of multiple scattering events of neutrons with carbon atoms of the substrate. Nevertheless, we have also carried out very simple Monte Carlo simulations to evaluate the broadening due to the geometry and the size of the sample in the experimental time of flight spectra on which our study is based. The distribution function of energy broadenings for two different sample is plotted in Fig. 3.2. In that case, the flying path only gets longer when multiple scattering occurs. This translates into an asymmetry of the scattering function, which is clearly observable in the resolution function, since it arises from the geometry and the size of the sample and not from the dynamics of the system.

3.2 Tof measurement on benzene adsorbed on graphite at different coverages and temperatures

As was already said, temperature and coverage affect complementary features of the diffusive behavior of benzene adsorbed on graphite. We cover a wide range of temperatures and coverages in the sub-monolayer range, with several measurements of time-of-flight spectra of benzene adsorbed on exfoliated graphite. The whole experimental data set has been measured on the time of flight spectrometer IN6 at the ILL. The forthcoming section gives an overview of the experimental data set and sketches qualitatively the role played by these two control parameters. However, the data treatment included in the following chapter contains the quantitative description of the diffusive process. Hence, no conclusions can be drawn from the direct presentation of the experimental results.

This section is organized in three paragraphs. The first one summarizes the experimental measurements on the exfoliated graphite substrate, *Papyex*, without any adsorbed benzene. The two subsequent paragraphs review the experimental data measured on hydrogenated and deuterated benzene adsorbed on exfoliated graphite.

3.2.1 The *Papyex* scattering function

We have a complete set of measurements devoted to the graphite substrate *Papyex* in all the interesting thermal range for surface diffusion: from 2K to 140K. The comparison between the scattering function of the graphite with the scattering function of benzene/graphite allows to identify the features arising exclusively from the substrate. We show the scattering function of graphite as a function of momentum transfer Q and energy transfer ΔE at 2K and 140K in Fig. 3.3. The temperature does not significantly affect the quasi-elastic spectrum of graphite. Thus, any change of the quasi-elsatic spectrum of benzene/graphite with temperature is related to benzene diffusion. On the other hand, the graphitic character of the sample is attested by the intense spot along the elastic line, at 1.80 Å^{-1} which is attributed to the [002] Bragg peak of the hexagonal and to the [003] Bragg reflexion of the rhombohedral phases of graphite [68].

The phononic spectrum of graphite is hardly observable in the scattering function because of its high energy range with respect to the quasi-elastic region and its weak intensity if compare with the elastic peak in the quasi-

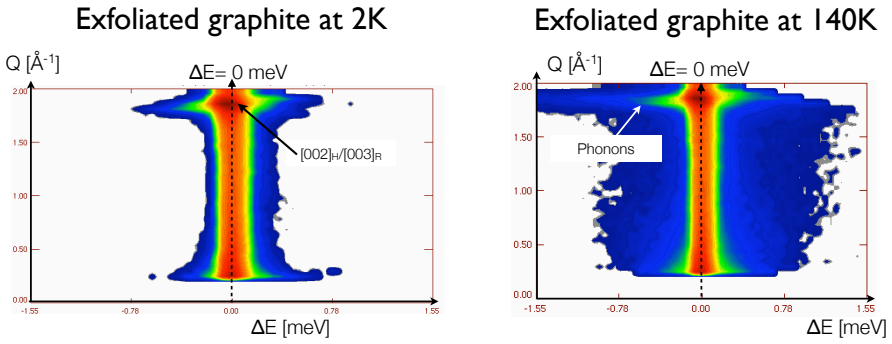

Figure 3.3: Scattering cross-section measured for exfoliated graphite at 2 K (left panel) and 140 K (right panel). The intense spot at 180 $Å^{-1}$ is the Bragg reflexion coming from the diffraction of the [002] hexagonal and the [003] rhombohedral families of planes in the graphite. The spectrum of graphite does not present any significant change with temperature in the quasi-elastic area. The beginning of acoustic phononic branches is visible at 140 K, but their intensity is too weak with respect to the Bragg peak, so that their contribution falls in the background.

elastic range. Fig. 3.4, plots the *non-rebinned spectrum* of graphite for 140K: the distribution of measured neutron intensities is not re-scaled when we change the variable from time-of-flight to energy transfer. This is a trick to keep the high energy range part of the spectrum visible. We observe the two phononic branches emerging from the Bragg peak. The comparison of Fig. 3.4 with the phononic dispersion curves in Ref. [118], suggests that these are longitudinal acoustic phonons along the [100] direction. Besides, this indicates that part of the background beyond -6 meV comes from phonons. We should avoid this region in the data analysis and only consider the energy window around the elastic peak where lies the cleanest quasi-elastic signal arising from benzene diffusion.

3.2.2 Measurement on hydrogenated benzene adsorbed on graphite: incoherent scattering

We recall that the hydrogenated benzene scattering is strongly dominated by incoherent incoherent (see scattering cross sections in Tab. 3.2). It probes the diffusion of single protons in the molecules. The scattering cross section $S(\mathbf{Q}, \Delta E)$ is the Fourier transform in time and space of the Van Hove self correlation function $G_s(\mathbf{r}, t)$ which yields the probability of finding an atom at a certain position $\mathbf{r}$ at time t if this very same atom was at the origin at $t = 0$. Hence, the experimental data in this section measure the statistical average of

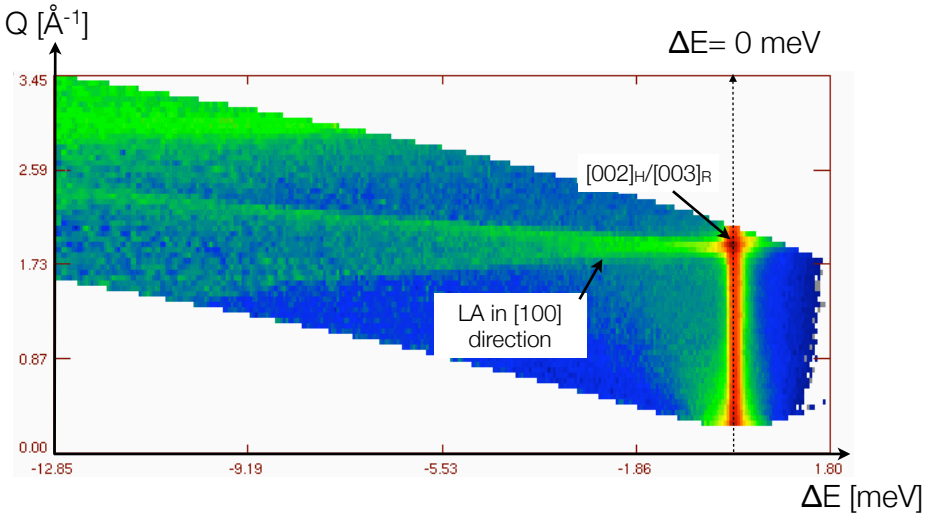

Figure 3.4: Non rebinned spectrum of exfoliated graphite at 140K. Inelastic features are still visible because we skip the re-scaling of intensities when we transform the neutron intensity as function of the time-of-flight into a function of the energy transfer. We observe two acoustic phononic branches starting at the Bragg peak and dispersing towards high energies. Comparing the map of intensities with the dispersion curves in Ref [118], suggests that these are the longitudinal acoustic (LA) phonons in the [100] direction.

proton trajectories on the surface.

Dependence of the diffusion on coverage Figs. 3.5 and 3.6 display the scattering cross section $S(Q, \Delta E)$ measured for hydrogenated benzene at 140 K for four coverages spanning from 0.1 ML to 1.0 ML. We can see the distribution of neutron intensity as a function of momentum transfer Q and energy transfer ΔE. The red zone around the zero energy transfer, $\Delta E = 0$ meV, is the elastic peak. It contains the diffraction pattern of the substrate and all the scattering coming from dynamical process which are too slow to be resolved by the energy resolution. The green area around the elastic peak is the *quasi-elastic area*. It arises from the interaction between neutrons and diffusing molecules. The shape of the quasi-elastic area as a function of the momentum transfer bears the signature of the diffusive behavior of molecules. The blue area is the background. It consists in the scattered intensity by fast motion falling out of the quasi-elastic energy window, like the graphite phonons. Finally, we recall that the shape of momentum / energy transfer space, $(Q, \Delta E)$, is due to the dispersion relation of free neutrons (see Fig. in Chap. 1) [80]. In the following sections we focus on the description and the

comparison of the quasi-elastic area (in green) for all the collection of coverages. The goal is to gain a deeper insight into the role of the interaction between adsorbates and with the substrate on their diffusion behavior.

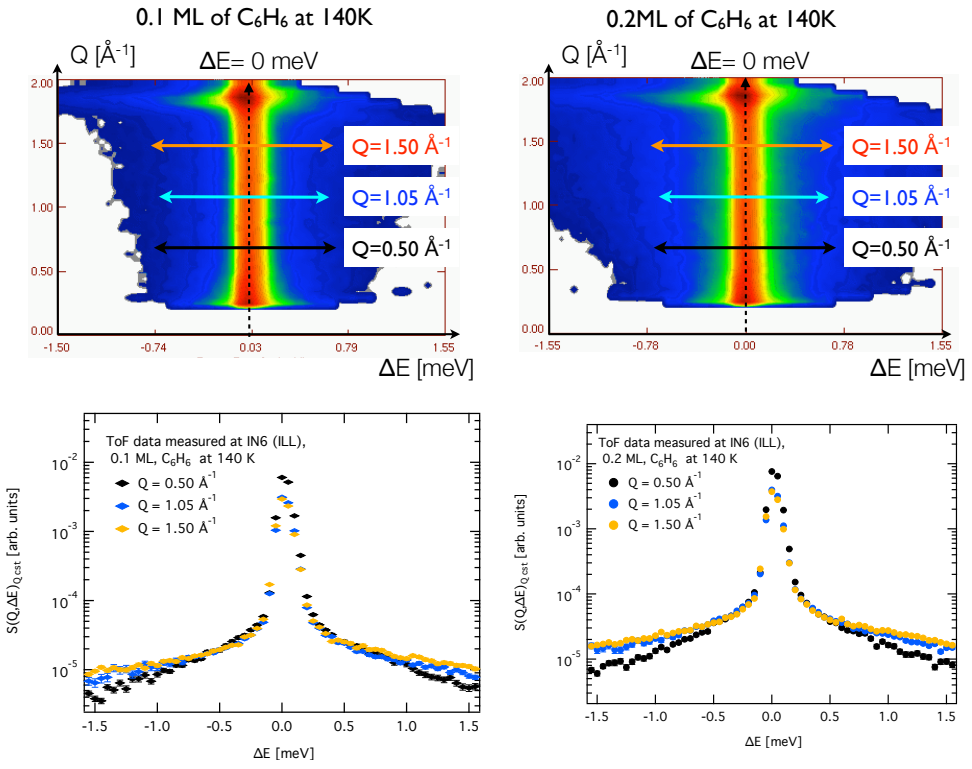

Figure 3.5: Top panel: Scattering function $S(Q, \Delta E = \hbar\omega)$ for the 0.1 ML (left) and 0.2 ML (right) of benzene adsorbed on exfoliated graphite at 140K. Bottom panel: scattering function as a function of the energy transfer ΔE at three constant values of Q: 0.5Å^{-1}, 1.05 Å^{-1} and 1.50Å^{-1}. The difference between low Q and high Q range are more appreciable at 0.2 ML. But the fitting to a theoretical model is required to establish the dependence of the HWHM of the energy profile with the momentum transfer.

First of all, we observe that the intensity of the quasi-elastic area increases with coverage. This is logical since the density of protons grows with the coverage. Consequently, the adsorbed layer scattering cross section rises and delivers a brighter scattering. We deduce that the effects of diffusion at low coverages are difficult to identify by a simple inspection of the scattering functions, since they can be hidden by the strong elastic peak. Actually the scattering function of the 0.1 ML sample is very similar to the one of exfoliated graphite at 140 K (see the left panel in Fig. 3.3). Only the fit of the data to theoretical models

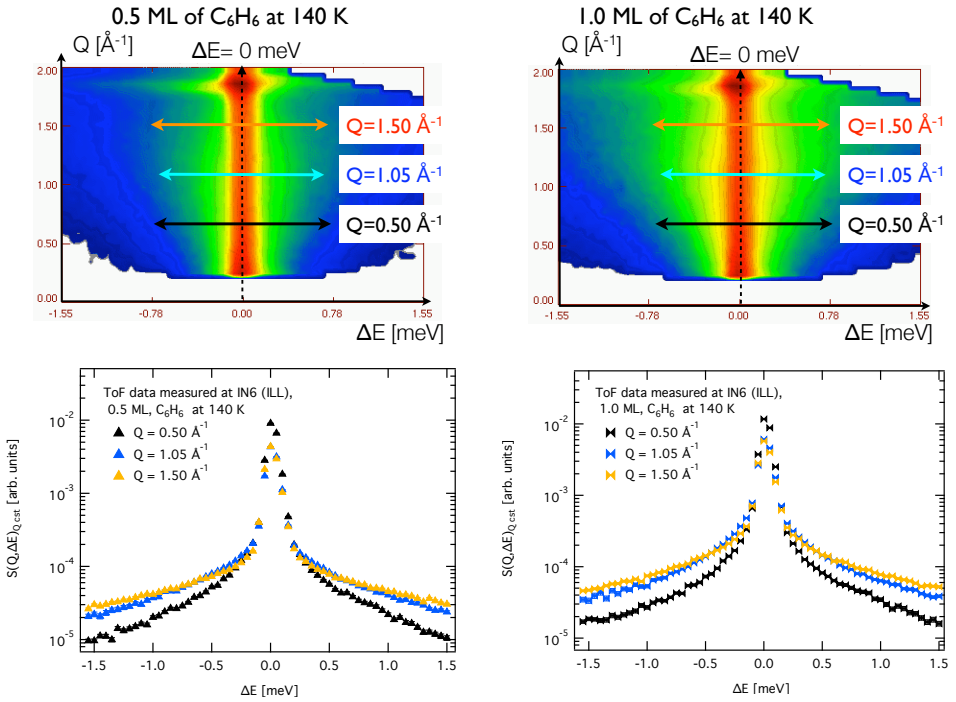

Figure 3.6: Top panel: Scattering function $S(Q, \Delta E = \hbar\omega)$ for the 0.5 ML (left) and 1.0 ML (right) of benzene adsorbed on exfoliated graphite at 140K. Bottom panel: scattering function as a function of the energy transfer ΔE at three constant values of Q: 0.5Å^{-1}, 1.05 Å^{-1} and 1.50Å^{-1}. The change of the quasi-elastic profile between 0.5Å^{-1} and 1.05 Å^{-1} becomes clearer, in contrast with the low coverage samples, in Fig. 3.5

provides quantitative and reliable information. Conversely, the shape of the quasi-elastic profile and its dependence on Q is clearly visible at high coverages (0.5 ML and 1.0 ML). The bottom panels of Figs. 3.5 and 3.6 gather vertical cuts of the scattering function at constant values of the momentum transfer. The quasi-elastic profiles exhibit a significant dependence on Q for the 0.5 ML and 1.0 ML samples. There is an inflection point at Q =1.05 Å^{-1} in the broadening of the quasi-elastic area with the momentum transfer . This particular value of the momentum transfer matches the size of the benzene molecule whose diameter is ca. 5 Å [119]: $Q = 1.05^{-1} = 2\pi/d$, $d \sim 6$Å. When the momentum transfer lies below 1.05 Å^{-1}, the scattering function $S(Q, \Delta E)$, is sensitive to long distance dynamics or large dimension scatterers compared to the size of single molecules. Hence, the scattering is dominated by the contribution of molecular clusters sliding across the surface or molecules performing long translations. On the contrary, at Q values lying above $Q = 1.05^{-1}$, the dynamics of single molecules becomes accessible. In special, very localized motion like rotations contribute substantially to the scattering function.

Dependence of the diffusion on temperature The group of vertical cuts in Fig. 3.7 compares the spectra measured at different temperatures. A single graph groups for each coverage the scattering functions measured along the whole thermal range at a given Q value. We pick up two representative values of the low and high momentum transfer range, 0.5 Å^{-1} and 1.5 Å^{-1}, to consider the thermal behavior of all the possible diffusive mechanism (long and short length scale). Finally, we include the resolution function measured at 2K as benchmark for the thermal broadening of the quasi-elastic peak. We attribute the strong asymmetry of the latter to the multiple scattering coming from the large sample dimensions.

First of all, we observe that the quasi-elastic profile gets broader with temperature for all the coverages and in all the ranges of the momentum transfer. However the thermal behavior of the quasi-elastic profiles depends on the coverage. We can see in both ranges of Q that the 0.1 ML quasi-elastic profiles are much less sensitive to temperature changes than the 0.5 ML or 1.0 ML profiles. The 0.1 ML quasi-elastic profiles in the range of 60K to 140K overlap at $Q = 1.50$ Å^{-1} in the energy window comprised within -2 meV / 2 meV. They progressively separate at 0.5 ML and become perfectly distinguishable at 1.0 ML coverage. The gap in the 0.1 ML spectra intensities between 40K and 60K spectra is shifted towards higher temperature at increasing coverages: it lies between 60K and 100K for 0.5 ML and between 100K and 140K for 1.0 ML. Benzene diffusion is an activated process: molecules require a certain thermal energy to overcome the energetic barriers for moving across the surface. Tunneling diffusion is excluded, since the De Broglie wavelength of the benzene

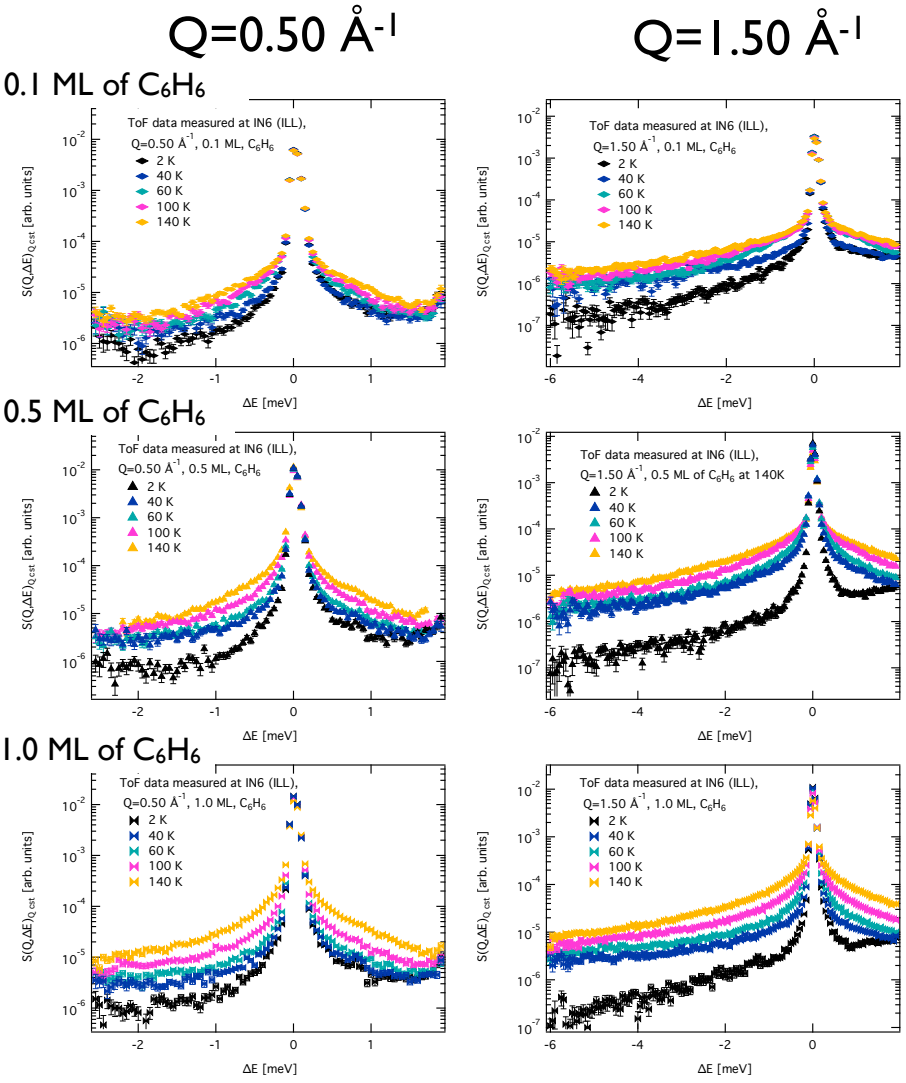

Figure 3.7: Set of neutron spectra at constant Q values. Columns group together the graphs displaying the spectra at the same $Qvalue$. The two different values of the momentum transfer 0.50 $Å^{-1}$ and 1.50 $Å^{-1}$ survey the thermal behavior of the quasi-elastic broadening at the long and short length scale respectively. Rows group the graphs at the same coverage. In every single graph spectra taken in the thermal range going form 2K to 140K are plotted. Coverage affects the thermal behavior of the quasi-elastic profile: high coverage spectra are more sensitive to a variation on temperatures than low coverage profiles. This suggests that diffusing mechanisms exists whose activation energy depends on the interaction between molecules.

molecule is too small in the temperature range that we survey (see Tab. 3.2). Thus, an intensity gap between two spectra at two different temperatures re-

flects the existence of one (or more) activation energies: molecules are free to move at temperatures above the diffusive threshold temperature while they remain trapped in the energy minima of the potential energy surface when the temperature is below the threshold. But the origin of potential energy barriers is ambiguous. On one side, energy barriers can come from the surface corrugation whose maximum estimated value is 15 meV [45] which corresponds to an activation temperature of 170 K. On the other side, the interaction of one molecule with its neighbors can also give rise to potential energy surface barriers hindering the motion of the molecule. The thermal evolution of the quasi-elastic profiles suggests that there are diffusion mechanisms whose activation energy is coverage dependent and is ruled by molecular interactions. However, only the fitting to a theoretical model and, specifically, the study of the HWHM of the quasi-elastic profile as a function of temperature and momentum transfer provides the required information to validate this hypothesis.

3.2.3 Measurement on deuterated benzene adsorbed on graphite: coherent scattering

The benzene molecule constitutes an excellent system to understand the different information delivered by neutron coherent and incoherent scattering. We can switch between a strongly incoherent scatterer, hydrogenated benzene (h-benzene C_6H_6), or a mostly coherent scatterer in the low Q range: deuterated benzene (d-benzene C_6D_6), see Tab. 3.2. The coherent scattering function is defined as the Fourier transformed in time and space of the Van Hove correlation function $G(\mathbf{r}, t)$ yielding the probability of finding a particle at a certain position $\mathbf{r}$ at time t provided the same or a different particle was at the origin at $t = 0$. Thus, the coherent scattering function is no longer sensitive to single particle averaged trajectories, in contrast to incoherent scattering. Conversely, it measures the averaged *relative trajectories* of particles in the system: the motion of the molecule with respect to its neighbors. Thereby, it should highlight the diffusive process from a complementary perspective.

Dependence on coverage We have measured the quasi-elastic spectrum for the deuterated benzene at two different coverages: 0.5 ML and 0.9 ML. The Figs. 3.8 and 3.9 compare the scattering function as a function of the energy ΔE and the momentum transfer Q for this two sample with the analogous coverages of h-benzene. We also include the scattering function at different Q values covering the whole momentum transfer range. The quasi-elastic area in green changes dramatically when passing from d-benzene to h-benzene. An important factor is that d-benzene has a smaller scattering cross section than

h-benzene. Hence, the brightness of the quasi-elastic area is reduced. Nevertheless, in the case of 0.5 ML d-benzene, the quasi-elastic area displays a larger energy width at low Q (at 0.5 Å^{-1}) than the 0.5 ML h-benzene scattering function. In the case of 0.9 ML of d-benzene, the quasi-elastic area is considerably reduced with respect to the 1.0 ML h-benzene quasi-elastic area. Furthermore it displays a peculiar dependence with Q which can be related to a jump diffusive behavior. This latter observation should be verify by fitting to the corresponding theoretical model. In the high Q range, the scattering intensity is dominated in both cases by incoherent scattering, since coherent scattering is not evenly distributed and drops at high momentum transfers. Thus the differences in shape between d-benzene and h-benzene should be attributed to the very low incoherent scattering cross section of d-benzene.

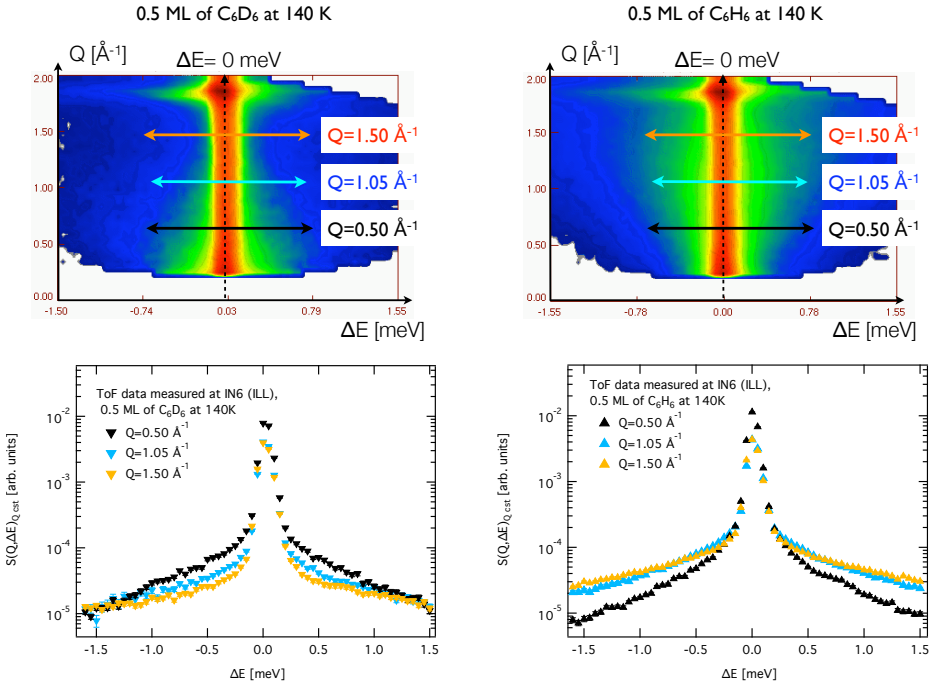

Figure 3.8: Top panel: Scattering function $S(Q, \Delta E = \hbar\omega)$ for coverages of 0.5 ML of d-benzene, C_6D_6 (left) and 0,5 ML (right) of h-benzene C_6H_6 at 140K. We plot the recorded neutron intensity versus the energy transfer ΔE (in the abscises axis) and the momentum transfer Q (in the ordinates axis). Bottom panel: scattering function versus the energy transfer ΔE at three constant Q values: 0.50 Å^{-1}, 1.05 Å^{-1} and 1.50 Å^{-1}. The dramatic change of the quasi-elastic area shape between deuterated and hydrogenated benzene is clearly visible in the dependence of the energy profile on Q. Furthermore, the difference for low Q values indicates that coherent and incoherent scattering deliver different information of the diffusion process.

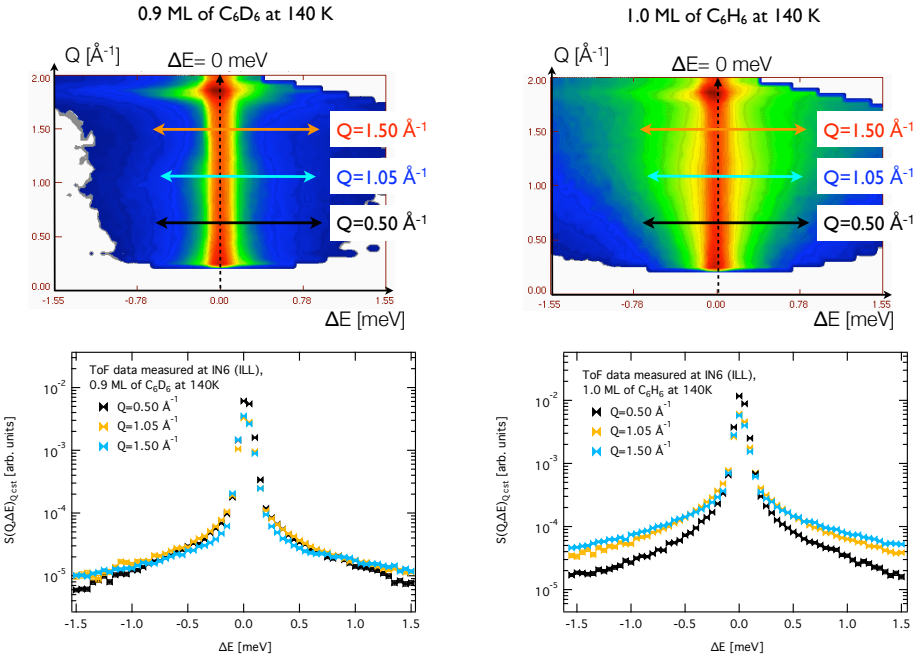

Figure 3.9: Top panel: Scattering function $S(Q, \Delta E = \hbar\omega)$ for coverages of 0.9 ML of d-benzene, C_6D_6 (left) and 1.0 ML (right) of h-benzene C_6H_6 at 140K. Bottom panel: scattering function versus the energy transfer ΔE at three constant Q values: 0.50 Å^{-1}, 1.05 Å^{-1} and 1.50 Å^{-1}. The quasi-elastic area is severely reduced in the deuterated benzene scattering function. This can be an effect of the very different scattering cross-section of the two samples. However, the dependence of the quasi-elastic broadening with the momentum transfer shows distinctly in the vertical cuts of the scattering function (bottom panel) the signature of different diffusing mechanisms or the same diffusive mechanism monitored from different standpoints. Coherent and incoherent scattering monitor the diffusion from different perspectives.

Dependence on temperature Fig. 3.10 shows the scattering function as a function of the energy transfer and at constant momentum transfer values of the 0.9 ML of d-benzene and the 1.0 ML of h-benzene. Each spectrum is measured at a different temperature covering the range between 20K and 140K. We maintain the selection of Q values: 0.50 Å^{-1} and 1.50 Å^{-1} because it shows the thermal behavior of diffusive processes involving different length scales. We recall that in the low momentum transfer range the scattering function probes long distance diffusive mechanisms like translations. Conversely, the high momentum range zooms into the short length scale where the scattering function becomes sensitive to the single molecule diffusion and confined motion like rotations. We observe in Fig.3.10 that the thermal behavior of

the scattering function at high Q values differs for d-benzene and h-benzene. The h-benzene scattering cross section is very sensitive to temperature variations and displays several gaps (between 20K and 40K and between 100K and 140K) while the thermal behavior of the d-benzene scattering cross section is very homogeneous in the whole thermal range.

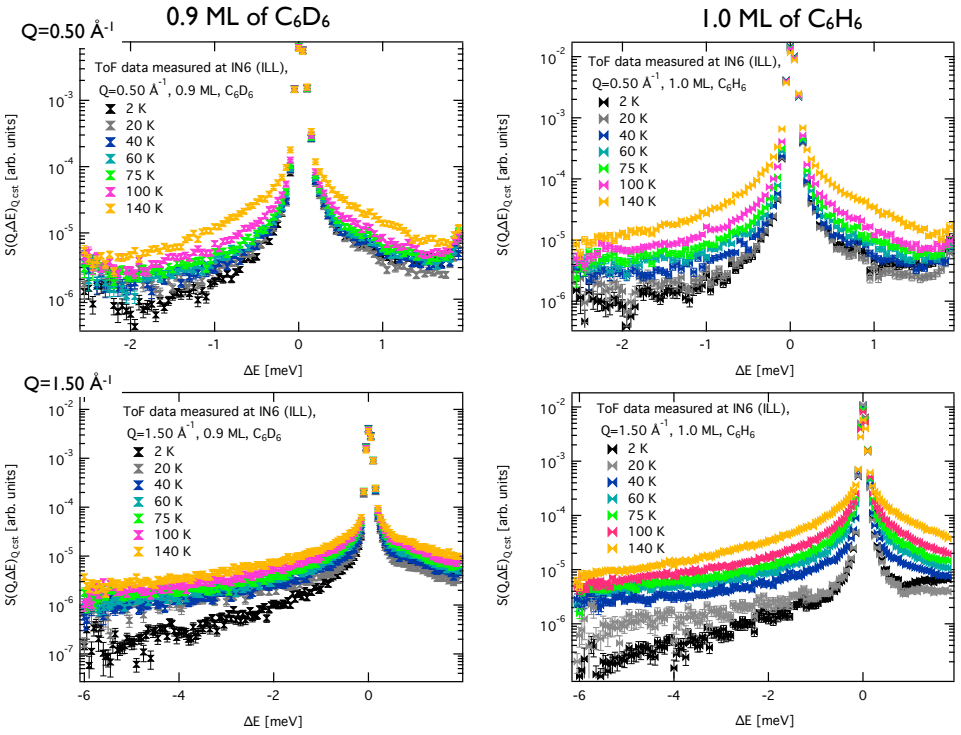

Figure 3.10: Cuts on the neutron coherent scattering function for the 0.9 ML of d-benzene (left panel) and on the incoherent scattering function for 1.0 ML of h-benzene (right panel) at two values of Q: 0.50 Å^{-1} and 1.50 Å^{-1}. The thermal behavior of the scattering cross-section changes at high momentum transfer between hydrogenated and deuterated benzene. This hints at a different perspective on the diffusive processes at work.

3.3 Conclusion

To briefly summarize this chapter, we have described the experimental procedure leading to the measurements of a whole set of data for different coverages and temperatures of the system: hydrogenated/deuterated benzene adsorbed on graphite. We have extensively surveyed the diffusive behavior of benzene

in the sub-monolayer regime and in a wide thermal range. Time of flight measurements on four samples of h-benzene and two samples of d-benzene give an overview of the action of coverage and temperature on the diffusion of benzene on graphite. In addition we have tested the existence of multiple scattering , due to the large dimensions of our samples: we have carried out measurements on different size samples and including cadmium shielding. We have also performed Monte Carlo simulations to evaluate the values of the energy broadening due to multiple scattered neutrons. It seems that most of the multiple scattered intensity lies in the regions of the scattering function dominated by carbon scattering (the very low Q range and the elastic Bragg peak of graphite). Finally the graphite phononic contribution has also been identified as contributing to the background intensity. Hence, we need to be careful during the data analysis and avoid the inelastic part of the scattering function in order to obtain a clean quasi-elastic signal only related to benzene diffusion.

The benzene diffusion on graphite is sensitive to both: temperature and coverage. However, the thermal behavior of the incoherent scattering cross-section changes with coverage and with the momentum transfer. A particularly interesting momentum transfer range is found above 1.05 Å^{-1} where neutron scattering access single molecule motion and very short length motion. In the next chapter, the fitting of the experimental data to different theoretical models should help to disentangle the different diffusive mechanisms at low and high momentum transfer, and also the differences between the information provided by incoherent and coherent scattering.

Chapter 4

Analysis of the experimental data

The exposition of the experimental data in chapter 4 gave a qualitative overview of the diffusion of benzene adsorbed on the basal plane of exfoliated graphite. The shape of the quasi-elastic scattering was shown to be sensitive to temperature and coverage. Furthermore, there is a marked contrast between the high and the low momentum transfer range. The goal of this chapter is to find a suitable theoretical model to fit the experimental data and complete the qualitative outline of the diffusive regime with a quantitative description. However, diffusive processes can hardly ever be described with a single model because of the several physical mechanisms underlying the dynamics of adsorbates on the substrate. Thus, the combination of diverse theoretical perspectives holds the key to tackle the complexity and dress a complete picture of the whole process.

In the following sections we discuss the fitting of the experimental spectra to a collection of theoretical models. We start with a brief survey on previous studies of the benzene diffusion on graphite, in order to set a context to our present analysis. In the following section we describe the most general theoretical profiles to fit quasi-elastic scattering data. The third section concerns the possible models to deal with the incoherent quasi-elastic scattering measured on the hydrogenated benzene/graphite system. The final section considers the analysis of the coherent quasi-elastic scattering arising from the deuterated benzene/graphite system.

4.1 Previous studies on benzene on graphite

Due to their central position in industry carbon based compound on graphite, like alkanes or aromatic rings, have been studied extensively by neutron scattering (diffraction, incoherent elastic scattering and QENS) [26]. Concerning aromatic systems such as benzene adsorbed on graphite, numerous thermodynamical studies and an important theoretical effort were performed [29–33]. The determination of the occupied surface area by benzene and its geometry of adsorption were a matter of debate during a long period: NMR experiments [37, 38] and neutron scattering data [39–41, 120] were giving conflicting results about the orientation of benzene rings: either parallel [41] or perpendicular [37,38,120,121] to the graphite surface. Finally neutron scattering [41, 122], LEED [44] and Penning ionization electron spectroscopy (PIES) measurements [42] in close collaboration with MD calculations [43] succeeded in revealing the structure of the adlayers of benzene adsorbed parallel to the surface. Careful re-analysis of the original NMR work yielded finally an agreement with the flat lying interpretation [123, 124]. Since then, further MD studies in the dynamics and the thermodynamical properties of the adsorbed layer has been carried out [34–36], helping for the interpretation of previous experimental results and giving a very detailed picture of the physical mechanisms underlying thermodynamical phase transitions such as the adsorbed layer melting process, for instance.

Apart from the structural characterization, the diffusive behavior of aromatic rings is a matter of study where quasi-elastic neutron scattering has proved to be a powerful tool. Ref. [120] presents different models to fit the diffusive behavior of benzene adsorbed on graphite. However, in this reference paper, the orientation of adsorbed benzene is still unclear. Hence the final model corresponds to a situation in which molecules are adsorbed perpendicular to the graphite surface. More recent neutron spin-echo, NSE, and helium-3 spin-echo, HeSE, spectroscopy have shown their suitability for the study of the fast dynamics on the picosecond time scale [45]. These measurements show a clear Brownian diffusive behavior of the benzene adsorbed flat on graphite, and it was the first experiment in which the microscopic dynamic friction coefficient could be established with a reasonable error bar [45]. In particular, the diffusive behavior of 0.5 ML of deuterated benzene was measured with NSE while hydrogenated benzene was used for the HeSE data. The intermediate scattering functions could be fitted to single exponential decays in a very wide range of the momentum transfer ($0< Q <1.5$ Å^{-1}) [45]. Furthermore, no dependence on the coverage of the diffusive regime was observed, and the friction coupling was mainly attributed to phononic processes [45]. However we

should not forget that both experiments measure a coherent scattering signal. In the case of NSE, this can be achieved by using fully deuterated benzene molecules [45], even though, the coherent signal decreases with the momentum transfer while the incoherent signal is evenly distributed in all the Q range and dominates for large momentum transfer values. In the case of HeSE, the scattering is always coherent [1], since Helium particles are scattered by the molecule's electronic cloud [1].

Finally, it is worth mentioning the theoretical effort for relating the diffusive behavior of benzene molecules on graphite with its internal degrees of freedom [125]. The hypothesis underlying this study is that there exist two different time scales related with the internal vibrations of the benzene molecule and the motion of its center of mass. The coexistence of the very fast dynamic of internal vibrations with the slower motion of the molecule's center of mass is the source of chaotic noise which affects the diffusion of the adsorbed molecule on the surface [125]. There are also more general theoretical approaches which combine diffusive and vibrational processes of adsorbate on surfaces [84]. In that case, adsorbates undergo continuous diffusion but can get trapped in potential wells, where they perform a vibrational motion (in that case the adsorbate is an atom and the vibrational motion is different from the internal degrees of freedom of a molecule). The question is how the combination of bound and unbound trajectories affects the diffusive regime [84].

In our study, we have oriented the research towards the effect of rotations in the diffusive process. Diffusion is a complex dynamical process and we need to combine complementary perspective to address a complete description of the phenomenon. We have decide to continue the research started in Ref. [45] and we have extensively survey the diffusion of hydrogenated benzene with time of flight, ToF, spectroscopy. Hydrogenated benzene produces an incoherent scattering signal, and ToF spectroscopy access a different dynamical window than the spin-echo technique (lower resolution but larger energy and momentum transfer window). The goal of this chapter is to find a suitable theoretical model to address the open question of the diffusive behavior of benzene. We wonder wether the differences and similarities of our study with Ref [45] are due to the coherent/incoherent nature of the scattering signal, to the spectroscopy technique in use or to a difference in the physical mechanisms underlying the diffusive regime.

4.2 Theoretical models for fitting QENS spectra

Theoretical models aim to describe the quasi-elastic profile on the basis of the physical mechanisms governing the dynamics of atoms or molecules adsorbed on the surface. Neutron scattering probes the loss of spatial correlation with time due to the displacement of atoms with respect to their original position at time $t = 0$ during the diffusive process. The *intermediate scattering function* (ISF), $I(\mathbf{Q}, t)$, monitors the correlation loss in time and reciprocal space (momentum transfer $\mathbf{Q}$). The decay of $I(\mathbf{Q}, t)$ with time reproduces exactly the drop of the probability to find an atom in its initial position. The scattering function (SF), $S(\mathbf{Q}, \Delta E)$, defined as the Fourier transform of the ISF, shows the effect of the correlation loss in the energy ΔE and momentum transfer $\mathbf{Q}$ domain. Here, diffusing adsorbates exchange kinetic energy with neutrons producing a continuous energy distribution around the elastic peak. This is the so-called *quasi-elastic profile* or *Q-peak* [85]. Since IN6 is a time of flight, ToF, spectrometer, the part of the quasi-elastic profile in the positive energy range is related with the loss of kinetic energy of neutrons which translates into a longer flying path in the ToF technique. Thus, it stems from processes like phonon excitations, or energy transfer to the diffusing molecules. Multiple scattering due to a large sample contribute as well to the positive range of the energy profile. Conversely, the negative part of the spectrum arises from processes where neutrons gain energy, like phonon annihilation or energy transfer from the diffusing elements. Nevertheless, it is important to stress that phonon creation/annihilation processes give rise to inelastic features, peaks at the corresponding frequency. Diffusive processes can also produce distinct spectral features in $S(\mathbf{Q}, \hbar\omega)$. In particular, frustrated lateral motion of atoms or molecules in the plane parallel to the surface gives rise to an inelastic feature: the *T-peak* [85]. Despite of that, we focus on the Q-peak since the benzene T-peak has not been observed in the surveyed quasi-elastic energy window. *Since the largest part of our experimental data consists in time-of-flight spectra, we seek for the theoretical description of the quasi-elastic scattering function. We are especially interested in two complementary features of the spectrum: the dependence of the shape of the quasi-elastic broadening and of its half-width-half-maximum, HWHM, as a function of the energy and the momentum transfer.* The theoretical framework within which quasi-elastic models are designed, was originally conceived to study incoherent quasi-elastic scattering. Nevertheless, it can be adapted to fit coherent scattering provided a number of assumptions are made [2, 99]. We firstly focus on the incoherent scattering models. Afterwards, we discuss the fitting of the deuterated benzene data. However, we will discuss the differences between the quasi-elastic coherent and incoherent scattering properly in the following chapter where the physical interpretation

of the fitting results is developed.

The incoherent SF, $S_{th}(\mathbf{Q}, \hbar\omega)$, for a system of identical diffusing particles on a surface can be split up into three contributions:

$$S_{th}(\mathbf{Q}, \Delta E) = [y_0 + \exp(-\left\langle \mathbf{u}_L^2 \right\rangle Q^2) A_{el}(Q)\delta(\Delta E) + S_{QENS}(\mathbf{Q}, \Delta E)]. \quad (4.1)$$

A flat background y_0 stems from the lattice phonon scattering. The delta function represents the elastic scattering from the non diffusing elements on the system and it basically reduces to the elastic substrate diffraction. The Debye-Waller factor, $\exp(-\left\langle \mathbf{u}_L^2 \right\rangle Q^2)$, which decreases the elastic intensity represents the contribution of substrate atoms vibrations, $\left\langle \mathbf{u}_L^2 \right\rangle$ being their mean square displacement, due to lattice phonons [56]. The last term contains the quasi-elastic scattering of the diffusing elements, $S_{QENS}(\mathbf{Q}, \hbar\omega)$ [56]. Its intensity is also affected by the internal vibrations of the molecule which produce a distinct Debye-Waller factor, $\exp(-\left\langle \mathbf{u}_V^2 \right\rangle Q^2)$, where $\left\langle \mathbf{u}_V^2 \right\rangle$ is the mean square displacement of the atoms vibrating in the molecule [56]. However, we embody this factor into the generic function $S_{QENS}(\mathbf{Q}, \hbar\omega)$ in order to clearly distinguish between the different contributions to the total SF, Eq. 4.1. Since the elastic intensity is namely due to the scattering from the substrate, while the quasi-elastic intensity can be attributed to the diffusing molecules, they are independent terms. Thus, the normalization of each term in the summation of Eq. 4.1 should be carried out separately. In particular, the *incoherent* quasi-elastic scattering function needs to satisfy the following requirement [60]:

$$\int_{-\infty}^{\infty} S_{QENS}(\mathbf{Q}, \Delta E) d\Delta E = 1. \quad (4.2)$$

In addition, the theoretical SF should fulfill a last requirement: the detailed balance principle. A completely classical SF is even in energy and momentum transfer: $S^{cl}(\mathbf{Q}, \Delta E) = S^{cl}(-\mathbf{Q}, -\Delta E)$ [56]. Quantum process break the symmetry in ΔE since inelastic processes involving neutron energy gain or loss are no longer equivalent [56]. The classical approximation of the SF is valid at long times and for long distances (small energy/momentum transfer), but, quantum effects should be taken into account in the short time-distance regime (high energy-momentum transfer). A good approximation of the actual SF is [56]:

$$S(\mathbf{Q}, \Delta E) = \exp\left(-\frac{\Delta E}{2k_B T}\right) S^{cl}(\mathbf{Q}, \Delta E). \quad (4.3)$$

We apply the detailed balance correction to the theoretical incoherent SF for diffusion on surfaces obtaining:

$$S_{th}(\mathbf{Q}, \Delta E) = \exp(-\left\langle \mathbf{u}^2 \right\rangle Q^2) \times \exp\left(-\frac{\Delta E}{2k_B T}\right) [y_0 + A_{el}(Q)\delta(\Delta E) + S_{QENS}(\mathbf{Q}, \Delta E)]. \quad (4.4)$$

The real fitting function, $S(\mathbf{Q}, \Delta E)$, results from the convolution of the theoretical SF with the resolution function $S_{res}(\mathbf{Q}, \Delta E)$ of the considered spectrometer:

$$\begin{aligned} S(\mathbf{Q}, \Delta E) &= S_{res}(\mathbf{Q}, \Delta E) \otimes S_{th}(\mathbf{Q}, \Delta E) \\ &= S_{res}(\mathbf{Q}, \hbar\omega) \otimes \left\{ \exp(-\left\langle \mathbf{u}^2 \right\rangle Q^2) \right. \\ &\left. \times \exp\left(-\frac{\Delta E}{2k_B T}\right) \left[y_0 + A_{el}(Q)\delta(\Delta E) + S_{QENS}(\mathbf{Q}, \Delta E) \right] \right\}. \end{aligned} \tag{4.5}$$

Fourier transforming Eq. 4.5 allows to pass to the time domain. Moreover, the convolution theorem turns the Fourier transformation of the convolution in Eq 4.5 into the product of the Fourier transformed functions [56]. Thus, the corresponding ISF is the product between the resolution function and the theoretical ISF:

$$\begin{aligned} I(\mathbf{Q}, t) &= I_{res}(\mathbf{Q}, t) \times I_{th}(\mathbf{Q}, t) \\ &= I_{res}(\mathbf{Q}, t) \times \frac{1}{\hbar} \int_{-\infty}^{\infty} S_{th}(\mathbf{Q}, \Delta E) \exp\left(\frac{i\Delta E t}{\hbar}\right) d\Delta E \end{aligned} \tag{4.6}$$

Note that the quantum corrections to the SF, give rise to a complex ISF since the Fourier transform of the detailed balance factor $\exp(-\Delta E/2k_B T)$ has an imaginary part. However, for a system made of benzene molecules, we can stay in the classical mechanics fram: Firstly, the De Broglie wavelength of benzene at temperatures above 40 K is ca. 0.08 Å which corresponds in the reciprocal space to 12.5 $Å^{-1}$. Thus, quantum effects are invisible in the momentum transfer range covered by IN6: the maximum Q value is 2 $Å^{-1}$ when the incoming wavelength is 5.12 Å. Secondly, the temperature should fulfill $T \gg \Delta E/k_b$ [126]. If we restrict the analysis to the quasi-elastic window where the maximum energy transfer is 6 meV, the threshold temperature is 70 K. However, most of the intensity is concentrated in the [-2 meV,2 meV] range, and in this case, the threshold lowers down to 20 K. As a result, for temperatures above 40K and a momentum transfer range below 2$Å^{-1}$ we can adopt a classical description of the benzene diffusion process and the theoretical ISF is real and reads [60]:

$$I(\mathbf{Q}, t) = I_{res}(\mathbf{Q}, t) \times \exp(-\left\langle \mathbf{u}^2 \right\rangle Q^2) \left[y_0\delta(t) + A_{el}(Q) + I_{QENS}(\mathbf{Q}, t) \right]. \tag{4.7}$$

The Fourier transformation of the SF changes constant terms in energy into delta functions of time and vice-versa. For instance, the constant background term in the SF becomes a delta function of the time fixing the initial intensity of the ISF. Conversely the elastic peak of the SF becomes a flat background in

the time domain (compare Eqs. 4.1 and 4.7). Finally, the quasi-elastic functions in time and energy are also related through the Fourier transformation:

$$I_{QENS}(\mathbf{Q},t) = \hbar \int_{-\infty}^{\infty} S_{QENS}(\mathbf{Q},\Delta E) \exp\left(\frac{i\Delta E t}{\hbar}\right) d\Delta E \tag{4.8}$$

The normalization condition for the incoherent quasi-elastic SF, Eq. 4.2, translates for the *incoherent* ISF [60]:

$$I_{QENS}(\mathbf{Q},0) = 1. \tag{4.9}$$

As we have seen in Chap. 2, very simple models exist like Brownian motion, jump motion or ballistic motion, which fit the experimental quasi-elastic data with a single quasi-elastic line. Nevertheless, in most cases, a single quasi-elastic profile is not enough to fit the experimental data in all the energy/momentum transfer or time/momentum transfer domain and for all the experimental conditions (temperature and coverage). Diffusion on surfaces is a complex process because it involves several physical mechanisms like translations, rotations, or clustering which take place simultaneously. Hence, we often need to combine several simple models in order to dress more realistic pictures of the dynamics of the system [1]. In this chapter we will focus on the mathematical aspect of the fitting process. Our goal is to find an explicit form of $S_{QENS}(\mathbf{Q},\Delta E)$ to fit our ToF experimental data. In the forthcoming sections we compare the suitability of different models for $S_{QENS}(\mathbf{Q},\Delta E)$, going from the most basic ones like a single Lorentzian or Gaussian function, towards more sophisticated models, which combine summations of Lorentzians and Gaussians. Of course, the choice of the models is not arbitrary and relies on a physical interpretation of the process (an accurate description of the underlying atomic dynamics).

4.3 Experimental data of h-benzene, C_6H_6, on graphite: incoherent scattering

The general form of the *incoherent* ISF for a system of diffusing atoms, as defined in Chap. 2, reads:

$$I_{QENS}(\mathbf{Q},t) = \frac{1}{N} \sum_{j=j'=1}^{N} \langle \exp(-i\mathbf{Q}\cdot\mathbf{r}_j(t)) \exp(i\mathbf{Q}\cdot\mathbf{r}_j(0)) \rangle. \tag{4.10}$$

From the classical mechanics standpoint, the Heisenberg operators for the single atom positions, $\mathbf{r}_j(t)$ commute at different times: $[\mathbf{r}_j(t), \mathbf{r}_j(0)] = 0$. If the Van Hove correlation function in space and time, $G(\mathbf{r},t)$, is a Gaussian function

of variable $\mathbf{r}$, the cumulant expansion of Eq. 4.10 reduces to the quadratic term of Q [60]. This is the well-known *Gaussian approximation* (see Chap. 2) [104]. It yields the incoherent ISF, $I_{QENS}(\mathbf{Q},t)$, as function of the mean square displacement (MSD) of single atoms on the surface, $\sigma^2_{\mathbf{Q}}(t) = \left\langle \Delta r^2_{\mathbf{Q}} \right\rangle (t)/2$, projected on the direction of the momentum transfer vector [60]:

$$I_{QENS}(\mathbf{Q},t) \simeq \exp\left[-\frac{Q^2}{2}\sigma^2_{\mathbf{Q}}(t)\right] \tag{4.11}$$

The corresponding SF is found by Fourier transforming Eq. 4.11:

$$S_{QENS}(\mathbf{Q},\Delta E = \hbar\omega) = \frac{1}{2\pi\hbar}\int_{-\infty}^{\infty} \exp\left[-\frac{Q^2}{2}\sigma^2_{\mathbf{Q}}(t)\right] \exp[-i\omega t]dt \tag{4.12}$$

In conclusion, the decay with time of the incoherent ISF or the profile with energy of the incoherent SF will only depend on the time evolution of the single atom MSD on the surface, $\left\langle \Delta r^2_{\mathbf{Q}} \right\rangle (t)$. It was already seen in Chap. 2 that there is a very general form of the ISF, Eq. 2.55, which reproduces correctly the long and the short time behavior of Eq. 4.11, and also the low (or ballistic) and the high (or Brownian) friction regimes [57]. The so-called *shape parameter*, χ^2 defined in Eq. 2.56, monitors the continuous change of the ISF time decay profile with the friction parameter η [57]. The very low friction regime provides a Gaussian shaped ISF [127] which is equivalent to the short time behavior of the ISF, as defined in Eqs. 2.57. This means that even in the Brownian regime, particles undergo ballistic motion (rectilinear and uniform displacements and quadratic dependence with time of the mean square displacement) in the lapse of time between two collisions [2]. When the density of adsorbed particles on the surface is very low such that the interactions between them are rare and can be accounted with instantaneous collisions, the friction parameter is very low [127]. As a consequence, the lapse of time between collisions, or equivalently the mean free path (the distance covered by a particle between two collisions), become very large [127] and the ballistic behavior of particles is conserved getting to be observable at experimentally accessible time scales (the pico-second time window for He and neutron ToF spectroscopy techniques). On the contrary, if the friction parameter is very high, the decay of the ISF rapidly converges to a single exponential decay corresponding to the long time behavior of the ISF, described in Eq. 2.58 [57]. In that case molecules display a Brownian diffusive behavior: the mean square displacement is linear with time [127], since the very frequent collisions due to a high density of adsorbed molecules, reduces the mean free path and the mean free time within which ballistic motion dominates. Thus, the range of ballistic diffusion in time and space gets so small that it is no longer observable experimentally. The key point that we want to stress is that *ballistic and*

Brownian diffusion are not different diffusive regimes [127]: molecules behave ballistically in the time lapse determined by the frequency of collisions, i.e. by the friction parameter η. Beyond this time window, the diffusion becomes Brownian in the sense that it results from the effect of many collisions, and the velocity autocorrelation function decays with time, depending on the value of the friction parameter. Finally, we deduce that η is the main parameter which tunes the extension of the domain in time and space where the ballistic diffusive behavior of Brownian particles is still accessible for experiments.

The last important comment before we start the detailed data analysis concerns the substrate. Exfoliated graphite *Papyex* does not present any particular ordering of the micro-crystals of graphite in the [0001] plane [68], while their normal direction should be well aligned to the normal direction of the macroscopic surface [68]. As a result, the measured ISF and SF should be averaged over all the possible relative directions of the neutron momentum transfer vector with respect to the graphite crystals in the [0001] plane [56,128]. Ref. [128] develops and applies a theoretical formalism to deduce the contribution to the scattering of what they call a *powder of planes* referring to the averaged orientation of the graphite micro-crystals basal plane in *Papyex* material. The basis of the theoretical framework is the definition of a distribution function for the orientation of the planes, $g(\alpha)$, which can be measured experimentally through a diffraction experiment [128]. The ISF or SF should be integrated using such a distribution function. Misoriented graphite crystals with respect to the normal contribution can affect seriously the shape of the SF which diverges from the theoretical line shapes for diffusion (Lorentzian or Gaussian) [128]. However, the convolution with the experimental resolution function allows to eliminate this effect [128]. The fraction of misoriented crystals in graphite is estimated to very low [68], although no precise numbers are given. We have not measured the experimental orientation distribution function, and we have assumed that the basal plane graphite crystals orientation is completely random, while their normal direction is well defined, parallel to the normal of the macroscopic surface. Furthermore, in the cases in which the motion is assumed to be isotropic on the surface (in terms of diffusion coefficients this means that $D_{\parallel} \sim D_{tot}, D_{\perp} \sim 0$), the projection of $\left\langle \Delta r^2_{\mathbf{Q}} \right\rangle (t)$ over any given direction of $\mathbf{Q}$ is constant and we only consider the dependence on the modulus: $\left\langle \Delta r^2_{\mathbf{Q}} \right\rangle (t) \equiv \left\langle |\Delta \mathbf{r}|^2 \right\rangle (t)$. Finally, we take as resolution function the experimental SF corresponding to the coverage to fit, measured at the base temperature of the cryostat, 2K.

4.3.1 Single quasi-elastic profile models

We have seen in Chap. 2 that there are two limiting cases for the time dependence of the atoms MSD on the surface: a linear or a quadratic law of time [58, 60]. The two first models give the ISF and the SF which correspond to these possibilities.

Model 1 A linear time dependence of the MSD, $\left\langle |\Delta\mathbf{r}|^2 \right\rangle \propto t$, gives rise to a single exponential decay with time of the quasi-elastic ISF, $I_{QENS}(Q,t)$:

$$I_{QENS,model1}(Q,t) = \exp\left[-\frac{t}{\tau(Q,T)}\right]; \frac{1}{\tau}(Q,T) = D(T)Q^2, \tag{4.13}$$

or equivalently a single Lorentzian profile of the energy transfer for the quasi-elastic profile of the SF:

$$S_{QENS,model1}(Q,\Delta E) = \frac{1}{\pi}\frac{\hbar/\tau(Q,T)}{(\hbar/\tau(Q))^2 + (\Delta E)^2}. \tag{4.14}$$

The inverse time constant $1/\tau$ has a quadratic dependence on Q: $1/\tau \propto Q^2$. It also depends on the temperature through the diffusion coefficient, D (see Sec 2.2 of Chap. 2). Finally, note that both, the incoherent quasi-elastic SF and ISF, satisfy the normalization condition enunciated in Eqs. 4.2 and 4.9. The first model for the incoherent SF reads :

$$S_{model1}(Q,\Delta E) = S_{res}(Q,\Delta E) \otimes \left[y_0 + A_{el}(Q,T)\delta(\Delta E) + A_{QENS}(Q,T)\frac{1}{\pi}\frac{\hbar/\tau(Q,T)}{(\hbar/\tau(Q,T))^2 + (\Delta E)^2}\right]. \tag{4.15}$$

We include the Debye-Waller factor in the elastic and quasi-elastic amplitude, which become temperature dependent.

Model 2 A quadratic time dependence of the MSD, $\left\langle |\Delta\mathbf{r}|^2 \right\rangle \propto t^2$, produces a Gaussian function of time for $I_{QENS}(\mathbf{Q},t)$:

$$I_{QENS,model2}(Q,t) = \exp\left[-\Gamma(Q,T)t^2\right]; \Gamma(Q,T) = \sqrt{2\ln 2\left\langle v^2\right\rangle}Q, \tag{4.16}$$

or a Gaussian function of energy transfer for the SF quasi-elastic profile $S_{QENS}(\mathbf{Q},\Delta E)$:

$$S_{QENS,model2}(Q,\Delta E) = \sqrt{\frac{2\ln 2}{4\pi\hbar^2\Gamma(Q,T)}}\exp\left[-\frac{\Delta E^2}{4\hbar^2\Gamma(Q,T)}\right]. \tag{4.17}$$

The HWHM, $\Gamma(Q,T)$, is linear with Q and depends on the mean square velocity $\left\langle v^2\right\rangle$ of the diffusing element (molecule or cluster). The latter can be evaluated

with the equipartition theorem for a two dimensional system: $\langle v^2 \rangle = 2/m\beta$, where m is the mass of the particle and $\beta = 1/k_B T$. Thus, the second model to fit the experimental data is:

$$S_{model2}(Q, \Delta E) = S_{res}(Q, \hbar\omega) \otimes \left\{ y_0 + A_{el}(Q,T)\delta(\Delta E) + A_{QENS}(Q,T) \sqrt{\frac{1}{4\pi\hbar^2\Gamma(Q,T)}} \exp\left[-\frac{\Delta E^2}{4\hbar^2\Gamma(Q,T)} \right] \right\}. \tag{4.18}$$

As before, the Debye-Waller factor is embodied in the amplitudes. We also underline that Eqs. 4.17 and 4.17 agree with the normalization condition in Eqs. 4.2 and 4.9.

We have performed a least square fit of the whole experimental data set to this two models, with the same fitting conditions for both models. The free parameters are: the background y_0, the elastic A_{el} and the quasi-elastic A_{QENS} amplitudes, and the HWHM of each quasi-elastic profile, $1/\tau(Q)$ or $\Gamma(Q)$. The fitting energy range is [-6 meV , 2 meV] to avoid the complicated background created by graphite phonons. The resolution function is the experimental SF at 2K. The results for the fitting of the 0.5 ML at 140 K are shown in Fig. 4.1. We also plot each one of the contributions to the SF, convoluted with the resolution function: the elastic part and the quasi-elastic profile.

Discussion of the fittings to model 1 and 2 Fitting results for 0.1 ML, 0.2 ML and 1.0 ML of h-benzene are summarized in Figs. 4.2 and 4.3. Tabs. 4.1 and 4.4 display the χ^2 parameter, characterizing the goodness of the fit. In terms of coverage (see Fig. 4.2 and Tab. 4.1), we observe that the 0.1 ML energy profile can be approximated by both models. The quality of the fit is very similar. Conversely the 0.2 ML profile has a more marked Lorentzian shape, specially at high Q values. Finally the quasi-elastic profiles for 0.5 ML and 1.0 ML are much better described by a Lorentzian function, even though the theoretical profile does not match perfectly the energy profile in the entire energy range. In contrast with the marked dependence of the quasi-elastic profile on the coverage, there is little change with temperature (see Fig. 4.3 and Tab. 4.4). The quasi-elastic profile of 0.1ML is always approximated with both models while the 0.2 ML and 1.0 ML profiles maintain its rather Lorentzian shape.

To sum up, the high coverage data are difficult to fit to a single quasi-elastic line, especially in the range of high momentum transfer Q . Conversely, the low

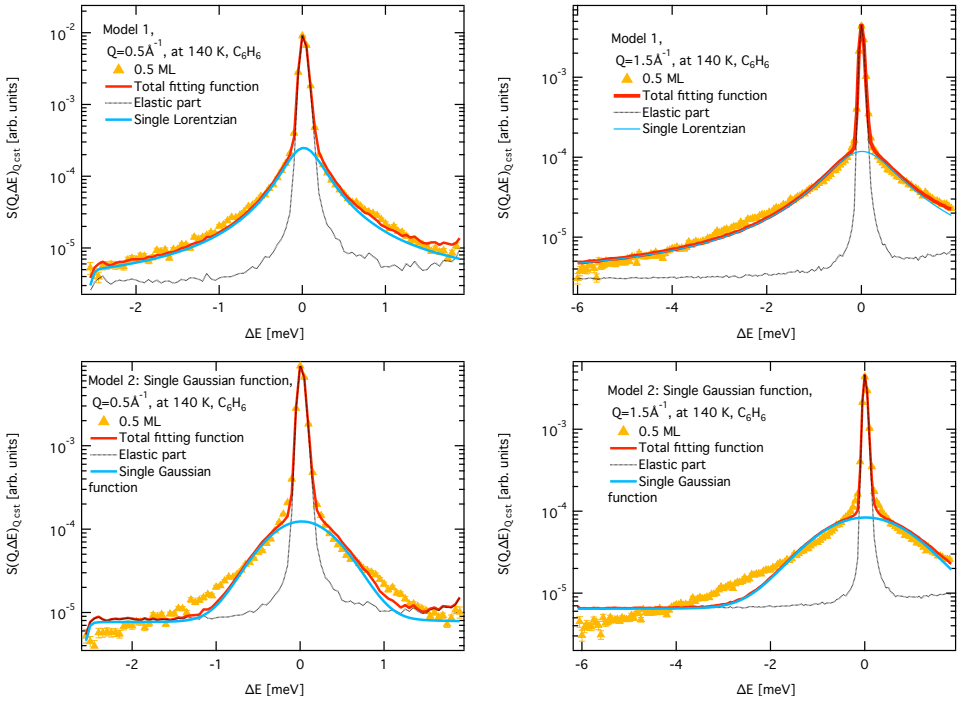

Figure 4.1: Fitting of the 0.5 ML data to a single Lorentzian (upper panel) and to a single Gaussian (lower panel) function. We include the different contributions: the elastic part given by the convolution of the resolution function to a delta function centered at $\Delta E = 0$ meV (black dotted line), the theoretical quasi-elastic profile (blue solid line) and the total function (red solid line). The Lorentzian profile fits correctly the data, even if we see that it does not match perfectly the high Q profile. Conversely the Gaussian profile strongly deviates from the data.

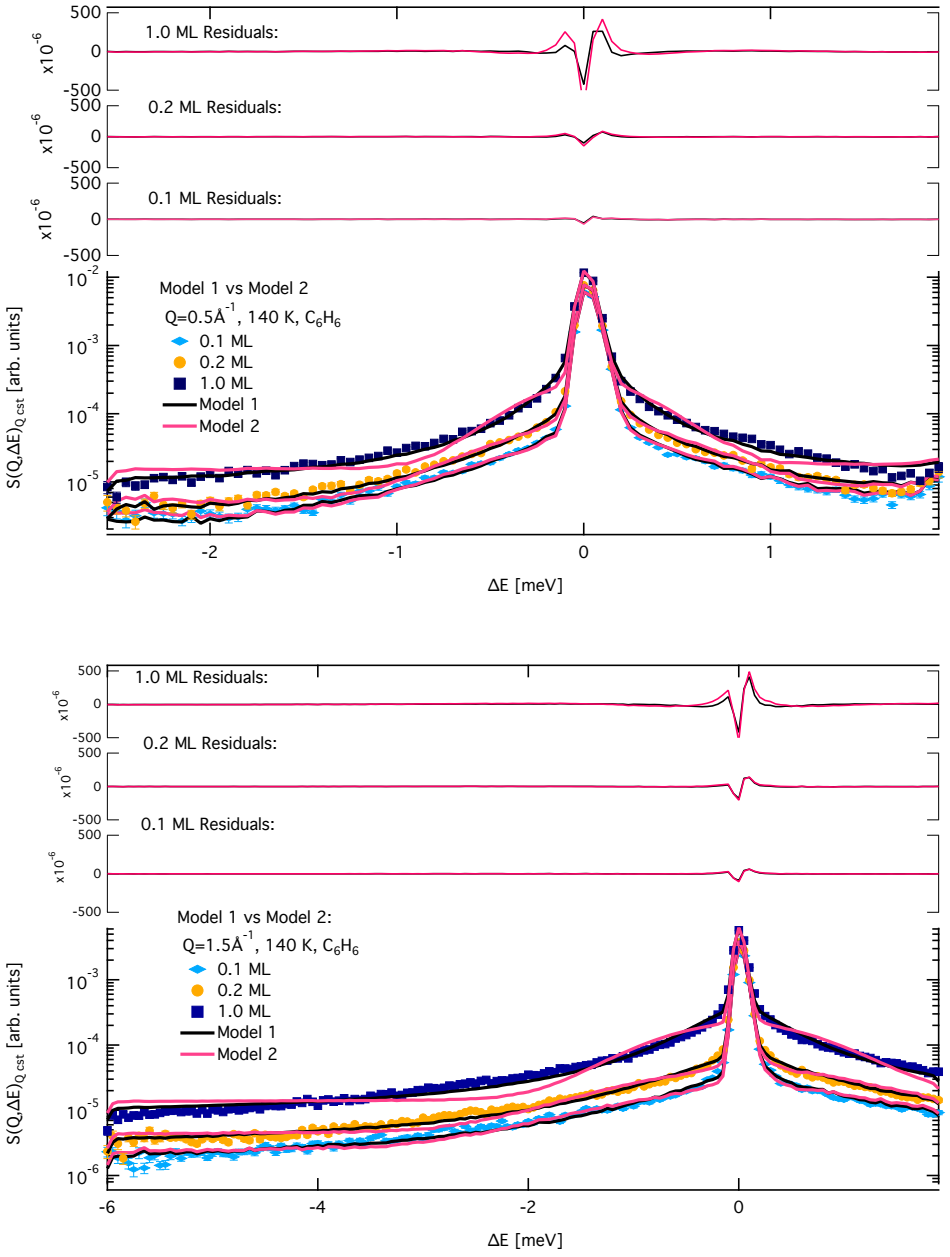

Figure 4.2: Fitting of the experimental data of 0.1 ML and 1.0 ML h-benzene coverage at $Q = 0.5^{-1}$ (upper) and $Q = 1.5^{-1}$ (bottom) with model 1 (a single Lorentzian function) and model 2 (single Gaussian profile) at 140 K. The quasi-elastic profile of 0.1 ML data can be approximated by the two models. On the contrary, the quasi-elastic profile of 1.0 ML data is better described by model 1.

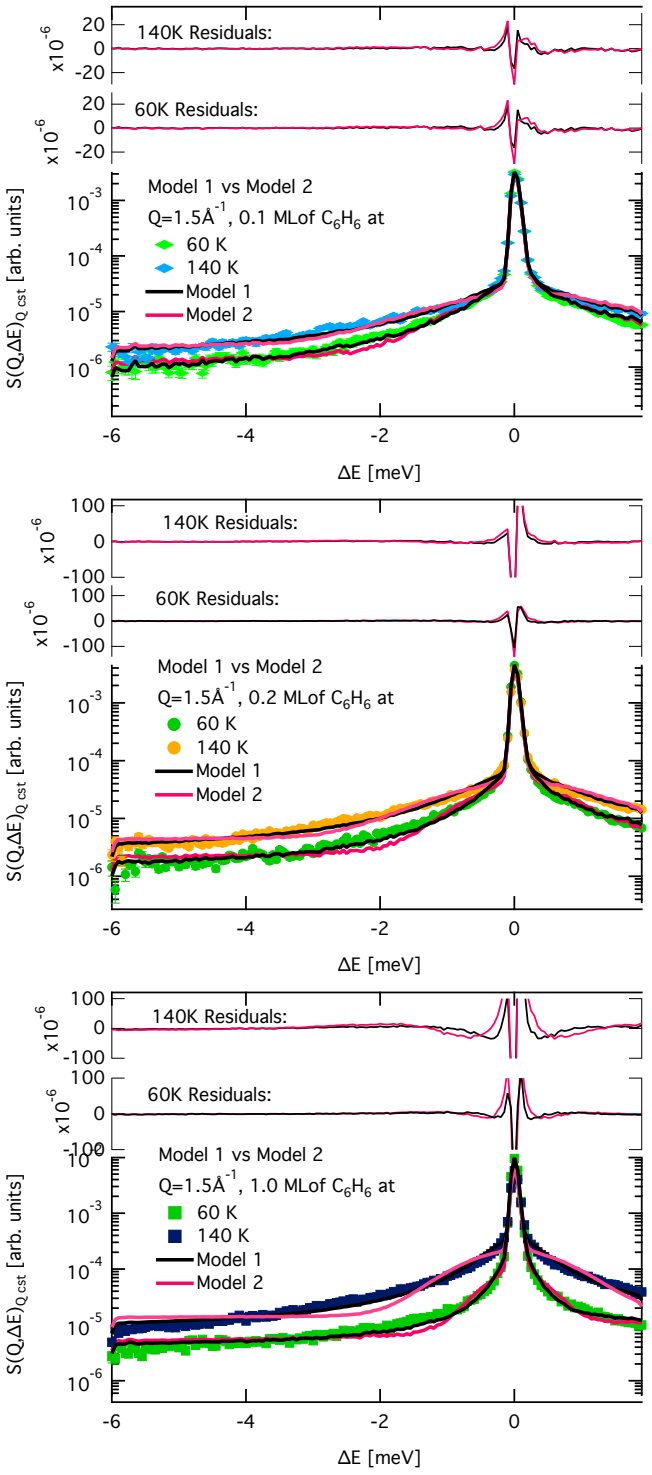

Figure 4.3: Fitting of the experimental data of 0.1 ML (upper panel) 0.2 ML (middle panel) and 1.0 ML (lower panel) h-benzene coverage at $Q = 1.5^{-1}$ with model 1 and 2 for temperatures between 60K and 140K.

Table 4.1: Goodness of the fit , χ^2 parameter divided by the number of fitted points, resulting from the fitting of all the data set at 140 K to models 1 and 2.

	Q=0.5 Å^{-1}		Q=1.5 Å^{-1}	
	Model 1	Model 2	Model 1	Model 2
0.1 ML	2.91	5.09	7.21	11.64
0.2 ML	3.87	8.04	12.22	21.86
0.5 ML	10.69	36.88	32.20	86.31
1.0 ML	12.40	47.95	40.64	158.99

Table 4.2: Goodness of the fit , χ^2 parameter divided by the number of fitted points, resulting from the fitting of all coverages in the whole thermal range to models 1 and 2 for $Q = 1.5$ Å^{-1}.

	0.1 ML		0.2 ML		1.0 ML	
	Model 1	Model 2	Model 1	Model 2	Model 1	Model 2
60 K	3.28	5.78	7.45	18.44	11.07	48.15
100 K	4.45	7.54	12.88	25.78	21.08	104.84
140 K	7.21	11.64	12.22	21.86	40.64	158.99

coverage data can be approximated by a single quasi-elastic line. Since a single quasi-elastic line is related to a single diffusive process, the failure of these two elementary models shows that there are probably two or more diffusive mechanisms which become apparent in the high Q range. Furthermore, a higher coverage seems to foster the multiplicity of diffusion processes: the deviations from single quasi-elastic lines are more pronounced for the high coverage than for the low coverage quasi-elastic profiles.

4.3.2 Multiple quasi-elastic profile models: Rotations and Translations

The addition of more than one quasi-elastic lines to fit the data correctly, is related to the existence of different diffusing mechanisms [56]. Furthermore, they do not appear necessarily at the same Q range, since they can involve different length scales. A clear example are the translations and the rotations of molecules adsorbed on the substrate. When molecules translate, they cover distances of several substrate unit cells and the mean square displacement, MSD, is an increasing function of time. The loss in spacial correlation

is observable across the entire momentum transfer range and the quasi-elastic broadening increases with the momentum transfer. On the other hand, when molecules rotate, the motion of the atoms within the molecule remains confined in a circle or a sphere (depending if the motion takes place on the surface or in three dimensional space). Their MSD reaches a constant value after a certain time [60] and the loss of spacial correlation is very localized. It becomes measurable at the Q values comparable to the size of the molecule. In the following paragraph, we describe the theoretical framework which allows to include molecular translations and rotations in the same model.

First, we need to factorize the ISF in Eq. 4.10 in terms of the motion of the center of mass (CoM) molecule and the motion of the atoms within the molecule with respect to the CoM frame. The position of each atom of the α-th molecule can split be into the CoM position, $\mathbf{R}^\alpha$, the position of equilibrium of this atom with respect to the CoM frame $\mathbf{r}_j^\alpha$, and the displacement of the atoms with respect to its equilibrium position, $\mathbf{u}_j^\alpha$, due to the molecular vibrations [58]:

$$\mathbf{r}_j = \mathbf{R}^\alpha + \mathbf{r}_j^\alpha + \mathbf{u}_j^\alpha \tag{4.19}$$

If *the position of the CoM, the orientation of the molecule and its vibrations are not correlated*, the ISF is factorable into a function depending on each one of the terms in Eq. 4.19 [56, 58, 60]. The independence of each term of the ISF is reliable if the characteristic energies of each kind of motion, (vibrations, translations and rotations) belong to a different dynamical window. The covalent bonding of the carbon atoms forming the aromatic ring provides the molecule with high internal vibration frequencies. The lowest vibrational frequencies are associated with out-of-plane distortions of the molecule [129]. Their energy have been measured with Raman or infrared spectroscopy and their values span in the range between 50.3 meV and 80.3 meV [129]. On the other hand, a typical value for the benzene free rotation around its six-fold symmetry axis can be evaluated from the flipping frequency [130] which is reported for hydrogenated and deuterated benzene in Tab. 3.2 of the Chap. 3. We find a rotational energy of 2.7×10^{-3} meV, which clearly lies in a different energy window than the internal vibration frequencies. We can suppose that rotational and translational energies are closer, since the physical parameter governing translational motion is the mass of the molecule while it is its moment of inertia for rotations. However, the assumption of uncorrelated translations and rotations, also known as the *weak hindered approximation* [81], applies whenever the orientation dependent inter-molecular forces are weak compared to the isotropic forces or if the center-of-mass of the molecule corresponds to its center of charge [81]. Although the interaction between benzene molecules (quadrupolar interaction [35]) is strongly anisotropic in the bulk, giving rise to

the T-configuration in solid benzene crystals [131], the adsorption process favors a coplanar configuration through the interaction with the substrate which weakens significantly the benzene-benzene interaction energy [35, 131]. The coplanar interaction energy becomes one third of the quadrupolar interaction energy at work in the T-configuration [35, 131]. In addition, benzene is a top symmetric molecule and no hydrogen bondings occur in the adsorbed phase. This argument has already been used to support the validity of the weak hindered approximation in liquid methane [81]. Thus, the weak hindered approximation can hold as well for the case of adsorbed benzene on graphite, allowing the uncoupling between translations and rotations. The assumption of uncorrelated vibrations, translations and vibrations draws two major consequences. First of all, the operators $\mathbf{R}^\alpha$, $\mathbf{r}_j^\alpha$ and $\mathbf{u}_j^\alpha$ commute. Secondly, the averaged product of three independent functions is the product of their averages [81]:

$$\begin{aligned}&\langle \exp[-i\mathbf{Q}\cdot(\mathbf{R}^\alpha(t)-\mathbf{R}^\alpha(0))]\exp[i\mathbf{Q}\cdot(\mathbf{r}_j^\alpha(t)-\mathbf{r}_j^\alpha(0))]\exp[i\mathbf{Q}\cdot(\mathbf{u}_j^\alpha(t)-\mathbf{u}_j^\alpha(0))]\rangle = \\ &\langle \exp[-i\mathbf{Q}\cdot(\mathbf{R}^\alpha(t)-\mathbf{R}^\alpha(0))]\rangle \times \langle \exp[i\mathbf{Q}\cdot(\mathbf{r}_j^\alpha(t)-\mathbf{r}_j^\alpha(0))]\rangle \times \left\langle \exp[i\mathbf{Q}\cdot(\mathbf{u}_j^\alpha(t)-\mathbf{u}_j^\alpha(0))]\right\rangle .\end{aligned} \tag{4.20}$$

Thus, neglecting the correlations between translations, rotations and internal vibrations we can approximate the total incoherent ISF as the product of three functions accounting for the molecule translations, $I_{QENS,Tr}(\mathbf{Q},t)$, rotations, $I_{QENS,Rot}(\mathbf{Q},t)$, and internal vibrations $I_V(\mathbf{Q},t)$:

$$\begin{aligned}I_{QENS}(\mathbf{Q},t) &= \exp[-\left\langle \mathbf{u}_v^2\right\rangle Q^2] \times \frac{1}{N_{mol}}\sum_{\alpha=1}^{N_{mol}} \langle \exp[-i\mathbf{Q}\cdot(\mathbf{R}^\alpha(t)-\mathbf{R}^\alpha(0))]\rangle \times \\ &\quad \frac{1}{N_{at}}\sum_{j=1}^{N_{at}}\langle \exp[i\mathbf{Q}\cdot(\mathbf{r}_j^\alpha(t)-\mathbf{r}_j^\alpha(0))]\rangle \\ &= \exp[-\left\langle \mathbf{u}_v^2\right\rangle Q^2] \times I_{QENS,Tr}(\mathbf{Q},t) \times I_{QENS,Rot}(\mathbf{Q},t)\end{aligned} \tag{4.21}$$

In the quasi-elastic range, the internal vibration contribution to the scattering is well approximated by the Debye-Waller factor [56]. N_{mol} is the number of molecules in the system and N_{at} is the number of atoms per molecule. We can now treat each part of the ISF separately. The next paragraph assumes the approximated form of the ISF and focuses on the description of its rotational part arising from uniaxial rotations of the benzene molecule around its sixfold symmetry axis. There are two different kind of rotations to be discuss: continuous rotations and jump rotations.

Uniaxial rotations

If molecules are performing rotations around a definite symmetry axis, while they lie flat on the scattering plane, the momentum transfer vector **Q** (see Fig. 4.4) and the atoms positions vectors $\mathbf{r}_j$ are coplanar. We can, thus, expand

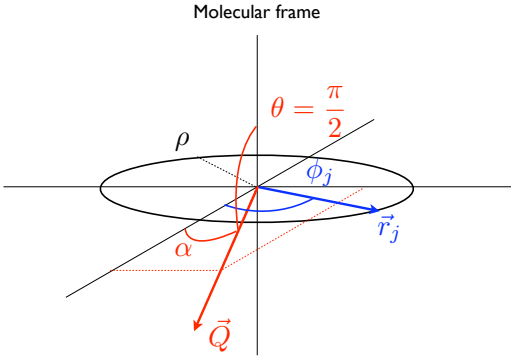

Figure 4.4: In plane geometry: the momentum transfer **Q** between the incoming and the scattered neutron is contained in the same plane on which molecules are lying flat on the substrate. The in plane geometry is obtained setting the incoming beam direction parallel to the macroscopic surfaces of the graphite disks in the sample holder, and measuring the scattered neutrons in the same plane.

the exponential function in terms of cylindrical Bessel functions [132]:

$$\exp[-i\mathbf{Q}\cdot\mathbf{r}_j(t)] = \exp[-iQ\rho\cos(\phi_j(t)-\gamma_\mathbf{Q})] = \sum_{n=-\infty}^{\infty} i^n J_n(-Q\rho)e^{in(\phi_j(t)-\gamma_\mathbf{Q})}, \tag{4.22}$$

where $\gamma_\mathbf{Q}$ is the direction of the momentum transfer vector **Q** with respect to the laboratory frame, $\phi_j(t)$ is the orientation of the molecule at time t and ρ is the radius of the molecule. Introducing Eq. 4.22 into Eq. 4.10, yields an expression for the rotational incoherent ISF:

$$I_{QENS,Rot}(\mathbf{Q},t) = \frac{1}{N_{at}}\sum_{j=1}^{N_{at}}\left\langle \sum_{n=-\infty}^{\infty} i^n J_n(-Q\rho)e^{in(\phi_j(t)-\gamma_\mathbf{Q})} \times \sum_{n'=-\infty}^{\infty} i^{n'} J_{n'}(-Q\rho)e^{in'(\phi_j(0)-\gamma_\mathbf{Q})}\right\rangle. \tag{4.23}$$

We can further integrate Eq. 4.23 over all the possible directions of the momentum transfer vector **Q**. This last step is useful to obtain the ISF associated to the scattering of rotating adsorbates on a *Papyex* substrate, which

does not present any preferential orientation of the graphite crystals in the xy plane [56, 68]. The integration on the angle $\gamma_{\mathbf{Q}}$ leads to[1] [56]:

$$I_{QENS,Rot}(Q,t) = \frac{1}{N_{at}} \sum_{j=1}^{N_{at}} \sum_{n=-\infty}^{\infty} J_n^2(Q\rho) \left\langle e^{in\Delta\phi_j(t))} \right\rangle \tag{4.24}$$

Note that in our case, the polar angle is fixed $\theta = \pi/2$ and the Bessel function depends only on the product of the moduli $Q\rho$. $\Delta\phi_j(t) = \phi_j(t) - \phi_j(0)$ stands for the angular displacement of atom j.

If molecules are subject to random and uncorrelated collisions, their angular velocity is randomized [133]. Moreover, the angular displacement is a random variable, whose change in time is due to a Gaussian stochastic process. Therefore, we can apply the cumulant expansion to the exponential functions of the angular displacement $\Delta\phi$ in Eq. 4.24 [100]. In addition, the angular velocity will be a Gaussian stochastic process [133] and the rotational analogue of the Van Hove self correlation function, $G(\phi(0), \phi(t))$, is a Gaussian distribution of the angular displacement $\Delta\phi$, according to the Doob theorem [134]. Thus, the Gaussian approximation holds and the cumulant expansion is reduced to the second term. As a result, the rotational ISF is a function of the mean square angular displacement $\left\langle \Delta\phi^2(t) \right\rangle$:

$$I_{QENS,Rot}(Q,t) \simeq \sum_{n=-\infty}^{\infty} J_n^2(Q\rho) \exp\left[-\frac{n^2}{2} \left\langle \Delta\phi^2(t) \right\rangle \right]. \tag{4.25}$$

Eq. 4.25 yields the analogous dependence of the ISF on the angular MSD, to the one that Eq. 4.11 gives for the translational ISF on the MSD. The angular MSD is related to the angular velocity correlation function in a similar way in which the MSD, $\left\langle |\Delta\mathbf{r}|^2 \right\rangle$, is connected to the translational velocity correlation function $\langle \mathbf{v}(t) \cdot \mathbf{v}(0) \rangle$ (see Chap. 2):

$$\Delta\phi_j(t) = \int_0^t dt' \omega_\alpha(t') \Rightarrow \left\langle \Delta\phi^2(t) \right\rangle = \left\langle \left(\int_0^t dt' \omega_\alpha(t') \right)^2 \right\rangle = 2 \int_0^t (t - t') \left\langle \omega_\alpha(0) \cdot \omega_\alpha(t) \right\rangle, \tag{4.26}$$

where ω_α is the angular velocity of molecule α. Following the Doob theorem, if the angular velocity is a stochastic process, its correlation function is an exponential decay [57, 133, 134]:

$$C_\omega(t') = \frac{\left\langle \omega_\alpha(0) \cdot \omega_\alpha(t) \right\rangle}{\left\langle |\omega(0)_\alpha|^2 \right\rangle} = \left\langle |\omega(0)_\alpha|^2 \right\rangle \exp\left(-\eta_{rot} t \right). \tag{4.27}$$

[1] The integration over all the directions of $\mathbf{Q}$ gives rise to delta functions, defined in its integral form:

$$\int_0^{2\pi} d\gamma_{\mathbf{Q}} e^{i(n+n')\gamma_{\mathbf{Q}}} = \delta_{n,-n'}.$$

where $\eta_{rot} = 1/\tau_\omega$ is the rotational friction parameter [133]. Making use of the same arguments than in the section 2.2 of Chap. 2 and following Ref. [57], we deduce a very general form of the rotational ISF by inserting Eq. 4.26 into Eq. 4.25:

$$\begin{aligned} I_{QENS,Rot}(Q,t) &\simeq \sum_{n=-\infty}^{\infty} J_n^2(Q\rho) \exp\left[-n^2 \int_0^t (t-t') \left\langle \omega_\alpha(0) \cdot \omega_\alpha(t) \right\rangle\right] \\ &= \sum_{n=-\infty}^{\infty} J_n^2(Q\rho) \exp\left[-\chi_n^2 (e^{-\eta_{rot} t} + \eta_{rot} t - 1)\right], \end{aligned} \tag{4.28}$$

where we define a *rotational shape parameter* equivalent to the shape parameter in Ref. [57], $\chi^2(Q)$:

$$\chi_n^2 = \frac{\left\langle \omega^2 \right\rangle}{\eta_{rot}^2} n^2, \tag{4.29}$$

but depending on the index of the expansion n and not on the momentum transfer modulus, Q.

As was explained in sec. 2.2 of Chap. 2. and in Ref. [57] for the translational ISF, Eq. 4.28 yields a rotational ISF whose profile in time can be tuned by the value of the rotational friction parameter, η_{rot}. In the *high friction regime*, the rotational ISF profile tends to a summation of single exponential decays:

$$I_{QENS,Rot}(Q,t) = \sum_{n=-\infty}^{\infty} J_n^2(Q\rho) \exp\left[-\frac{t}{\tau_n}\right]; \; \frac{1}{\tau_n} = \chi_n^2 \eta_{rot} = \frac{\left\langle \omega^2 \right\rangle n^2}{\eta_{rot}} \tag{4.30}$$

The equipartition theorem provides a mean square angular velocity, $\left\langle \omega^2 \right\rangle = 1/I\beta$, such that the time constant reads:

$$\frac{1}{\tau_n} = \frac{k_B T n^2}{I \eta_{rot}} = D_r n^2, \tag{4.31}$$

where D_r is the rotational diffusion coefficient [73] and I is the moment of inertia. Note that the same ISF is obtained in Refs. [56, 120, 132], by solving the master equation for uniaxial rotational diffusion [135]. In the energy transfer domain, the corresponding high friction SF is a summation of Lorentzian functions:

$$S_{QENS,Rot}(Q,\Delta E) = \frac{1}{\pi} \sum_{n=-\infty}^{\infty} J_n^2(Q\rho) \frac{\hbar/\tau_n}{(\hbar/\tau_n)^2 + (\Delta E)^2}, \tag{4.32}$$

Conversely in the *low friction regime*, the ISF in Eq. 4.28 becomes a summation

of Gaussian shaped decays:

$$I_{QENS,Rot}(Q,t) = \sum_{n=-\infty}^{\infty} J_n^2(Q\rho) \exp\left[-\frac{\langle\omega^2\rangle\, n^2}{2} t^2\right]; \Gamma_n = \sqrt{2\ln 2\,\langle\omega^2\rangle} n. \tag{4.33}$$

The resulting SF is a summation of Gaussian functions:

$$S_{QENS,Rot}(Q,\Delta E) = \sum_{n=-\infty}^{\infty} J_n^2(Q\rho) \sqrt{\frac{2\ln 2}{4\pi\hbar^2\Gamma_n}} \exp\left[-\frac{\Delta E^2}{4\hbar^2\Gamma_n}\right]. \tag{4.34}$$

Eq. 4.34 should be compared with the free rotational SF developed in Ref. [59] . However, we only consider uniaxial rotations, whereas Ref. [59] treats three dimensional rotations. Hence, the partial wave expansion, the Eq. 40 of Ref. [59], is the equivalent to our expansion of the exponential functions in terms of first kind Bessel functions in Eq. 4.23. Furthermore, uniaxial rotations allows us to use the one dimensional Maxwell-Boltzmann distribution of angular velocities which is a single Gaussian function $\Phi(\omega) \propto \exp(-I\omega^2/2\beta)$. In contrast, three dimensional Maxwell-Boltzmann distribution, $\Phi(\omega) \propto \omega^2 \exp(-I\omega^2/2\beta)$, is required for rotations in 3-d space [133]. We believe that this explains the main differences between the SF in Eq. 4.34 and the partial SFs in Eqs. 50 and 53 of Ref. [59].

To sum up, the ISF and SF profiles produced by free uniaxial rotational diffusion is an infinite summation of terms. Each one of the elements in the sum is weighted by a squared Bessel function of the first kind and order n, $J_n(Q\rho)$, depending on the product of the momentum transfer modulus Q and the radius of the molecule, ρ. Fig. 4.5 displays squared Bessel functions of the first kind, for orders ranging from $n = 0$ to $n = 6$. The term associated to $n = 0$ corresponds to the case in which there are no rotations. The corresponding ISF is a constant and, accordingly, the profile in energy is a delta function, $\delta(\Delta E)$. The remaining indexes $n > 0$ are can be understood as the modulus of the angular momentum, which for uniaxial rotations is parallel to the axis of rotations and is reduced to its z component. We observe that for increasing values of n, the intensity of the corresponding terms in the summation is shifted towards larger Q values. This is the mathematical reason explaining why rotations are not visible at low Q but become the dominant scattering contribution at high values of Q, matching the diameter, 2ρ, of the molecules. We also observe that there is a specific value of the momentum transfer, at $Q\rho \sim 1$ Å^{-1} for which the zero order Bessel function reaches its minimum. At this particular value of the momentum transfer, corresponding to the inverse of the molecule radius, only the terms weighted by higher order Bessel function contribute to the scattering profile, and thus, the effect of rotations on the quasi-elastic profile can be directly analyzed. The last comment

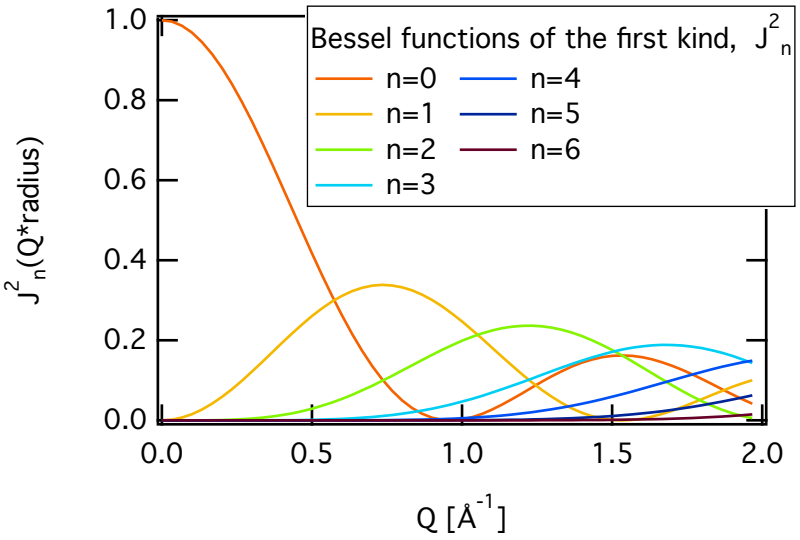

Figure 4.5: Bessel functions of first kind and n order squared, as a function of the product between the momentum transfer and the radius of the molecule. The radius of a benzene molecule is 2.5 Å [119].

concerns the normalization condition. Since Eqs. 4.32 and 4.32 to 4.34 should be normalized, the summation of squared Bessel functions should converge: $\sum_{n=-\infty}^{\infty} J_n^2(Q\rho) = 1$. On the contrary, the quasi-elastic broadening, HWHM, of each term is independent of the momentum transfer. It only depends on the index n of the expansion. But, the total SF's quasi-elastic broadening depends on Q, since $S_{QENS,Rot}(Q, \Delta E)$ is a summation of functions with varying HWHM and whose amplitudes, the Bessel functions, are functions of Q [132]. The ideal model would consist in the direct application of Eq. 4.28 allowing the extraction of a rotational friction parameter, without any additional assumption. Unfortunately, this is not possible, because the Fourier transform of Eq. 4.28 is written in terms of complete and uncompleted Gamma functions [57]. Such a SF is very difficult to handle and to use for fitting purposes. Furthermore we often need to take their asymptotic behavior. The following models combine the molecule's rotational and translational motion in the two extreme cases of the diffusive regime: very high and very low friction. We start from the factorized form of the quasi-elastic ISF in Eq. 4.21, and we adopt single Lorentzian or Gaussian functions for describing the diffusion of the molecular CoM (translations) and summations of Lorentzians or Gaussians (like in Eqs. 4.32 and 4.34) to account for the rotations. Nevertheless, the addition of more quasi-elastic lines increases the number of fitting parameters. It is, hence, desirable to link together the new fitting variables in order to min-

imize the number of free parameters during the fitting. Unfortunately, this is not always possible and models can fail because there are too many free fitting variables.

Model 3 The third model describes the high friction limit of the ISF, as written in Eq. 4.30, when translations and rotations are dumped because of the frictional coupling of the adsorbates with the substrate or with the neighboring molecules. It assumes a single exponential decays for describing the scattering due to translations and a summation of Lorentzian functions standing for the rotational contribution to the ISF:

$$I_{QENS,model3}(Q,t) = \sum_{n=-\infty}^{\infty} J_n^2(Q\rho) \exp\left[-\left(\frac{1}{\tau(Q)} + \frac{1}{\tau_n}\right) t\right] \tag{4.35}$$

The term $n = 0$ indexes the purely translational motion contribution, while the other terms with $n > 1$ mix translations and rotations. The total time constant of the each of the terms in the sum is the summation of the time constant related with translations $1/\tau(Q)$ and a time constant related with rotations, $1/\tau_n$, labelled with the index of the summation n. The corresponding quasi-elastic SF is a summation of Lorentzian functions:

$$S_{QENS,model3}(Q,\Delta E) = \frac{1}{\pi} \sum_{n=-\infty}^{\infty} J_n^2(Q\rho) \frac{\hbar(1/\tau(Q) + 1/\tau_n)}{(\hbar(1/\tau(Q) + 1/\tau_n))^2 + (\Delta E)^2}, \tag{4.36}$$

The total fitting function is:

$$S_{model3}(Q,\Delta E) = S_{res}(Q,\Delta E) \otimes \left\{ y_0 + A_{el}(Q)\delta(\Delta E) + A_{QENS}(Q) \frac{1}{\pi} \sum_{n=-\infty}^{\infty} J_n^2(Q\rho) \frac{\hbar(1/\tau(Q) + 1/\tau_n)}{(\hbar(1/\tau(Q) + 1/\tau_n))^2 + (\Delta E)^2} \right\}. \tag{4.37}$$

The free parameters of this model are: the background, the elastic and quasi-elastic amplitudes and the translational and rotational time constants. The two quasi-elastic broadenings for translations $1/\tau(Q)$ and rotations $1/\tau_n$ need to be connected and reduced to a single parameter. We relate them through the model of binary collisions between hard disks (adapted from the original model of hard spheres in Refs. [103, 136]). The rotational and translational friction in a system of hard disks, colliding randomly with each other reads:

$$\begin{aligned} \eta_{smooth}(\theta,T)|_{\lambda=0} &= \frac{d}{A}\left(\frac{2\pi}{\mu}\right)^{1/2} \times \theta\sqrt{k_B T} \\ \eta_{trans}(\theta,T) &= \frac{\kappa}{\kappa+1}\left\{\frac{3}{2} + \frac{1}{\kappa}\right\} \eta_{smooth}(\theta,T) \\ \eta_{rot}(\theta,T) &= \left(\frac{1}{\kappa+1}\right) \eta_{smooth}(\theta,T) \end{aligned} \tag{4.38}$$

The first friction parameter, $\eta_{smooth}(\theta, T)$ is related to smooth collisions where there is only a transfer in linear momentum between the two hard disks. Its inverse, $\eta_{smooth}^{-1} = \tau_E$, is the Enskog relaxation time [103] whose expression we adapt to the case of hard disks. The detail of the calculations for the friction parameter of hard disks collisions is reported in Annex ?. We find that for disks, $\eta_{smooth} = \tau_E^{-1}$ depends on CoM distance of the two disks when they collide $d = \rho_1 + \rho_2$, the area of a substrate unit cell A, the reduced mass of the system of the two disks $\mu = m_1 m_2/(m_1 + m_2)$, coverage θ and temperature T. The same dependence of the smooth friction with coverage and temperature is found in Ref. [57] which deals with the diffusion of atoms on the surface. The actual translational and rotational friction parameters are proportional to the smooth friction and depend on the geometry of the benzene. In particular, the term $\kappa = 2I/\mu d^2$ contains the moment of inertia - reduced mass ratio which determines the part of kinetic energy converted into angular kinetic energy during the collision. Finally, the HWHM of the Lorentzian functions in Eq. 4.37 is:

$$\frac{1}{\tau(Q)} + \frac{1}{\tau_n} = \frac{k_B T}{m\eta_{trans}} Q^2 + \frac{k_B T}{I\eta_{rot}} n^2 = \left[\frac{2}{3\kappa + 2}\frac{Q^2}{m} + \frac{n^2}{I}\right](\kappa+1)\left(\frac{k_B T}{\eta_{smooth}(\theta, T)}\right). \tag{4.39}$$

The two fitting parameters $1/\tau(Q)$ and $1/\tau_n$ are reduced to a single one: $1/\eta_{smooth}(\theta, T)$. The top panel of Fig. **??** summarizes the fitting to the 0.5 ML data. We also include all the single terms in the summation in Eq. 4.36 at low (left panel) and high (right panel) momentum transfer value. We observe that at low Q only the Lorentzian functions corresponding the small indexes $n = 0$ (only translations), $n = 1$ and $n = 2$ have a significant contribution. Conversely, in the high Q range, the Lorentzian functions for $n = 3$, $n = 4$ and $n = 5$ come into play. Finally, the intensity of the Lorentzian profiles for indexes above $n > 5$ is negligible. Hence, the summation in Eq. 4.36 can be safely truncated at $n = 5$.

Model 4 The fourth model considers the low friction regime where translations and rotations are performed free. Hence the quasi-elastic ISF is consists in Gaussian functions of time for translations and rotations:

$$I_{QENS,model4}(Q, t) = \sum_{n=-\infty}^{\infty} J_n^2(Q\rho) \exp\left[-\left(\Gamma(Q) + \Gamma_n\right) t^2\right], \tag{4.40}$$

which gives rise to a summation of Gaussian functions of the energy transfer:

$$S_{QENS,model4}(Q, \Delta E) = \sum_{n=-\infty}^{\infty} J_n^2(Q\rho) \sqrt{\frac{1}{4\pi\hbar^2(\Gamma(Q) + \Gamma_n)}} \exp\left[-\frac{\Delta E^2}{4\hbar^2(\Gamma(Q) + \Gamma_n)}\right]. \tag{4.41}$$

As for the previous model, the term $n = 0$ labels the purely translational SF, while the other indexes correspond to the mixture of translations and rotations. The total fitting fucntion

$$S_{model4}(Q,\Delta E) = S_{res}(Q,\Delta E) \otimes \{y_0 + A_{el}(Q)\delta(\Delta E)\} + S_{res}(Q,\Delta E) \otimes \left\{ A_{QENS}(Q) \sum_{n=-\infty}^{\infty} J_n^2(Q\rho) \sqrt{\frac{2\ln 2}{\pi}} \frac{1}{(\Gamma(Q)+\Gamma_n)} \exp\left[-\frac{\Delta E^2}{(\Gamma(Q)+\Gamma_n)^2} \right] \right\}. \tag{4.42}$$

In this model, the free parameters are: background, elastic and quasi-elastic amplitudes and the HWHM of the Gaussian terms. The latter reads:

$$\Gamma(Q) + \Gamma_n = \hbar\sqrt{\ln 2\,(\langle v^2\rangle\, Q^2 + 2\,\langle\omega^2\rangle\, n^2)}. \tag{4.43}$$

We can easily relate the mean squared velocity of a single molecule $\langle v^2\rangle$ and its mean square angular velocity $\langle\omega^2\rangle$ via the equipartition theorem:

$$\langle v^2\rangle = \frac{2}{m\beta},\ \ \langle\omega^2\rangle = \frac{1}{I\beta} = \frac{2}{m\rho^2\beta} \Rightarrow \langle\omega^2\rangle = \frac{\langle v^2\rangle}{\rho^2}. \tag{4.44}$$

where the moment of inertia I is calculated by identifying the benzene molecule of radius ρ to a disk, $I = m\rho^2/2$. Hence, determining the mean square velocity is equivalent to evaluate the quasi-elastic broadening which reads:

$$\Gamma(Q) + \Gamma_n = \hbar\sqrt{\ln 2\left(Q^2 + \frac{2}{\rho^2}n^2\right)\langle v^2\rangle}. \tag{4.45}$$

The bottom panel of Fig. 4.6 shows the fitting of the 0.5 ML data to model 4. We also plot the elastic profile, the quasi-elastic profile which is the summation of Gausssians and each one of the terms contributing to this summation. We observe that the Gaussian functions corresponding to indexes above 5, $n > 5$, have a weak intensity and do not contribute significantly to the total quasi-elastic profile.

Jump rotational diffusion

Molecules are not always free to move: under certain condition energy barriers rise on the potential energy surface and the motion is severely hindered. The dynamics is no longer continuous but should be performed in a stepwise fashion. The Chudley-Elliot model treats translational jump diffusion [107]. The rotational jump diffusion is developed in Ref. [137]. The goal is to deduce the ISF produced by a N-fold symmetry molecule performing $2\pi/N$ rotational jumps on a circle. This model suits perfectly the benzene molecule reorientations around its $\pi/6$ symmetry axis.

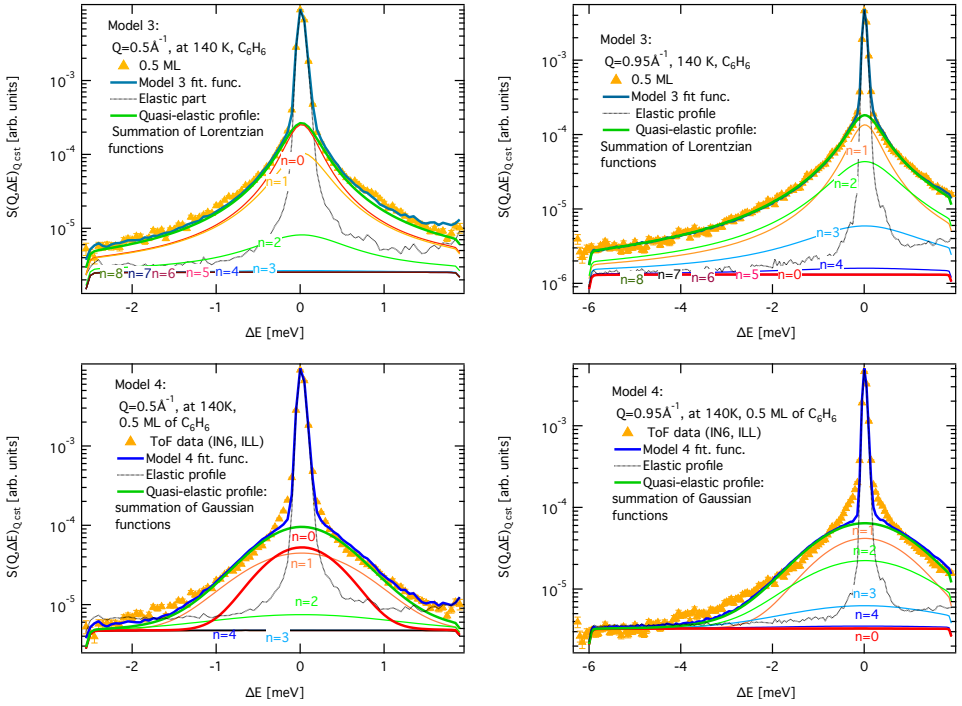

Figure 4.6: Fitting of the 0.5 ML data to models 3 and 4. We include the different contributions to the energy profile: the elastic profile (black dotted line), the quasi-elastic profile (green solid line) and the different terms contributing to the quasi-elastic profile. At $Q = 0.95^{-1}$, the purely translational term, $n = 0$ vanishes and the quasi-elastic profile results from the convolution of the rotational and the translational profiles.

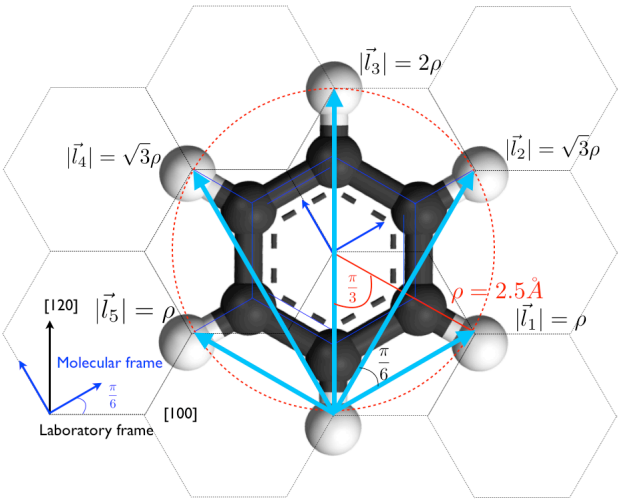

Figure 4.7: Benzene reorientations around its six-fold symmetry axis, provokes the jump of protons from their original site to a different site among the six available sites on the circle.

We now summarize the jump rotation model. In a similar way than the Chudley-Elliot treats jump translations (see Chap. 2), the probability $p(r_j^{(\mu)}, t)$ of finding the j-th atom of the molecule at the μ-th site of the circle at a certain time t follows a master equation of the form [138]:

$$\frac{\partial}{\partial t} p(r_j^{(\mu)}, t) = \sum_{\nu}^{N} \frac{1}{\tau_{\mu\nu}} \left[p(r_j^{(\nu)}, t) - p(r_j^{(\mu)}, t) \right] \tag{4.46}$$

Solving Eq. 4.46 requires the knowledge of the probabilities $\{p(r_j^{(\nu)}, t)\}_{\nu}^{N}$ for the rest of the sites, since the probability to find a particle in site μ is coupled to the probabilities of finding the particle at the sites $\mu-1$ or $\mu+1$. The master equation is very similar to the equations of motions of the linear chain [97,138], except that in the latter, the atom displacement $\mathbf{u}$ is subject to a double derivative of time whereas for the jump dynamics, there is a single derivative of time. In both situations, we need to solve a N coupled equations system, which can be casted, for jump rotations, into a matrix equation of the form [138,139]:

$$\frac{d}{dt} \mathbf{P}_j(t) = [\mathbf{M}]\, \mathbf{P}_j(t) \tag{4.47}$$

We also adopt the Born-Von Karman cyclic boundary conditions [138], where the atom position vector satisfies: $\mathbf{r}_j^{\mu} = \mathbf{r}_j^{\mu+N}$. $\mathbf{P}_j(t)$ is a vector whose coordinates are the different probabilities $\{p(r_j^{(\nu)}, t)\}_{\nu}^{N}$ of finding the atom j at the different circle sites, and $[\mathbf{M}]$ is the $N \times N$ jump matrix. If we restrict

the the jump to first neighboring sites and we assume that clockwise and anti-clockwise are equivalent directions so that they are weighted by the same jump rate, $1/\tau$, the terms of the jump matrix read as follows [138]:

$$[\mathbf{M}]_{\mu\nu} = \frac{1}{\tau}\left(\delta_{\mu\nu+1} + \delta_{\mu\nu-1} - 2\delta_{\mu\nu}\right). \tag{4.48}$$

The general solution of Eq. 4.47 stems from conventional algebraic methods, and in particular, from the diagonalization of the jump matrix in the basis set of its eigenfunctions [137,138]. The similitude between the problem of phonons in a linear chain of atoms and the jump rotational diffusion between neighboring sites is useful to find the corresponding eigenvectors and eigenvalues of the jump matrix [97]:

$$\mathbf{P}_j(t) = [\mathbf{V}]\,[\boldsymbol{\Lambda}]\,[\mathbf{V}]^{+}\,\mathbf{P}_j(0) \Rightarrow \quad \begin{cases} [\mathbf{V}]_{\alpha\mu} = \exp\left(i\dfrac{2\pi}{N}\alpha\mu\right) \\ [\boldsymbol{\Lambda}]_{\mu\nu} = e^{\lambda_\mu t}\delta_{\mu\nu} \\ \lambda_\mu = -4\dfrac{1}{\tau}\sin^2\left(\dfrac{\pi}{N}\mu\right) \end{cases}, \tag{4.49}$$

where $[\mathbf{V}]$ is the matrix of the set of eigenvectors, $[\boldsymbol{\Lambda}]$ is the resulting diagonal jump matrix and λ_μ are the corresponding eigenvalues [138]. We easily deduce the conditioned probability, $p(r_j^\mu, r_j^\nu(0), t)$, of finding atom j in site μ at time t if it was lying at site ν at $t = 0$ by taking the real part of Eq. 4.49:

$$\begin{aligned} p(r_j^\mu, r_j^\nu(0), t) &= \mathrm{Re}\left[\sum_{\alpha=1}^{N} \exp(\lambda_\alpha t)\exp\left(i\frac{2\pi}{N}\alpha(\mu-\nu)\right)p(r_j^\nu, 0)\right] \\ &= \sum_{\alpha=1}^{N} \exp(\lambda_\alpha t)\cos\left(\frac{2\pi}{N}\alpha(\mu-\nu)\right)p(r_j^\nu, 0) \end{aligned} \tag{4.50}$$

The same result is given in Ref. [137] but with a different formulation: it is the probability that the j atoms reaches site μ after $n = t/\Delta t$ steps starting from site ν at $t = 0$, when the step duration, Δt, tends to zero (instant jumps) and all the initial sites are equally probable, $p(r_j^\nu, 0) = 1/N$. The Van Hove self-correlation function $G_s(r_j^\mu, t)$, defined as the probability of finding an atom in the site μ at time t if it was in the site ν at $t = 0$, averaged over all the possible initial site (assuming equal initial probabilities for each one of them) [140] is a function of the conditioned probability:

$$G_s(r_j^\mu, t) = \frac{1}{N}\sum_{\nu=1}^{N} p(r_j^\mu, r_j^\nu(0), t) = \frac{1}{N^2}\sum_{\alpha=1}^{N} \exp(\lambda_\alpha t)\cos\left(\frac{2\pi}{N}\alpha(\mu-\nu)\right) \tag{4.51}$$

The ISF is readily find by Fourier transforming in space Eq. 4.51 and reads [137]:

$$I_{QENS,rot}(\mathbf{Q},t) = \frac{1}{N}\sum_{\nu=1}^{N} p(r_j^N, r_j^\nu(0), t)\exp[i\mathbf{Q}\cdot(\mathbf{r_N}-\mathbf{r}_\nu)]. \tag{4.52}$$

As we have done for continuous rotations, the exponential term $\exp[i\mathbf{Q}\cdot(\mathbf{r_N}-\mathbf{r}_\nu)]$ can be expanded according to Eq. 4.23 and integrated over all the possible orientations of $\mathbf{Q}$ in the plane of rotations, yielding a Bessel function of the first kind and index $n=0$. Thus, the theoretical ISF reads:

$$I_{QENS,rot}(\mathbf{Q},t) = \frac{2\pi}{N}\sum_{\alpha=1}^{N} A_\alpha(Q)\exp(\lambda_\alpha t) \tag{4.53}$$

where the amplitude of each single exponential decay is shown in Fig. 4.8 and reads:

$$A_\alpha(Q) = \frac{1}{N}\sum_{\nu=1}^{N} J_0\left[2Q\rho\sin\left(\frac{\pi\nu}{N}\right)\right]\cos\left(\frac{2\pi}{N}\alpha(N-\nu)\right). \tag{4.54}$$

Note that in Ref. [137] the average over all the direction of momentum transfer

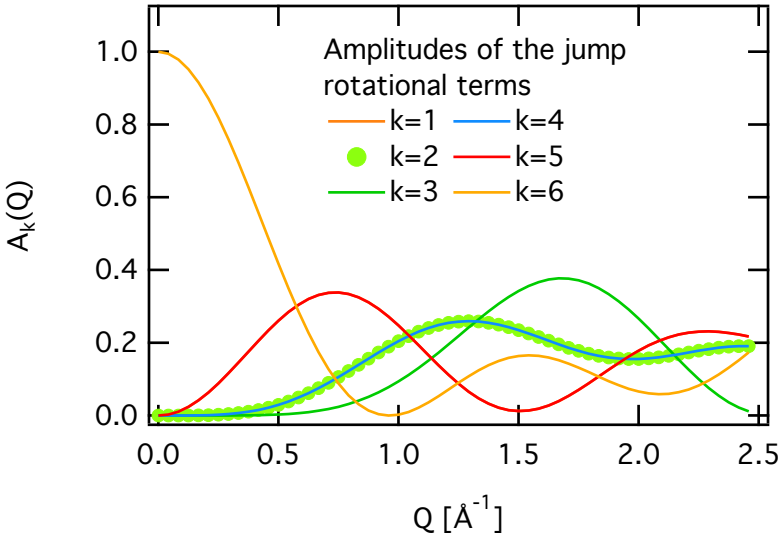

Figure 4.8: Amplitudes of the terms in the summation of the ISF arising from 6-fold jump rotations.

is performed in three dimension in order to study powder samples. In our experimental set-up, the polar angle, called β in Ref. [137], is fixed to $\pi/2$ (the

incoming beam of neutrons is parallel to macroscopic surface of the *Papyex substrate*). Finally, the Fourier transformation in time of Eq. 4.55, yields the incoherent rotational SF for jump rotational motion:

$$S_{QENS,rot}(\mathbf{Q},\Delta E) = \sum_{\alpha=1}^{N} A_\alpha(Q)\frac{\hbar\lambda_\alpha}{[\hbar\lambda_\alpha]^2+(\Delta E)^2} \tag{4.55}$$

which is a summation of N Lorentzian functions. The last comment is that in the jump rotational model, the term which does not give any quasi-elastic contribution is the one related to $\alpha = N$ (see Eq. 4.49). Thus, the effect of rotations dominates at $Q \sim 1^{-1}$, where the amplitude A_N reaches its minimum (see Fig. 4.8)

Model 5 The last model that we propose combines jump rotations with translations in the high friction regime and producing a Lorentzian shaped quasi-elastic profile. It reads as follows:

$$I_{QENS,model5}(\mathbf{Q},t) = \frac{2\pi}{N}A_N(Q)\exp\left[-\frac{t}{\tau_T(Q)}\right]+\frac{2\pi}{N}\sum_{\alpha=1}^{N-1}A_\alpha(Q)\exp\left[\left(\frac{1}{\tau(Q)}+\frac{1}{\tau_\kappa}\right)t\right] \tag{4.56}$$

where we replace $\lambda^{(\kappa)}$, by its inverse, $1/\tau_\kappa$ and $1/\tau_T(Q)$ represents the time constant associated to translations. We recall that, in contrast with the previous models, it is the term corresponding to the index $\alpha = N$ which stands for the purely translational contribution. The corresponding SF is a summation of Lorentzian functions:

$$S_{QENS,model5}(\mathbf{Q},\Delta E) = \frac{2\pi}{N}A_N(Q)\frac{\hbar(1/\tau_T(Q))}{[\hbar(1/\tau(Q))]^2+(\Delta E)^2} + \frac{2\pi}{N}\sum_{\alpha=1}^{N-1}A_\alpha(Q)\frac{\hbar(1/\tau_T(Q)+1/\tau_\kappa)}{[\hbar(1/\tau_T(Q)+1/\tau_\kappa)]^2+(\Delta$$

(4.57)

The convolution between the resolution function and the theoretical SF function provides the final fitting function:

$$S_{model5}(Q,\Delta E) = S_{res}(Q,\Delta E)\otimes\{y_0 + A_{el}(Q)\delta(\Delta E) + A_{QENS}(Q)S_{QENS,model6}(\mathbf{Q},\Delta E)\}\,. \tag{4.58}$$

One of the weakness of the model is that we do not know how to connect the translational and the jump rotational times constants, $1/\tau_T(Q)$ and $1\tau_k$ respectively. Thus, we need to fix at least one of the variables, according to other fitting (the Lorentzian broadening extracted from model 3, for instance). The special fitting parameter of this model is the jump rate, $1/\tau$ which quantifies the frequency of jumps at a given temperature. It should be Q independent.

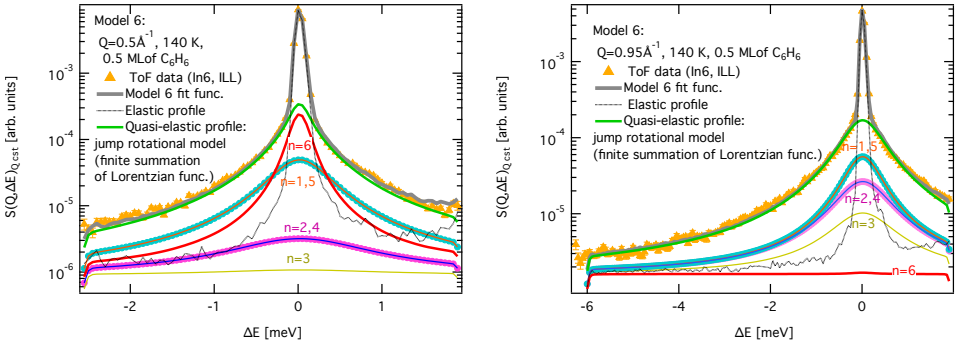

Figure 4.9: Fitting of the 0.5 ML data to model 5. We include the different contributions: the elastic part given by the convolution of the resolution function to a delta function centered at $\Delta E = 0$ meV (black dotted line), the total quasi-elastic profile (green solid line) and the total function (grey solid line). We plot the model and the data at low Q value, 0.5 Å^{-1} in the left panel and at high Q value in the right panel.

Dicussion of models 3, 4 and 5 We discuss now the results of the fitting of the three precedent models. Fig. 4.10 compares the fitting to the models 3, 4, 5 and 6 of the 0.1 ML and 1.0 ML data at140K and for two values of the momentum transfer: 0.5 Å^{-1} and 0.95 Å^{-1}. We recall that at the latter value for the momentum transfer, the effect of translations appears only convoluted with the quasi-elastic profile of translations. The 0.1 ML energy profile can be fitted with the four models, even though at high Q models 3 and 6 fit better the low energy transfer range. On the contrary, in the 1.0 ML data the differences between models are more pronounced. Model 4 nor 5 provide a good fitted profile. The deviation between the fitted and the experimental profile are visible at high Q. On the other hand, models 3 and 6 seem better suited and give rise to a very similar fitted profile. The 0.5 ML data are also displayed and fitted to the theoretical models in Figs. 4.6 and 4.9. By far, the best fitting is achieved with models 3 and 6. Thus, in the medium/high coverage regime, rotational motion is better accounted with Lorentzian rather than with Gaussian shaped profiles.

Fig. 4.11 summarizes the fitting results for 0.1 ML and 1.0 ML in the thermal range from 60K to 140K. At low temperature, the 0.1 ML data can not be fitted by model 3. But its shape is still ambiguous and only the dependence of the fitted parameters with the momentum transfer can determinate the best model. The 1.0 ML data, displays mainly a Lorentzian line shape and model 3 and 6 give a better fit than models 4 and 5. In conclusion, the rotational and the translational scattering functions in the high coverage regime display a Lorentzian profile.

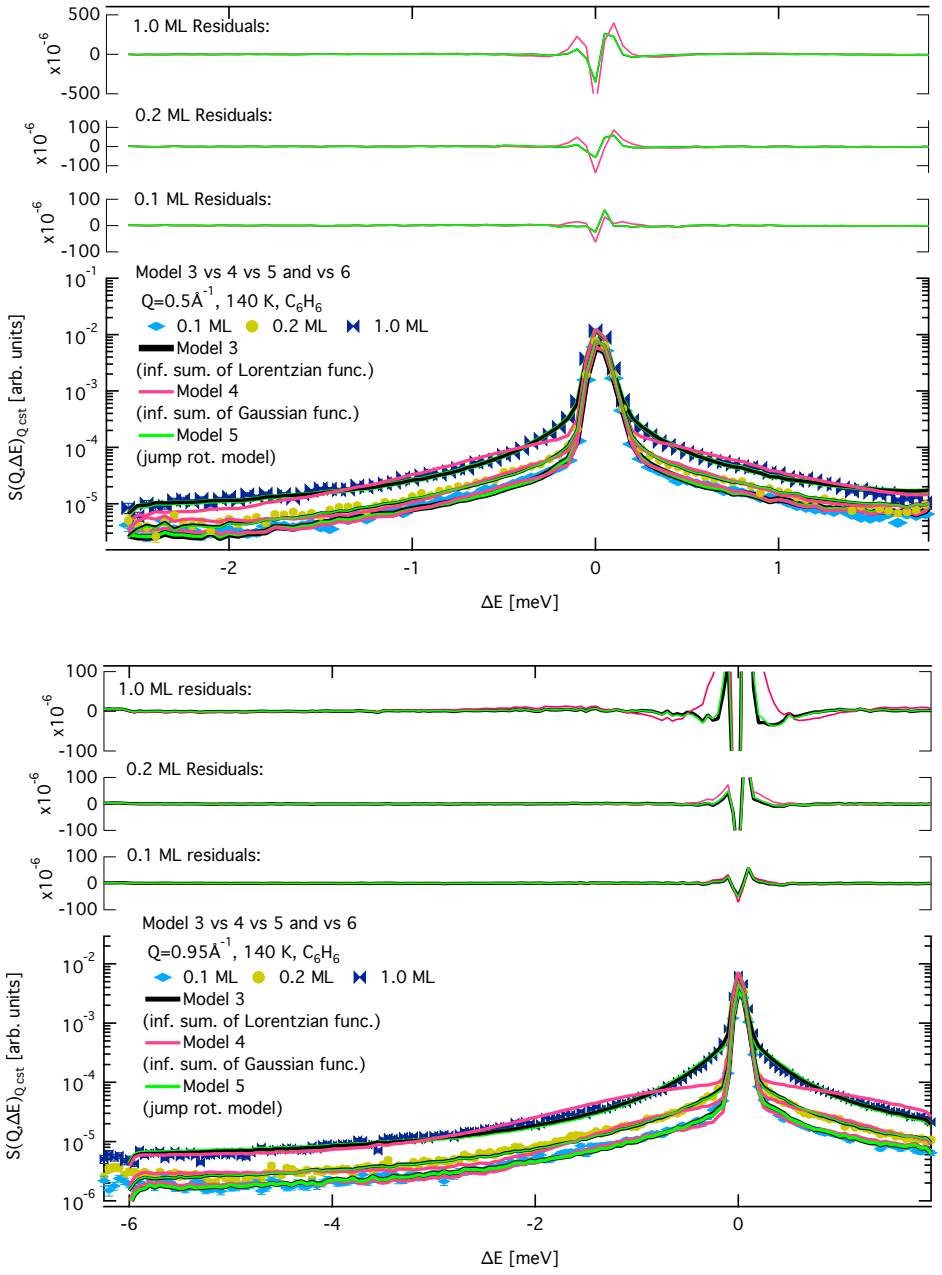

Figure 4.10: Fitting of the experimental data of 0.1 ML, 0.2 ML and 1.0 ML h-benzene coverage at low Q (top) and high Q (bottom) value with models 3, 4 and 5.

Table 4.3: Goodness of the fit , χ^2 parameter divided by the number of fitted points, resulting from the fitting of all the data set at 140 K to models 3, 4 and 5.

	Q=0.5 Å^{-1}			Q=0.95 Å^{-1}		
	Model 3	Model 4	Model 5	Model 3	Model 4	Model 5
0.1 ML	3.07	2.91	2.62	2.19	3.62	2.79
0.2 ML	2.67	7.40	4.45	3.57	10.33	6.88
0.5 ML	5.95	41.64	7.86	7.37	42.14	32.27
1.0 ML	8.19	62.21	11.82	10.35	78.38	33.47

Table 4.4: Goodness of the fit , χ^2 parameter divided by the number of fitted points, resulting from the fitting of 0.1 ML and 0.2 ML coverages in the whole thermal range to models 3, 4 and 5 for $Q = 0.95$ Å^{-1}.

	0.1 ML			0.2 ML		
	Model 3	Model 4	Model 5	Model 3	Model 4	Model 5
60 K	2.20	2.53	2.35	3.04	4.96	4.12
100 K	2.52	2.93	2.59	4.33	10.46	7.41
140 K	2.19	3.62	2.79	3.57	10.33	6.88

To sum up, we observe that the addition of a rotational contribution has improved the fitting results at medium and high coverage. This result is in contrast with the study on deuterated benzene reported in Ref. [45], where a single exponential decay gave a good fitting of the 0.5 ML data. Furthermore, their quasi-elastic profiles have a marked Lorentzian character. The question is now wether rotations are performed in a continuous or in a jump stepwise fashion. The analysis of the fitted parameters, the HWHM of the translational term and the jump rate will help to elucidate which is the most realistic description The low coverage data display an ambiguous profile and could already be fitted with a single quasi-elastic profile. All the models except model 3 at low temperatures give a reasonable fit. Hence, we should analyze the fitted parameters in order to decide which is the best theoretical description. On the contrary,

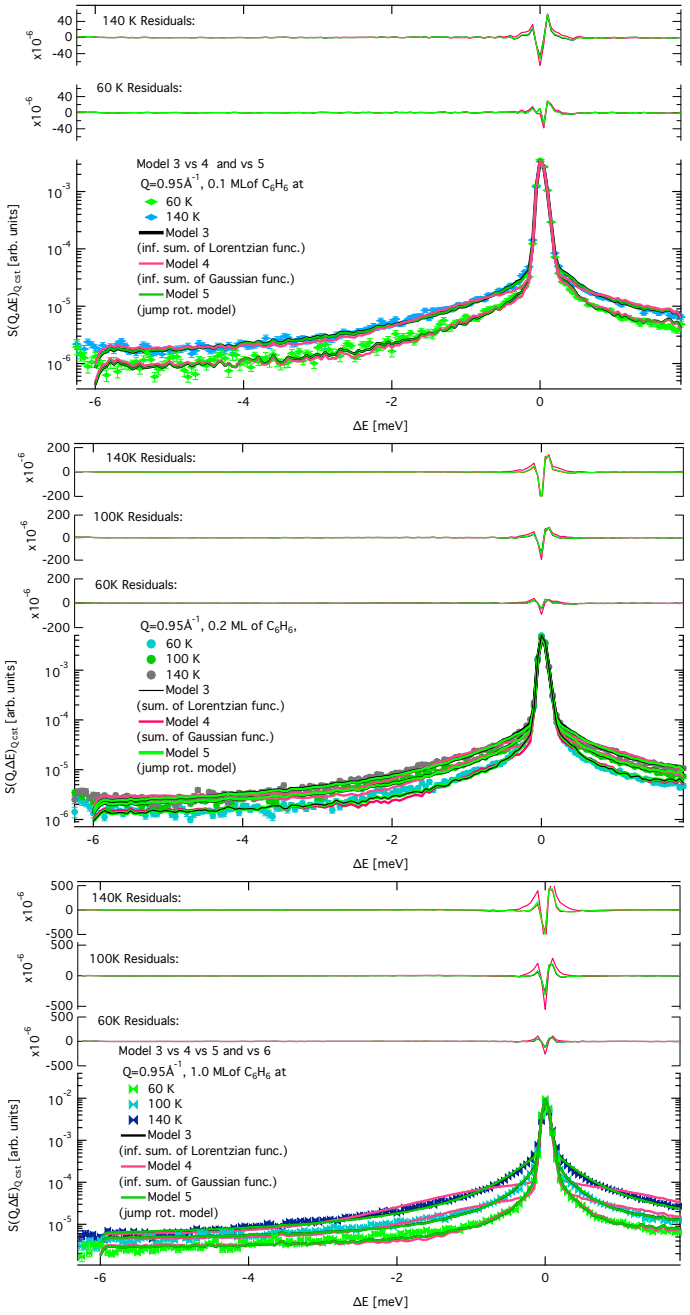

Figure 4.11: Fitting of the experimental data of 0.1 ML (upper, 0.2 ML (middle) and 1.0 ML (lower) h-benzene coverage at $Q = 0.95^{-1}$ with model 3, 4 and 5.

Table 4.5: Goodness of the fit , χ^2 parameter divided by the number of fitted points, resulting from the fitting of 1.0 ML in the whole thermal range to models 3, 4 and 5 for $Q = 0.95$ Å^{-1}.

	1.0 ML		
	Model 3	Model 4	Model 5
60 K	4.05	6.19	8.84
100 K	5.89	35.08	28.19
140 K	10.35	78.38	33.47

4.4 Experimental data of d-benzene, C_6D_6, on graphite: coherent scattering

The fitting of the d-benzene data provides a complementary perspective to the analysis and interpretation of h-benzene data. We have already stress that coherent scattering is sensitive to the relative motion of molecules. In the situations where no correlated motion exists, the coherent and the incoherent scattering functions are identical [75]. But the existence of correlations introduces differences between the coherent and the incoherent scattering [75]. As we have already mentioned, the incoherent scattering models can be applied for the analysis of coherent scattering provided some approximations are done [1]. One of the most useful tools was developed by George Vineyard in Ref. [99]. It allows to relate the coherent and the incoherent scattering function on the basis *convolution approximation* [99]. It consist in writing the Van Hove correlation function $G(\mathbf{r})$ as the convolution of the radial density function $g(\mathbf{r})$ with the self-correlation function $G_s(\mathbf{r})$ [99]. However, this approximation holds for the low coverage regime and its application in the high coverage regime remains uncertain. One of the most striking differences between the coherent and the incoherent data appears in the sensitivity to jump diffusion.

The jump diffusion model according to coherent scattering Coherent scattering does not follows the jump of single atoms, as incoherent scattering does. Hence, we need dynamical variables assigned to the collection of atoms and standing for the molecule: these are the so-called *configurations* developed by G. Coddens in Refs. [97, 141, 142]. For instance, the configuration of a

molecule in the μ-th orientation is defined in the reciprocal space:

$$\mathcal{F}_\mu(\mathbf{Q},t) = \frac{1}{\sqrt{N}} \exp\left(i\mathbf{Q}\cdot\mathbf{R}(t)\right) \sum_j^N \exp\left[i\mathbf{Q}\cdot\mathbf{r}_j^{(\mu)}(t)\right], \tag{4.59}$$

where the index j runs over all the atoms in the molecule, and the position of the atoms has been split into the position of the molecule's center of mass (CoM), $\mathbf{R}$ and the atomistic positions with respect to the CoM frame, $\mathbf{r}_j^{(\mu)}$. We do not include the scattering length b in contrast with the cited Refs. to preserve the scattering function free of the neutron-matter interaction effects. Note as well that in the case of independent molecules performing reorientations, configuration is equivalent to orientation [141]. The coherent intermediate scattering function can be written in terms of the configurations:

$$I_{coh}(\mathbf{Q},t) = \frac{1}{n} \sum_{\nu\mu} \mathcal{F}_\nu^*(\mathbf{Q}) p_\nu(0) P(\mu,\nu(0),t) \mathcal{F}_\mu(\mathbf{Q}) \tag{4.60}$$

where $P(\mu,\nu(0),t)$ is the probability of finding the molecule in the μ-th orientation at time t, provided it was at the ν-th orientation at $t=0$. The initial orientations are weighted by the probabilities $p_\nu(0)$, and n are the different orientations amongst which the molecule can lie. The case of benzene undergoing 60 degrees jump rotations is easily tractable within this framework. First of all, we note that a $\pi/3$ rotation does not change the benzene molecule orientation: the position of the atoms in the molecule and the configurations fulfill the following relation,

$$\mathbf{r}_j^{\mu+1} = \mathbf{r}_{j-1}^{\mu} \Rightarrow \mathcal{F}_{\mu+1}(\mathbf{Q}) = \left[\sum_j^N \exp\left(i\mathbf{Q}\cdot\mathbf{r}_j^{\mu+1}\right)\right] = \left[\sum_j^N \exp\left(i\mathbf{Q}\cdot\mathbf{r}_{j-1}^{\mu}\right)\right], \tag{4.61}$$

Thus, the effect of the jump rotation in the configuration is invisible because we can rename the indexes $j' = j-1$ (see Fig. 4.12) obtaining:

$$\mathcal{F}_{\mu+1}(\mathbf{Q}) = \left[\sum_{j'}^N \exp\left(i\mathbf{Q}\cdot\mathbf{r}_{j'}^{\mu}\right)\right] = \mathcal{F}_\mu(\mathbf{Q}). \tag{4.62}$$

As we did for the incoherent jump rotation, we can define a master equation which governs the dependence with time of finding the benzene molecule on the orientation/configuration μ [97, 141, 142]. However, if benzene is constrained to perform six-fold rotations, it always lies in the same configuration: $p_\mu = p_{\mu+1} = \cdots = p_{\mu+N}$. The master equation is equal to zero:

$$\frac{\partial}{\partial t} p_\mu(t) = \sum_\nu \frac{1}{\tau_{\mu\nu}} \left[p_\nu(t) - p_\mu(t)\right] = 0 \Rightarrow p_\mu = 1, \tag{4.63}$$

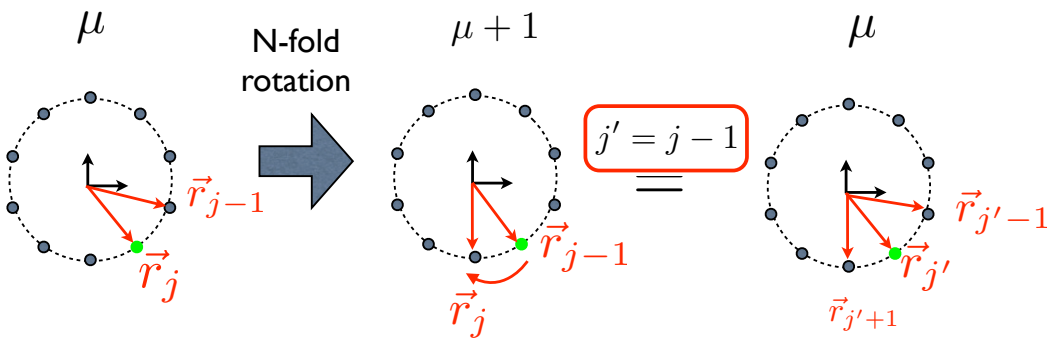

Figure 4.12: Effect of a N-fold rotation on a molecule with a N-fold symmetry axis on the configuration $\mathcal{F}_{c_\mu}$. We can see that the equivalence between configurations is easily recovered after a N-fold rotation by relabeling the j indexes of the atoms.

and we deduce that $\{p_\mu\}$ are all constants equal to the unity. Consequently the conditioned probability in Eq. 4.60 is constant and equals 1, and the coherent ISF is constant as well and equals unity. The corresponding scattering function is a delta function of the energy $\delta(\Delta E)$. In conclusion, coherent scattering is not able to record motions in which the initial and the final state (configurations or orientations in that case) are preserved. This applies to the case of benzene molecule when it performs a jump of $n2\pi/6$, n being an integer. Conversely, reorientations of $2\pi/n6$ would be visible, since in that case the orientation of the molecule changes and, hence, the initial and the final configurations are not the same.

Fig. 4.13 plots the data of 0.5 ML and 0.9 ML of d-benzene for 140K together with the fitting resulting from models 1 to 5 at 140K and for values of the momentum transfer of 0.5 Å^{-1} and 0.95 Å^{-1}. We do no longer consider the jump rotation model for six-fold rotation, since the coherent scattering function is unsensitive. First of all, we can discard the Gaussian models 2 and 4, since the profile for both coverages is closer to a Lorentzian shape than to a Gaussian profile. The mismatch is clearly seen at $Q = 0.95$ Å^{-1}. In addition, we observe that the model 1 delivers a fitted profile which clearly diverges from the 0.9 ML data at high Q. Hence, these models which combine translations and rotations are better suited for the high coverage data . Conversely, the 0.5 ML data is fitted by all the Lorentzian models, which provide very similar fitted profiles. Fig. 4.14 shows the fitting of the 0.9 ML at three temperatures: 60K, 100K and 140K. In the low momentum transfer range (upper panel), all the models give rise to the same fitted energy profile. But at high Q values the experimental profile displays a clear Lorentzian profile. However we observe that at low temperatures, 60K, all the fitted profiles are very similar. In that case, the

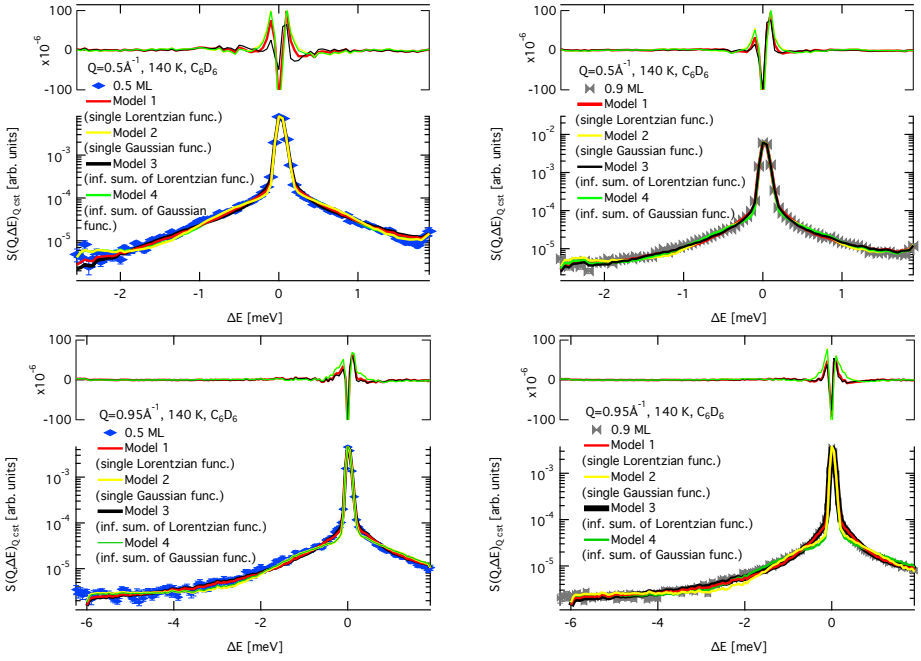

Figure 4.13: Fitting of the experimental data of 0.5 ML (left) and 0.9 ML (right) d-benzene at 140K with models 1 to 4, for two values of the momentum transfer: $Q = 0.5$ Å^{-1} (top) and $Q = 0.95$ Å^{-1} (bottom).

Table 4.6: Goodness of the fit , χ^2 parameter divided by the number of fitted points, resulting from the fitting of all the deuterated benzene data set at 140 K to models 1, 2, 3 and 4.

	Q=0.5 Å^{-1}				Q=0.95 Å^{-1}			
	Model 1	Model 2	Model 3	Model 4	Model 1	Model 2	Model 3	Model 4
0.5 ML	4.77	13.99	4.23	6.92	4.02	6.12	2.43	5.69
0.9 ML	5.84	12.81	4.85	11.23	7.74	17.51	6.88	21.66

quasi-elastic profile is very close to the resolution function. Furthermore the scattered signal is severely reduced because of the low scattering cross section of deuterated benzene. Hence it is difficult to decide which is the most accurate model.

In conclusion, we observe that the deuterated benzene quasi-elastic profile

Table 4.7: Goodness of the fit , χ^2 parameter divided by the number of fitted points, resulting from the fitting of all the deuterated benzene data set at 140 K to models 1, 2, 3 and 4.

	Q=0.5 Å^{-1}				Q=0.95 Å^{-1}			
	Model 1	Model 2	Model 3	Model 4	Model 1	Model 2	Model 3	Model 4
60 K	3.12	4.18	2.99	3.62	4.49	7.75	4.23	9.35
100 K	3.81	5.70	3.54	4.68	5.03	11.82	4.58	14.67
140 K	5.84	12.81	4.85	11.23	7.74	17.51	6.88	21.66

have a Lorentzian shape. This is similar to the quasi-elastic scattering function of hydrogenated benzene. On the other hand, the 0.9 ML data can not be fitted with a single Lorentzian function, which indicates that molecules undergo rotations. However, coherent scattering can only see continuous rotations or jump rotations of $2\pi/nN$ degrees, with $n > 1$. Thus six-fold reorientations are hidden by the symmetry of the molecule. Conversely the 0.5 ML data can be fitted with all the Lorentzian models, and only the shape of the quasi-elastic broadening with the momentum transfer holds the key for the interpretation of the experimental data. The very low coverage remains unknown since the small scattering cross-section of the d-benzene adsorbed layer prevents us to go further down to 0.1 ML. In what concerns the thermal dependence of the 0.9 ML d-benzene data, all the models converge at low temperature. But the interpretation of the fitted profiles is not easy since the quasi-elastic signal is very close to the resolution function width and its signal is weak.

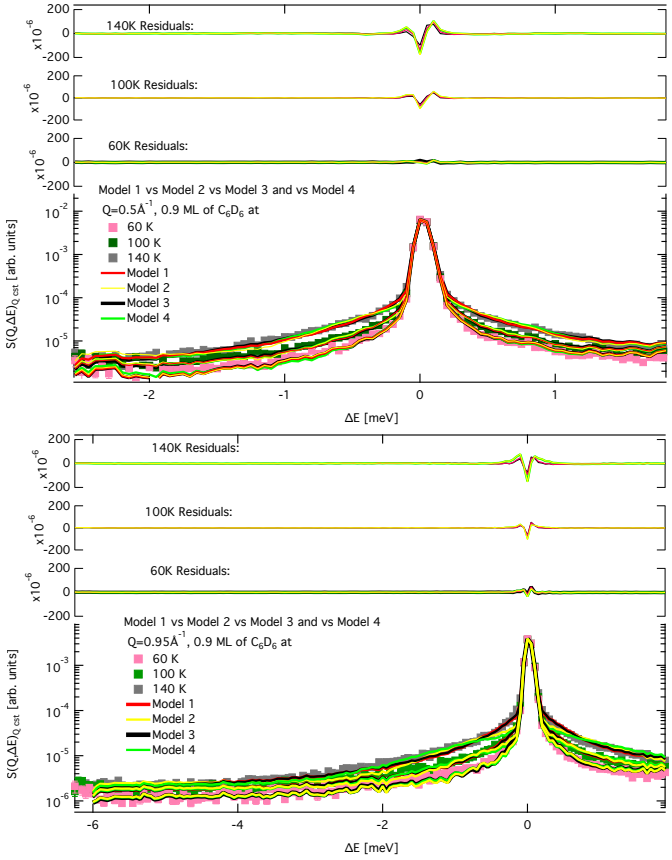

Figure 4.14: Fitting of the experimental data of 0.9 ML d-benzene at 60K, 100K and 140K with model 1 to 4. The upper panel groups the low Q value spectra while the bottom panel shows the high Q data spectra.

4.5 Conclusion

In this chapter we have reviewed 6 possible models to fit the quasi-elastic profiles arising from the diffusion of hydrogenated or deuterated benzene molecules. The discussion is restricted to the energy profiles without entering in the detail of the fitted parameters. We observe that the shape of the quasi-elastic profile is sensitive to coverage. The low coverage data can be fitted with a Lorentzian or a Gaussian function and the resulting fitted profiles are very similar. Conversely the medium-high coverage display a clear Lorentzian shaped profile. Furthermore, the models which include the effect of rotations (the addition of quasi-elastic lines) provide a better fit, than those which consist in a single quasi-elastic profile. This is in marked contrast with what was found for the diffusion of the deuterated benzene and the hydrogenated benzene measure in the Helium spin-echo as reported in Ref. [45]. The last important point is that coherent scattering is not sensitive to six-fold jump rotations, because of the symmetry of the benzene molecules. Thus, if rotations are detected in the coherent data, they should be continuous or jump wise provided that the angle of rotation is of $2\pi/nN$ degrees, with $n > 1$.

In the following chapter we concentrate in the physical interpretation of the fitting results. The fitted parameters are discussed in detail. In particular we will study the quasi-elastic broadening since its dependence with the momentum transfer bears the signature of the diffusive process. In addition, the comparison of the h-benzene and d-benzene analysis brings enlightening perspectives on the identification of continuous or jump rotations.

Chapter 5

Results and discussions of the experimental data analysis

The previous chapter describes the fitting of the data set to a collection of models addressing the question of the diffusive behavior of benzene molecules adsorbed flat on the basal plane of graphite substrates. We test from very simple models describing single diffusive processes, to more complex theoretical approaches which combine molecular translations and rotations. We observe important changes in the diffusive behavior related to the coverage and the temperature. Furthermore, the addition of a rotational part seems to improve the fitting quality. In this chapter we summarize the resulting parameters from the fitting of the experimental data set. We discuss in detail the dependence of the quasi-elastic broadening on the momentum transfer deduced from the fit of the data to each model because it is the experimental fingerprint of the molecular diffusive regime on the surface. We will also see that its dependence on the temperature and the coverage allows to identify the main physical mechanisms governing the diffusive process.

In the first section of the chapter we review all the models, emphasizing the expected behavior of the quasi-elastic broadening with the momentum transfer. In the second section the fitted parameters for the hydrogenated benzene are displayed and described. The final section concerns the fitting results of deuterated benzene data. It includes a comparison between the physical information extracted from the hydrogenated (incoherent), the deuterated (namely coherent at low Q values) benzene scattering and the spin-echo results reported in Ref. [45].

5.1 Summary of the previous models

Theoretical models predict he dependence of the quasi-elastic energy profile and the quasi-elastic broadening on the momentum transfer, according to the atomistic dynamics which characterizes a given diffusive regime. Tab. 5.1 summarizes the models under consideration for the analysis of the experimental data on benzene diffusion on the graphite basal plane, emphasizing the shape of the quasi-elastic energy profile and the expected dependence of its HWHM, the so-called *quasi-elastic broadening*, on the momentum transfer Q and temperature T. Remember that the theoretical lineshapes should be convoluted to the instrumental resolution function in order to fit the experimental data. The resolution function is, in our case, the set of spectra measured at 2 K.

Table 5.1: Summary of the previous models.

Model: theoretical quasi-elastic SF	Characteristic QENS broadening dependence on Q, T and θ	Diffusive processes and physical information extracted from the fitting
Model 1: single Lorentzian function, $\mathcal{L}(Q, \Delta E)$	$\frac{\hbar}{\tau}_T(Q,T) = \hbar D_T(T) Q^2$	Brownian motion: random and continuous walk of the molecules on the substrate. We can extract the diffusion coefficient $D_t(T, \theta)$ which depends on the temperature, T. It is related to the friction parameter, η, through the Einstein relation: $D(T) = \frac{k_b T}{m\eta}$. m is the mass of the molecule. If the friction is related to phonons or electron/hole pair creation and annihilation, phononic friction η_{ph} and electronic friction η_{el} respectively, then it is temperature and coverage independent [143]. Conversely, if it is collisional friction it follows a square root of temperature and it is proportional to the density of adsorbed particles (coverage) [2, 103].
Model 2: single Gaussian function, $\mathcal{G}(Q, \Delta E)$	$\Gamma_T(Q,T) = \sqrt{2 \ln 2 \langle v^2 \rangle} Q$	Ballistic motion: rectilinear and uniform motion of the adsorbates on the substrate. We can extract the mean square velocity $\langle v^2 \rangle$ of the adsorbates, which is a function of temperature T and can be calculated via the equipartition theorem: $\langle v^2 \rangle = \frac{2 k_B T}{m}$, where m is the mass of the molecule.

Model 3: infinite summation of Lorentzian functions weighted by Bessel functions: of the first kind: $S(Q,\Delta E) = J_0^2(Q\rho)\mathcal{L}_0(Q,\Delta E)$ $+ 2\sum_{n=1}^{\infty} J_n^2(Q\rho)\mathcal{L}_n(Q,\Delta E).$	Translational quasi-elastic broadening, (term in the SF with index $n = 0$) : $\frac{\hbar}{\tau}_T(Q,T) = \hbar D_T(T)Q^2.$ Rotational quasi-elastic broadening: $\frac{\hbar}{\tau_n}(T) = \hbar D_R(T)n^2.$ Total quasi-elastic broadening of the terms in the SF with index $n \geq 1$: $\frac{\hbar}{\tau}_T + \frac{\hbar}{\tau_n} = \hbar(D_T(T)Q^2 + D_R(T)n^2).$	Combination of brownian translations and brownian uniaxial rotations. We can extract the translational D_T and rotational D_R diffusion coefficients. They are related to the translational η_T and rotational η_R friction parameters by the Einstein relation: $D_T(T) = \frac{k_b T}{m\eta_T}$ or its equivalent relation for rotations: $D_R(T) = \frac{k_b T}{I\eta_R}$. m is the mass of the molecule and I is its moment of inertia. The translational and rotational friction parameters can be related in the frame of the collision model (see Eq. 4.38 in Chap. 4). In that case, the friction parameters depend on temperature and coverage. If friction comes from an alternative source to collisions, like the electronic or the phononic friction, we simply assume that the rotational and the rotational friction parameters are equal, $\eta_T = \eta_R$. In addition the phononic and the electronic friction parameters are temperature and coverage independent
Model 4: infinite summation of Gaussian functions weighted by Bessel functions: of the first kind: $S(Q,\Delta E) = J_0^2(Q\rho)\mathcal{G}_0(Q,\Delta E)$ $+ 2\sum_{n=1}^{\infty} J_n^2(Q\rho)\mathcal{G}_n(Q,\Delta E)$	Translational quasi-elastic broadening, (term in the SF with index $n = 0$) : $\Gamma(Q,T)_{trans} = \sqrt{2\ln 2\left\langle v^2\right\rangle}Q$ Rotational quasi-elastic broadening: $\Gamma_{n,R}(T) = \sqrt{2\ln 2\left\langle \omega^2\right\rangle}n$ Total quasi-elastic broadening of the terms in the SF with index $n \geq 1$: $\Gamma_n = \sqrt{2\ln 2(\left\langle v^2\right\rangle Q^2 + 2\left\langle \omega^2\right\rangle n^2)}$	Ballistic translations and ballistic uniaxial rotations. We can extract the mean square velocity, $\left\langle v^2\right\rangle$, and the mean square angular velocity, $\left\langle \omega^2\right\rangle$ which are functions of the temperature T. We can estimate their theoretical value via the equipartition theorem: $\left\langle v^2\right\rangle = \frac{2k_B T}{m}, \left\langle \omega^2\right\rangle = \frac{k_B T}{I} \Rightarrow \left\langle \omega^2\right\rangle = \frac{\left\langle v^2\right\rangle}{\rho^2}$
Model 5: single Lorentzian function for translations combined with jump model for six-fold reorientations $S(Q,\Delta E) = A_{N=6}(Q\rho)\mathcal{L}_{trans}(Q,\Delta E)$ $+ \sum_{n=1}^{5} A_n\mathcal{L}_n(Q,\Delta E)$	Translational quasi-elastic broadening, (term in the SF with index $n = N$) : $\frac{\hbar}{\tau}_T(Q,T) = \hbar D_T(T,\theta)Q^2$ Rotational quasi-elastic broadening, $\frac{\hbar}{\tau_k} = 4\frac{\hbar}{\tau}(T)\sin^2\left(\frac{\pi}{N}k\right)$ Total quasi-elastic broadening of the terms in the SF with index $n = 1,\ldots,5$: $\frac{\hbar}{\tau}_T + \frac{\hbar}{\tau_k} = \hbar\left[D_T Q^2 + 4\frac{\hbar}{\tau}\sin^2\left(\frac{\pi}{N}k\right)\right]$	Brownian continuous translations and six fold jump rotation. From the translational component (index n=N), we can extract the translational diffusion coefficient and the corresponding friction parameter. From the rotational terms, we can extract the jump rate $1/\tau(T)$ for reorientations. Since jump rotations are an activated process, the jump rate should follow an Arrhenius law of temperature. Conversely, it should be Q independent.

In general terms, all the models make use of Lorentzian and Gaussian shaped profiles to describe the quasi-elastic energy profile related to the diffusive regime of molecules on the surface. We can establish very general laws governing the dependence of the quasi-elastic broadening with the momentum transfer. For models consisting in a single quasi-elastic line (model 1 and 2), the HWHM of the Lorentzian profiles follows a quadratic law of the momen-

tum transfer while the Gaussian HWHM is linear with Q. Models made of a summation of functions, due to the introduction of a rotational part, should be separated into two parts. The purely translational part corresponds to the element in the summation whose index is $n = 0$. Its HWHM will display the same momentum transfer dependence than for the single quasi-elastic line models: a quadratic law of Q if the quasi-elastic line is a Lorentzian function or a linear law of Q if it is Gaussian shaped. Conversely, the terms in the summation of Lorentzian, or Gaussian functions indexed with $n > 1$ and standing for the rotational part of the SF, are characterized by a Q independent HWHM. The HWHM of the total rotational quasi-elastic profile depends on Q, but we can not establish an analytical formulation for it, since the HWHM of a summation of functions is not well defined. Furthermore, its Q dependence comes mainly from the Bessel functions weighting each term of the summation [132].

The friction parameter Friction is the key parameter determining the division between ballistic and diffusive regimes in the Brownian model. We recall that Brownian particles undergo ballistic motion (rectilinear and uniform displacements or the equivalent for rotations) in the lapse of time between collisions. Hence, friction is a measure of the frequency of collisions. In the very low friction regime, collisions are rare. The mean free path where particles show a ballistic diffusion increases and it is clearly visible in the time/energy window probed by neutron or helium time of flight spectroscopy techniques. In particular, the mean square displacement of the molecules on the substrate grows quadratic with time. Conversely, in the high friction regime, collisions are very frequent and the mean free path reduces dramatically. This is the so-called diffusive regime, characterized by a mean square displacement of the molecules on the substrate linear with time. A precision is important at this stage: collisions are not restricted to adsorbate-adsorbate instantaneous interactions (this is the so-called *collisional friction*), but can happen between adsorbates and phonons on the substrate leading to phonon creation and annihilation, *phononic friction* [144] or between adsorbates and electrons of the substrate exciting electron-hole pairs, *electronic friction* [11]. In other words, there exists different sources of friction (comlicating the diffusive process), and each kind displays a characteristic dependence on temperature and sometimes on coverage too. In particular, phononic and electronic friction should not display any dependence with coverage nor with temperature [143]. On the contrary, collisional friction strongly depends on these two parameters [57] (see Eqs. 4.38 of Chap. 4). Phononic and electronic friction arise from the interaction between the adsorbate and the substrate, while collisional friction is due to adsorbate-adsorbate interaction. The temperature independence of phononic friction holds when the vibration frequency of the adsorbate on the adsorption

site, ω_0, is small with respect to the Debye frequency ω_D [143]. In a similar way, electronic friction is temperature independent if ω_0 is small if compare with the Fermi energy [143]. The small-amplitude frequency of the benzene at the adsorption site is related to the height of the potential energy surface, U_0 at the adsorption site and can be approximated by $\omega_0 \simeq (2\pi/a)\sqrt{U_0/m}$ [143], where a is the graphite lattice constant, 2.45 Å for graphite [145], and m is the mass of the adsorbate. The graphite surface corrugation is estimated of 17 meV [45], delivering a small amplitude frequency of benzene of the order of $3.72\times10^{12}\mathrm{s}^{-1}$ or in terms of energy of 0.24 meV. Thus, the conditions for the thermal independence of electronic and phononic friction are satisfied since the very high Debye temperature of the basal plane of graphite, 1400 K [116] yields a Debye frequency of 120 meV and the Fermi level of graphite is found at 8.6 eV [146]. In addition, we can roughly estimate the phononic friction of graphite damping the small oscillations of a benzene molecule [143]:

$$\eta_{ph} = 0.12\frac{m}{\rho}\left(\frac{\omega_0}{C_T}\right)^2\omega_0 \tag{5.1}$$

where ρ is the density of the adsorbate (2.267×10^3 kg.m^{-3} for graphite), C_T is the transversal velocity of sound, which in the [0001] basal plane is of 4040 m.s^{-1} (estimated from the elastic constant $C_{33} = 3.71 \times 10^{11}$ dyn.cm^{-2} Ref. [118], $C_T = \sqrt{C_3 3/\rho}$). The resulting phononic friction is 1.98×10^{10} s^{-1}. Thus, the analysis of the results arising from data at different coverages and temperatures provides enlightening information to identify the main source of friction in the system of benzene adsorbed on the graphite basal plane.

Free parameters in the different models One of the problems that models combining translations and rotations encounter is the multiplication of free variables to fit. We have already stressed in the previous chapter the need of theoretical tools to link the translational and the rotational quasi-elastic broadening. However, each model is related to a defined diffusive regime and the linking should be done accordingly. In the case of model 3, the connexion between the translational and the rotational quasi-elastic broadening is based on the relation between the translational and the rotational friction parameters. The collision model provides the theoretical frame to interrelate η_T and η_R [103,136,147] as it is seen in Eq. 4.38 of Chap. 4. Eventually, we reduce the two-folded quasi-elastic broadening to a single quasi-elastic broadening which integrates the contribution of translational and rotational friction (see Eq. 4.39 of Chap. 4). On the other hand, if friction has a phononic or electronic nature, we simply assume that the translational and the rotational friction parameters are equal. In model 4 we can easily connect the mean square velocity and

the mean square angular velocities thanks to the equipartition theorem (see Eq. 4.44 of Chap 4). Thus, we deduce a total quasi-elastic broadening which depends only on the mean square velocity (see Eq. 4.45). Finally, model 5 is the most difficult model to handle since we ignorate any possible link between the jump rate for the six-fold reorientations and the translational diffusion coefficient. Thus, we take the values of the translational quasi-elastic broadening extracted from model 3 and we leave as free parameter the jump rate. This is the only way to obtain a stable fit with this model.

To conclude, the fitting of the experimental data to the different models listed in Tab. 5.1 allows to extract valuable information about the diffusive process. In particular, the dependence of the quasi-elastic broadening on the momentum transfer allows to identify the diffusive regime of the molecules adsorbed on the graphite. We can also deduce the friction parameter, linked to one or more possible sources (electrons, phonons or adsorbates). In the following sections we will compare the output of the different models for the hydrogenated and deuterated benzene, discussing the similarities and divergences of the extracted parameters. This is essential to decide which model suits better the benzene diffusive behavior under different coverage and thermal regimes.

5.2 Hydrogenated benzene

All the theoretical models contain parameters which are not exclusively related to the diffusive regime of the molecule. We recall that the general form of the fitting function is lenghtly discussed in Sec. 4.2 of Chap. 4 and is defined in Eq. 4.5. Here we write a very schematic formulation of the fitting function in use:

$$S_{fit}(\mathbf{Q},\Delta E) = S_{res}(\mathbf{Q},\Delta E) \otimes [y_0 + A_{el}(Q)\delta(\Delta E) + A_{QENS}(Q)S_{QENS}(\mathbf{Q},\Delta E)].$$

This is the convolution between the experimental resolution function $S_{res}(\mathbf{Q},\Delta E)$, measured for every coverage at 2K, and a theoretical function. The latter consists in the summation of various terms like a flat background stemming from the surface phonons whose characteristic frequency falls out of the dynamical range, an elastic part arising namely from the atoms of carbon in the substrate and a quasi-elastic part coming from the adsorbed layer. $S_{QENS}(\mathbf{Q},\Delta E)$ corresponds to the quasi-elastic line which has been modeled according to the diffusive regime of the benzene molecules (see the different theoretical line shapes in Tab. 5.1). The elastic intensity corresponds to the ratio elastic/total scattered intensity. It is, thus, directly related to the amount of graphite atoms

N_G (which are the elastic scatterers in the system) with respect to the total number of atoms in the system $N_G + N_{C_6H_6}$, where $N_{C_6H_6}$ is the number of atoms belonging to the adsorbed layer. Hence the elastic amplitude displays a dependence on coverage since $A_{el} \propto N_G/(N_G + N_{C_6H_6})$ and $N_{C_6H_6}$ depends on the coverage θ: $\theta = N_{C_6H_6} A_{C6H6}/A_{eff}$ (where A_{C6H6} is the experimental area of a benzene molecule lying flat on graphite, 36.7 Å, and A_{eff} is the effective surface area for adsorption for *Papyex* exfoliated graphite, 25.5 m^2/g). Inversely, the quasi-elastic amplitude is linked to the ratio quasi-elastic/total scattered intensity and, hence $A_{QENS} \propto N_{C_6H_6}/(N_G+N_{C_6H_6})$. Its dependence on Q can be viewed more as an inverse mirror of the decaying of the elastic amplitude with the momentum transfer rather than a characteristic feature of the diffusive regime. No particular physical information on diffusion can be extracted from both amplitudes, nor from the flat background.

5.2.1 The common fitted parameters: amplitudes and background

Fig. 5.1 summarizes the elastic, quasi-elastic amplitudes and the background for the 0.1 ML and the 1.0 ML data, resulting from the fitting of all the models. In general terms, the fitting to Lorentzian shaped models gives very similar fitted parameters, while the Gaussian profile models 2 and 4 give slightly different values, especially for the high coverage data. We also observe that the low coverage fitted parameters display smaller values for the quasi-elastic and the offset parameters than the 1.0 ML fitted parameters. This is due to the smaller cross-section of the adsorbed layer of the 0.1 ML sample if compared with the 1.0 ML adsorbed layer cross-section (there are ten times more benzene molecules in the latter than in the former sample). Conversely, the elastic amplitude of 0.1 ML remains closer to the unity, since the realteive amount of graphite with respect to the quantity of adsorbed molecules is very high and elastic intensity constitute the major part of the scattered intensity. In terms of coverage, the low coverage data shows very similar fitted parameters resulting from the fitting of the different models. The most sensitive parameter to the different models is, logically, the quasi-elastic amplitude, but it does not show a particular trend with Gaussian or Lorentzian shape models. This is congruent with the results of the previous chapter, where we found that the energy profile could be fitted with almost all the models. In contrast, for the 1.0ML, the models made of Gaussian functions (models 2 and 4) provide fitted parameters which differs from the general trend. These results were expected since we saw in the previous chapter that the energy profile of the medium-high coverage data is markedly Lorentzian shaped. Hence, we shall retain only the results extracted from models 1, 3, and 5 which consist in a single or summa-

tion of Lorentzian functions.

Finally, note that the summation of the elastic, quasi-elastic amplitudes and

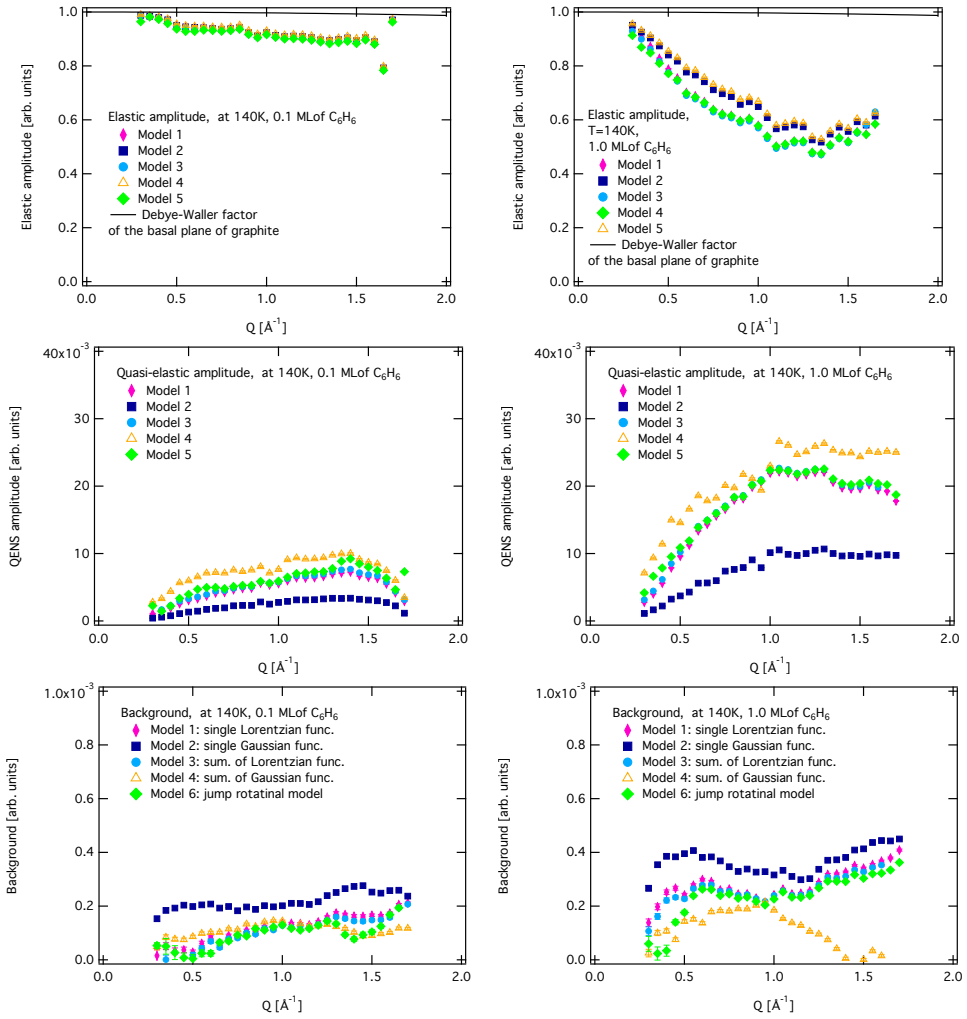

Figure 5.1: Fitted parameters extracted from the application of models 1 to 6 to the 0.1 ML (left) and the 1.0 ML (right) data. Top panel: elastic amplitudes. We also include the theoretical graphite Debye-Waller factor. Medium panel: quasi-elastic amplitude. Bottom panel: background.

the offset is not equal to unity. This is because, the experimental spectra and the experimental resolution function have been normalized to the incoming flux of neutrons and the vanadium scattering function (which provides the initial neutron energy distribution arising from the instrument scattering). Thus, $S(\mathbf{Q}, \Delta E = 0) \neq 1$, but it can be easily verify that the summation of all the parameters, multiplied to the intensity of the experimental resolution function

delivers the experimental intensity of the SF at $\Delta E = 0$.

5.2.2 The quasi-elastic broadening

In this section we discuss the quasi-elastic broadenings obtained with the fitting to the different models of the hydrogenated benzene scattering function. We recall that the quasi-elastic broadening, allows to identify the diffusive regime taking place in the system: Its dependence with the momentum transfer is the experimental signature of the molecule's diffusive behavior. Furthermore, we can extract valuable information such as the diffusion coefficients and the friction parameters, yielding an understanding of the physical mechanism underlying the diffusive behavior of the molecules within the adsorbed layer.

Each theoretical model predicts two important features of the quasi-elastic scattering function $S_{QENS}(Q, \Delta E)$: the energy profile and the dependence of the HWHM of such energy profile, the so-called quasi-elastic broadening, on the momentum transfer. Both features never appear separately since they reveal the dynamics at the atomic level characterizing each diffusive regime. Both of them should be fulfilled by the experimental data which display the typical signature of a given diffusive regime.

Comparison between the different models

Figs. 5.2 and 5.3 summarize the quasi-elastic broadenings related to translations extracted from the fitting to all the theoretical models for the low coverage (0.1 ML and 0.2 ML) and the high coverage (0.5 ML and 1.0 ML) data at 140K. In the case of simple models such as model 1 and 2 the translational quasi-elastic broadening is directly the HWHM of the Lorentzian or the Gaussian function respectively. For models 3 and 4 involving a summation of quasi-elastic lines, the translational quasi-elastic broadening corresponds to the HWHM of the term indexed with $n = 0$. In the case of low coverage data (see left panel of Fig. 5.2), the Gaussian models, 2 and 4, provide linear quasi-elastic broadenings for the 0.1 ML data in the range of momentum below 1Å^{-1}, while the quasi-elastic broadenings extracted from Lorentzian shaped models, 1 and 3 (or equivalently 5, where we fix the HWHM of the $n = N$ term to the model 3 fitted result), do not follow the expected quadratic law of Q. This difference suggest that molecules undergo ballistic diffusion in this low coverage regime. On the other hand, the right panel of Fig. 5.2 displays the translational quasi-elastic broadenings extracted from the fitting of the 0.2 ML data. The quasi-elastic broadenings for the Gaussian models 2 and 4 behave as predicted theoretically (linear with Q) but the results of the fittings show that

the quasi-elastic energy profile presents a rather Lorentzian shape: the goodness of the fit parameter, χ^2, for model 2 (single Gaussian function), 21.86, is almost the double than the χ^2 related to model 1 (single Lorentzian function) of 12.22 at 140K for a value of $Q = 1.4\text{Å}^{-1}$ (see Tab. 4.1 in Chap. 4). An important difference is also found between the χ^2 characterizing model 3 fitting, 3.57, versus the one arising from model 4 fitting, 10.33 for $Q = 0.95$ Å^{-1} at 140 K (see 4.3). On the other hand, the Lorentzian models 1 and 3 display a quadratic law of Q in a narrow range of the momentum transfer between 0.5 Å^{-1} and 1.5 Å^{-1}. Important deviations are observable below and above this window. At low Q deviations can be attributed to the poor quasi-elastic signal (the scattering intensity is dominated by the graphite scattering, see Fig. 5.1). Conversely, at high Q, the deviations from the quadratic law can be due to the raising of the scattering signal related to rotations, while simultaneously the intensity of translations is significantly reduced (we recall that in model 3, the intensity of the translational term, with index $n = 0$, is weighted by a Bessel function of the first kind and order $n = 0$). The results for the 0.5 ML and 1.0

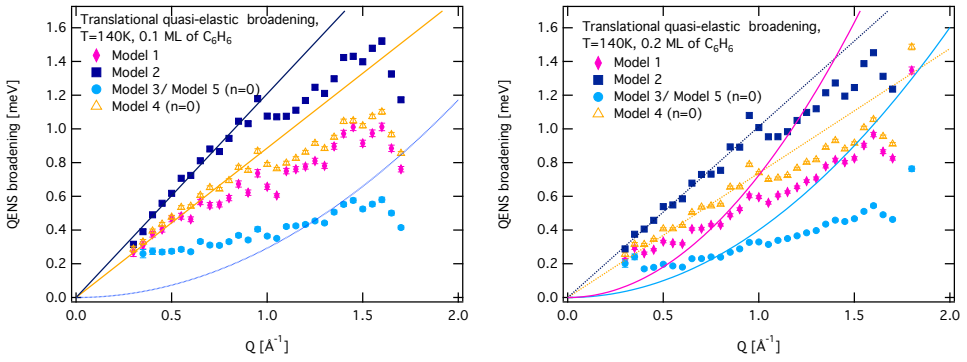

Figure 5.2: Quasi-elastic broadening extracted from the fitting of the experimental data for all the coverages to the theoretical model at 140K. We have included guides to the eye to underline the linear or quadratic dependence of the quasi-elastic broadening on the momentum transfer.

ML data can be found in Fig. 5.3. We only display the quasi-elastic broadening of the Lorentzian shaped models, since we have already seen that their quasi-elastic energy profile has a marked Lorentzian character. As it happens with the 0.2 ML, the quasi-elastic broadenings only satisfies the quadratic law of Q in the range of momentum transfer spanning from 0.5 Å^{-1} and 1.5 Å^{-1}. However, we observe that the high Q range values for the quasi-elastic broadening, especially for the 1.0 ML, seems to follow a quadratic different law with a lower diffusion coefficient. But this can be simply an effect of the rotational

quasi-elastic broadening becoming very important at this range of Q values (remember that at $Q > 1$ Å^{-1} we probe distances comparable with the size of the benzene molecule). To finish with the comparison between models, we wish

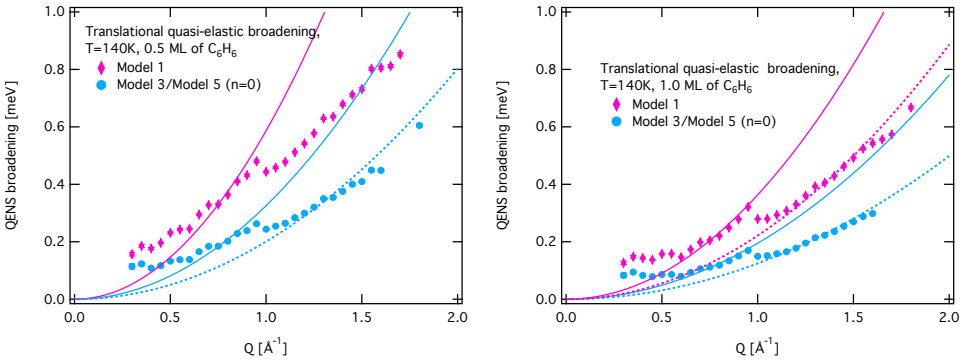

Figure 5.3: Quasi-elastic broadening extracted from the fitting of the experimental data for all the coverages to the theoretical model at 140K. We have included guides to the eye to underline the linear or quadratic dependence of the quasi-elastic broadening on the momentum transfer.

to comment the differences between the quasi-elastic broadenings arising from single quasi-elastic and multiple quasi-elastic profiles models. In general terms, the quasi-elastic broadenings of model 1 and 2 display higher values than for models 3 or 4. In the former models there is a single quasi-elastic line and the quasi-elastic broadening is the HWHM of the total quasi-elastic energy profile of the scattering function (see Figs. 4.1, for instance). Conversely, models 3 and 4 are made of a summation of Lorentzian and Gaussian functions arising from the separation between translational and rotational motion (see Eq. 4.21 in the previous chapter). What we call the translational quasi-elastic broadening is the HWHM of the term in the summation with index $n = 0$, and it only contains a portion of the total HWHM observable in the SF. Accordingly, its values should be much smaller than the ones arising from models where a single quasi-elatic line is considered.

Dependence on coverage

We have already seen when comparing the different models, that there are significant changes of the diffusive regime with the coverage. In this section we fit the quasi-elastic broadenings to the theoretical dependence with the momentum transfer established by each model. We expect to obtain valuable information about the diffusion process, like the mean square velocity of the

molecules for the very low coverage sample, where ballistic motion is observed, or the friction parameter for higher coverage samples.

We display in the left panel of Fig. 5.4 the translational quasi-elastic broadenings (the HWHM of the Gaussian function for model 2 or the HWHM of the Gaussian function with index $n = 0$ for model 4) extracted from the fitting of the 0.1 ML scattering function to models 2 and 4. In the right panel of the same figure, we show the rotational quasi-elastic broadening (the HWHM of the Gaussian function with index $n = 1$) arising from the fitting of the 0.2 ML data to model 4. We recall that model 2 is made of a single Gaussian function and does not consider separately translations and rotations, while model 4 which is a summation of Gaussian does. We fit the translational quasi-elastic broadenings to a linear law of the momentum transfer where the slope is proportional to the mean square velocity of the molecules on the surface (as stated theoretically, see Tab. 5.1). Conversely the rotational quasi-elastic broadening should be Q-independent and its value is also related to the mean square angular velocity. The extracted mean square velocity and mean square angular velocity are summarized in Tab. 5.2.

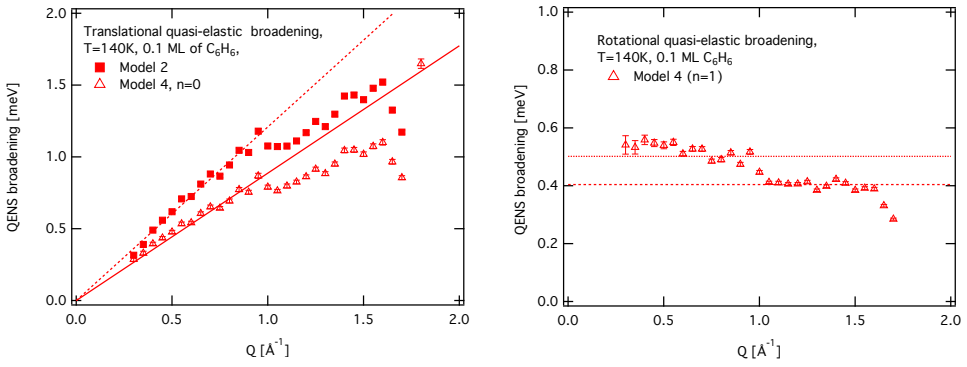

Figure 5.4: Translational quasi-elastic broadening extracted from the fitting of the 0.1 ML scattering function to models 2 and 4 at 140K. For model 2, the translational quasi-elastic broadening is directly the HWHM of the quasi-elastic profile. For model 4, this is the HWHM of the term $n = 0$ in the summation of Gaussians. We have fitted both quasi-elastic broadening to a linear law of Q, as established by the theoretical models.

Model 4 provides fitted values for the mean square velocities which are in better agreement with the equipartition theorem than those deduced from model 2. This indicates that molecules not only undergo ballistic translations, but they also perform ballistic rotations. However, we should note that the

Table 5.2: Results for the mean square velocity resulting from the fitting of the quasi-elastic broadening from models 2 and 4 to a linear law of the momentum transfer. We also include the mean square angular velocity extracted from the fitting of the rotational quasi-elastic broadening (the HWHM of the $n = 1$ term in the summation of Gaussian functions of model 2). We compare the fitted values with the equipartition theorem prediction.

	Model 2	Model 4	Equipartition theorem
$\langle v^2 \rangle$ [Å^2.ps^{-2}]	4.87±0.04	2.62±0.02	2.98
$\langle \omega^2 \rangle$ [10^{-1} ps^{-2}]		low Q: 4.20±0.03/ high Q: 3.07±0.04	4.77

agreement with the equipartition theorem is excellent when we consider the fit for the low Q range (below 1.0 Å^{-1}), but it deviates at higher Q values, especially for the mean square angular velocity. This follows from the fact that the translational quasi-elastic broadening deviates from the linear law for $Q > 1.0$ Å^{-1}, suggesting that in this high Q range the separation between translations and rotations is not properly accounted by model 2. In this very high momentum transfer range, the contribution of translations is strongly reduced, while the rotational contribution to the scattering becomes dominating. Furthermore, at this high Q values, the Gaussian approximation might no longer hold and the effect of non-Gaussian effects (we should consider further terms of the cumulant expansion, see Eq. 2.30 in Chap. 2) can enter into play [102]. We observe a reduction of the 20% between the experimental value of the quasi-elastic broadening at $Q = 1.5$ Å^{-1} (1.10 meV) with respect to the theoretical prediction of the linear law of Q (1.4 meV). A similar effect is described in Ref. [102] where they also found in the liquid argon scattering function a decrease of the HWHM of the scattering function of 20% when they include the non-Gaussian correction terms.

We discuss now the results for higher coverage data. We choose the results arising from model 3 rather than model 1 on the basis of the quality of the fitting. We observe that the distinction between translational and rotational motion improves the goodness of the fitting. The left panel of Fig. 5.5 displays the translational quasi-elastic broadenings (the HWHM of the term $n = 0$ in the summation of Lorentzian function of model 3) extracted from the fitting of 0.2 ML, 0.5 ML and 1.0 ML to model 3. The fittings to a square law of the momentum transfer are also displayed, and the resulting diffusion coef-

ficient and friction parameters are listed in Tab. 5.3. The quadratic law of the momentum transfer is satisfied in a very narrow range of Q, where the translational part of the scattering dominates. At very low Q (below 0.5 Å^{-1}) the substrate scattering is very intense while at high Q, model 3 encounters the problem of a very large rotational contribution in comparison with a tiny translational part. In addition, the interpretation of the high Q range dependence of the quasi-elastic broadening gets complicated by the possibility that the Gaussian approximation on which the model is based does not hold. In any case, we should stress that the extracted diffusion coefficients and friction parameters display a strong dependence on coverage. This is the fingerprint of collisional friction, since phononic and electronic friction are coverage independent. Furthermore the estimated phononic friction value, 2.2×10^7 s^{-1}, is too small to account for the very high extracted friction. We have also computed the collisional friction related to benzene molecules enduring binary collisions and exchanging translational and rotational momentum, as it is proposed in Refs. [103, 136] (see Eqs. 4.38). The resulting values are included in the tables, to provide a theoretical benchmark for comparison with the experimental parameters. We observe that binary collisions between benzene molecules generate a too small friction parameter. Besides, the dependence with coverage is not exactly proportional. A possible improvement consists in consider the collision of single benzene molecule with small clusters. This situation is compatible with the phase diagram of the benzene monolayer adsorbed on graphite where the existence of a solid-liquid coexistence phase is observed at around 130 K [34,41]. Besides, the experimental translational diffusion coefficients are in good agreement with MD simulations studying the melting process of the complete monolayer of benzene on graphite (1.0 ML) [34], were a value of 0.60 $\text{Å}^2.\text{ps}^{-1}$ is reported at 140K. The collisional friction in that situation can still be accounted in the theoretical frame of uncorrelated binary collisions [147], but considering that the system presents a mixture of different kind of particles: single benzene molecules in one hand, and small clusters in the other. In that case, the friction parameter would scale with the mass of the small clusters if we consider it as a rigid disk. In the case of the rotational motion, the quasi-elastic broadening is the HWHM of the term indexed with $n = 1$ in the Lorentzian function summation of of model 3. The right panel of Fig. 5.5 contains the rotational quasi-elastic broadening. Following model 3, it should be Q independent, and from its value we can deduce the rotational diffusion coefficient and the rotational friction parameter. The fitted results can be found in Tab. 5.4. In that case, the dependence with coverage is still very strong. Furthermore, the rotational friction parameters present much higher values than the translational ones. However, care must be taken since the rotational quasi-elastic broadening displays a Q dependence, even if theoretically this is not predicted. The resulting values of the rotational diffusion coefficient and

the friction parameter come from the high Q range fitting, where there also exists important deviations of the translational quasi-elastic broadening to the square law of the momentum transfer. It is true that rotations dominate the scattering intensity at this range of Q. But they can coexist with strong deviations from the Gaussian approximation which reduce the apparent HWHM of the scattering function.

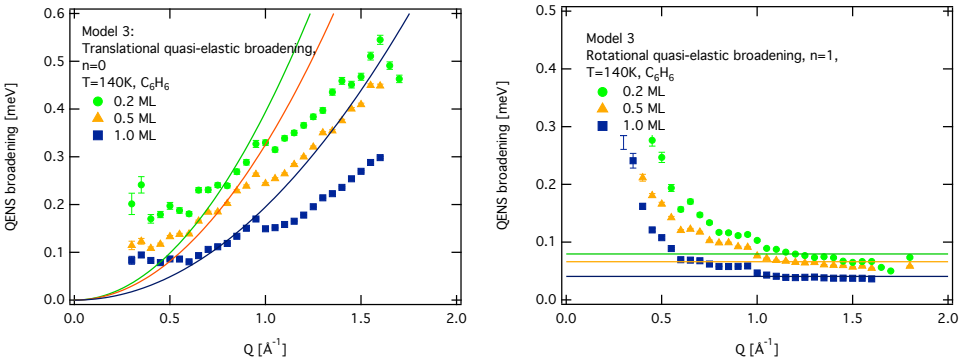

Figure 5.5: Quasi-elastic broadening extracted from the fitting of the experimental data for all the coverages to the theoretical model at 140K. We have included guides to the eye to underline the linear or quadratic dependence of the quasi-elastic broadening on the momentum transfer.

Table 5.3: Results for the *translational* diffusion coefficient and the friction parameter extracted from the fitting of the 0.2 ML, 0.5 ML and 1.0 ML data to model 3 and 6 at 140K.

	$D_T[10^{-1}$ Å^2.ps$^{-1}]$	η_T [ps^{-1}]	
	Model 3	Model 3	Collision model
0.2 ML	5.93±0.03	2.5±0.1	0.35
0.5 ML	4.95±0.02	3.012±0.009	0.94
1.0 ML	2.97±0.01	5.03±0.02	1.87

To conclude, the strong dependence of the translational and rotational friction parameter suggest that the main source of friction comes from the interaction between adsorbates, rather than with the substrate (phononic or electronic friction). Furthermore, the range of coverage under study displays the transition from the ballistic regime at low coverages, 0.1 ML, to a Brownian diffusive regime at higher coverage. Such a transition is entirely driven by the density of adsorbates on the substrate. We can readily calculate the mean free

Table 5.4: Results for the *rotational* diffusion coefficient and the friction parameter extracted from the fitting of the 0.2 ML, 0.5 ML and 1.0 ML data to model 3 and 6 at 140K.

Coverage	$D_R[10^{-1}$ ps$^{-1}]$	η_R [ps^{-1}]	
	Model 3	Model 3	Collisional model
0.2 ML	1.210±0.005	7.72±0.03	0.25
0.5 ML	1.006±0.002	9.28±0.01	0.68
1.0 ML	0.618±0.001	15.10±0.03	1.35

path of the molecule on the surface as a function of coverage [2]:

$$\bar{l} = \frac{1}{2\sqrt{2}\rho\sigma} \tag{5.2}$$

where ρ is the radius of the benzene molecule and σ is the adsorbate substrate density, which is a function of coverage: $\theta = \sqrt{3}a^2\sigma$, where a is the lattice constant of graphite. Hence, the mean free path is inversely proportional to coverage. The theoretical values of the different coverages are shown in Tab. 5.5. We have also computed the equivalent reciprocal space distance. As we can see, the mean free path for 0.1 ML coverage is very large, meaning that the ballistic behavior of the molecules is already visible at very low Q, above 0.4 Å^{-1}. This range of momentum transfer matches perfectly the range of Q where the linear behavior of the translational quasi-elastic broadening with the momentum transfer is observable (see Fig. 5.4). Higher coverages reduce the mean free paths and the ballistic regime is shifted towards higher values of the momentum trasnfer. In the case of 0.2 ML, we can still observe a hint of ballistic diffusion at very Q, in a range which already matches the size molecule. But, coverages of 0.5 ML and 1.0 ML provide very small values of the mean free path. The corresponding range of momentum transfer where ballistic diffusion is visible falls out of the reciprocal space window that we survey. All this considerations leads us to think that benzene molecules display a Brownian diffusive behavior, where we can tune the extend of the low friction regime by playing with the coverage. At very low coverage, the adsorbate-adsorbate interactions (collisions) are not frequent and molecules undergo ballistic motion. The increase of the coverage leads to an increase of the interaction frequency, and, eventually we measure the diffusive regime. However, the friction related to binary collisions between benzene molecules is too small. Thus, we suggest that collisions take place between single benzene molecules and small cluster of molecules (or group of molecules which stick together for a lapse of time). This is congruent with the picture of a melting process where coexistence between

Table 5.5: Mean free path evaluated from elementary kinetics theory [2, 101, 148] for the different coverage samples.

	$\bar{l}$ Å	$\bar{Q} = 2\pi/\bar{l}$ Å^{-1}
0.1 ML	15.3	0.41
0.2 ML	7.7	0.82
0.5 ML	3.1	2.1
1.0 ML	1.5	4.1

liquid and solid phase takes place. The dependence on temperature, that we will discuss in the following section, should bring new clues to understand the diffusive behavior of benzene molecules.

Dependence on temperature

In the previous section, it was seen that the experimental friction parameters for translations and rotations are coverage dependent. We want to study now its dependence on temperature, since this is a key marker for identifying the main source of friction. Phononic and electronic friction should be temperature independent, while collisional friction changes with temperature. We summarize the data found for the different coverages.

0.1 ML data We consider now the temperature evolution of the translational and rotational quasi-elastic broadening extracted from model 4. We recall that at very low coverage the ballistic translations and rotations of the molecules on the surface becomes apparent. The dynamics is completely driven by temperature, since the main parameter is the mean square velocity which determines the slope of the linear law of Q followed by the translational quasi-elastic broadening. Values for the resulting mean square velocity, are shown in Fig. 5.6 and summarized in Tab. 5.6. We include the theoretical mean square velocities calculated via the equipartition theorem for comparison.

The resulting values of the mean square velocity at different temperatures follow the equipartition theorem, supporting the hypothesis that the translational diffusive behavior of the benzene molecules is ballistic. The interpretation of the mean square angular velocity is more problematic, since we distinguish two Q regimes. In Tab. 5.6 we summarize the obtained values

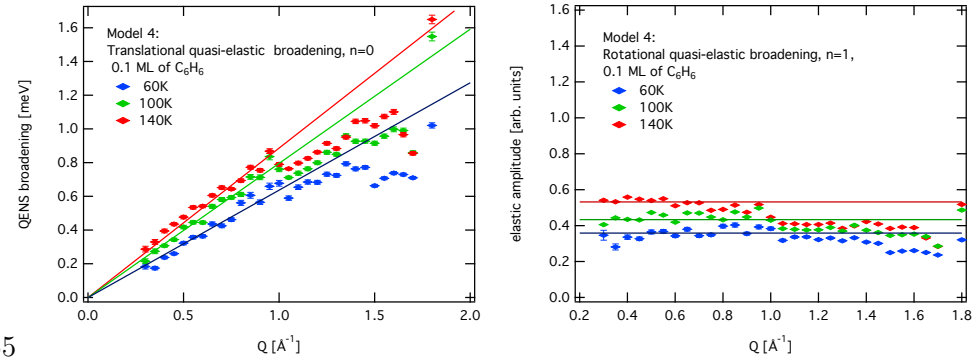

55

Figure 5.6: Right panel: Translational quasi-elastic broadening extracted from the fitting of the 0.1 ML data to model 4. Left panel:Rotational quasi-elastic broadening extracted from the fitting of the 0.1 ML data to model 4. For the translational component, we have performed a linear square fit to a linear law of the momentum transfer, while for the rotational quasi-elastic broadening we consider a constant value. We observe in both cases that the experimental data deviates from theoretical predictions in the Q range matching the molecule dimensions.

Table 5.6: Mean square velocity and mean square angular velocity from fitting of the 0.1 ML data to and 4. We include the theoretical values calculated via the equipartition theorem

Temperature [K]	$\langle v^2 \rangle$ [Å^2.ps^{-2}]		$\langle \omega^2 \rangle$ [10^{-1} ps^{-2}]		
	Model 4	Equipartition theorem	Model 4 (low Q)	Model 4 (high Q)	Equipartition theorem
60	1.35±0.02	1.28	2.14±0.03	1.83±0.01	2.05
100	2.11±0.03	2.13	3.12±0.04	2.36±0.01	3.41
140	2.62±0.02	2.98	4.70±0.04	3.07±0.01	4.77

from the fitting of the low Q range. The mean square angular velocity and translational velocity are very easily connected, $\langle\omega^2\rangle = \langle v^2\rangle / \rho^2$ (ρ being the radius of the molecule). In the fitting process, we have used this relation to connect the HWHM of the translational part (the Gaussian term with $n = 0$) to the HWHM of the rotational part (of the Gaussian functions with $n > 1$ in the summation of Eq. 4.42). We observe that the linear law of Q is violated at high Q values, suggesting that a more reliable value for $\langle v^2\rangle$ can be obtained from restricting the fitting to the low Q values. Conversely, rotations dominate the scattering signal at high Q values, and, thus we should prefer the resulting $\langle\omega^2\rangle$ values extracted from the fitting of the high Q range data. But, we should also be awared of the effects of non Gaussian terms in the SF for high Q values. We estimate reductions bewtween the 14 % up to the 35 % of the fitted $\langle\omega^2\rangle$ values at high Q with respect to their estimated values at low Q range. This is compatible with the reduction of the HWHM of the SF for high values of the momentum transfer, due to the inclusion of non-Gaussian corrections, as studied in Ref. [102].

0.2 ML, 0.5 ML and 1.0 ML data In contrast with the low coverage data, the medium and high coverage data are, better fitted by Lorentzian shaped models such as model 3 or 6. These models describe a situation in which molecules undergo translations and rotations, but there exist a substantial friction (model 3) or energy barriers (model 6) hindering the motion. We recall that model 3 and 6 have the same translational quasi-elastic broadening corresponding to the HWHM of the Lorentzian function indexed with $n = 0$ in model 3. We perform a least square fit of the translational quasi-elastic broadening to a quadratic law of the momentum, as predicted by the two models. We extract the diffusion coefficient related to translations and the corresponding friction parameter. The experimental quasi-elastic broadening and the fitted results are displayed in Fig. 5.8, and the extracted translational diffusion coefficients and friction parameters are summarized in Tabs. 5.7 and 5.8 respectively. The quasi-elastic broadening due to the rotational motion is taken from the first term of the rotational scattering function indexed with n=1. It should be independent from the momentum transfer, and we can deduce the rotational diffusion coefficient and the frictional parameter. The resulting diffusion coefficient and friction parameters can be found in Tabs. 5.9 and 5.10 respectively.

As we already saw in the coverage analysis, the translational quasi-elastic broadening follows the theoretical quadratic law in a very narrow range of Q values. The dependence with temperature of the diffusion coefficient and the friction parameter is smoother if compare with their strong variation with

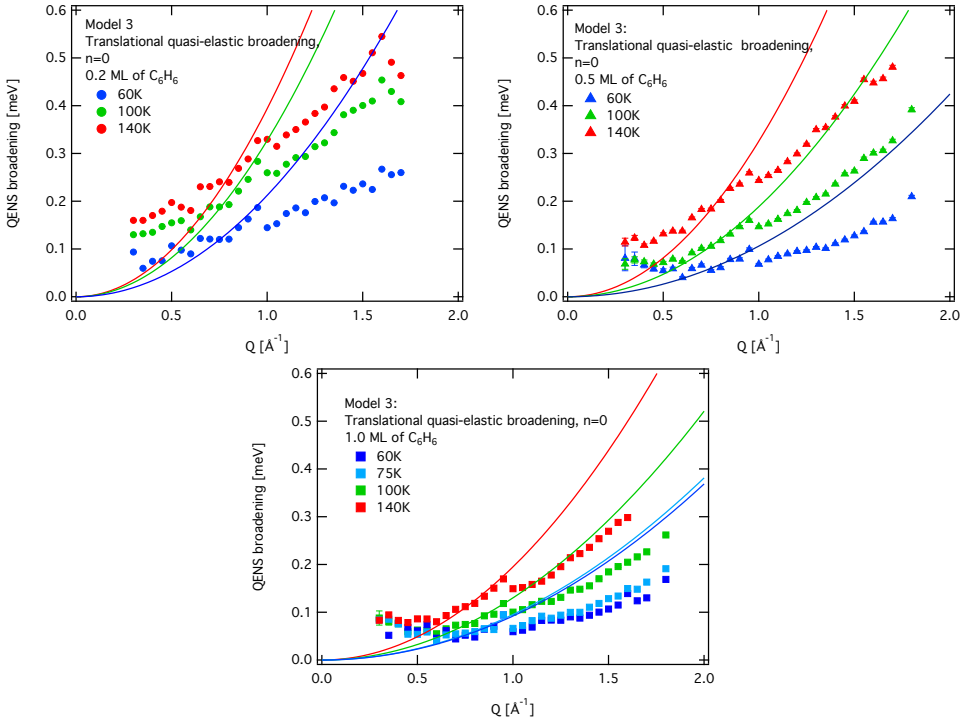

Figure 5.7: Translational quasi-elastic broadening extracted from the fitting of the 0.2 ML, (top left) 0.5 ML (top right) and 1.0 ML (bottom) to models 3. We have performed a linear square fit to a quadratic law of the momentum transfer, to check if the extracted parameter agree with the theoretical predictions. The solid line corresponds to the fitting to model 3. We recall that model 6 presents the same translational quasi-elastic broadening.

Table 5.7: *Translational* diffusion coefficient extracted from the fitting of the 0.2 ML, 0.5 ML and 1.0 ML data to model 3.

	$D_T[10^{-1}$ Å^2.ps$^{-1}]$			
Temperature [K]	0.2 ML	0.5ML	1.0 ML	1.0 ML simulated in Ref. [34]
60	3.22±0.05	1.61±0.02	1.39±0.03	0.25
75			1.44±0.02	0.5
100	4.50±0.04	2.87±0.02	1.98±0.02	1.0
140	5.9±0.3	4.95±0.02	2.97±0.01	5.5

Table 5.8: *Translational* friction parameter extracted from the fitting of the 0.2 ML, 0.5 ML and 1.0 ML data to model 3. We include the friction parameter calculated with the collision model

	η_T [ps^{-1}]					
Temperature [K]	0.2 ML		0.5 ML		1.0 ML	
60	1.98±0.02	0.3	3.97±0.04	0.61	4.8±0.1	1.22
75					5.54±0.06	1.37
100	2.14±0.02	0.30	3.71±0.02	0.79	5.39±0.04	1.58
140	2.5±0.31	0.35	3.012±0.009	0.94	5.03±0.02	1.87

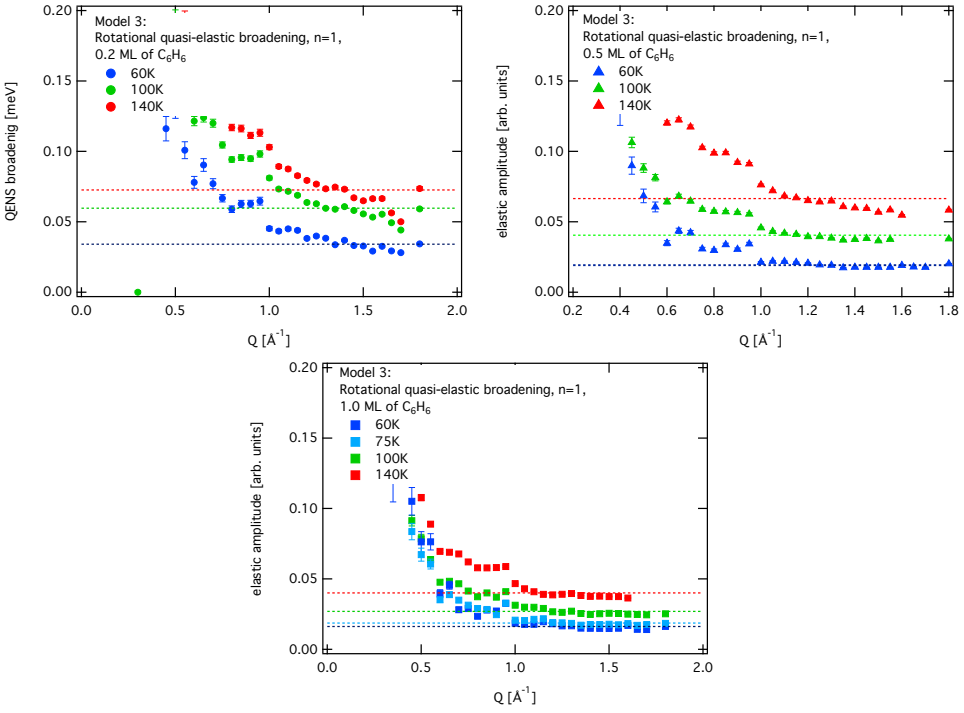

Figure 5.8: Rotational quasi-elastic broadening extracted from the fitting of the 0.2 ML, (top left) 0.5 ML (top right) and 1.0 ML (bottom) to model 3. Since models established this is a Q independent parameter, we have fitted it to a constant value. The dotted line represents the fitted line.

Table 5.9: *Rotational* diffusion coefficient extracted from the fitting of the 0.2 ML, 0.5 ML and 1.0 ML data to model 3.

	$D_R[10^{-1}$ ps$^{-1}]$		
Temperature [K]	0.2 ML	0.5ML	1.0 ML
60	0.518±0.003	0.292±0.001	0.247±0.001
75			0.284±0.001
100	0.906±0.003	0.591±0.002	0.410±0.001
140	1.103±0.005	1.006±0.002	0.608±0.001

Table 5.10: *Rotational* friction parameter extracted from the fitting of the 0.2 ML, 0.5 ML and 1.0 ML data to model 3. We include the friction parameter calculated with the collision model

	η_R [ps^{-1}]					
Temperature [K]	0.2 ML		0.5 ML		1.0 ML	
60	7.72±0.05	0.17	13.70±0.05	0.44	16.21±0.09	0.89
75					17.63±0.08	0.99
100	7.36±0.02	0.22	11.28±0.03	0.57	16.29±0.04	1.14
140	8.46±0.03	0.25	9.28±0.01	0.68	15.36±0.03	1.35

coverage. This suggest that the key parameter governing diffusion is coverage more than temperature. In the case of 0.2 ML, we observe that the friction parameter increases with temperature, which is in agreement with the collisional model, even though the theoretical and the experimental values strongly differ (one order of magnitude). Conversely the decreasing 0.5 ML and 1.0 ML of the friction parameter with increasing temperature contradicts the predictions of the collisional model. We also compare the diffusion coefficients measured for the 1.0 ML data, and the values extracted from MD simulations in Ref. [34]. The simulated results display a sudden increase of the diffusion coefficient between 100K and 140K, which is also present in our experimental data, but in an attenuated way. This is related to the melting process of the adsorbed layer between 130 K - 140 K described and analyzed in Ref. [34]. From this perspective, the jump rotational model 6 is enlightening: a trace of jump diffusion can exist at high coverages related with the melting process of the adlayer studied in Ref. [34] and with the observed tendency of benzene molecules to form two dimensional clusters [41]. This can explain the very high rotational friction parameters that we extract from the fitting. The existence of activated process can also explain the decrease with temperature of the translational and the rotational friction parameters. If there is a combination of continuous and jump diffusive behaviors, two thermally sensitive processes affecting the mobility of the molecules will take place simultaneously with the rising of temperature. First of all, the collisional friction will increase with temperature reducing the mobility (the diffusion coefficient) of the molecules. Simultaneously, a rising of the temperature allows to overcome the activation barrier and the diffusivity of the molecules is enhanced. This two effects can balance each other, and the dependence with temperature of the diffusion coefficient and the friction parameter is attenuated. Fig. 5.9 displays the jump rates extracted from the fitting to the experimental data and Tab. 5.11 summarizes the results of the fitting of the jump rate to a constant value. We recall that the jump rate is, in theory, Q independent. Therefore it should be fitted to a constant value whose change in temperature follows an Arrhenius law of the form [56]:

$$\frac{\hbar}{\tau} = \frac{\hbar}{\tau_0} \exp[-\frac{E_a}{K_b T}], \tag{5.3}$$

where $\frac{1}{\tau_0}$ is the prefactor and E_a is the activation energy. The results are summarized in Tab 5.12 and the fitted data are displayed in the bottom right part of Fig. 5.9. The resulting activation energy changes slightly with coverage passing from 6 meV for the 0.2 ML to 10 meV for 0.5 ML. We observe that a similar activation energy of 17 meV was measured in Ref. [45]. An energy barrier of 8 - 10 meV corresponds to an activation temperature of 90 K - 120 K respectively.

To conclude, we observe that the dependence of the diffusion coefficient

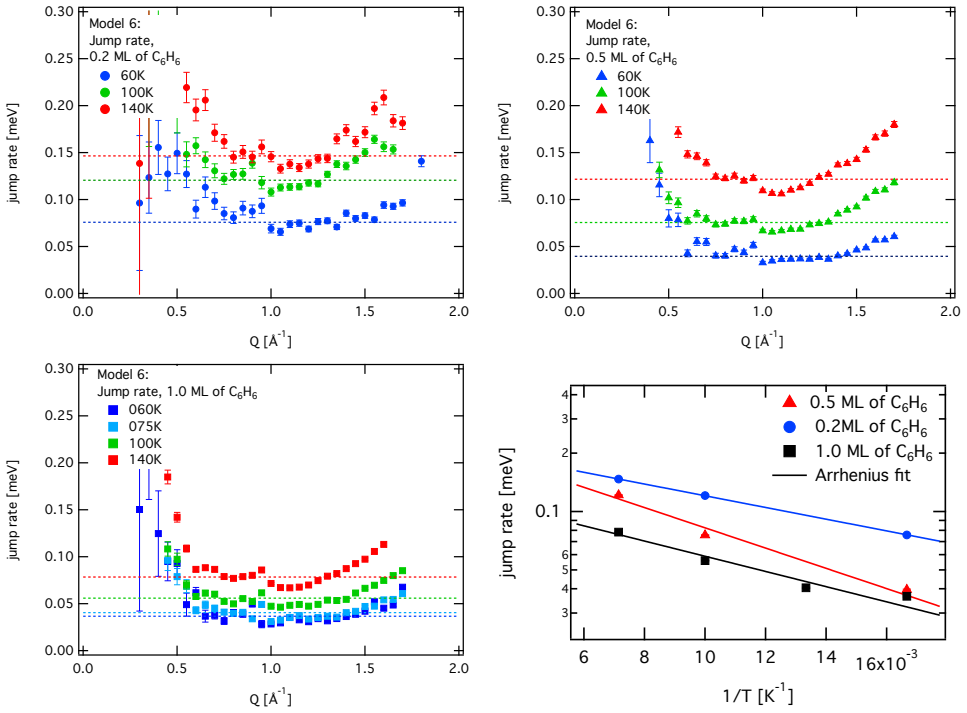

Figure 5.9: Jump rate extracted from the fitting of the 0.2 ML, (top left) 0.5 ML (top right) and 1.0 ML (bottom) to models 6. We fit set of jump rates to a constant value, and the resulting fitted jump rates are adjusted to an Arrhenius (bottom right).

Table 5.11: Fitted values resulting from the fitting to a constant of the jump rate arising from the fitting of the 0.2 ML, 0.5 ML and 1.0 ML data to model 6.

	$1/\tau$ [$\times 10^{-1}$ps^{-1}]		
Temperature [K]	0.2 ML	0.5ML	1.0 ML
60	0.76±0.01	0.396±0.004	0.366±0.003
75			0.405±0.003
100	1.21±0.01	0.756±0.004	0.559±0.003
140	1.47±0.01	1.216±0.005	0.784±0.003

Table 5.12: Prefactor and activation energy arising from the fitting to an Arrhenius law of the jump rates

Coverage	$\hbar/\tau_0$ [10^{-1} meV]	E_a [meV]	E_a/k_B [K]
0.2 ML	2.42±0.04	6.0±0.9	70±1
0.5 ML	2.74±0.03	10.3±0.9	120±1
1.0 ML	1.45±0.01	7.77±0.08	90.2±0.9

and the friction parameters on temperature is not as strong as it is with coverage. Thus, the density of molecules adsorbed on the substrate (coverage) is the principal parameter governing the diffusive behavior of the molecules. We have identify the main source of friction as the adsorbate-adsorbate interaction since the phononic and the electronic friction are temperature and coverage independent. Besides, the estimated value for the phononic friction, $1.98\times10-2.\mathrm{ps}^{-1}$, is far too small to match the very high friction parameters that we extract from the fitting of the experimental data. On the other hand, the simplistic collisional model considering only binary collisions between single benzene molecules also provides very small values for the translational and the rotational friction parameter. Furthermore, we observe that only the friction parameters extracted from the 0.2 ML increase with temperature as stated by the collisional model. For higher coverage, the friction parameter tends to decrease (very smoothly) with temperature, even though it is still presenting a remarkably high value at 140 K. An improvement of the collisional model would consist in estimating the friction arising from the collision of single benzene molecules with small clusters of molecules. On the one hand, the estimated collisional friction would increase proportionally with the mass of the cluster, and in the other hand this situation is compatible with the melting process of the adsorbed monolayer of benzene on graphite which yields a solid-liquid coexistence phase between 130 K and 160 K, studied in Ref. [34] and with the tendency of benzene molecules to aggregate in two dimensional clusters [41]. From this point of view, we have extracted an activation energy of 10 meV from the thermal dependence of the rotational jump rates of model 6, suggesting that there is a combination of jump and continuous diffusive regimes, in the high coverage regime above 0.5 ML. This could be related to the coexistence of free molecules with clusters characterizing melting processes.

5.3 Deuterated benzene

In the previous section we discussed with detail the diffusive regime of hydrogenated benzene on graphite as a function of coverage and temperature. We concluded that coverage is the parameter governing the diffusive behavior of the adsorbates. At very low coverages (0.1 ML) the ballistic motion related to the very short time behavior of Brownian particles is apparent. As soon as the coverage increases (0.2 ML) the mean free path is so strongly reduced that only the diffusion regime, characterized by the linear mean square displacement with time, is observable. For high coverages, above 0.5 ML, we also measure an activation energy barrier which could be related with the coexistence of small clusters and free molecules, as it typically happens in melting processes. In this section, we turn our attention to the diffusive behavior of deuterated benzene. We have measured two distinct coverages: 0.5 ML and 0.9 ML. The small scattering cross section of deuterated benzene does not allow us to measure smaller coverages, and we should restrict our study to the high coverage regime. In the previous chapter, we analyzed the quasi-elastic energy profiles arising from the diffusion of deuterated benzene on the basal plane of graphite. A number of models have been applied to understand the diffusive behavior of the hydrogenated data. The same models have also been applied to the deuterated benzene experimental data. We analyze in the following the output of the different theoretical approaches to the diffusion of deuterated benzene. The dependence on coverage and temperature is also discussed, since it contains the signature of the main source of friction in the system and allows to identify the atomistic mechanisms which govern the diffusive process.

5.3.1 Comparison between models

As we have done previously with hydrogenated benzene, we test several models describing different diffusive behaviors. We start discussing the dependence on Q of these parameters on which the diffusion models do not state any particular form. Fig 5.10 summarizes the elastic amplitude, the quasi-elastic amplitude and the offset arising from the fitting of models 1 to 4 to the 0.5 ML and the 0.9 ML deuterated benzene data.

The elastic amplitude: adsorbed layer diffraction pattern The first striking difference between deuterated and hydrogenated benzene scattering is that the elastic amplitude of the former does not decay with the momentum transfer. The 0.9 ML data elastic amplitude displays a peak at $Q = 1.12\text{Å}^{-1}$ which is identified as the (01) reflexion of the adsorbed benzene layer, accord-

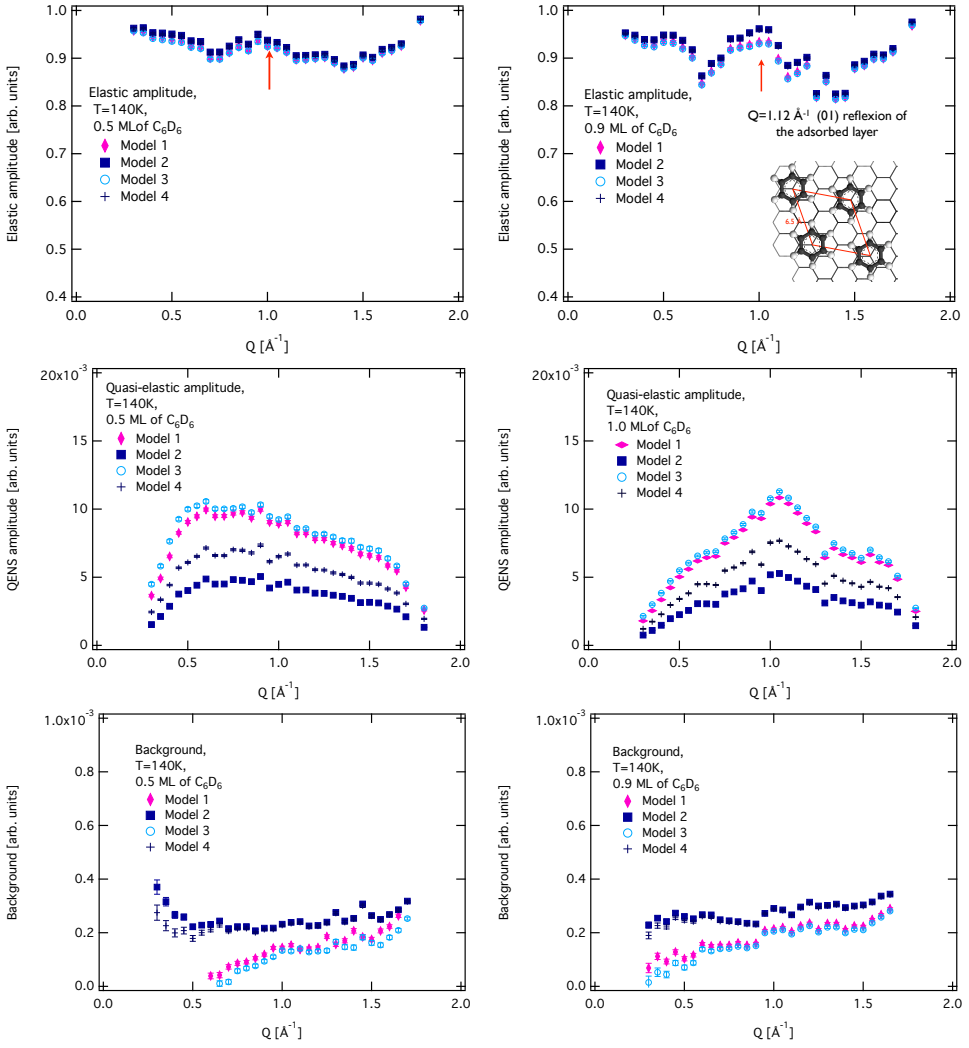

Figure 5.10: Top panel: elastic intensities for the 0.5 ML (left) and the 0.9 ML (right) deuterated benzene data. Medium panel: quasi-elastic intensities for the 0.5 ML (left) and the 0.9 ML (right) deuterated benzene data. Bottom panel: background for the 0.5 ML (left) and the 0.9 ML (right) deuterated benzene data.

ing to Ref. [41]. The same peak is also present in the elastic amplitude of the 0.5 ML data, but with a weaker intensity (because of the lower density of adsorbed benzene molecules). We recall that deuterated benzene is characterized by a strong coherent scattering cross-section and, hence, the scattered elastic amplitude contains not only the diffraction pattern of the graphite substrate, but depends as well on the diffraction pattern of the adsorbed layer. The observation of the (01) reflexion indicates the presence of an ordered two dimensional adsorbed layer with hexagonal symmetry and a lattice parameter of 6.5 Å(see inset in Fig. 5.10) [41]. However, the presence of the same peak at two different coverages, 0.5 ML and 0.9 ML suggest that molecules do not spread evenly on the surface, otherwise the lattice parameter and, hence, the position of the Bragg peak would be coverage independent [41]. This is a clear indication that benzene molecules form two dimensional clusters on the surface, and supports our hypothesis that the very high friction observed in the hydrogenated benzene data comes from the collision between benzene molecules and aggregates.

The quasi-elastic broadening We continue the discussion with the comparison of the quasi-elastic broadenings arising from the fitting of the data to the different models. Fig. 5.11 displays the resulting quasi-elastic data for the 0.5 ML and the 0.9 ML data. We should keep in mind that in models 3 and 4, where summation of quasi-elastic lines are considered, the translational quasi-elastic broadening is the HWHM of term indexed with $n = 0$ in the summation. As it happens with the hydrogenated benzene data, there are two clearly ranges of momentum transfer. The Gaussian shaped models 2 and 4 provide quasi-elastic broadenings which follow the theoretically predicted linear law of Q in the low Q range. However we saw in the previous chapter, that the shape of the quasi-elastic profile displays a clear Lorentzian shape and is better fitted by model 1, and specially, by model 3. However, the resulting quasi-elastic broadening for model 3 only follows the expected quadratic law of the momentum transfer at high Q values, while it is flat in the low Q range where the coherent signal is at its maximum. This is logical since the Bragg peak of the adsorbed layer is located in $Q = 1.12$ Å^{-1}. Hence, we understand the Lorentzian line shape of the spectrum [149] and the flat Q dependence of the coherent quasi-elastic broadening in the momentum transfer range nearby the Bragg peak: The quasi-elastic broadening is shadowed by the strong elastic intensity coming from the Bragg scattering in this particular direction, and the dynamics taking place in this Q range remains hidden. As soon as the influence of the Bragg peak decreases (in the high Q range), we recover the quadratic law of the momentum transfer.

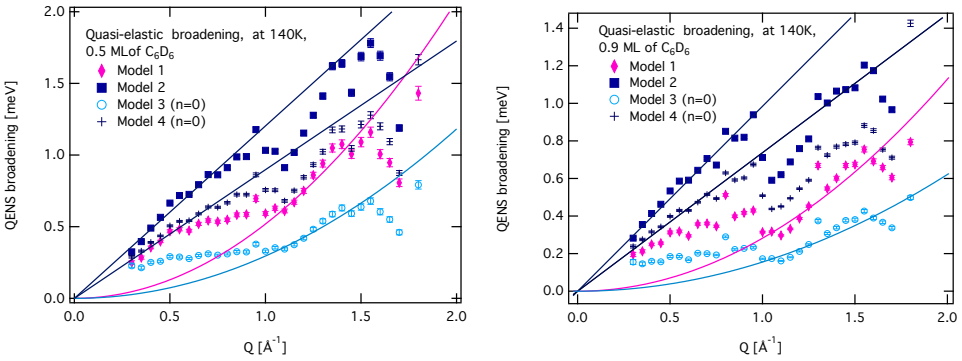

Figure 5.11: Quasi-elastic broadenings extracted from the fittings of the 0.5 ML (left) and 0.9 ML (right) deuterated benzene scattering function to all the models. We recall that models 3 and 4 contain summations of quasi-elastic lines. The corresponding quasi-elastic broadenings is the HWHM of the quasi-elastic line indexed with $n = 0$. We include guides for the eye, underlining the linear or quadratic dependence on Q

5.3.2 The quasi-elastic broadening dependence on coverage

In this section we analyze the dependence of the quasi-elastic broadening on coverage. We already saw with the hydrogenated benzene results that coverage plays an essential role and determines the diffusive behavior of the molecules. In the case of deuterated benzene, the statistical quality of the signal is limited by the small scattering cross-section of the adsorbed layer. Thus the low coverage regime can not be probed, and we only have experimental data for the medium, 0.5 ML, and the high 0.9 ML coverage regimes. Fig. 5.12 shows the translational and the rotational quasi-elastic broadening for 0.5 ML and 0.9 ML of deuterated benzene and the fitting to a quadratic law of the momentum transfer. Remember that the translational quasi-elastic broadening is the HWHM of the Lorentzian function whose summation index is $n = 0$, while we call rotational quasi-elastic broadening to the HWHM of the Lorentzian function index with $n = 1$. Tab. 5.13 summarizes the diffusion coefficients and the corresponding friction parameters.

As it was the case for hydrogenated benzene, the diffusion coefficients and the friction parameters of deuterated benzene are highly dependent on coverage. This confirms that the main friction source comes from the adsorbate-adsorbate interaction, and more probably from the collisions between molecules and clusters coexisting on the surface. The agreement between the translational friction parameter of hydrogenated and deuterated benzene, proves that in the high Q range, deuterated benzene molecules become incoherent scatter-

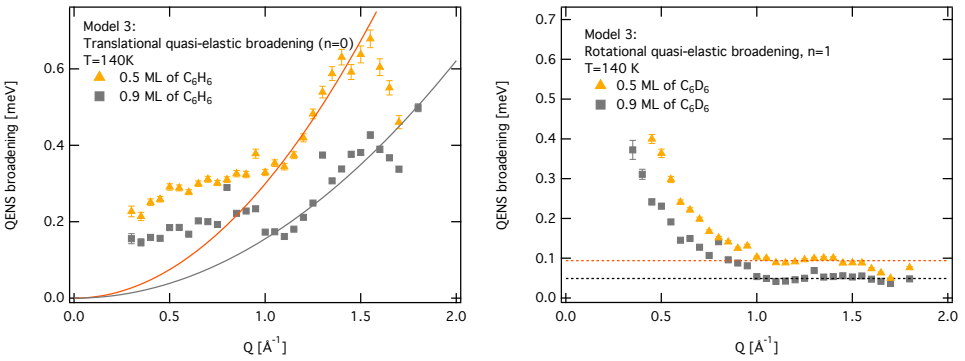

Figure 5.12: Translational (left) and rotational (right) quasi-elastic broadening resulting from the fitting of the 0.5 ML and 0.9 ML deuterated benzene data to model 3 at 140K. The solid lines stand from the leas square fit of the translational quasi-elastic broadening to a square law of Q, or to a constant value in the case of the rotational quasi-elastic broadening.

Table 5.13: Deuterated benzene data at 140K fitted values for the diffusion coefficient and friction parameter.

Coverage	$D_{trans}[10^{-1}$ Å^2.ps$^{-1}]$	η_T [ps^{-1}]	$D_R[10^{-1}$ ps$^{-1}]$	η_R [ps^{-1}]
0.5 ML	4.56±0.05	3.03±0.05	1.43±0.03	5.0±0.1
0.9 ML	2.36±0.01	5.87±0.03	0.75±0.01	9.6±0.1

ers. We shall analyze with more detail the comparison between hydrogenated and deuterated benzene in the last section.

5.3.3 Dependence on temperature

Even though temperature has not the decisive influence on the diffusive regime that coverage has, the thermal evolution of the quasi-elastic broadening allows to identify the physical mechanisms underlying diffusion. In particular, we know that phononic and electronic friction are temperature independent. Conversely, collisional friction and activated diffusion process display strong changes with temperature. In this section, we analyze the effect of temperature in the 0.9 ML d-benzene data. The translational and rotational quasi-elastic broadenings for the thermal range comprised between 60K and 140K are displayed in Fig. 5.13 and Tab. 5.14 summarizes the numerical values of the diffusion coefficients and the friction parameters extracted from the fittings.

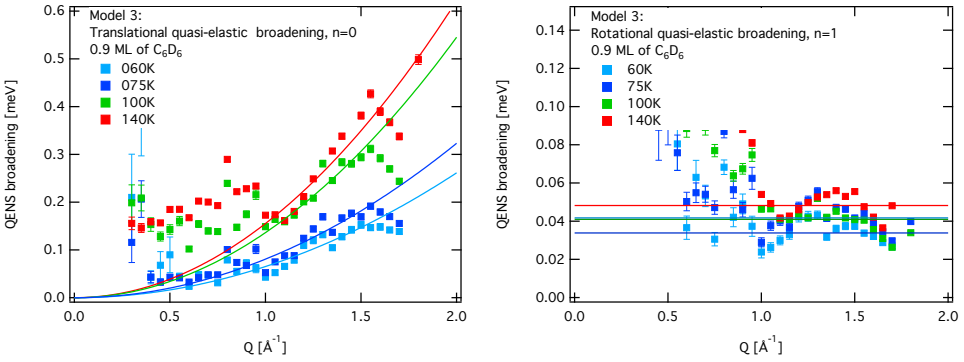

Figure 5.13: Translational (left) and rotational (right) quasi-elastic broadening resulting from the fitting of the 0.9 ML deuterated benzene data to model 3 in all the range of temperatures. The solid lines stand from the leas square fit of the translational quasi-elastic broadening to a square law of Q, or to a constant value in the case of the rotational quasi-elastic broadening.

We observe that the friction coefficients are depending on the temperature in agreement with what was observed for hydrogenated benzene, and with the hypothesis that friction arises from collisions between adsorbates. However, we observe that the trends of the translational and the rotational friction parameters with temperature are different. The translational friction changes smoothly with temperature and displays a minimum for 100K. Conversely the rotational friction increases with temperature, obeying the predictions of the collisional model. Nevertheless, we have to stress that the rotational quasi-elastic broadening is meant to be Q independent, while experimentally

Table 5.14: 0.9 ML d-benzene data estimated values for translational and rotational diffusion coefficient and friction parameter.

Temperature [K]	$D_T[10^{-1}$ Å^2.ps$^{-1}]$	η_T [ps^{-1}]	$D_R[10^{-2}$ ps$^{-1}]$	η_R [ps^{-1}]
60	0.99±0.02	6.01±0.09	5.14±0.08	5.99±0.09
75	1.12±0.02	6.11±0.08	6.34±0.08	6.07±0.07
100	2.07±0.02	4.79±0.04	6.2±0.1	8.3±0.2
140	2.36±0.01	5.87±0.02	7.5±0.1	9.6±0.1

it presents variations on Q, even though they are appreciable in a narrow energy window (note that the energy scale in the right panel of Fig. 5.13 is tighter to the data).

To conclude, the study of the diffusive behavior of deuterated benzene brings enlightening perspectives which support and improve the understanding of the diffusive behavior of benzene adsorbed on graphite that we had already undertaken with the study of hydrogenated benzene diffusion. 1) the observation of the (01) Bragg reflexion of the adsorbed layer at different coverages, indicates that benzene tends to aggregate in clusters with a well defined hexagonal symmetry and a lattice parameter of 6.5 Å. This is in agreement with the picture of the adsorbed layer melting process taking place between 130 K and 160 K, where liquid and solid phases coexist. Furthermore, this supports the hypothesis that the very high friction measured for translations and rotations comes from the collision of free benzene molecules and clusters, and that there is a trace of jump diffusive processes related to jump reorientations of the molecules within clusters. 2) The presence of the Bragg peak at $Q = 1.15$Å^{-1} shadows the quasi-elastic intensity, and the dynamics taking place in this distance window is hidden. As a result the coherent quasi-elastic broadening in the low range of Q is flat and Q independent, because it is not related to a dynamical process. It simply arises from neutron diffracted intensity in this direction of the space. This does not happens with hydrogenated benzene, because its scattering is largely dominated by protons which display a very large incoherent scattering cross-section 3) We recover the incoherent scattering at high values of Q, when the influence of the adsorbed layer Bragg peak decreases. Then, the quasi-elastic broadening follows a quadratic law of the momentum transfer, like in the hydrogenated benzene situation, from which we extract the diffusion coefficients and the friction parameters for translations and rotations. Both parameters show a strong dependence on coverage and temperature, confirming that the main source for friction in the

system benzene/graphite should come from adsorbate-adsorbate interactions (more precisely, collisions). We shall now compare with more detail the hydrogenated and deuterated benzene results, in order to verify the quality of our results and the validity of our assumptions.

5.4 Comparison of the hydrogenated and deuterated benzene experimental results

The comparison between the quasi-elastic broadening of hydrogenated and deuterated benzene and the resulting diffusion coefficients and friction parameters is an essential step to verify the validity of our assumptions and conclusions on the diffusive behavior of benzene adsorbed on graphite. In this section we compare the 0.5 ML ToF data with the results obtained using helium and neutron spin-echo reported in Ref. [45].

5.4.1 Comparison of the 0.5 ML data at 140K

From the collection of diffusion models that we presented in chapter 4, we have see that the Lorentzian shaped models 1 and 3 provide a good quality fitted profile for the medium coverage data. Hydrogenated and deuterated time of flight scattering functions have both been fitted to these two models. On the other hand, the Helium and neutron spin echo experimental results reported in Ref. [45] show that the intermediate scattering functions of 0.5 ML of hydrogenated deuterated benzene at 140K can be fitted to a single exponential decay in all the Q range up to 1.5 Å^{-1}. Fig 5.14 compares the quasi-elastic broadenings extracted, from our time of flight measurements on hydrogenated and deuterated benzene to the Helium and neutron spin-echo results published in Ref. [45]. The left panel of Fig. 5.14 displays the quasi-elastic broadenings extracted from model 1 which is the same theoretical model than the authors of Ref. [45]: a single Lorentzian function in energies corresponds to a single exponential decay in the time domain. Important deviations exist between the time of flight and the spin-echo quasi-elastic broadenings: The former display a higher energy mobility (especially for the deuterated benzene molecule) and does not follow a parabola of Q. The right panel of 5.14 displays the translational broadenings extracted from model 3 together with the helium and neutron spin echo data. We recall that model 3 consists in a summation of Lorentzian functions in the energy domain, or equivalently, in a summation of exponential decays in the time domain. We observe that the h-benzene quasi-elastic broadening (the HWHM of the term indexed with $n = 0$) matches the range of values of the Helium spin-echo broadening at the low Q range (where

the diffusive behavior is observable) while the d-benzene data match the high Q range, where its scattering intensity becomes namely incoherent. The diffusion coefficients and the friction parameters are summarized in Tab. 5.16.

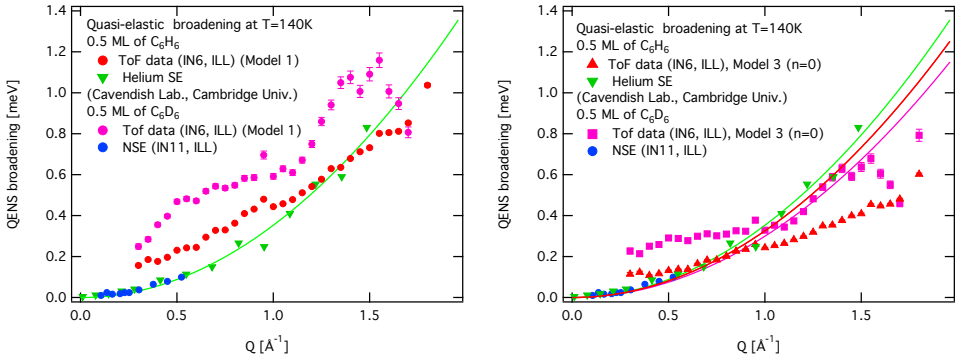

Figure 5.14: Comparison of the quasi-elastic broadening measured on 0.5 ML of hydrogenated and deuterated benzene at 140K with different techniques. In the left panel we display the quasi-elastic broadening of the ToF data according to model 1. In the right panel we display the translational quasi-elastic broadening which corresponds to the HWHM of the term $n = 0$ in the summation of Lorentzian functions forming the quasi-elastic profile. The helium and neutron spin-echo data have been taken from Ref. [45]. The time of flight data are the fitting results arising from the application of model 3 to the experimental spectra.

Table 5.15: 0.5 ML of hydrogenated and deuterated benzene data estimated values for the *translational* diffusion coefficient and friction parameter.. We include the ratios the deuterated and hydrogenated diffusion coefficients which should agree with the ratio of the hydrogenated and deuterated benzene masses, $m(C_6H_6)/m(C_6D_6) = 1.08$

	$D_T[10^{-1}$ Å^2.ps$^{-1}]$	Ratio $D(C_6H_6)/D(C_6H_6)$	η_T [ps^{-1}]
0.5 ML C_6H_6 (IN6)	4.95±0.01	1.06	3.012±0.009
0.5 ML C_6D_6 (IN6)	4.65±0.05	1.0	2.98±0.03
0.5 ML C_6H_6 (Helium SE)	5.32±0.01	1.14	2.805±0.007

The excellent agreement of the diffusivities and the friction parameters confirms that benzene molecules perform translations and rotations and that model 3 allows to distinguish between these two kind of motion. Indeed, the quasi-elastic broadening measured with helium and neutron spin-echo was interpreted as the energy broadening arising from molecules translating on the surface [45]. No mention to any rotational motion is done, since the experimen-

Table 5.16: 0.5 ML of hydrogenated and deuterated benzene data estimated values for the *rotational* diffusion coefficient and friction parameter.

	$D_R[10^{-1}$ ps$^{-1}]$	η_R [ps^{-1}]
0.5 ML C_6H_6 (IN6)	1.71±0.03	5.5±0.1
0.5 ML C_6D_6 (IN6)	1.006±0.002	9.28±0.01

tal ISF are fitted to a single exponential decay. Conversely, when we try to fit the ToF experimental quasi-elastic profiles to a single Lorentzian, the resulting quasi-elastic broadening is far too energetic if compare with the spin-echo results. On the other hand, when the ToF quasi-elastic profiles are fitted to a summation of Lorentzians, we observe that the HWHM of the purely translational term (the term indexed $n = 0$) matches perfectly the spin-echo results. The reason why the rotational motion is hidden for helium spin-echo, while it is clearly visible with neutron ToF is probably due to the different interaction with matter of helium and neutron probes. Helium particles are scattered by the electronic cloud of the molecule. Hence the benzene molecule appears as a hard disk, and only the motion of the CoM is visible. On the contrary, neutrons are scattered by nuclei, and the continuous rotations of the benzene molecule contributes to the coherent and incoherent scattering. Note that the neutron spin-echo data [45] cover a very low Q range, where all the terms related to rotations in model 3 (with index $n > 1$) have a negligible intensity. The only observable term is the purely translational one and the summation of Lorentzian/exponential functions is reduced to this single term. In the case of rotations we observe very important differences between the hydrogenated and the deuterated benzene values. However this large divergence is related to the fact that we considered the high Q range values of the rotational quasi-elastic broadening (see Fig. 5.8) which can be affected by the narrowing of the scattering function arising from the non validity of the Gaussian approximation for the incoherent scattering, in this range of the momentum transfer.

5.5 Conclusion

To conclude and summarize the main results, we have seen that coverage is the main parameter governing the diffusive behavior of the benzene molecules adsorbed on graphite. Ballistic diffusion is clearly visible at 0.1 ML, while Brownian diffusion dominates from 0.2 ML up to the full monolayer 1.0 ML. The resulting diffusion coefficients and friction parameters are thermally dependent, indicating that the main source for friction in this system is collisional

friction between adsorbates. However collisions between single molecules deliver a too small friction parameter. This suggest that benzene molecules collide with bigger entities like clusters. The tendency of benzene to form cluster has already been observed [41] and we find experimental evidence of the existence of clusters in our data. The elastic amplitude of the deuterated benzene scattering function displays a peak at $Q = 1.12\text{Å}^{-1}$ which corresponds to the (01) Bragg reflexion of the adsorbed layer. The position of the peak indicates that clusters present a well ordered hexagonal lattice charecterized with a lattice constant of 6.4 Å. Since the Bragg reflexion appears in the same Q position at 0.9 ML and 0.5 ML, we deduce that molecules do not spread evenly on the surface but prefer to aggregate. This is also compatible with the melting process of the adsorbed monolayer which has been studied with MD simulations in Ref. [34]. The simulated diffusion coefficients of the molecules on the plane are compatible with our experimental results. The existence of clusters is also congruent with the traces of activated diffusion in the high coverage regime, where an activation energy of 10 meV is estimated for 0.5 ML. Besides, the presence of the Bragg peak of the adsorbed layer can explain the strong differences observed between coherent and incoherent scattering: the quasi-elastic broadening is hidden by the strong elastic intensity in this range of Q and thus displays a constant energy broadening which is more related with the width of the Bragg peak than with any dynamical process on the surface. Finally, the comparison of our translational diffusion coefficient with the ones measured with helium and neutron spin-echo, confirms our interpretation of the experimental data: benzene molecules undergo translations and rotations. Indeed, helium spin-echo can not access the rotational motion of top symmetrical molecules, since it is scattered by the electronic cloud. Hence, molecules appear as hard disks and only the motion of their center of mass is visible. Conversely neutrons are scattered by the nuclei of the atoms, and are sensitive to rotations. Thus, the matching between the Helium spin-echo quasi-elastic broadening and the so-called translational broadening of model 3, confirms that molecules do rotate and that this model separates accurately the two contributions (translations and rotations).

Chapter 6

Final conclusions and future perspectives

This final chapter is devoted to summarize the main conclusions drawn from our experimental study of the diffusive behavior of benzene molecules adsorbed on the basal plane of graphite and to establish possible lines of further development of the present study.

This dissertation aims to address some of the open questions arising from the diffusion of benzene molecules on graphite surfaces and which were already explored in recent studies [45]. The experimental results published in Ref. [45] arise from neutron spin-echo, NSE, and helium-3 spin-echo, HeSE, spectroscopy measurements on 0.5 ML of benzene molecules at 140K on the basal plane of graphite substrate. They show a clear Brownian diffusive behavior of the benzene adsorbed flat on graphite. The intermediate scattering functions is fitted to single exponential decays in a very wide range of the momentum transfer ($0< Q <1.5$ Å^{-1}) [45] and it was the first experiment in which the microscopic dynamic friction coefficient could be established with a reasonable error bar [45] yielding a value of of 2.2 ps^{-1}. The interpretation of the experimental results conclude that friction is originated by phonons annihilation/creation processes on the substrate since no significant dependence on coverage is observed. Our main concern has been to understand the effects of coverage and temperature on the diffusive behavior of the adsorbates. For this purpose we have perform several measurements of neutron quasi-elastic spectrum of benzene adsorbed on graphite, at four different coverages: from the very low coverage regime 0.1 ML to the complete monolayer 1.0 ML and in a wide range of temperatures, from 60K to 140K. We use the neutron spectroscopy technique of time-of-flight and we combine measurements on hydro-

genated C_6H_6 and deuterated benzene C_6D_6. Since neutrons can be coherent or incoherently scattered, the resulting quasi-elastic spectra arising from C_6H_6 or C_6D_6 displays differences which can be attributed to correlated dynamics in time and space.

The experimental results yields different conclusions from the ones expected accordingly to Ref. [45].

- First of all we observe that the fitting of the quasi-elastic spectrum measured with time of flight, requires a summation of quasi-elastic lines in contrast with the single exponential decay which suits the HeSE and NSE data in Ref. [45]. In chapter 4 we fit the quasi-elastic energy profile to several models made of single (models 1 and 2) or summations (models 3 to 5) of quasi-elastic lines. The quality of the quasi-elastic profile fit for all the coverages improves significantly reducing in between 70 - 80 % the χ^2 parameter when we pass from model 1 (single Lorentzian function) to model 3 (summation of Lorentzian functions). The summation of quasi-elastic lines comes from the combination of translations and rotations [56, 59, 73, 81, 132]. Thus, we conclude that benzene molecules on the substrate undergo simultaneously translation and rotational motion.

- Secondly, the shape of the quasi-elastic profile depends on the coverage. The 0.1 ML data can be fitted with Lorentzian and Gaussian shaped models yielding very similar χ^2 parameter ~ 3 for models 3 (summation of Lorentzian) and 4 (summation of Gaussians). Conversely the 0.2 ML, 0.5 ML and 1.0 ML quasi-elastic profiles display a marked Lorentzian character: the χ^2 parameter increases between 65 - 85 % when passing from model 3 (Lorentzian functions summation) to model 4 (Gaussian functions summation). As a result the diffusive behavior of benzene adsorbed flat on the graphite basal plane is strongly dependent on the coverage.

- In third place and in connection with the previous point, the effect of coverage is also apparent in the dependence of the quasi-elastic broadening with the momentum transfer, as studied in Chapter 5. The 0.1 ML translational quasi-elastic broadening, extracted from the HWHM of the purely translational term ($n = 0$) of model 4, clearly follows a linear law of Q. Besides, the excellent agreement of the extracted mean square velocity with the equipartition theorem proves that benzene molecules behave as an ideal two-dimensional gas at very low coverages. Furthermore, the mean free path evaluated from its dependence with coverage, $\bar{l}$ =15.3 Å corresponds in the reciprocal space to $\bar{Q}$ =0.41 Å^{-1} and shows

that ballistic motion is perfectly observable in the range of Q covered by IN6 in the experimental conditions under which we operate (5.12Å of incoming wavelength). Conversely, at higher coverages, the translational quasi-elastic broadening display a rather quadratic dependence on Q, between 0.5 $Å^{-1}$ and 1.0 $Å^{-1}$, at distances which are larger than the molecule size. This is in agreement with the decreasing of the mean free path with increasing coverage: for 0.2 ML we calculate $\bar{l}$ =7.65 Å, yielding $\bar{Q} \sim 0.8$ $Å^{-1}$ and for 1.0 ML, $\bar{l}$ =1.53 Åcorresponding to $\bar{Q}$ =4.1 $Å^{-1}$. Thus, we recover an essential result of the elementary kinetic energy: increasing the density of adsorbates on the substrate (i.e. the coverage) reduces their mean free path (the length over which molecules behave ballistically, in the lapse of time between two collisions) [2]. Consequently, in the reciprocal space, the ballistic behavior of molecules will only be visible at values of Q higher than $\bar{Q} = 2\pi/\bar{l}$. When the monolayer is full, the mean free path of the molecules is so small, that the ballistic range of Q falls completely outside of the experimental window. In that case, we only measure the diffusive regime, dominated by collisional friction.

- The next important point is that the extracted diffusion coefficients and friction parameter change significantly with coverage, and also with temperature. In addition, a rough estimation of the phononic friction contribution provides a very low value, 1.98×10^{10} s^{-1} for the friction parameter. We deduce that the main origin of friction lies in the interaction between adsorbates. However a simple model of single molecules undergoing binary and rough collisions (exchanging linear and angular momentum) does neither deliver values matching the experimental friction.

- The study of deuterated benzene behavior brings also very interesting insight in the diffusive process. The presence of the Bragg peak attributed to the (01) reflexion of bidimensional structures formed by the adsorbates at two different coverages, 0.5 ML and 0.9 ML, is an experimental evidence of the existence of clusters. This is congruent with the melting transition of the adsorbed layer between 130K and 160K [34, 41],and can explain the very high friction parameters that we measure through the collisions between single molecules and clusters. We also study the activated diffusion of molecules and we obtain a very low energy barrier of 10 meV, which might be related to the reorientation of molecules in clusters.

- Finally, the good agreement between the translational diffusion coefficients and the diffusion coefficient extracted from the HeSE and NSE study published in Ref. [45], support the hypothesis that molecules not

only translate but also rotate. The main differences between the two techniques can be attributed to the nature of the interaction between helium particles or neutrons and matter. In conclusion, molecules do not only exchange linear momentum with their colliding target, but also angular momentum.

Future perspectives

There are several lines which can be inspected in the future. An important point is the need to model the friction parameter that we observe. We suggest that the high friction parameter measured in the system benzene/molecules arise from the interaction of single molecules with clusters. An improvement of the collisional model can be achieved, following Ref. [147], and in particular the method for calculating the friction parameter in heterogeneous systems. On the other hand, we could not explore with detail molecular dynamics simulations results performed on the system of benzene/graphite in the same range of coverages and temperatures. It would be useful to extract values for the diffusion coefficient and the friction parameter for the whole molecule but also for its center of mass. In this way, the possible coupling between translational and rotational motion can be analyzed and the role of rotations in the dynamics of the adlayer can be understood. Finally, we can measure the diffusion of very similar systems such as naphthalene and pyrene adsorbed on graphite. The change of symmetry and mass/moment of inertia ratio can affect the diffusion of these adsorbates with respect to benzene molecules. The comparison between this similar systems yields interesting information about the role of rotations, and the internal degrees of freedom of the molecules in its diffusive behavior.

Bibliography

[1] A. P. Jardine, H. Hedgeland, G. Alexandrowicz, W. Allison, J. Ellis, Prog. Surf. Sci. **84**, 323 (2009).

[2] R. Martínez-Casado, J. L. Vega, A. S. Sanz, S. Miret-Artes, J. Phys.: Condens. Matter **19**, 305002 (2007).

[3] S. J. Stranick, A. N. Parikh, D. L. Allara, P. S. Weiss, The Journal of Physical Chemistry **98**, 11136 (1994).

[4] T. Ala-Nissila, R. Ferrando, S. C. Ying, Advances in Physics **51**, 949 (2002).

[5] J. V. Barth, Surf. Sci. Rep. **40**, 75 (2000).

[6] A. G. Naumovets, Physica A **357**, 189 (2005).

[7] X. Xia, S. Xie, M. Liu, H.-C. Peng, N. Lu, J. Wang, M. J. Kim, Y. Xia, Proceedings of the National Academy of Sciences (2013).

[8] T. Sherwood, XXth Int. Congr. Pure appl. Chem (1965).

[9] Y.-z. Hu, T.-b. Ma, H. Wang, Friction **1**, 24 (2013).

[10] Y. Mo, K. T. Turner, I. Szlufarska, Nature **4**, 1116 (2009).

[11] B. Persson, Surface Science Reports **33**, 83 (1999).

[12] R. Guerra, U. Tartaglino, A. Vanossi, E. Tosatti, Nature Mat. **9**, 634 (2010).

[13] A. Barreiro, R. Rurali, E. R. Hernández, J. Moser, T. Pichler, L. Forró, A. Bachtold, Science **320**, 775 (2008).

[14] D. Dundas, E. J. McEniry, T. N. Todorov, Nat Nano **4**, 99 (2009).

KEY: Dundas:2009aa
ANNOTATION: 10.1038/nnano.2008.411

[15] H. L. Tierney, C. J. Murphy, A. D. Jewell, A. E. Baber, E. V. Iski, H. Y. Khodaverdian, A. F. McGuire, N. Klebanov, E. C. H. Sykes, Nat Nano **6**, 625 (2011).

KEY: Tierney:2011aa
ANNOTATION: 10.1038/nnano.2011.142

[16] A. P. Jardine, G. Alexandrowicz, H. Hedgeland, W. Allison, J. Ellis, Phys. Chem. Chem. Phys. **11**, 3355 (2009).

[17] D. A. Reed, G. Ehrlich, Surface Science **102**, 588 (1981).

[18] J. P. Boon, S. Yip, *Molecular hydrodynamics* (Courier Dover Publications, 1980).

[19] A. Einstein, Annalen der Physik **4**, 289 (1906).

[20] R. Kubo, Reports on Progress in Physics **29**, 255 (1966).

[21] J. P. Hansen, I. R. McDonald, *Theory of Simple Liquids* (Academic Press, 2005).

[22] González, M.A., JDN **12**, 169 (2011).

[23] P. Fouquet, M. R. Johnson, H. Hedgeland, A. P. Jardine, J. Ellis, W. Allison, Carbon **47**, 2627 (2009).

[24] J. Z. Larese, Current Opinion in Solid State and Materials Science **2**, 539 (1997).

[25] I. Calvo-Almazán, P. Fouquet, The European Physical Journal Special Topics **213**, 149 (2012).

[26] S. M. Clarke, Current Opinion in Colloid and Interface Science **6**, 118 (2001).

[27] R. Thomas, Progress in Solid State Chemistry **14**, 1 (1982).

[28] R. Zacharia, H. Ulbricht, T. Hertel, Physical Review B **69**, 155406 (2004).

[29] A. A. Isirikyan, A. V. Kiselev, The Journal of Physical Chemistry **65**, 601 (1961).

[30] R. Pierotti, Chemical Physics Letters **2**, 420 (1968).

[31] C. Pierce, The Journal of Physical Chemistry **73**, 813 (1969).

[32] W. Rudzínski, Physics Letters A **31**, 504 (1970).

[33] L. Battezzati, C. Pisani, F. Ricca, J. Chem. Soc., Faraday Trans. **71**, 1629 (1975).

[34] M. A. Matties, R. Hentschke, Langmuir **12**, 2495 (1996).

[35] A. Vernov, W. A. Steele, Langmuir **7**, 3110 (1991).

[36] A. Vernov, W. A. Steele, Langmuir **7**, 2817 (1991).

[37] B. Boddenberg, J. A. Moreno, Journal de Physique **38**, C4 (1977).

[38] J. Tabony, J. White, J. Delachaume, M. Coulon, Surface Science Letters **95**, L282 (1980).

[39] M. Monkenbusch, R. Stockmeyer, Berichte der Bunsengesellschaft für physikalische Chemie **84**, 808 (1980).

[40] M. Monkenbusch, R. Stockmeyer, in *Ordering in Two Dimensions* (S. K. Sinha, ed.), pp. 223–226 (North Holland, Amsterdam, 1980).

[41] P. Meehan, T. Rayment, R. K. Thomas, G. Bomchil, J. W. White, J. C. S. Faraday pp. 2011–2016 (1980).

[42] H. Kubota, T. Munakata, T. Hirooka, T. Kondow, K. Kuchitsu, K. Ohno, Y. Harada, Chemical Physics pp. 399 – 403 (1984).

[43] C. Bondi, P. Baglioni, G. Taddei, Chemical Physics **96**, 277 (1985).

[44] U. Bardi, S. Magnanelli, G. Rovida, Surface Science Letters **165**, L7 (1985).

[45] H. Hedgeland, P. Fouquet, A. P. Jardine, G. Alexandrowicz, W. Allison, J. Ellis, Nature Phys. **5**, 561 (2009).

[46] L. W. Bruch, R. D. Diehl, J. A. Venables, Rev. Mod. Phys. **79**, 1381 (2007).

[47] H. Brune, Ann. Phys. **18**, 675 (2009).

[48] R. Gomer, Rep. Prog. Phys. **53**, 917 (1990).

[49] E. Seebauer, C. Allen, Progress in Surface Science **49**, 265 (1995).

[50] B. Lehner, M. Hohage, P. Zeppenfeld, Chemical Physics Letters **379**, 568 (2003).

[51] X. D. ZHU, Modern Physics Letters B **06**, 1217 (1992).

[52] J. J. Zhao, S. C. Bae, F. Xie, S. Granick, Macromolecules **34**, 3123 (2001).

[53] M. Ternes, C. P. Lutz, C. F. Hirjibehedin, F. J. Giessibl, A. J. Heinrich, Science **319**, 1066 (2008).

[54] M. Alba, M. Castro, S. Clarke, A. Perdigón, Solid State Nuclear Magnetic Resonance **23**, 174 (2003).

[55] C. P. Slichter, Annual Review of Physical Chemistry **37**, 25 (1986).

[56] M. Bée, *Quasielastic Neutron Scattering* (Adam Hilger, Bristol, 1988).

[57] R. Martínez-Casado, A. S. Sanz, J. L. Vega, G. Rojas-Lorenzo, S. Miret-Artés, Chem. Phys. pp. 180–193 (2010).

[58] S. W. Lovesey, *Theory of Neutron Scattering from Condensed Matter. Volume 1: Nuclear Scattering* (Clarendon Press, Oxford, 1984).

[59] V. F. Sears, Canadian Journal of Physics **44**, 1279 (1966).

[60] G. L. Squires, *Introduction to the theory of thermal neutron scattering* (Cambridge University Press, 1978).

[61] V. F. Sears, Neutron News **3**, 26 (1992).

[62] M. Castro, S. Clarke, A. Inaba, T. Arnold, R. Thomas, Journal of Physics and Chemistry of Solids **60**, 1495 (1999).

[63] M. A. Castro, S. M. Clarke, A. Inaba, T. Arnold, R. K. Thomas, The Journal of Physical Chemistry B **102**, 10528 (1998).

[64] M. A. Castro, S. M. Clarke, A. Inaba, T. Arnold, R. K. Thomas, Phys. Chem. Chem. Phys. **1**, 5017 (1999).

[65] J.Z., Larese, Physica B: Condensed Matter **248**, 297 (1998).

[66] C. Bockel, J. Coulomb, N. Dupont-Pavlovsky, Surface Science **116**, 369 (1982).

[67] Y. Finkelstein, D. Nemirovsky, R. Moreh, G. Kimmel, Physica B: Condensed Matter **291**, 213 (2000).

[68] E. P. Gilbert, P. A. Reynolds, J. W. White, J. Chem. Soc., Faraday Trans. pp. 1861–1868 (1998).

[69] D. D. L. Chung, Journal of Materials Science **22**, 4190 (1987).

[70] G. Witte, Surface Science **502–503**, 405 (2002).

[71] V. Sears, A. E. O. C. LIMITED., C. R. N. Laboratories, *Theory of thermal neutron scattering* (Chalk River Nuclear Laboratories, 1978).

[72] T. Springer, in *Springer Tracts in Modern Physics, Volume 64*, *Springer Tracts in Modern Physics*, vol. 64, pp. 1–100 (Springer Berlin / Heidelberg, 1972).

[73] V. F. Sears, Canadian Journal of Physics **44**, 1299 (1966).

[74] A. C. Zemach, R. J. Glauber, Phys. Rev. **101**, 118 (1956).

[75] L. van Hove, Phys. Rev. **95**, 253 (1954).

[76] K. Sköld, D. Price, *Neutron Scattering. Methods of Experimental Physics* (Elsevier Science, 1987).

[77] A. C. Zemach, R. J. Glauber, Phys. Rev. **101**, 129 (1956).

[78] C. Cohen-Tannoudji, B. Diu, F. Laloe, *Quantum Mechanics* (Wiley-Vch, 1977).

[79] V. F. Sears, V. F., Physics Reports **82**, 1 (1982).

[80] J. R. D. Copley, T. J. Udovic, Journal of Research of the National Institute of Standards and Technology **98**, 71 (1993).

[81] V. F. Sears, Canadian Journal of Physics **45**, 237 (1967).

[82] K. E. Larsson, Physical Review A **3**, 1006 (1971).

[83] A. P. Jardine, W. Allison, J. Phys.: Condesn. Matter **14**, 6173 (2002).

[84] R. Martínez-Casado, J. L. Vega, A. S. Sanz, S. Miret-Artes, Phys. Rev. Lett. **98**, 216102 (2007).

[85] J. L. Vega, R. Guantes, S. Miret-Artés, Journal of Physics: Condensed Matter **16**, S2879 (2004).

[86] H. Schober, in *Neutron Applications in Earth, Energy and Environmental Sciences* (L. Liang, R. Rinaldi, H. Schober, eds.), Neutron Scattering Applications and Techniques, pp. 37–104 (Springer US, 2009).

[87] T. Springer, R. E. Lechner, in *Diffusion in Condensed Matter* (P. Heitjans, J. Kärger, eds.), pp. 93–164 (Springer Berlin Heidelberg, 2005).

[88] ILL, *The Yellow Book 2008* (Institut Laue Langevin, Grenoble, 2008).

[89] A. Meyer, R. M. Dimeo, P. M. Gehring, D. A. Neumann, Review of Scientific Instruments **74**, 2759 (2003).

[90] M. T. F. Telling, K. H. Andersen, Phys. Chem. Chem. Phys. **7**, 1255 (2005).

[91] N. Kirov, I. Dozov, J. Jordanova, M. P. Fontana, G. B. Hadjichristov, Journal of Molecular Structure pp. 7 – 15 (2006).

[92] F. Mezei, Z. Phys. **255**, 146 (1972).

[93] F. Mezei, ed., *Neutron Spin Echo*, *Lecture Notes in Physics*, vol. 128 (Springer, Berlin, 1980).

[94] M. DeKieviet, D. Dubbers, C. Schmidt, D. Scholz, U. Spinola, Phys. Rev. Lett. **75**, 1919 (1995).

[95] J. Rush, J. Rowe, Physica B+C **137**, 169 (1986).

[96] R. Hempelmann, *Quasielastic Neutron Scattering and Solid State Diffusion* (Clarendon Press, Oxford, 2000).

[97] Coddens, G., J. Phys. IV France **10**, Pr1 (2000).

[98] S. Miret-Artes, E. Pollak, J. Phys.: Condens. Matter **17**, S4133 (2005).

[99] G. H. Vineyard, Phys. Rev. **110**, 999 (1958).

[100] R. Kubo, Journal of the Physical Society of Japan **17**, 1100 (1962).

[101] D. MCQUARRIE, *Statistical Mechanics* (Univ. Science Books, 1976).

[102] B. Nijboer, A. Rahman, Physica **32**, 415 (1966).

[103] D. Chandler, The Journal of Chemical Physics **60**, 3500 (1974).

[104] A. Rahman, K. S. Singwi, A. Sjölander, Phys. Rev. **126**, 986 (1962).

[105] F. Guillaume, JDN **12**, 3 (2011).

[106] P. Egelstaff, *An Introduction to the Liquid State*, Oxford Series on Neutron Scattering in Condensed Matter Series (CreateSpace Independent Publishing Platform, 1994).

[107] C. T. Chudley, R. J. Elliott, Proceedings of the Physical Society **77**, 353 (1961).

[108] J. P. Beaufils, Molecular Physics **55**, 433 (1985).

[109] F. E. Tuddenham, H. Hedgeland, A. Jardine, B. A. J. Lechner, B. J. Hinch, W. Allison, Surface Science **604**, 1459 (2010).

[110] S. Chandrasekhar, Reviews of Modern Physics **15**, 1 (1943).

[111] W. Steele, Chemical Reviews **93**, 2355 (1993).

[112] Barrat, J.-L., Vuilleumier, R., JDN **12**, 15 (2011).

[113] J.-F. Dufrêche, N. Malikova, M. Jardat, G. Mériguet, E. Dubois, B. Rotenberg, V. Marry, J. Molina, P. Turq, JDN **12**, 263 (2011).

[114] Papyex, Tech. Rep., Le Carbone-Lorraine, 41 rue Jean Jaurés, 92231 Gennevilliers, France.

[115] I. Gameson, T. Rayment, Chemical physics letters **123**, 150 (1986).

[116] J. P. Biberian, M. Bienfait, J. B. Theeten, Acta Crystallographica Section A **29**, 221 (1973).

[117] L. Wirtz, A. Rubio, Sol. State Comm. **131**, 141 (2004).

[118] R. Nicklow, N. Wakabayashi, H. G. Smith, Physical Review B **5**, 4951 (1972).

[119] L. Pauling, *The Nature of the Chemical Bond* (Cornell University Press, 1960).

[120] R. Stockmeyer, H. Stortnik, Surface Science **81**, L315 (1979).

[121] B. Boddenberg, J. A. Moreno, Z. Naturforsch. A **31**, 853 (1976).

[122] R. Stockmeyer, M. Monkenbusch, in *Vibrations at Surfaces* (R. Caudano, J. Gilles, A. Lucas, eds.), pp. 483–498 (Plenum Press, New York, 1982).

[123] B. Boddenberg, R. Gorsse, Zeitschrift fur Physikalische Chemie Neue Folge (1986).

[124] R. Grosse, B. Boddenberg, Z. Phys. Chem. **152**, 1 (1987).

[125] A. S. de Wijn, A. Fasolino, Journal of Physics: Condensed Matter **21**, 264002 (2009).

[126] k. Autor, *Laboratory Course Neutron Scattering Lectures*, Schriften des Forschungszentrums Jülich (Forschungszentrum, Zentralbibliothek, 2010).

[127] R. Martínez-Casado, J. L. Vega, A. S. Sanz, S. Miret-Artés, Phys. Rev. E **75**, 051128 (2007).

[128] J. P. Coulomb, M. Bienfait, P. Thorel, J. Physique **41**, 293 (1981).

[129] R. C. Lord, D. H. Andrews, The Journal of Physical Chemistry **41**, 149 (1937).

[130] R. Zare, *Angular momentum: understanding spatial aspects in chemistry and physics*, George Fisher Baker non-resident lectureship in chemistry at Cornell University (Wiley, 1988).

[131] A. V. Vernov, Pure and Appl. Chem. **65**, 2151 (1993).

[132] A. J. Dianoux, F. Volino, H. Hervet, Molecular Physics **30**, 1181 (1975).

[133] J. O'Dell, B. J. Berne, The Journal of Chemical Physics **63**, 2376 (1975).

[134] J. L. Doob, Annals of Mathematics **43**, 351 (1942).

[135] L. D. Favro, in *Fluctuation phenomena in solids*, *Pure and applied physics*, vol. 19 (R. E. Burgess, ed.), chap. 3, pp. 79 – 101 (Academic Press, New York and London, 1965).

[136] D. Chandler, The Journal of Chemical Physics **60**, 3508 (1974).

[137] J. D. Barnes, The Journal of Chemical Physics **58**, 5193 (1973).

[138] G. Coddens, Phys. Rev. B **63**, 064105 (2001).

[139] F. E. Tuddenham, H. Hedgeland, J. Knowling, A. P. Jardine, D. A. MacLaren, G. Alexandrowicz, J. Ellis, W. Allison, J. Phys.: Condens. Matter, accepted (2009).

[140] J. M. Rowe, K. Sköld, H. E. Flotow, J. J. Rush, J. Phys. Chem. Solids **32**, 41 (1971).

[141] G. Coddens, S. Lyonnard, Physica B: Condensed Matter **226**, 28 (1996).

[142] G. Coddens, Eur. Phys. J. B **31**, 533 (2003).

[143] B. N. J. Persson, Phys. Rev. B **48**, 18140 (1993).

[144] B. N. J. Persson, *Sliding friction. Physical principles and applications* (Springer, Berlin, 2000), 2nd edn..

[145] I. A. Gospodarev, K. V. Kravchenko, E. S. Syrkin, S. B. Feodos'ev, Low temperature physics **35**, 589 (2009).

[146] H. Zaidi, F. Robert, D. Paulmier, Thin Solid Films **264**, 46 (1995).

[147] B. J. Berne, J. A. M. Jr, Molecular Physics **32**, 363 (1976).

[148] S. Chapman, T. Cowling, *The Mathematical Theory of Non-uniform Gases: An Account of the Kinetic Theory of Viscosity, Thermal Conduction and Diffusion in Gases*, Cambridge Mathematical Library (Cambridge University Press, 1970).

[149] P. D. Gennes, Physica **25**, 825 (1959).